

Design of a light weight supporting structure for next generation telescopes

Semester Project Report Spring 2016

Supervision: Professor Chatzi Eleni

Assistants: Egger Adrian, Martín-Sanz Henar

In collaboration with Institute for Particle Physics

Professor Biland Adrian and Müller Sebastian, Ahnen Max and Neise Dominik

Authors:

Georgios Zinas

Spyridon Daglas

June 2016

Acknowledgements

We would like to thank, first of all, our Professor Mrs Chatzi Eleni and her assistants Mr Egger Adrian and Mrs Martín-Sanz Henar for giving us this unique opportunity to work on such a novel project. Moreover, we would like to give a great Thanks to the team of astrophysics, from the Institute of Particle Physics of ETHZ, consisting of the Doctoral candidates Mr Müller Sebastian, Mr Neise Dominik and Mr Ahnen Max. We would like to acknowledge their priceless contribution and their passion in their field of expertise. Last, but not least, we would like to thank Professor Fontana Mario for his helpful advice for the procedure of this research.

Table of contents

1	Introduction	16
1.1	Problem definition	16
1.2	Motivation	17
1.3	Software	18
2	Requirements	19
2.1	Site selection	19
2.2	Target Geometry	20
2.2.1	Imaging Reflector	20
2.2.2	Restricted volumes	22
2.2.3	Mirror facets	23
2.2.4	Image sensor	23
2.3	Geometry margins	24
2.3.1	Image sensor relative to reflector	24
2.3.1.1	z displacement	24
2.3.1.2	x, y displacement	25
2.3.1.3	misalignment x, y	25
2.3.1.4	misalignment in z	26
2.3.2	Image sensor	26
2.3.3	Reflector deformation	26
2.3.3.1	Slow and predictable deformations	27
2.3.3.2	Unforeseen deformations	27
2.4	Movements	27
2.4.1	Fast repositioning	27
2.4.2	Slow tracking	28
2.4.3	Range	28
2.5	Geometry tracking	29
2.6	Maintenance	29
2.7	Threat due to sunlight	29
2.8	Price estimates	30
3	Conceptual work	31
3.1	Existing telescopes	31
3.2	Potential designs	36

3.2.1 "Arecibo-type" design	36
3.2.2 Sebastian's design	38
3.2.3 Altitude-Azimuth design	39
4 Assumptions and parameters of the simulation and design procedure	40
4.1 Loading assumptions	40
4.1.1 Dead Load	40
4.1.2 Wind Load	41
4.1.3 Earthquake Load	43
4.1.3.1 Construction of the design Spectra	43
4.1.3.2 Time History Analysis	46
4.1.4 Temperature Load	49
4.2 Analysis assumptions	50
4.2.1 Linear elastic analysis	50
4.2.2 Elastic analysis taking into account geometric non linearity with the incremental method	50
4.2.3 Large displacements elastic analysis	51
4.2.4 Non Linear analysis algorithms	51
4.3 Design parameters	51
4.4 Materials	54
5 Initial simulations	57
5.1 "Mock" design of a traditional Altitude Azimuth mount telescope (High Energy Stereoscopic System I)	57
5.1.1 Introduction	57
5.1.2 Idea and reasons for this simulation	57
5.1.3 Geometry and simulation	58
5.1.4 Loading of the "mock" design	61
5.1.5 Design procedure	62
5.2 Sebastian's design	64
5.3 Conclusions of initial simulations	66
6 Imaging reflector structure	67
6.1 Mirror facets	67
6.2 Space frame	68
6.3 Alt-azimuth design	72
6.4 TheBigLebowSky design	73
6.5 Ribbed dome	73
7 The Altitude-Azimuth concept	75
7.1 Initial Image Sensor Structure (Quadrupod) for the Altitude-Azimuth concept	75
7.1.1 Truss topology investigation for the optimal design of the Image Sensor Structure (Quadrupod) for the Altitude Azimuth concept.	75
7.1.2 Design of the Image Sensor Structure (Quadrupod) for the Altitude Azimuth concept	77
7.2 Base structural designs for the Altitude-Azimuth concept	85
7.3 Construction of the Altitude-Azimuth concept	87
8 TheBigLebowSky concept	98
8.1 The Main Dish Structure	98

8.2	The Image Sensor Structure-Robocrane	104
8.2.1	Robocrane general	104
8.2.2	Towers	110
8.3	The alternative Image Sensor Structure-Cross-Arch	112
9	Complex Sections Design	117
9.1	Cross-Arch Structure	117
9.2	Tension ring	120
10	Results of the main concepts	123
10.1	The Altitude Azimuth concept	123
10.1.1	Displacements	123
10.1.1.1	Survival situations	123
10.1.1.2	Operational situations	124
10.1.2	Dynamic analysis results	129
10.2	TheBigLebowSky concept	130
10.2.1	Displacements	130
10.2.1.1	Main Dish Structure	130
10.2.1.1.1	Survival situations	130
10.2.1.1.2	Operational situations	131
10.2.1.2	Image Sensor Structure (Robocrane)	132
10.2.1.2.1	Survival situations	132
10.2.1.2.2	Operational situations	133
10.2.1.3	Alternative Image Sensor Structure-Cross-Arch	134
10.2.1.3.1	Survival situations	134
10.2.1.3.1	Operational situations	135
10.2.2	Dynamic analysis results	135
10.2.2.1	Main Dish Structure	136
10.2.2.2	Image Sensor Structure (Robocrane)	136
10.2.2.3	Alternative Image Sensor Structure (Cross-Arch)	137
10.3	Time History analysis results	137
11	Quantity survey and cost estimation	138
11.1	Quantity Survey	140
11.2	Alt-Azimuth	142
11.3	TheBigLebowSky	144
12	Conclusions	146
13	Bibliography	147
13.1	Cables and Arches	147
13.2	Carbon Fibre Reinforced Polymers	147
13.3	Existing telescopes	147
13.4	Loading and site specifics	147

13.5 Truss topology and optimization	147
13.6 Bibliography table	147

Table of tables

Table 1: Basic telescope dimensions in arbitrary units (a.u.)	20
Table 2: Typical mirror facets on IACTs. s is the spacing of the facets, i.e. the flat to flat diameter of the hexagonal facets.	23
Table 3: typical image sensor dimensions of IACTs including all housing components	23
Table 4: Image sensor displacement z.....	24
Table 5: image sensor displacement x, y	25
Table 6: image sensor misalignment x, y	25
Table 7: repositioning velocity	27
Table 8: Tracking velocity.....	28
Table 9: Telescope range.....	28
Table 10: Sampling rate	29
Table 11: Image sensor x, y and z tracking accuracy	29
Table 12: Image sensor tilt in x, y (β), and z tracking accuracy	29
Table 13 Final selected values of wind speed.....	42
Table 14 Weight of the truss configurations examined for the truss optimisation of the initial Image Sensor Structure. (Robocrane)	76
Table 15 Final Cross-Sections and their respective material of the design of the Image Sensor Structure. The analysis results are summarized below.	81
Table 16 Deformation shape of the Image Sensor Structure to Self-Weight and Image Sensor concentrated load.	81
Table 17 Maximum Structure displacements and displacements of the Image Sensor (nodal) for the self-weight and concentrated load of the Image Sensor. (Direction of the displacements according to the coordinate system of the images above).....	82
Table 18 Characteristics of the CFRP material created for the simulation of the Image Sensor Structure.[18]	82
Table 19 Maximum CFRP Structure displacements and displacements of the Image Sensor (nodal) for the self-weight and concentrated load of the Image Sensor. (Direction of the displacements according to the coordinate system of the images above)	83
Table 20 Axial force distribution of the K-Truss chords with only one side of the Image Sensor Structure evident. (Tension: Yellow, Compression: Blue)	84
Table 21 Axial force distribution of the K-Truss diagonals/posts with only one side of the Image Sensor Structure evident. (Tension: Yellow, Compression: Blue).....	84
Table 22 Steps of the Altitude Azimuth design construction. From left to right, pictures 1-5 are the construction steps and 5-10 the rotation of the dish and Image Sensor Structure.	95
Table 23 Modal analysis results for the Alt-azimuth design in the zenith position.....	129
Table 24 Modal analysis results for the Alt-azimuth design in 60° from the zenith position.	129
Table 25 Modal analysis results for the Main Dish Structure.	136

Table 26 Modal analysis results for the Robocrane Image Sensor Structure.....	136
Table 27 Modal analysis results for the Cross-Arch Image Sensor Structure.	137
Table 28 Quantity survey of the Altitude Azimuth design.....	140
Table 29 Quantity survey of TheBigLebowSky Main Dish Structure design.....	140
Table 30 Quantity survey of TheBigLebowSky Robocrane Image Sensor Structure design.....	141
Table 31 Quantity survey of TheBigLebowSky Cross-Arch Image Sensor Structure design.	141
Table 32 Summary of the total weight of the Structures.	141
Table 33: Cost estimation of the Alt-Azimuth design	142
Table 34 Raw Material & Steel Structure cost distribution (top) and Telescope Structure and Optomechanical Systems cost distribution (bottom) of the Altitude-Azimuth design.	143
Table 35 Raw Material & Steel Structure cost distribution (top) and Telescope Structure and Optomechanical Systems cost distribution (bottom) of TheBigLebowSky design.	145

Table of figures

Figure 1 Cherenkov light cone. Basic dimensions.....	16
Figure 2: Alma telescope site in Chile	19
Figure 3: Grid of hexagonal facets	20
Figure 4: z positions of the facets.....	21
Figure 5: Parabolic alignment of the facets	21
Figure 6: Blind center region on principal aperture plane found in ray tracing simulations. The brighter the aperture, the more it contributes to the image. Here the aperture diameter is 50 m. The blind center region is at least 10% of the overall diameter, about 5m in this figure.....	22
Figure 7: Objects in the yellow area will reduce the effective aperture area. The more intense the yellow is, the more important it is to keep this region free. Figure is to scale; aperture diameter is 100 a.u....	22
Figure 8: z displacement	24
Figure 9: x, y displacement.....	25
Figure 10: misalignment x, y	26
Figure 11 Existing telescopes and their major properties.....	35
Figure 12: Separate dish - image sensor structure, dish on the ground	36
Figure 13: Parabolic reflector on the ground - limitations.....	37
Figure 14: Active spherical reflector on the ground.....	37
Figure 15 First drawing of the concept, with basic dimensions.....	38
Figure 16 Main advantages and disadvantages of Sebastian's concept in comparison with a traditional altitude azimuth mount telescope structure.....	38
Figure 17 Daily variation of the wind speed. The speed was averaged over data obtained in five minutes. Dots indicate all data, and thick lines show median of the data.[4].....	41
Figure 18 Cumulative distributions of air temperature at Cerro Chajnantor (cc), Cerro Negro (ng), and the Chajnantor plateau (cb) [6]	41
Figure 19 Modal analysis parameters window in the analysis software	43
Figure 20 Active masses and Newmark combinations with the Complete Quadratic Combination (CQC) modal combination rule.	44
Figure 21 Probability to exceed a certain ground acceleration in 30,50 and 100 years at A.L.M.A. Chajnator site.[9]	44
Figure 22 Elastic horizontal design spectrum Type 1 for $a_g=5\text{m/s}^2$, $\zeta=5\%$, $S=1.2$, $\beta=0.2$, $T_B=0.15\text{s}$, $T_c=0.5\text{s}$ and $T_D=2\text{s}$	46
Figure 23 Elastic vertical design spectrum Type 1 for $a_g=4.5\text{m/s}^2$, $\zeta=5\%$, $S=1$, $\beta=0.2$, $T_B=0.05\text{s}$, $T_c=0.15\text{s}$ and $T_D=1\text{s}$	46
Figure 24 Athens 1999 transversal accelerogram.	47
Figure 25 Kobe 1995 transversal accelerogram.	47
Figure 26 Northridge 1995 transversal accelerogram. (La Habra Station)	48
Figure 27 El Centro 1940 East-West component-transversal accelerogram.....	48
Figure 28 Response History Analysis of Kobe 1995 earthquake and Reileigh damping parameters. .	49

Figure 29 Incremental load application method. (graphical representation)	50
Figure 30 Nonlinear analysis algorithms and their basic parameters	51
Figure 31 Structural Steel S460 properties	54
Figure 32 Cable Steel Y1860 properties	54
Figure 33 Concrete C70/85 properties	55
Figure 34 CFRP HexTow_IM10 with 12K Epoxy properties	55
Figure 35 CFRP of preliminary design properties	56
Figure 36 Rigid links properties	56
Figure 37 Base structure of “mock” design	58
Figure 38 Main dish structure of “mock” design	58
Figure 39 Image sensor structure of “mock” design	59
Figure 40 Counter weight structure of “mock” design	59
Figure 41 Final “mock” design. Analytical model in 90° from zenith position in structural scale.....	60
Figure 42 Positions examined for the “mock” design. From left to right: Zenith, 45° from zenith and 90° from zenith position.	60
Figure 43 Member definition for the “mock” design.....	62
Figure 44 Top view of the analytical model	64
Figure 45 Front view of the analytical model.....	64
Figure 46 3D View of the first model created.	65
Figure 47 Mirror facets geometry.	67
Figure 48 Distance between mirror facets due to projection.....	68
Figure 49 Grid and supporting points	68
Figure 50 Dish grid. (upper nodes).....	69
Figure 51 First layer of the Space Frame	69
Figure 52 MERO Space frame system properties	69
Figure 53 Space Frame. (First and second layer).....	70
Figure 54 Space frame (First two layers with diagonals)	70
Figure 55 Front and side view of the imaging reflector structure.	70
Figure 56 Imaging reflector. 3D representation.....	71
Figure 57 Third (grey) and fourth (red) layer of the space frame for the Altitude-Azimuth design.....	72
Figure 58 Alt-azimuth imaging reflector space frame	72
Figure 59 3D visualisation of the Imaging reflector space frame of TheBigLebowSky design in structural scale. (Rigid links are also visible)	73
Figure 60 3D visualisation of the Ribbed dome.	74
Figure 61 Deformation shape of the ribbed dome structure in 90°. (free rotating supports in the centre)	74
Figure 62 Truss Configurations and their respective nodal displacements. (from top: Simple bar element, Pratt truss, Pratt/Howe combination and K-Truss).....	75
Figure 63 Design of the aforementioned configuration according to ULS for the combination Dead Load and Concentrated Load on the edge. All trusses were designed maximizing the optimization by grouping the design elements according to their function (e.g. Obere Gurt/Top Chord in tension has different cross section than Untere Gurt/Bottom Chord in compression and the same applies for Diagonals and vertical rods).....	76
Figure 64 Image Sensor Structure composed of three cantilevers under a concentrated load in the edge and axial force distribution along the members. The Tension is shown in yellow (green bars) and the Compression in blue (red bar).	77
Figure 65 Final configuration of the triangular K-Truss cantilever. Side view (left) and top view (right). Different colors correspond different elements of the truss on each side.	78
Figure 66 Final configuration of the triangular K-Truss cantilever. Close 3D view. Different colors correspond different elements of the truss on each side.	78

Figure 67 3D view of the Image Sensor Structure System. (Bracing system with light and dark blue, with purple the cables and with orange supporting bars of the triangular truss)	79
Figure 68 3D view of the final Image Sensor Structure in the analysis software.....	80
Figure 69 Design of the Image Sensor Structure. Elements` group.	81
Figure 70 Deformation shape of the CFRP Image Sensor Structure to Self-Weight and Image Sensor concentrated load.	83
Figure 71 Base design No.1. Custom sized elements. (Front view on the left, Side view on the right)	85
Figure 72 Base design No.1. Custom sized elements. (3D view)	85
Figure 73 Base design No.2. Modular Design. (Front view on the left and Side view on the right).....	86
Figure 74 Base design No.2. Modular Design. (3D view)	86
Figure 75 Modules considered for the base design No.2 (Modular design).	86
Figure 76 Comparison of the structural scale for the two base designs.	87
Figure 77 3D visualisation of the base of the Altitude Azimuth design. (Design groups visible)	88
Figure 78 Analytical base model of the Altitude Azimuth design.	88
Figure 79 3D visualisation of the dish rack of the Altitude Azimuth design....	89
Figure 80 Analytical dish rack model of the Altitude Azimuth design.....	89
Figure 81 3D visualisation of the dish space frame of the Altitude Azimuth design. (Design group visible)	90
Figure 82 Front view of the dish space frame of the Altitude Azimuth design. (Design group visible ..	90
Figure 83 Analytical model of the Altitude Azimuth design. Final dish structure without Image Sensor Structure.	90
Figure 84 3D visualisation of the Image Sensor rack of the Altitude Azimuth design. (Design groups visible.....	91
Figure 85 Analytical model of the Image Sensor rack of the Altitude Azimuth design. Final dish structure also visible.....	91
Figure 86 Image Sensor rack dimensions.....	91
Figure 87 Side view of the Image Sensor Structure with cables and CFRP edge.....	92
Figure 88 Dimensions of the Image Sensor Structure (Quadrupod).....	92
Figure 89 Analytical model of the total Altitude Azimuth design.	93
Figure 90 3D illustration of Altitude-Azimuth design in zenith position.	96
Figure 91 3D illustration of Altitude-Azimuth design 60° from zenith position.....	97
Figure 92 Side view of TheBigLebowSky proposal.....	98
Figure 93 Research for the maximal Zenith angle of the dish, taking into account the shadowing of the effect of the columns.	99
Figure 94 Final choice of the maximum zenith angle and basic dimensions.....	99
Figure 95 3D view of the final Main Dish Structure (3D visualization on the left and the analytical model in structural scale on the right)	100
Figure 96 Main dish structure. Analytical model in structural scale and group assignment for design purposes.....	100
Figure 97 Tension ring Cross-Section dimensions	101
Figure 98 Groups of Space Frame dish structure for design purposes. (horizontal/layer elements with blue and diagonals with red)	101
Figure 99 Cables` min/max stress in Dead Load case (left), worst seismic combination (middle) and Dead Load+Operational Wind of 15m/s case (right).....	102
Figure 100 Detail of the Tension ring with the Space Frame and the Cables` connection. (Rigid links with purple, Tension ring with green, Cables with black and Space Frame elements with red and blue) The offsets are with a light blue dashed line evident.	103
Figure 101 Proposal for the detail of the connection of the Space Frame with the Tension ring. (Special elements with grey)	103
Figure 102 Basic dimensions of the Robocrane Image Sensor Structure.	104
Figure 103 3D illustration of the Robocrane Image Sensor Structure.	105

Figure 104 Robocrane housing structure	106
Figure 105 Robocrane Structure. Design groups for the pre-stressing assembly case.	106
Figure 106 Design groups for the Image Sensor Robocrane Structure.....	107
Figure 107 TheBigLebowSky design with the Robocrane Image Sensor Structure. Dimensions and miscellaneous assignments.	108
Figure 108 3D Visualisation of TheBigLebowSky design.....	109
Figure 109 Base module of the steel tower.....	110
Figure 110 Modules used in the upper parts of the steel tower.	110
Figure 111 Steel tower 3D view (left) and in front view. (right)	111
Figure 112 Arched Image Sensor Structure.....	112
Figure 113 Catenary Bending Moments, Axial forces and displacements to its Dead Load (max Uz=- 5.6mm, My,max=3.02kNm, Cmax=1498.8kN)-Proof of the correct function of the catenary curve....	113
Figure 114 Deformation shape in Side view of the two arch solutions. Catenary on the right (Uz,max=- 218.5mm) and Parabola on the left (Uz=-337.4mm) Notable is that for the Catenary Uz,max occurs on the top node. (Image Sensor) The displacement of the same node (Image Sensor) for the Parabola is Uz=+181.8mm.	114
Figure 115 Axial forces and Moment diagrams of the catenary hyperbolic curve with Dead load and Image Sensor concentrated load. (Compression with blue)	114
Figure 116 Axial forces and Moment diagrams of the parabolic curve with Dead load and Image Sensor concentrated load. (Compression with blue)	114
Figure 117 3D visualisation of TheBigLebowSky concept with the Cross-Arch Image Sensor Structure (sun sets/rises)	115
Figure 118 3D visualisation of TheBigLebowSky concept with the Cross-Arch Image Sensor Structure (sun in zenith position).....	116
Figure 119 Deformation shape of the Cross-Arch Structure for the critical load combination of destructive wind in X direction.	117
Figure 120 Global stress analysis for the Cross-Arch Structure.	118
Figure 121 Global stress analysis of the Cross-Arch Structure. (element definition).....	118
Figure 122 Detailed stress analysis for the critical Cross-Section of the Cross-Arch Structure.	119
Figure 123 Deformation shape of the Tension ring for the critical seismic load combination.....	120
Figure 124 Global stress analysis for the Tension ring Structure.	121
Figure 125 Global stress analysis of the Tension ring Structure. (element definition).....	121
Figure 126 Detailed stress analysis for the critical Cross-Section of the Tension ring Structure.	122
Figure 127 Deformation shape of the Alt-Azimuth design in zenith position for the critical survival combination. (1*X+0.3*Y+0.3*Z)	123
Figure 128 Deformation shape of the Alt-Azimuth design in 60° from the zenith position for the critical survival combination. (1*X+0.3*Y+0.3*Z).....	124
Figure 129 Deformation shape of the dead load case for the dead load case.	124
Figure 130 Envelope of the deformation shapes for all operational wind load combinations.	125
Figure 131 Marginal area of the operational displacements of the Image Sensor in zenith position..	125
Figure 132 Dish upper nodal displacements for Dead load case and all operational wind load combinations.	126
Figure 133 Dish upper nodal displacements for Dead load case and all operational wind load combinations.	127
Figure 134 Marginal area of the operational displacements of the Image Sensor in 60° from zenith position.	128
Figure 135 Deformation shape of the Main Dish Structure for the critical survival combination. (0.3*X- 1*Y-0.3*Z).....	130
Figure 136 Deformation shape of the Main Dish Structure for the operational load combinations. (Wind X+ left and Wind X+Y- right).....	131

Figure 137 Front view of the dish upper nodal displacements of the Main Dish Structure for the operational load combination (Wind in X+ direction).....	131
Figure 138 3D view of the dish upper nodal displacements of the Main Dish Structure for the operational load combination (Wind in X+ direction).....	132
Figure 139 Deformation shape of the Robocrane Image Sensor Structure for the survival wind combination in X+Y- direction.....	132
Figure 141 Deformation shape of the Robocrane Image Sensor Structure for the operational load combination. (Wind in X+ direction).....	133
Figure 142 Deformation shape of the Robocrane Image Sensor Structure for the operational load combination. (Wind in X+Y- direction).....	133
Figure 143 Deformations of the Image Sensor (Housing) for the static/dead load situation (left), operational wind in X+ direction (middle) and operational wind in X+Y- direction.	134
Figure 144 Deformation shape of the Cross-Arch Image Sensor Structure for the survival wind load combination. (55m/s wind in X+ direction)	135
Figure 145 Top view of the operational displacements of the Cross-Arch Structure for wind in X+ direction.	135
Figure 146 Top view of the operational displacements of the Cross-Arch Structure for wind in X+Y- direction.	135
Figure 147 Breakdown of costs of steel frame for a typical multi-storey commercial building.....	138
Figure 148: The cost estimation of TheBigLebowSky design	144

1 Introduction

With the aim of pushing the boundaries of science, telescopes have been steadily increasing in dimension. As a result, simply scaling up existing support structures has now become uneconomical. This has prompted investigations into novel types of support structures that can more efficiently carry the loads. As most unwanted deflections of the support structure are assumed to originate from the comparatively heavy image sensor, suspended above the dish and then anchored to the support structure, decoupling these two structures presents itself as a natural means of improvement. Utilizing a novel type of support structure and corresponding construction materials may additionally prove to go hand in hand with additional benefits such as reduced costs, less material use, easier construction and maintainability, as well as better repositioning characteristics.

The aim of this project is to develop a novel support structure for next generation telescopes. Starting with a study of alternatives, a combination of structure and material is then chosen, designed and dimensioned, supported by finite element analysis software. Within the parameters of the constraints, an optimization should be attempted. Finally, as rough cost estimate aims to help evaluate the fundability of the proposed design.

1.1 Problem definition

The next generation telescopes mentioned in this Project belong to the category of imaging air Cherenkov telescopes, or IACTs. The IACTs are used for the observation of the Cherenkov light, which is emitted when charged particles are moving through the atmosphere with a velocity larger than the local speed of light (the speed of light in this medium). An IACT consists of a large upward-facing mirror to focus the Cherenkov light generated by the air shower onto an array of UV-sensitive photomultipliers (image sensor).

This light is emitted on a narrow cone around the direction of the particle. The opening angle alpha is a function of the density of the air and, thus, of the height of emission. It is increasing downwards but is always less than about 1.4 degrees. From each part of the particle track, the Cherenkov light arrives on a ring on the ground. In an air shower, the initial particle interacts with the air atoms, producing many new particles. Most of these particles will be stopped or decay before they reach the ground. The Cherenkov light of all these shower particles moving faster than the local speed of light overlaps on the ground.

From this early stage of the problem definition, the development of a large scale Cherenkov telescope meets its first boundary. As the maximum area projected into the earth's atmosphere has an aperture of approximately 120m, the diameter of the telescope's reflecting area should be equal or less than this maximum value.

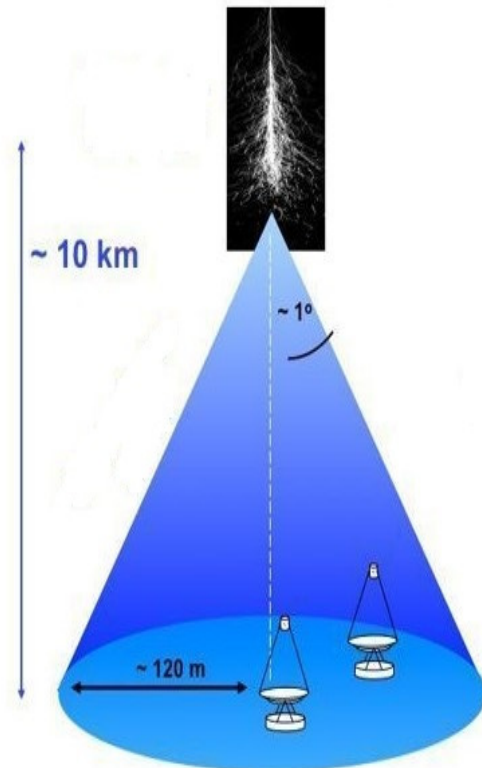


Figure 1 Cherenkov light cone. Basic dimensions.

1.2 Motivation

By pushing the boundaries of science, the development of a new generation of IACTs aims not only in increasing the dimensions of the primary mirror, but also in being able to reposition quickly in every point in the sky.

The size of the telescope and specifically the aperture of the reflecting area affects the image quality the most, as a larger mirror reflects more photons to the image sensor. The repositioning speed affects also the performance of the telescope. The Cherenkov light flash lasts only 5 to 20 ns, thus a fast repositioning mode is of great importance in order to capture as many of these extreme rapid events as possible.

Both the size, as well as the repositioning speed of the telescope are basic parameters to be considered for the definition of the telescope's structure as they affect greatly the structure's stiffness and self-weight. To maintain the structure's stiffness within the required operational levels is becoming extremely difficult, while the size of the telescope increases, especially for the supporting structure of the image sensor. On the other hand, achieving a higher repositioning speed comes in contradiction with the self-weight of the structure. As a consequence, speed and size are contradictory parameters which influence the performance of the telescope and have a great influence to the structural system setting the upper boundaries for the current technologies.

Overcoming these boundaries with the existing methods is feasible, but considering the cost parameter it becomes extremely unprofitable. The use of alternative materials such as the Carbon Fiber Reinforced Polymer for increasing stiffness and reducing the self-weight could be a solution for the large telescopes but considering the cost of such materials, this solution meets also an upper limit in terms of size.

The basic motive for building a ICT of a 50m aperture scale, which is the aim of this Project, was the development of a new image sensor technology. This new technology, based on the recreation of the image due to calculation of the angle of the incident light beams, allows larger tolerances in all degrees of freedom in the focal point of the image sensor. As a consequence, the design of a huge cantilever supporting structure for an almost 30tn image sensor at a distance approximately 75m above the reflector seems feasible even with the use of common materials which will reduce the overall cost. In addition, these large tolerances make possible the development of another revolutionary design, which is based in the idea of separating the image sensor from the telescope's dish and the use of cables for the suspension and movement of them both.

The new technology was the inspiration and the motive behind this Project which is aiming in developing a large-scale and cost efficient Cherenkov Telescope.

1.3 Software

Throughout the whole project the simulation, analysis and design software Autodesk Robot Structural Analysis Professional 2017 (RSAP 2017) was used. Some substructures were also checked with Computers and Structures SAP2000 v18. Due to the complexity and size of the structures a Building Information Modelling (BIM) link between Autodesk Autocad 2017 and RSAP 2017 was created. Moreover, for some details Autodesk Revit 2017 was also used. With this process, a significant amount of time for the creation of the geometry was saved.

An overview of the Programs used for the creation of this project is presented as follows.

Simulation, Analysis and Design

- Autodesk Robot Structural Analysis Professional 2017 (RSAP 2017)
- Computers and Structures SAP2000 v18

Geometry definition

- Autodesk Autocad 2017
- Autodesk Revit 2017

Reports and presentations

- Microsoft Office Word/Excel/Powerpoint 2016

Graphics, 3D design and mathematic formulas

- Adobe InDesign CC 2015 and Photoshop CS6
- SnagIt
- Mathtype 6.9

Citation

- Mendeley

2 Requirements

The requirements of an IACT of such scale were provided by the Institute of Particle Physics. These refer to the site selection for the construction of the telescope, important geometrical parameters, optical restrictions, characteristics of the image sensor and the mirror facets, as well as movement requirements for repositioning and slow tracking. Important characteristics and limitations of the new imaging technology such as the allowed tolerances in all DOF and tolerances of the vibration frequencies were also provided. Additionally, information for the maintenance, potential threads and an upper cost limit were specified. For many of these requirements the astrophysicist's team specified three acceptable levels, which correspond to mandatory, good and perfect compliance.

2.1 Site selection

The Telescope shall be located at high altitude e.g. 5000m above sea level. on the ALMA telescope site in Chile. Firstly, this is because at high altitudes less Cherenkov light from the air showers is absorbed in the atmosphere, which allows having the lowest cosmic ray energy threshold possible. Secondly, the 3D reconstruction power of the Telescope vanishes for features which are far above the aperture. So, the goal is to bring the telescope as close as possible to the air showers and the Cherenkov light production altitudes. Also the site shall have dark night skies without artificial light pollution. Since most cosmic objects that are going to be observed are in the Milky Way's plane or center, the desirable site would be located on the southern hemisphere to have low zenith distances during observation.

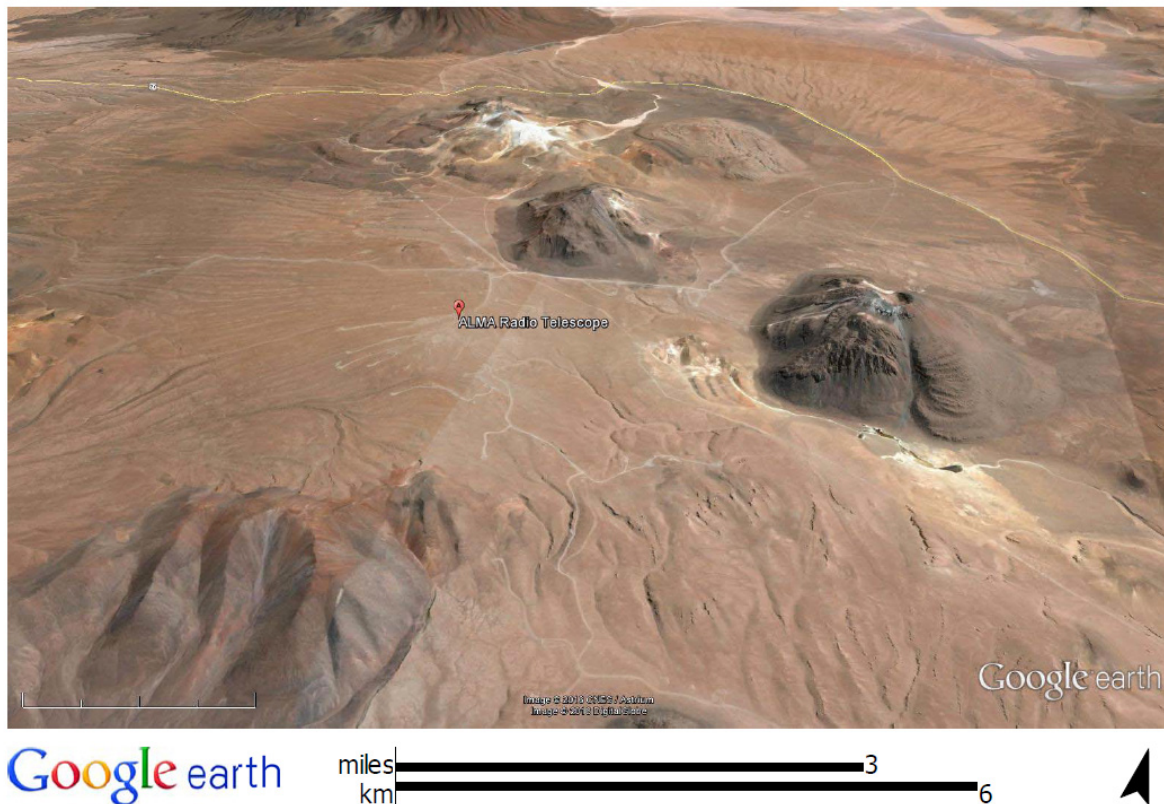


Figure 2: Alma telescope site in Chile

2.2 Target Geometry

In this section the most desirable target geometry of the telescope is defined. All active actuators, which are moving the dish and the image sensor, should try to reach the target geometry during operation. All the relevant for the optics, in the reflector frame, components are being defined. The x-y plane in the origin of the reflector frame is called principal aperture plane. Along the z axis is the optical axis of the reflector. Table 1 shows the basic relative dimensions of the telescope. Fix design keys of the telescope are its focal ratio of $f/D = 1.5$ and its field of view of 6.5° .

Aperture diameter D	100a.u.
Focal length f	150a.u.
F-number of focal ratio, f/D	1.5
Image sensor distance d	159.7a.u.
image sensor diameter	17a.u.
image sensor housing diameter	20.4a.u.
Image sensor field of view α	6.5°

Table 1: Basic telescope dimensions in arbitrary units (a.u.)

The image sensor distance is:

$$d = \frac{1}{\frac{1}{f} - \frac{1}{g}}$$

It depends on the absolute target object distance of about $g \approx 2500\text{m}$. So a telescope of an aperture diameter $D = 50\text{m}$ will have an image sensor distance $d = 77.3\text{m}$ and a telescope of $D = 100\text{m}$ will have $d = 159.7\text{m}$.

2.2.1 Imaging Reflector

A segmented imaging reflector with identical facets is used. All mirror facets have the same hexagonal aperture and focal length f . The x and y position of a mirror facet is defined by the hexagonal grid of the facets.

The relative z components of the mirror facets are defined by a parabolic component

$$z_{P_a}(r) = \frac{1}{4f}r^2,$$

which depends on the facet's distance to the optical axis r . A global offset q is added so that the position of the i -th facet is

$$\vec{m}_i = \begin{pmatrix} r_i \cos(\varphi_i) \\ r_i \sin(\varphi_i) \\ z_{P_i}(r_i) + q \end{pmatrix}$$

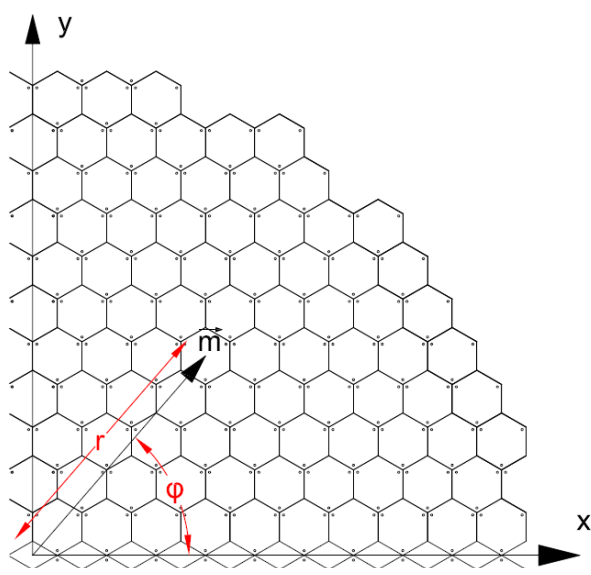


Figure 3: Grid of hexagonal facets

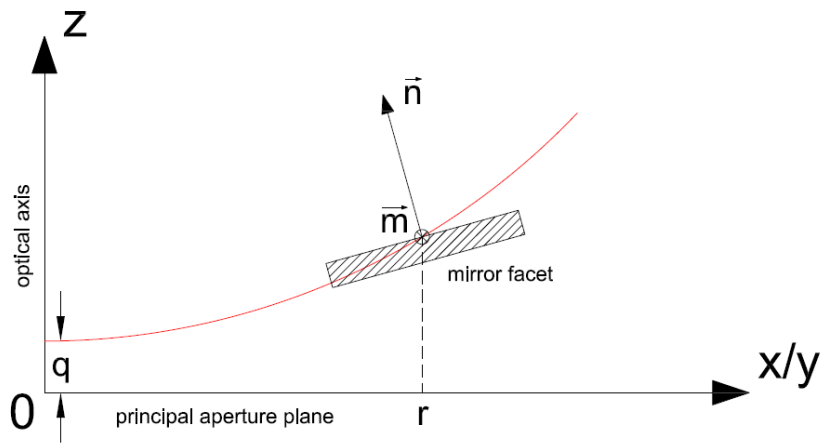


Figure 4: z positions of the facets

The common offset q is chosen so that the average distance between all the N facet centers \vec{m} and the focal point $\vec{f} = (0,0,f)^T$ becomes the focal length

$$f = \frac{1}{N} \sum_i^N |\vec{m}_i - \vec{f}|.$$

The facet orientations along the z axis is defined by the hexagonal grid of the facets. The x and y orientations are chosen so that the i -th mirror facet surface normal

$$\vec{n}_i = \frac{2\vec{f} - \vec{m}_i}{|2\vec{f} - \vec{m}_i|}$$

is pointing towards the $2\vec{f}$ point.

x/y

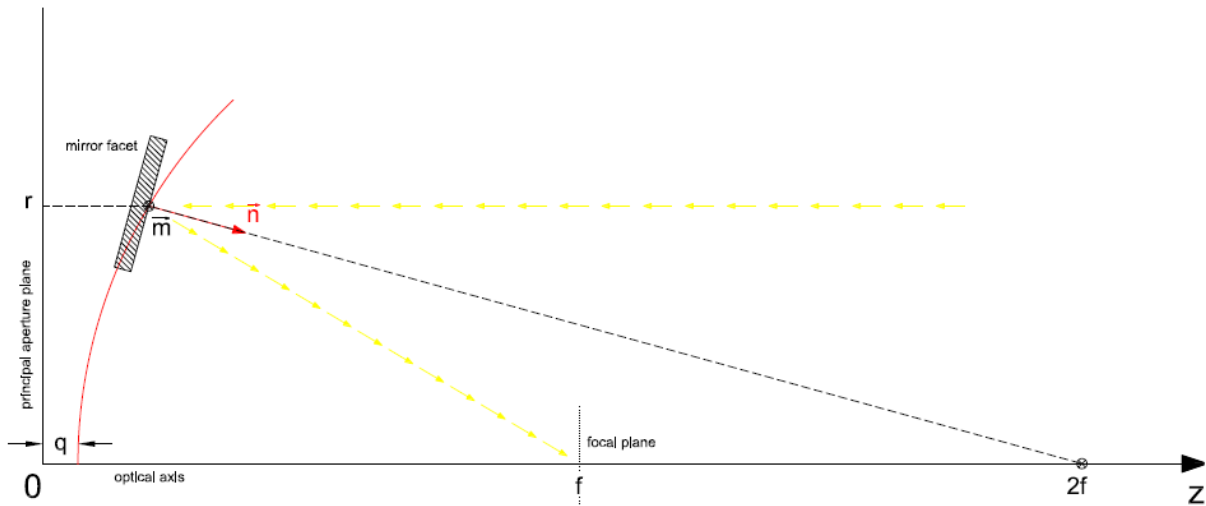


Figure 5: Parabolic alignment of the facets

2.2.2 Restricted volumes

To not reduce the effective aperture area of the telescope, some volumes should be kept free of obstacles. Figure 7 shows the restricted volumes on the telescope in yellow. There is a blind cone in the center of the reflector which can be blocked to have additional support structures, see also Figure 6. Support structures, that have to be in the restricted volumes, should be shaped so that the shadowing is minimal, e.g. using steel cables or at structures which are elongated along the optical axis.

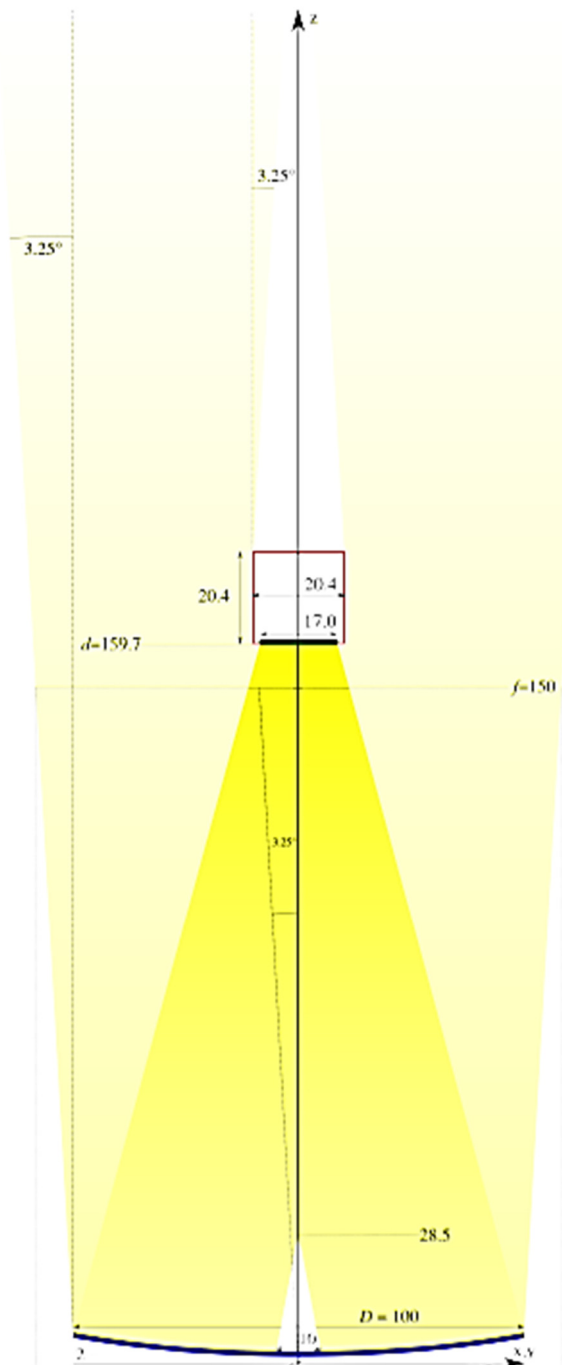


Figure 7: Objects in the yellow area will reduce the effective aperture area. The more intense the yellow is, the more important it is to keep this region free. Figure is to scale; aperture diameter is 100 a.u.

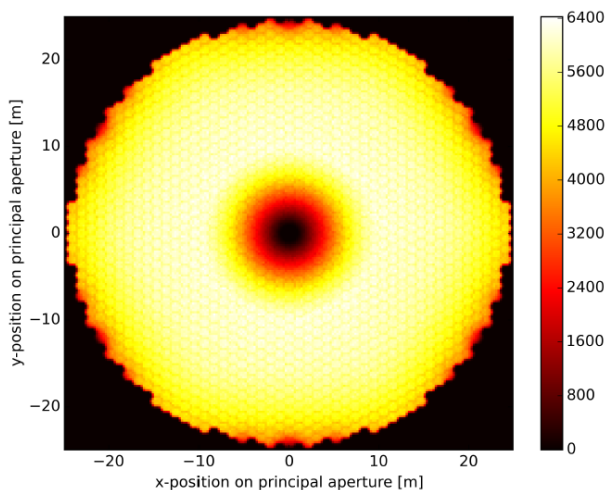


Figure 6: Blind center region on principal aperture plane found in ray tracing simulations. The brighter the aperture, the more it contributes to the image. Here the aperture diameter is 50 m. The blind center region is at least 10% of the overall diameter, about 5m in this figure.

2.2.3 Mirror facets

All mirror facets are the same and are interchangeable with each other. The imaging mirror facets have a focal length f and a hexagonal shaped aperture. Table 2 shows mirror facets and their properties of some telescopes. We will adopt the hexagonal CTA LST mirror facets since they are the biggest facets which have proven to be mass producible today. The weight of a two axis actuator for the facets is 5 kg/facet regardless of the size of the facet.

Type designation	Shape	$A[m^2]$	$s[m]$	$m[kg]$	$\rho_A[kg/m^2]$ raw	$\rho_A[kg/m^2]$ with actuators
MAGIC 1 st gen.	square	0.25	0.50	4.0	16.0	21.0
MAGIC 2 nd gen.	hex	0.96	0.96	13.4	14.0	19.2
VERITAS	hex	0.32	0.61	10.4	32.4	48.0
FACT/HEGRA	hex	0.32	0.61	5.5	17.6	33.7
CTA MST INAF	hex	1.25	1.20	25.0	20.0	24.0
CTA LST INAF	hex	1.97	1.50	45.0	22.8	25.3

Table 2: Typical mirror facets on IACTs. s is the spacing of the facets, i.e. the flat to flat diameter of the hexagonal facets.

2.2.4 Image sensor

The shape of the image sensor is circular. It has pixel apertures of $\Delta\alpha \approx 0,067^\circ$. The image sensor diameter is:

$$D_{sensor} = 2f \tan\left(\frac{\alpha}{2}\right)$$

It is defined by the desired field of view α and the focal length f . We expect the image sensor housing to have a size overhead of 120%. For $D = 100$ a.u. this yields to $D_{sensor} = 17.04$ a.u. and a housing diameter of $D_{sensor\ housing} = 20.45$ a.u. We expect the electric compartment of the image sensor to be rather flat, maybe 2 a.u. to 4 a.u. in height. The cylindrical image sensor housing is only as tall as it is width, because of the Robocrane mount in order to tilt the image sensor. The sensor part itself is more like a flat disc. Table 3 shows the typical image sensor dimensions of IACTs. For the sensor electronic part, we expect our image sensor to be as lightweight as the lightest IACT image sensor units, which is about $\rho_A = 550$ kg/m². However, because of the height of the image sensor housing for the Robocrane mount we better be conservative and expect it to be heavy as $\rho_A = 1000$ kg/m².

Type designation	$A[m^2]$	$m[kg]$	$\rho_A[kg/m^2]$
CAT France	0.19	110	560
MAGIC	0.85	450	530
VERITAS	0.42	-	-
FACT	0.12	175	1458
HESS 1	1.35	800	593
HESS 2	3.14	2800	891

Table 3: typical image sensor dimensions of IACTs including all housing components

2.3 Geometry margins

The novel image sensor of this telescope will allow some misalignments and displacements between the image sensor and the imaging reflector.

2.3.1 Image sensor relative to reflector

2.3.1.1 z displacement

The deviation in z direction of the image sensor distance to its target distance is

$$\Delta d = d_{actual} - d_{target}$$

and may vary since the novel image sensor is able to reconstruct the effect when d_{actual} is known.

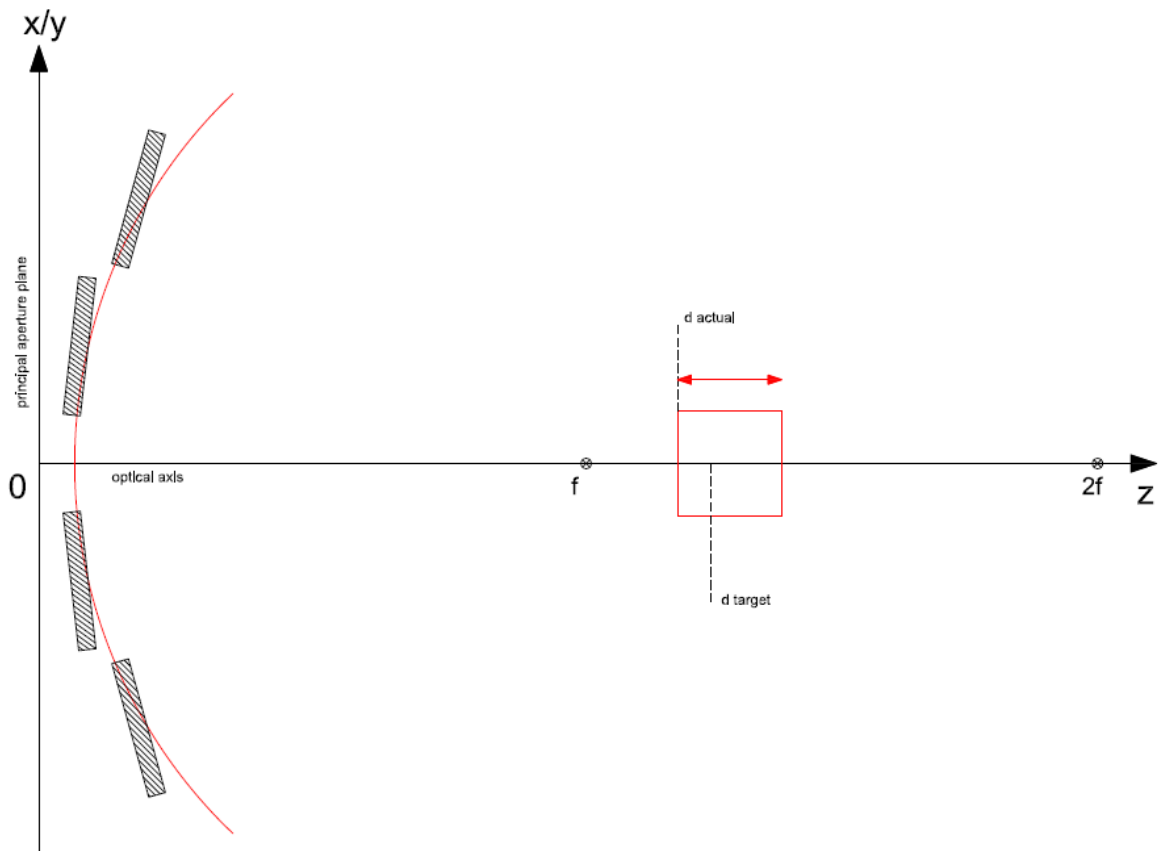


Figure 8: z displacement

Image Sensor displacement z	Δd [a.u.]
Mandatory	$-4.6 < \Delta d < 7.9$
Good	$-2.3 < \Delta d < 3.8$
Perfect	$-1.1 < \Delta d < 1.9$

Table 4: Image sensor displacement z

2.3.1.2 x, y displacement

An image sensor offset Δxy to the optical axis can be accepted, when the x and y position of the image sensor with respect to the imaging reflector are known.

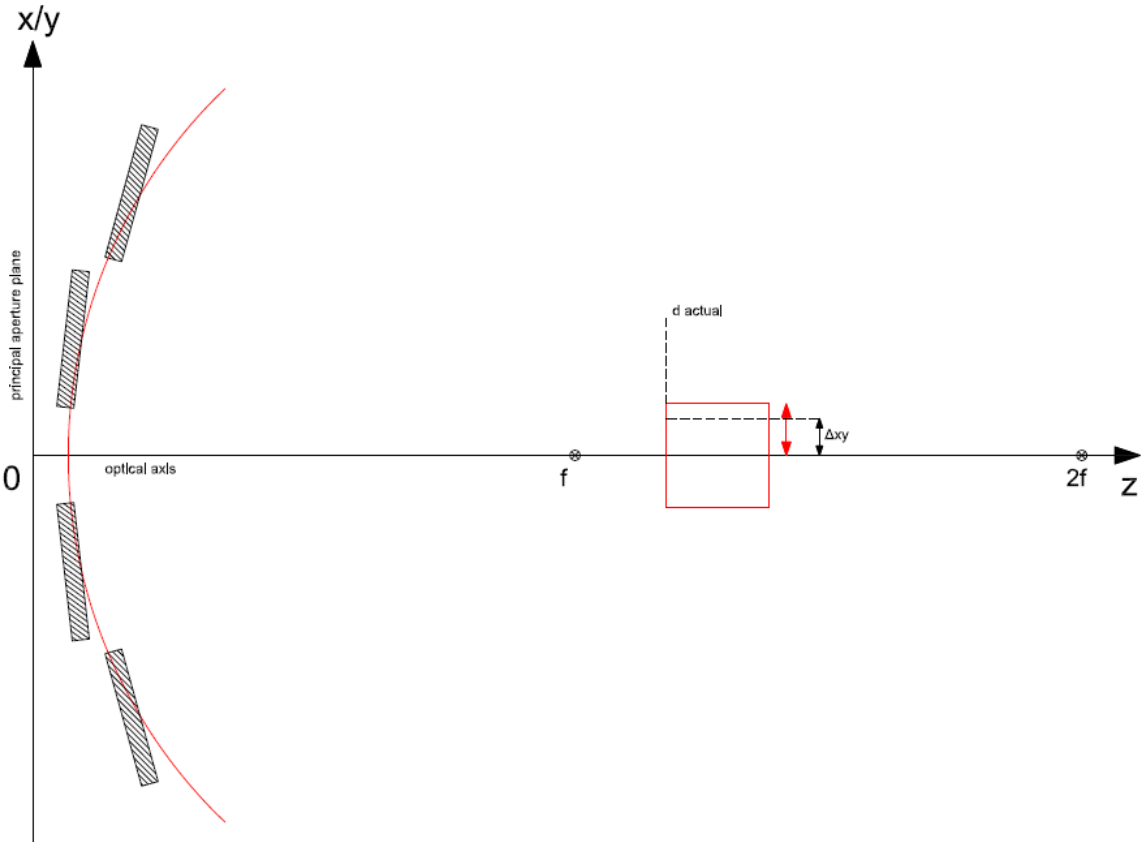


Figure 9: x, y displacement

image sensor displacement x, y	Δxz [a.u.]
Mandatory	< 0.72
Good	< 0.36
Perfect	< 0.18

Table 5: image sensor displacement x, y

2.3.1.3 misalignment x, y

A misalignment β of the imaging reflector optical axis against the image sensor optical axis can be accepted, when β is known. The novel image sensor is still able to reconstruct the image as recorded by well aligned image sensor. However, there is a loss in effective aperture area A_{eff} , since the image sensor has a view cone restriction of which is just enough to fit the aperture once.

image sensor misalignment x, y	β [deg]	A_{eff} [%]
Mandatory	< 3.0	90.0
Good	< 1.5	95.0
Perfect	< 0.75	97.5

Table 6: image sensor misalignment x, y

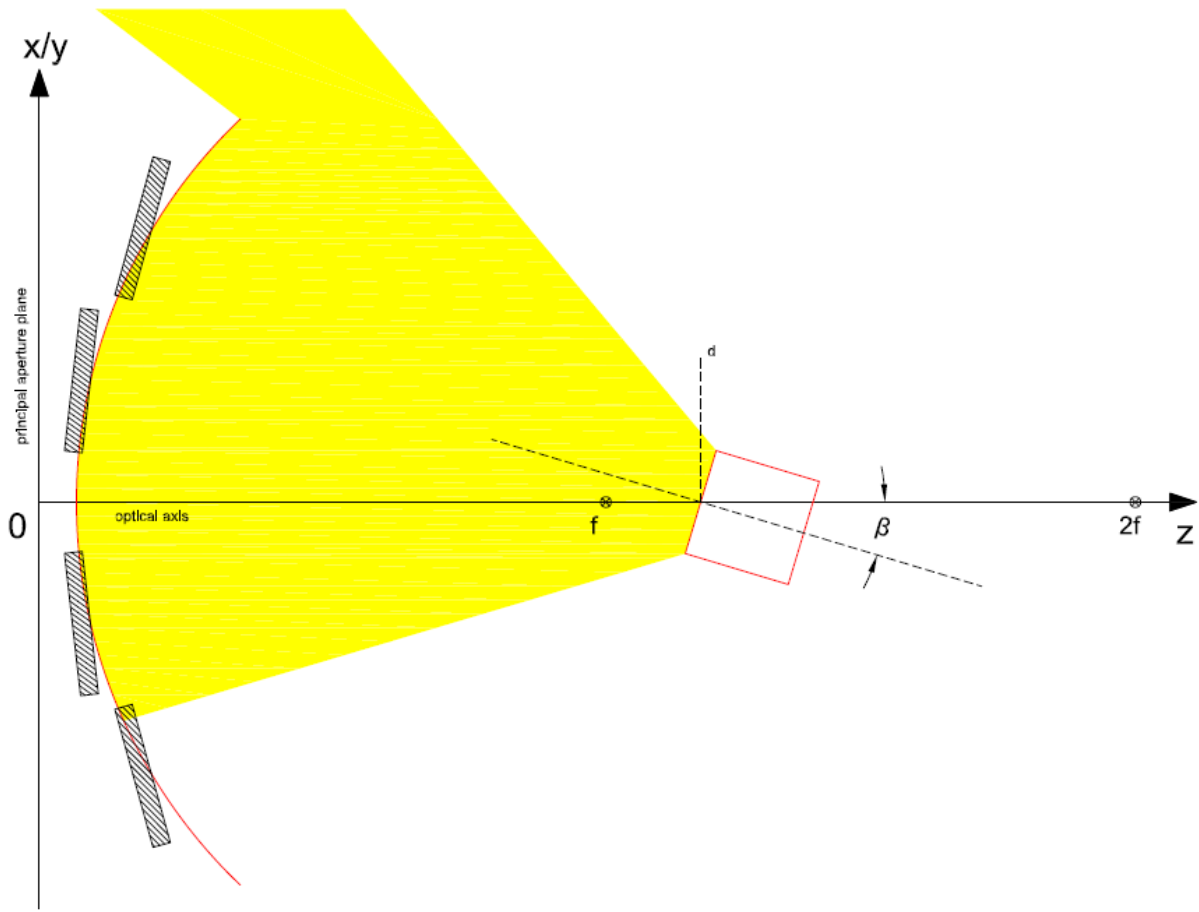


Figure 10: misalignment x, y

2.3.1.4 misalignment in z

The image sensor may be arbitrarily rotated along the z axis, as long as the rotations are known.

2.3.2 Image sensor

The image sensor itself is assumed to be stiff, i.e. the image sensor plane does not bend or deform more than 0.05 a.u. across its diameter.

2.3.3 Reflector deformation

As a rule of thumb, the actual tilt of a mirror facet against its target tilt, caused by deformations of the dish, shall not exceed $\frac{\Delta\alpha}{2} \approx 0,034^\circ$, i.e. half the image sensor pixel size.

$$\arccos(\vec{n}_{target} \cdot \vec{n}_{actual}) < \frac{\Delta\alpha}{2}$$

2.3.3.1 Slow and predictable deformations

When using mirror facet actuators, slow and predictable deformations of the dish support structure which even exceed $\frac{\Delta\alpha}{2}$ can be accepted, as they might be caused by gravitational slump. Here, slow means, that the mirror actuators can easily keep up with the deformations of the dish while the telescope is slowly tracking a source. (The MAGIC actuators can tilt a facet with $0.5^\circ / \text{s}$). Predictable means, that the deformation will always be the same for a given telescope orientation, so that they can be learned once and then be applied later. (This is what is successfully done on the MAGIC telescope). In case there are no deformations above $\frac{\Delta\alpha}{2}$ anyhow, the case of neglecting the mirror facet actuators could be considered, which would simplify the maintenance of the telescope a lot and also reduce its initial cost.

2.3.3.2 Unforeseen deformations

Deformations of the reflector dish by e.g. wind cannot be foreseen. In general, the relative additional tilts of the facets shall not exceed $\frac{\Delta\alpha}{2} \approx 0,034^\circ$. Ray tracing simulations of the deformed dishes could be performed to see the effect on the imaging performance. A feedback loop of mechanical deformation simulations and optical simulations could be also established for the optimization of the overall performance of the telescope.

2.4 Movements

The telescope has two different modes of movements during operation. A slow mode to observe sources on the sky dome, and a fast mode to switch between the sources. The avoidance of singularities in the inverse kinematics near the zenith is desirable. For example, the zenith singularity on the classic Altitude-Azimuth mount hinders fast repositioning.

2.4.1 Fast repositioning

When the telescope is pointing to a different source on the sky dome, the image sensor is not recording. During the fast repositioning, the target geometry does not need to be fulfilled. A high speed repositioning of $90^\circ / \text{min}$ will enable gamma ray burst hunting, which would be a nice to have but is not mandatory.

Fast repositioning velocity	$\Theta[\text{deg}/\text{min}]$
Mandatory	9
Good	30
Perfect	90

Table 7: repositioning velocity

2.4.2 Slow tracking

When the telescope is slowly tracking a source on the sky dome, it is only counteracting the rotation of the earth $\Theta_{Earth} = 0.25^\circ / \text{min}$. During slow tracking, the telescope has to try to reach its target geometry. The telescope image sensor is only recording air showers in the slow tracking mode. For some observations, it is useful to move around a source in a spiral movement, which demands for telescope tracking velocities Θ which are three times higher than Θ_{Earth} .

Tracking velocity	$\Theta[\text{deg}/\text{min}]$
Mandatory	0.25
Good	0.5
Perfect	0.75

Table 8: Tracking velocity

2.4.3 Range

For the full azimuth range, the telescope should reach zenith distances Θ as high as 45° .

Zenith distance	$\Theta[\text{deg}]$
Mandatory	30
Good	45
Perfect	60

Table 9: Telescope range

2.5 Geometry tracking

All displacements and misalignments of the image sensor with respect to the imaging reflector can only be accepted when the tracking of the actual position and orientation of the image sensor relative to the reflector is possible. A sampling rate to track these displacements and misalignments is needed, one order of magnitude higher than the dominant Eigen frequencies of the structure. The MAGIC telescope arch has a Eigen frequency of ≈ 1 Hz. Assuming that the dominant Eigen frequencies on the developed bigger telescope will not be higher, a sampling rate f_{sample} of 10 Hz might be sufficient.

Sampling rate	f_{sample} [Hz]
Mandatory	10
Good	25
Perfect	50

Table 10: Sampling rate

Image sensor x, y and z tracking accuracy	[a.u.]
Mandatory	$\pm 7.2 \cdot 10^{-3}$
Good	$\pm 3.6 \cdot 10^{-3}$
Perfect	$\pm 1.8 \cdot 10^{-3}$

Table 11: Image sensor x, y and z tracking accuracy

Image sensor tilt in x, y (β), and z tracking accuracy	[deg]
Mandatory	± 0.03
Good	± 0.015
Perfect	± 0.0075

Table 12: Image sensor tilt in x, y (β), and z tracking accuracy

A tracking implementation must be able to work at night without artificial illumination. No light in the wavelength range of 200 nm to 1200 nm shall be emitted to track the positions, otherwise the image sensor will be blinded. If artificial illumination is mandatory for the tracking, the duty cycle of the illumination system shall be as small as possible, best below 1%.

2.6 Maintenance

Since the surfaces of the mirror facets degrade over time and the actuators of the facet will break over time, the mirror facets shall be reachable from below, for maintenance.

2.7 Threat due to sunlight

The main imaging reflector dish of the telescope can be a threat when it projects the image of the sun on nearby objects. For a focal ratio of 1.5, the imaging reflector can project an image of the sun with up to $6 \text{ MW} / \text{m}^2$.

$$\frac{I_{\text{sun image}}}{I_{\text{solar constant}}} = \frac{\text{aperture area}}{\text{image area}} = \frac{(D^2/4)\pi}{(DF\tan(0.25^\circ))^2\pi}$$

A telescope mount where the image sensor is mounted independently of the imaging reflector, is profitable in the sense that the image sensor could be separated from the dish and be parked in a save position. As long as the imaging reflector lies flat on the ground, it cannot incinerate objects on the

ground. However, it might still heat up the nearby support structures. Solutions which do not need additional mechanics, like e.g. domes or lids, would be preferable.

2.8 Price estimates

The CTA mirror facets cost about 3000 € / m² including the actuators. The raw silicon photo electric converters for the image sensor cost about ≈ 640'000 €. For a $D = 50$ m telescope, the silicon for the image sensor costs ≈ 32'000'000 €.

3 Conceptual work

In this chapter a review of the existing telescope structures is being made as an attempt to find new ideas for the development of the innovative extremely large structure of the Cherenkov telescope. The first part handles with the different types of the existing telescopes and highlights the aspects that contribute the most to the development of the various structural systems. An overview of these characteristics is presented to underline the differences of these structures. In the second part, the potential designs which serve the purpose of this project are presented along with their evaluation which lead to new concepts being evolved or to the exclusion of some of the initial ones.

3.1 Existing telescopes

The existing telescope structures that are being reviewed in this section are divided into three categories according to the wavelength and into two categories with respect to their mount. The Gamma-ray range telescopes to which the Cherenkov telescopes belong are not the only ones to be reviewed. The optical and radio telescopes were also included as they have larger apertures and bigger structural systems. Trying to find which particular characteristics contribute the most to the size of these telescopes would be extremely helpful for the purpose of this Project. The telescope mount has an important role not only to the size but also affects the whole concept from the supporting structure, the separation or not of the imaging reflector and imaging sensor to the movement of the telescope, its range and its operational goals in general. For that reason, the traditional alt-azimuth designs as well as designs with separate imaging reflector and sensor were included (e.g. Arecibo).

With respect to the requirements chapter, a table of the most important characteristics was constructed. These include the imaging reflector diameter, the optical layout, the focal length and the focal ratio, information about the image sensor and the mirror facets, the mount type and the movement of the telescope, the materials used in the various structures and the overall weight. Moreover, some special remarks regarding the structural system of the investigated telescopes were made. As mentioned before this information will serve as a guideline and will form the wider frame for reaching the projects aim.

Telescope	View	Type	Dish	Focal length, f/D	Image sensor, mirror facets	Altitude, Azimuth drive	Material	Overall weight	Special structural attributes
H.E.S.S II	 A large red steel truss structure supporting a large parabolic dish antenna.	Gamma-ray	Dish dimensions 32.6m×24.3m, D=28m effective aperture, parabolic layout	f=36m f/D≈1.2	2.8 tn image sensor weight, 875 hexagonal facets	100°/min rack and pinions, 200°/min bogies on 36 m rail	Steel space frame	580tn (mirror facets 21.9tn)	Traditional alt-azimuth design, trusses used the quadrupod structure
MAGIC	 A large white parabolic dish antenna mounted on a green hillside.	Gamma-ray	D=17m, parabolic layout	f=17m f/D≈1.2	450kg image sensor weight, 943 square mirror facets	1 servomotor for altitude (+105° - 80°), 2 servomotors for azimuth, 6 bogies in a hexagonal array≈24Ø, very fast repositioning≈20sec	CFRP tubes (80-100mm), $\frac{1}{2}$ defor-mations compared to aluminum, $\frac{1}{3}$ compared to steel	≈60tn, main structure≈8.7 tn	2-layer dish space frame in tetrahedral layout (stiffest basic element), 2630 CFR tubes and 950 nodes, rod – knot system MERO, 26 cables in arch structure
VERITAS	 A large blue parabolic dish antenna supported by a complex steel truss structure.	Gamma-ray	4 reflectors ×12m (array), Davies-Cotton layout	f=12m, f/D≈1.0m	0.42m ² image sensor, 350 hexagonal mirror facets on each reflector	altitude-over-azimuth positioner and tubular steel Optical Support Structure (OSS), max slew speed 0.3°/sec	Steel space frame	OSS weight, mirrors, counter-weights and detector ≈16tn	Quadrupod camera support

Effelsberg	 A large white parabolic dish antenna mounted on a tall steel truss tower, set against a backdrop of green hills under a blue sky with white clouds.	Radio	D=100m paraboloid	f=30m f/D=0.3	2352 panels	64m azimuth track 30°/min, 28 m radius elevation gear 7°-94°, 16°/min	Steel	3200 tn overall weight, tillable part≈195;0tn	Achieve high accuracy by incorporating intelligent softness, homology, inverted umbrella structure
Parkes Observatory	 A large yellow parabolic dish antenna mounted on a tall concrete supporting tower, set against a backdrop of green trees and a blue sky with white clouds.	Radio	D=64m paraboloid	f=24m, f/D=0.31	3 types of different panels according to target observing wavelength	Az: 0-360 deg., El: 30.5-88.5 deg.	Steel dish, reinforced concrete supporting tower	Dish: 300tn Counter-weights: 475tn, Total weight: 1000tn	Circular space truss backup structure, central hub, tripod cabin support, not optimal resulting reflector deformations, limited movement range
Green Bank	 An aerial view of a large white parabolic dish antenna mounted on a tall steel truss tower, set against a backdrop of green trees and a blue sky with white clouds.	Radio	D _{eff} =100m, offset geometry	f/D (prime) = 0.29 f/D (Gregorian) = 1.9	2004 panels	Az: 16 wheels, 64m rail, ±270°, 40°/min El: 46m elevation axle, 30m radius gear, 5°-95°, 20°/min	Steel	8500tn	Rocking chair design

LMT		Radio	D=50m, Cassegrain	f/D≈0.30	180 active surface segments arranged in 5 concentric rings, 2.5m secondary mirror	-	Steel sub frame and axial bars, aluminum base plate	-	High precision measurements due to the active reflector surface concept, extreme wind conditions
Lovell		Radio	D=76.2m, paraboloid	f=23m, f/D≈0.3	Collecting area 4560m²	107.5 diameter rail track, 15°/min, 50.5m elevation axis height, 10°/min	Steel	Total weight 3200tn Bowl weight 1500tn	Elevation bearings distant, huge rim girder to reduce the sag
Arecibo		Radio	D=305m single aperture, spherical reflector	f=150m	38778 aluminum panels, collecting area 73000m²	separate structures for reflector and receiver, bow shaped track 93m long for the azimuth arm	Steel for the receiver and the cables, Reinforced concrete Towers	Receiver 900tn	Mesh of steel cables supporting the panels

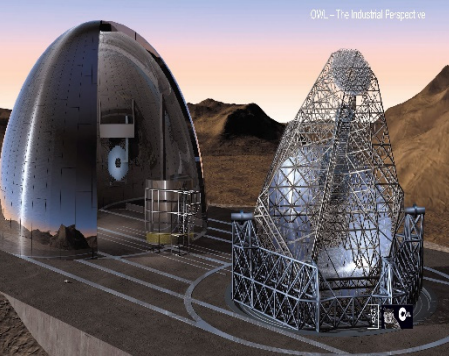
E-ELT		Optical	D=39.3m D _{sec} =4.09m D _{tert} =3.75m	f=34.5m f/D≈10	Collecting area 978 m ² 798 hexagonal segments 1.45m, 50mm thick, 6000 actuators	A rocking chair mount, hydrostatic type, Az: 34m and 51.5m tracks, central pier	Steel	Main structure 2800tn, Altitude structure 1498tn	Dome for protection, low Eigen frequency of 2.9 Hz,
OWL (conceptual design)		Optical	D=100m	f=175m f/D≈17.5	Collecting area ≈6000m ²	Azimuth structure embedded in to the foundation, central azimuth roller bearing & annular tracks, two altitude cradles, two roller bearings	Steel	Moving weight: 14800tn	Fractal design (base module), altitude movement by filling the spherical foundation, heavy construction, ropes for stiffness

Figure 11 Existing telescopes and their major properties.

3.2 Potential designs

After reviewing the existing literature on big telescopes, some useful ideas came up regarding the design of the supporting structure. A Cherenkov telescope of such scale has never been built or designed before, therefore new ideas for the whole telescope structure would have to be implemented. A traditional telescope structure with an Altitude-Azimuth mount and a structure with separate dish and image sensor (Arecibo-type) are going to be investigated in this chapter. Test models for both of these designs are going to be developed initially in the scale of the existing telescopes (H.E.S.S. I, Arecibo Observatory) and afterwards these models will be scaled up to meet the target size of dish diameter $D = 50\text{m}$. This chapter refers to the initial telescope design approaches. A short description of the different concepts will be given and the best alternatives will be investigated more later.

3.2.1 “Arecibo-type” design

In order to overcome the limitations of a large scaled structure regarding the deformations, the stiffness and the movement of the telescope the idea of separating the image sensor from the dish seems very promising. Inspiration to the development of the first design was the design of the Arecibo Observatory. The term “Arecibo-type” was given for that reason although the designs which are going to be presented in this section differ a lot from the original Arecibo design.

The imaging reflector would be supported on the ground on rails which will allow its movement and transfer the loads directly to the foundations. The imaging sensor would be suspended with pre-stressed cables from towers. To this point there are two options regarding the geometry of the imaging reflector, which will result to two different design concepts.

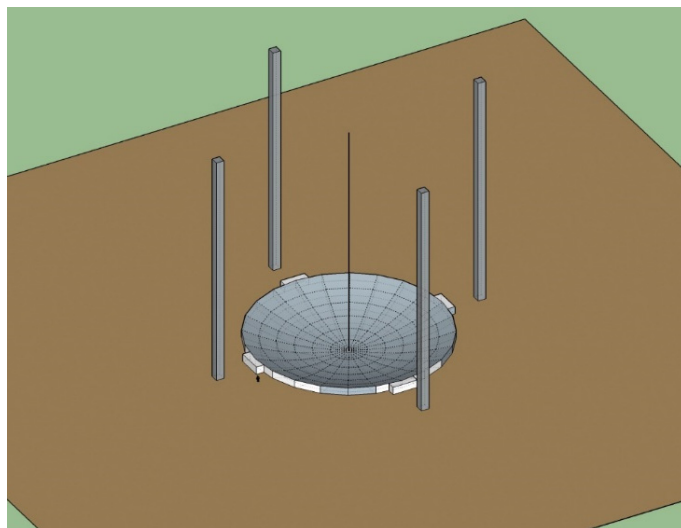


Figure 12: Separate dish - image sensor structure, dish on the ground

The first option is the imaging reflector to have a diameter of approximately 50 m or larger and a parabolic geometry. By placing this dish on the ground the required movements of the telescope had to be investigated. In order for the dish to be placed on the ground and also to be movable in a satisfying range, huge excavations or extremely high velocities would have to be achieved. For these reasons, presented also in Figure 13: Parabolic reflector on the ground - limitations **Error! Reference source not found.** this first option had to be excluded.

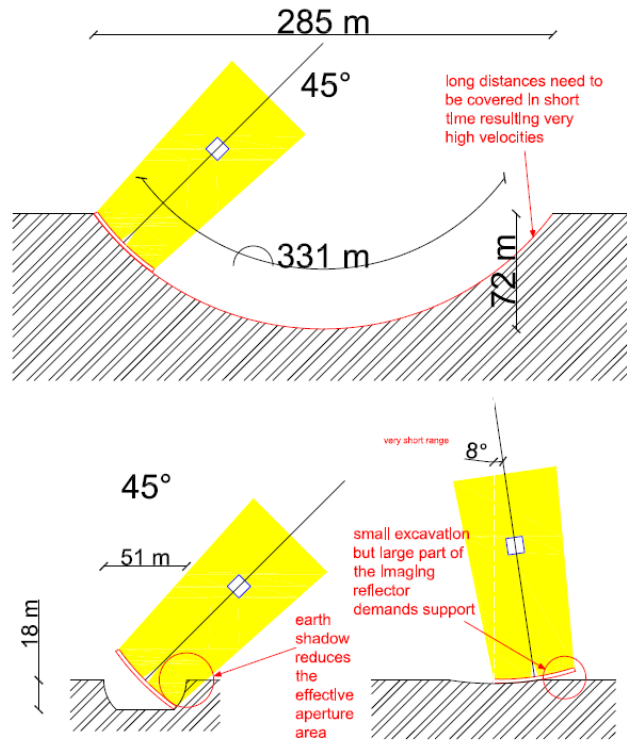


Figure 13: Parabolic reflector on the ground - limitations

The second option is to design a much larger spherical reflector, which will have the ability to deform itself and partially take the parabolic shape required for the operation of the under development telescope. This approach resembles more the Arecibo design (large spherical reflector on the ground – image sensor suspended with cables) but with the main difference that the reflector can deform itself. This concept of an active reflector is going to be constructed for the FAST telescope in China and although it is very promising it has also some significant restrictions. One of them is that it demands the construction of a huge spherical reflector which should be able to support the actuators and the mirror facets, which in this case of a Cherenkov telescope are much heavier than these in the FAST case (Radio telescope). The mirror facets not only are heavier, but also very expensive. The idea of having a large number of mirror facets that will not be usable, as the image sensor focuses on only one part of the spherical area, makes the whole concept not very attractive. The technology for an active reflector is an innovative one and is going to be implemented for the first time in the FAST telescope. This fact adds one more drawback to the whole concept, as the not yet tested technology increases the uncertainties for putting it into effect, even in the case of a radio telescope (Fast), more so for the case of a Cherenkov telescope. As a consequence, the concept of the active spherical image reflector is also excluded from any further investigation.

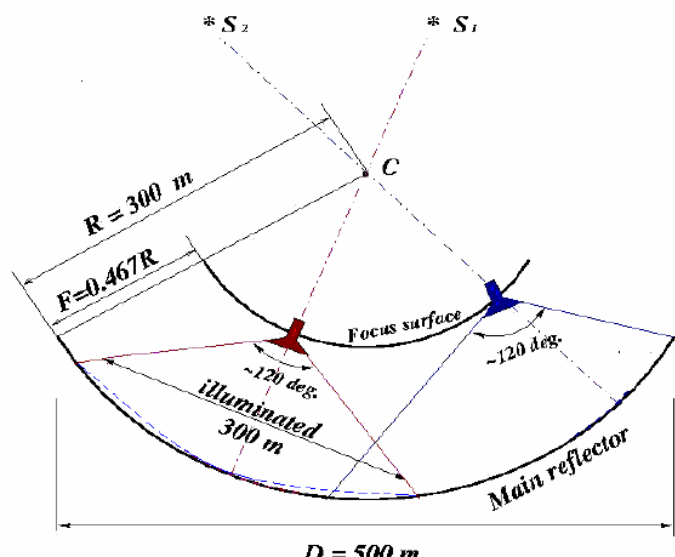


Figure 14: Active spherical reflector on the ground

3.2.2 Sebastian's design

The basic idea for this design, comes from Sebastian Müller a PhD Student at the Institute for Particle Physics at ETH. The concept behind it is a separate Image Sensor Structure holding and positioning the Image Sensor via Cables over the dish, which is supported and positioned by its own structural system.

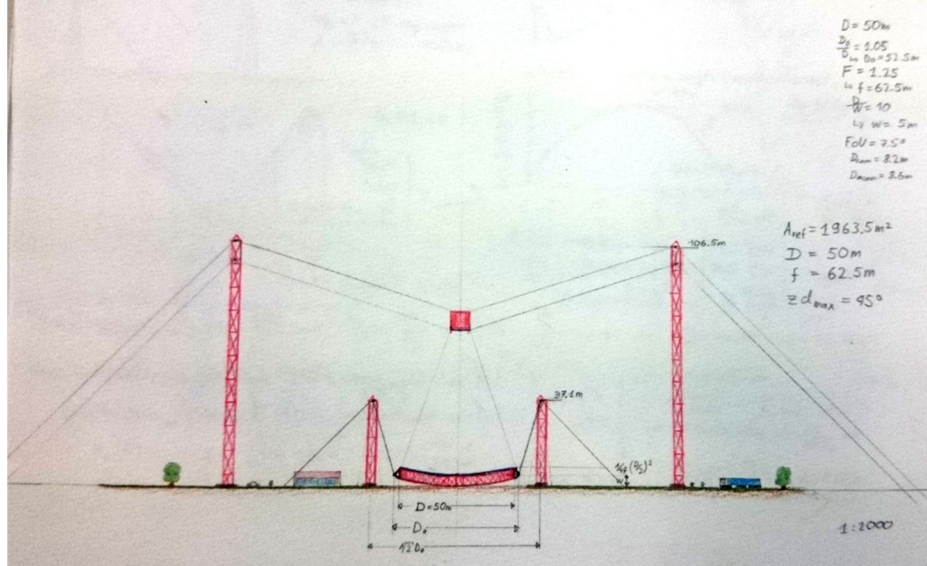


Figure 15 First drawing of the concept, with basic dimensions.

This concept poses a lot of advantages both in the astrophysics side, as well as in the structural engineering side. However, many disadvantages occur too, that need to be examined further in detail, in order to evaluate the realization of such a design.

Below, there is a list of advantages and disadvantages of this concept in comparison with a traditional Altitude-Azimuth mount telescope.

Advantages	Disadvantages
<ul style="list-style-type: none"> Almost no shadowing on the dish effective area. 	<ul style="list-style-type: none"> Very soft and potentially unstable systems, especially to dynamic loading such as wind.
<ul style="list-style-type: none"> By introducing two separate structural systems, the decomposition of the structural problem in smaller sub-problems is easier. (e.g. The deformations of the dish do not influence the Image Sensor position.) 	<ul style="list-style-type: none"> Controlling the deformations of the Image Sensor structure and aligning them with these of the dish, introduces a challenge to Control and Robotics science, especially for a structure of such a large size.
<ul style="list-style-type: none"> Potentially easier Image Sensor and mirror facets' maintenance. 	<ul style="list-style-type: none"> Pre/Post tensioned cables need surveillance and monitoring, which results in higher maintenance need.
<ul style="list-style-type: none"> Potentially more cost efficient. 	<ul style="list-style-type: none"> Potentially expensive mechanical parts and electrical equipment.
<ul style="list-style-type: none"> Potentially faster construction, due to modular capabilities of the structures. 	<ul style="list-style-type: none"> Impossible to cover 100% of the celestial concave, as dish rotation is limited to less than 90°.

Figure 16 Main advantages and disadvantages of Sebastian's concept in comparison with a traditional altitude azimuth telescope structure.

3.2.3 Altitude-Azimuth design

An alt-azimuth mount is a simple two-axis mount for supporting and rotating the telescope about two perpendicular axes – one vertical and the other horizontal. Rotation about the vertical axis varies the azimuth (compass bearing) of the pointing direction of the instrument. Rotation about the horizontal axis varies the altitude (angle of elevation) of the pointing direction.

In the case of traditional alt-azimuth design an existing Cherenkov telescope was selected (H.E.S.S. I) and simulated with a FEM model. The aim was to try to scale up the structure to see its behavior and its limits.

4 Assumptions and parameters of the simulation and design procedure

4.1 Loading assumptions

Loading conditions in our structures are divided into:

- Dead load due to the structure's self-weight
- Dead load of the mirror facets including the actuators
- Dead load of the image sensor
- Accidental earthquake load
- Operational wind load
- Survival wind load
- Temperature fluctuation load

Apart from the dead load, all other loads are site dependent. For the purpose of this research, the site chosen is located in the Atacama Desert in Chile, exclusively due to astrophysical reasons such as altitude, distance from external lighting sources, position on the earth globe etc. as described in 2.1. More precisely the site will be located in Chajnator area close to ALMA Radio telescope. (Latitude: -23.0234342, Longitude: -67.7538335, Sea level: ~5000m)

4.1.1 Dead Load

The dead load of the construction was used, taking into account the specific weight of the materials.

- Structural Steel 77kN/m³
- Cables' Steel 65kN/m³
- Concrete 25kN/m³

For the Image Sensor dead load, an Image Sensor of 25tn mass was used and simplistically the conversion to weight has been done with a $g=10\text{m/s}^2$, equaling a total weight of 250kN.

Finally, for the dead load of the mirror facets and the actuators, the surface density of the CTA large size telescope was used as a reference, which was considered simplified 25kg/m². [1][2][3] Using the exact simplified procedure as above and multiplying with the mirror facet area, the total weight of 60kg per mirror facet is calculated. Taking into account that each mirror facet is supported on 3 nodes of the upper layer of the space frame, a concentrated weight of 0.6kN is assigned to each upper layer node. (each node supports one third of the weight of three neighboring mirror facets. The actuators are taken into consideration as a portion of the mirror facet self-weight)

4.1.2 Wind Load

Wind loading in telescope structures is divided in two different categories. The first one resembles the operational phase (operational wind load), whereas the second one is considered for the ultimate limit state of the structure. (survival wind load) Even though one could assume that the second category is the most influential for the design, this is not true due to the fact that the ultimate limit state of the structure depends mostly on earthquake loading. So, the operational wind plays the most important role in the overall behavior of the structure. The reason for that is mainly the accuracy of the image sensor and the resulting pointing errors, due to the oscillations of the image sensor structure. As a result, it is deemed necessary that the appropriate stiffness is provided, so that the oscillations in serviceability limit state are kept within the limits specified by the sensor manufacturer.

The wind analysis of the structure was conducted with the simplified Computational Fluid Dynamics procedure of Autodesk Robot Structural Analysis 2017 assigning a constant vertical wind profile along the height of the structure. In order for the program to calculate the wind pressure loads on the different structure elements the wind speed was needed, so a survey of the average wind speeds from different sources was conducted.

In the first study the wind speed in this site was measured from April 2006 to April 2007 and was averaged over five minutes. Wind was always coming from the west and had a peak around the evening.[4]

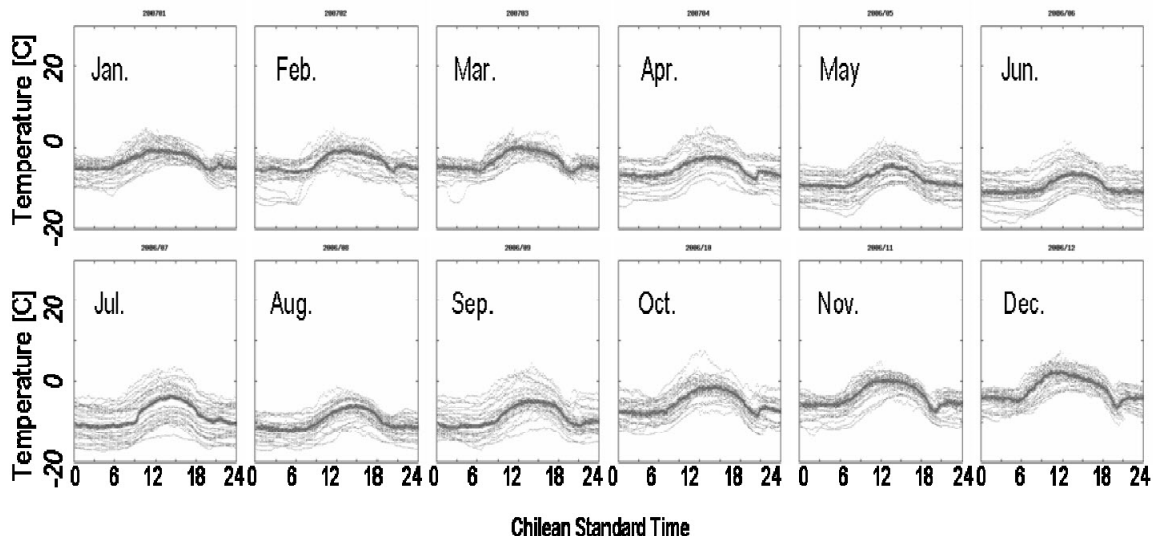


Figure 17 Daily variation of the wind speed. The speed was averaged over data obtained in five minutes. Dots indicate all data, and thick lines show median of the data.[4]

Another study conducted from May 1995 through April 1996 showed around the same results with a median of 9m/s. The data were recovered in 10 minute cycles.[5]

A final research confirms the previous results.

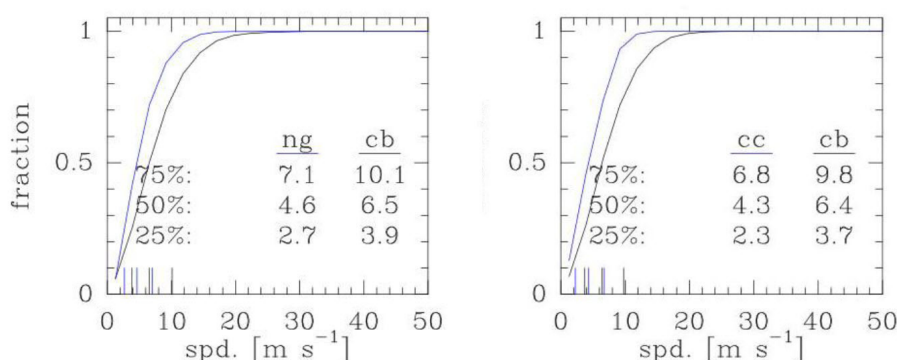


Figure 18 Cumulative distributions of air temperature at Cerro Chajnantor (cc), Cerro Negro (ng), and the Chajnantor plateau (cb) [6]

As it is clearly shown from the graph above, the average wind speed is ~10m/s with a 75% probability of not being exceeded.

Taking into account the aforementioned studies the decision was made to use as a loading case for the operational wind the value of 15m/s.

The survival wind was measured from May 1995 to April 1996 33m/s (max wind speed for this time period).[5] As it is later proven that the survival wind speed for this site is not decisive for most of the structures, the value of 55m/s is adopted and no further research is conducted.

Operational wind speed	Survival wind speed
15m/s	55m/s

Table 13 Final selected values of wind speed

4.1.3 Earthquake Load

4.1.3.1 Construction of the design Spectra

The accidental earthquake load in this specific site poses the decisive factor for the design in ultimate limit state. This is pretty obvious as Chile is one of the most seismic active regions in the world. The procedure of designing according to EN1998-1:2004 was followed and implemented in the analysis software.

For all structures examined, the first step was to conduct a Modal analysis to clarify the dynamic behavior of the structures. Although many different structures were examined the procedure was almost the same. In the beginning the mass of the system was defined from the Dead load of the structure, the mirror facets and the image sensor, which will always be present during the operation of the telescope. As far as the Modal analysis parameters are concerned, a lumped with allowable rotations mass matrix was implemented. Due to the cables in most of the examined structures and the odd structural shape with irregular mass distribution along the height, the Block Lanczos algorithm approach was followed to reduce the calculation time. In order to achieve a high mass participation factor, and as a result reliable results, the Seismic (pseudo-mode) was selected and a mass participation factor of over 80% for all directions was selected. This way, when the sum of the relative mass participation factors got over 80% for all directions the analysis was automatically stopped and the respective Eigen modes were saved. Another feature implemented was the Sturm check, which allowed the program to check for missing eigenvalues that had very close results. For example, if mode 10 and 11 had the same Period, without the selection of the Sturm check, only one of them would be considered. This is the same approach used for the seismic analysis of the SST-GATE telescope of the Cherenkov telescope array.[7]

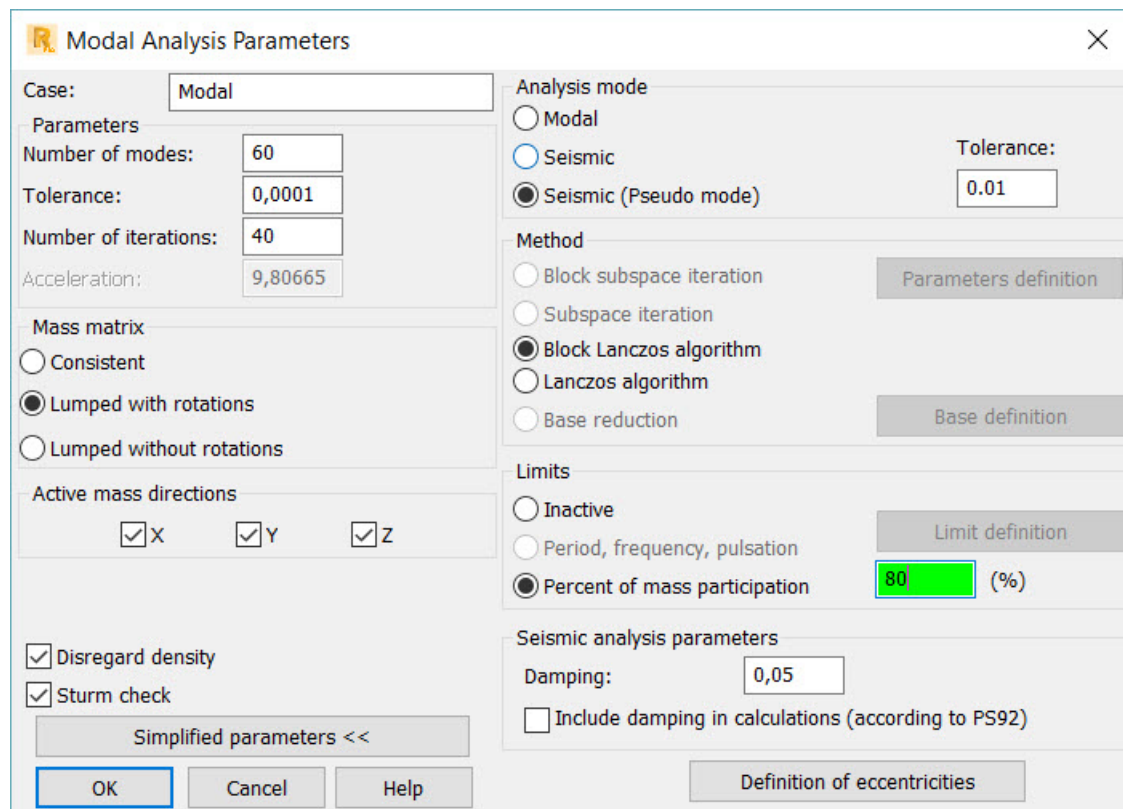


Figure 19 Modal analysis parameters window in the analysis software

After the dynamic properties of the structure were defined, load cases for the three active mass directions (X, Y, Z) were created and their resulting Newmark combinations for their interaction.

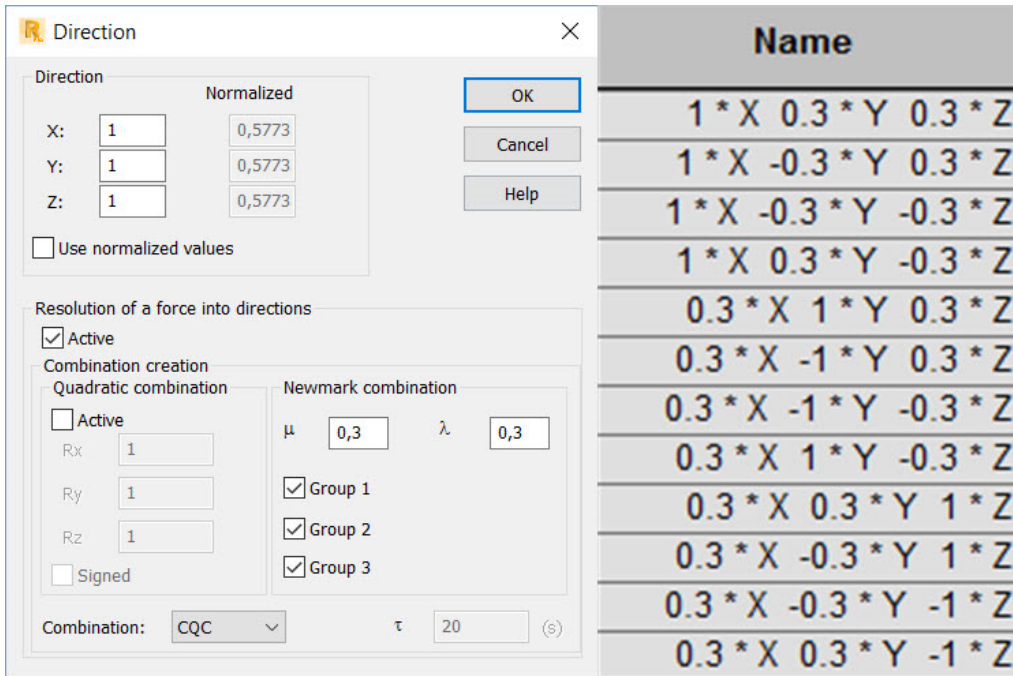


Figure 20 Active masses and Newmark combinations with the Complete Quadratic Combination (CQC) modal combination rule.

The final step was to import the necessary site specific data to create the elastic design spectrum according to EN1998-1:2004. These consist of:

- The Peak Ground Acceleration (PGA)
- The Ground type
- The Direction and
- The Spectrum type

According to the Regional Seismological Centre for South America, known as CERESIS there is a 10% probability that surface acceleration will exceed 400cm/s² in the next 50 years. In other words there is a 90% probability surface acceleration will not exceed 400cm/s² in 50 years.[8]

On the other hand, according to a study conducted to the location of the Atacama Large Millimeter Array (A.L.M.A.), in the next 50 years there is a 90% that the ground acceleration will exceed ~220cm/s² as it is shown in the graph below.[9]

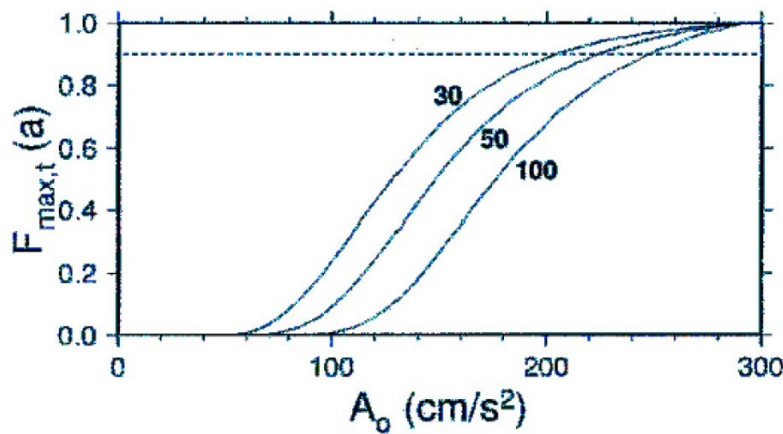


Figure 21 Probability to exceed a certain ground acceleration in 30,50 and 100 years at A.L.M.A. Chajnator site.[9]

However, taking into account another study “according to the ground motion attenuation relationship between distance and magnitude along the Wadati-Benioff zone, it is expected that an acceleration of 25%g will not be exceeded within 100 years at 90% probability levels” [10]

These contradictions prove that a more detailed analysis in this area could be of potential interest, even though only scientific-purposed structures lie in this area. (Atacama Desert)

For the purpose of this study a rather conservative value of 500cm/s^2 is selected closer to the CERESIS proposal, with an increased time interval. In any case, most of the examined designs are very flexible with fundamental periods of over 2 seconds, which means that in the elastic design spectra lie after T_D branch. This allow us to assume that the exact value of ground acceleration is not of utter importance.

For the ground type definition, the selection of the class B according to the EN1998-1:2004 was selected. This assumption is based on the geology field campaigns by *Geoconsultores S.A.* under contract with *National Radio Astronomy Observatory (N.R.A.O.)* and the supervision of the *European Organization for Astronomical Research in the Southern Hemisphere. (E.S.O.)* These revealed that the best case scenario is massive rock, whereas the worst case scenario is weathered rock.[10] Even though these upper layers of weathered rock are only a few centimeters thick (and they are created due to the frost/defrost cycle) we consider the conservative type B as a more representative ground type.

The directions of the earthquake loading are the horizontal X and Y and the vertical Z, which in our cases is considered due to the particularity of the structures.

Finally, according to the EN1998-1:2004 chapter 3.2.2.2 (2) the chosen Spectrum type is 1 and no further investigation of the surface seismic waves is conducted, as it is of no importance for fundamental structure periods of over 2 seconds.

The final elastic design spectrums are shown in the figures in the next page.

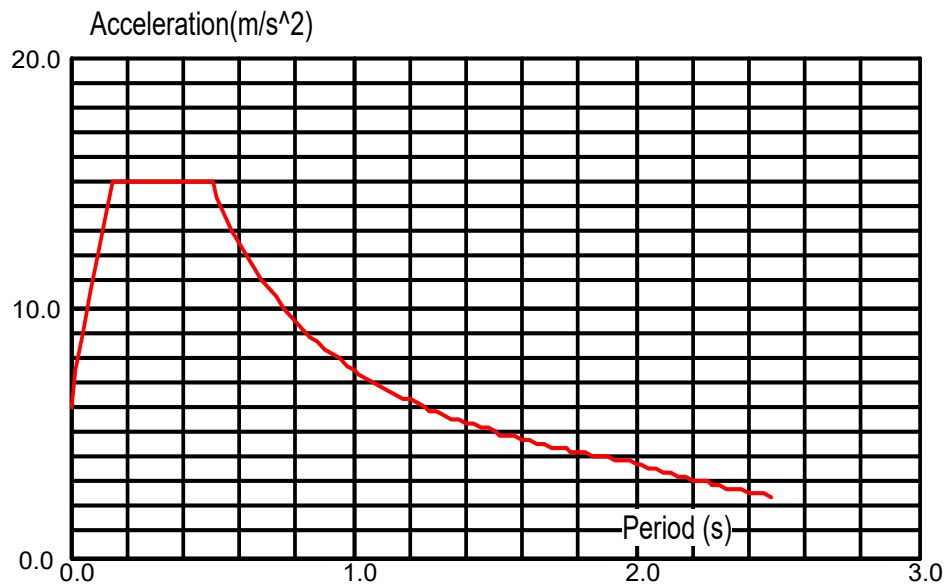


Figure 22 Elastic horizontal design spectrum Type 1 for $a_g=5\text{m/s}^2$, $\zeta=5\%$, $S=1.2$, $\beta=0.2$, $T_B=0.15\text{s}$, $T_c=0.5\text{s}$ and $T_D=2\text{s}$

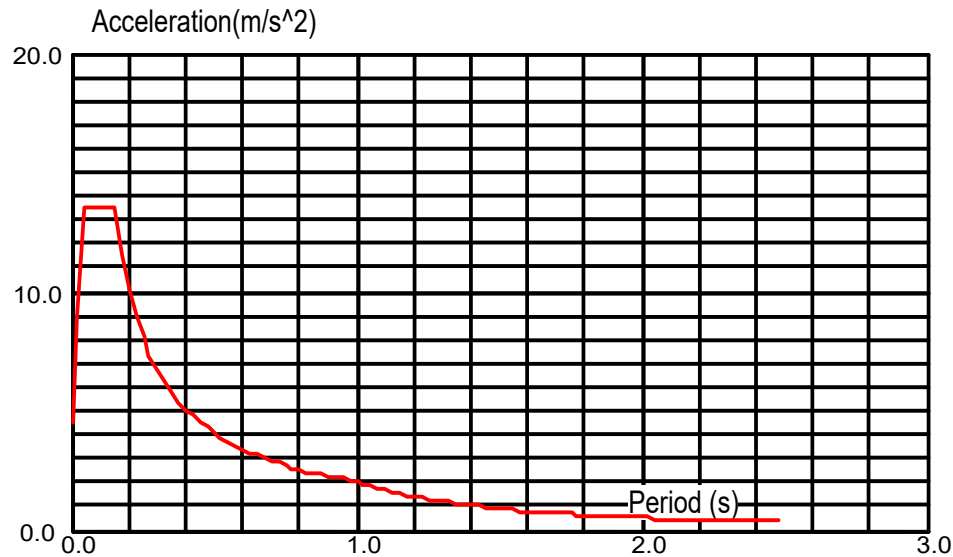


Figure 23 Elastic vertical design spectrum Type 1 for $a_g=4.5\text{m/s}^2$, $\zeta=5\%$, $S=1$, $\beta=0.2$, $T_B=0.05\text{s}$, $T_c=0.15\text{s}$ and $T_D=1\text{s}$

4.1.3.2 Time History Analysis

Due to lack of reliable data concerning the earthquake loading, and also because the seismic excitation is considered to be the driving factor of our design in terms of ultimate limit state, an elastic Response (Time) History Analysis was conducted with four different representative earthquakes that occurred around the world. This procedure allowed us to confirm and validate our designs.

The four chosen earthquakes (and a representative accelerogram for each one of them) are:

- Athens 1999. The earthquake occurred on September 7 at 2:56:50 pm local time and lasted approximately 15 seconds. The Moment Magnitude M_w was registered 6. More than 100 buildings (including three major factories) across those areas collapsed and overall 143 people lost their lives, while more than 2000 were severely injured. The highest recorded PGA was 0.3g, at 15 km from the epicenter, with attenuation predicting 0.6g acceleration at the center.[11]

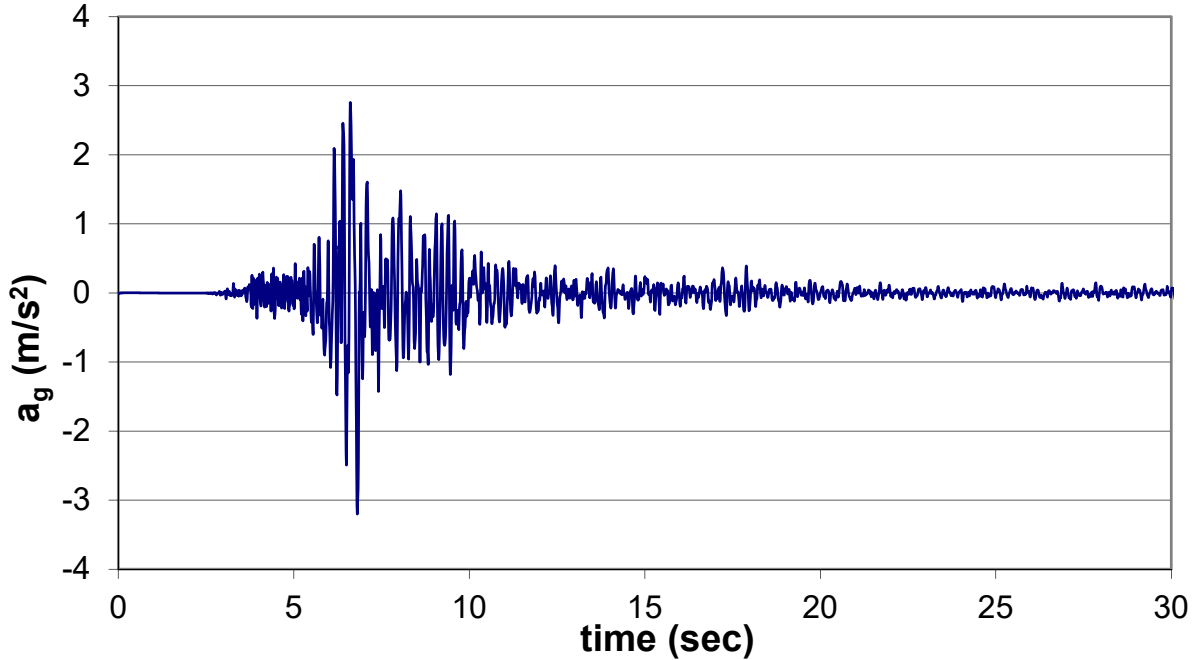


Figure 24 Athens 1999 transversal accelerogram.

- Kobe 1995. The earthquake occurred on January 16 at 20:46:53UTC in Japan, near Kobe, with the moment magnitude M_w being measured 6.9 and a maximum PGA of 0.8g. The tremors lasted nearly 20 seconds and around 6500 people lost their lives. This is considered the second most devastating earthquake in Japan in the 20th century.[12]

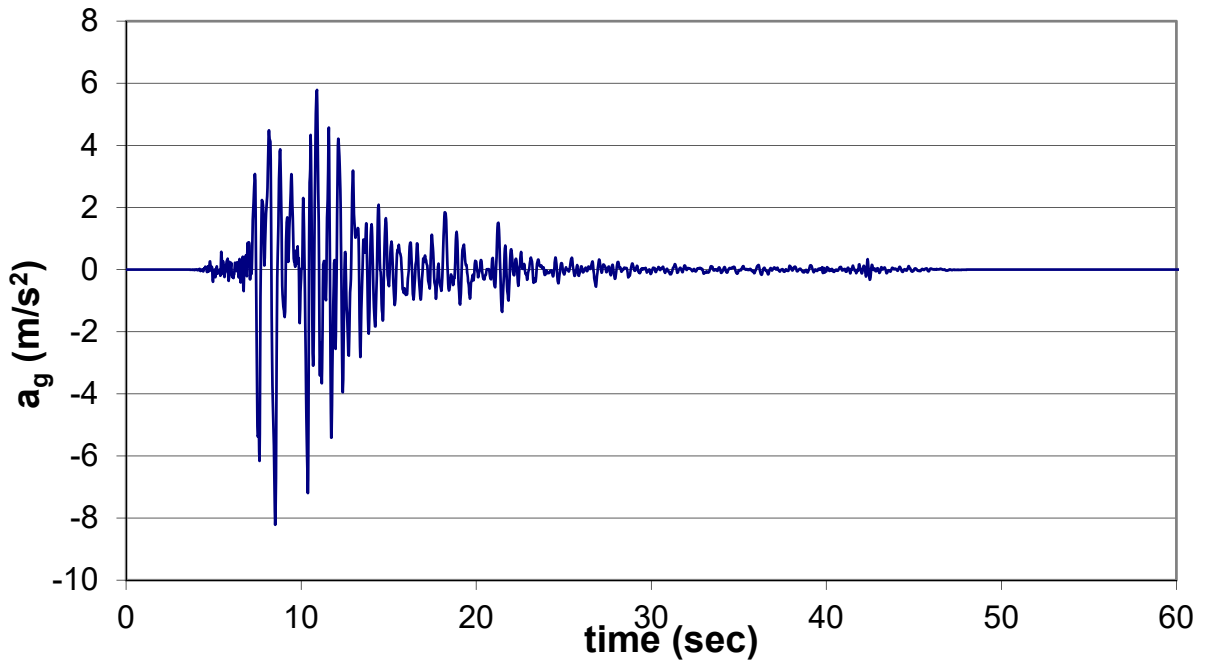


Figure 25 Kobe 1995 transversal accelerogram.

- Northridge 1994. The 1994 Northridge earthquake occurred on January 17, at 4:30:55 a.m. PST and had its epicenter in Reseda, a neighborhood in the north-central San Fernando Valley region of Los Angeles, California. It had a duration of approximately 10–20 seconds. The blind thrust earthquake had a moment magnitude M_w of 6.7, which produced ground acceleration that was the highest ever instrumentally recorded in an urban area in North America; measuring 1.8g. The peak ground velocity in this earthquake was 183cm/s, the fastest peak ground velocity ever recorded.[13]

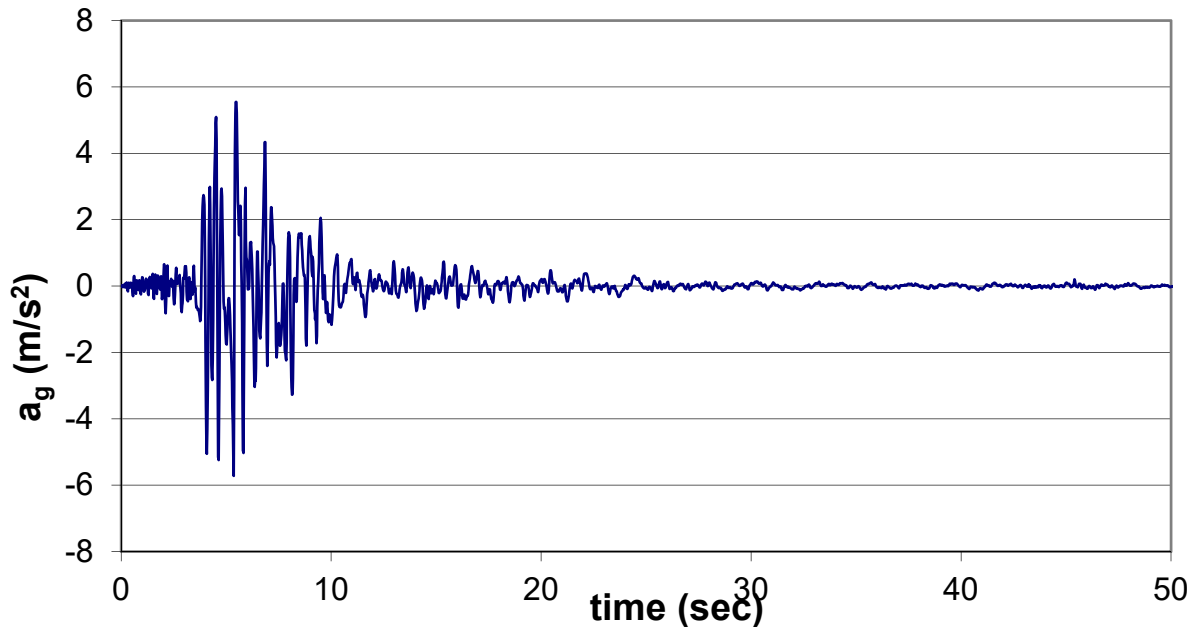


Figure 26 Northridge 1994 transversal accelerogram. (La Habra Station)

- El Centro 1940. The 1940 El Centro earthquake (or 1940 Imperial Valley earthquake) occurred at 05:35 UTC on May 19 in the Imperial Valley in southeastern Southern California near the international border of the United States and Mexico. It had a moment magnitude of 6.9 and a maximum perceived intensity of X (*Extreme*) on the Mercalli intensity scale.[14]

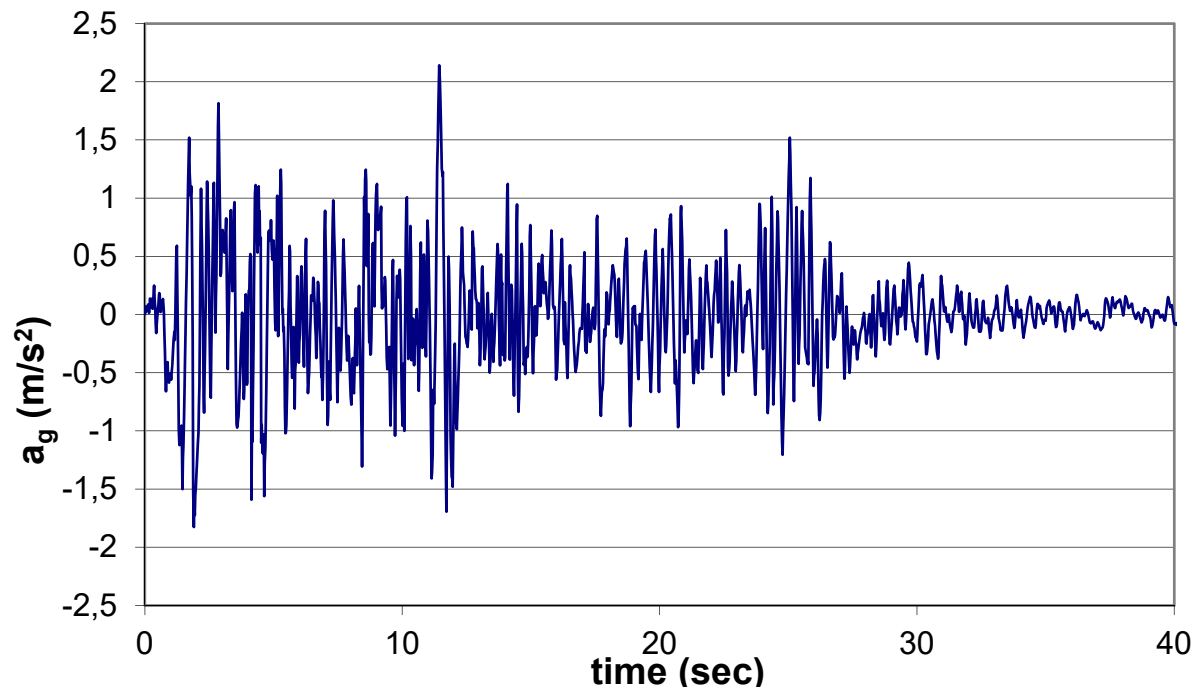


Figure 27 El Centro 1940 East-West component-transversal accelerogram.

The Response History Analysis was based in the 1*longitudinal+0.3*transversal+0.3*vertical acceleration combination. The time step was 0.1 second for all the analysis and a respective time period for each earthquake was chosen, bearing in mind the duration of the earthquake as described in its accelerograms. Another notable aspect is the use of Reileigh damping according to the Newmark acceleration method in the analysis software. The necessary parameters α (alpha) and β (beta) were computed automatically by inputting the damping coefficients (ζ was simplified assumed 0.05) and the two first cyclic frequencies ω_1 and ω_2 .

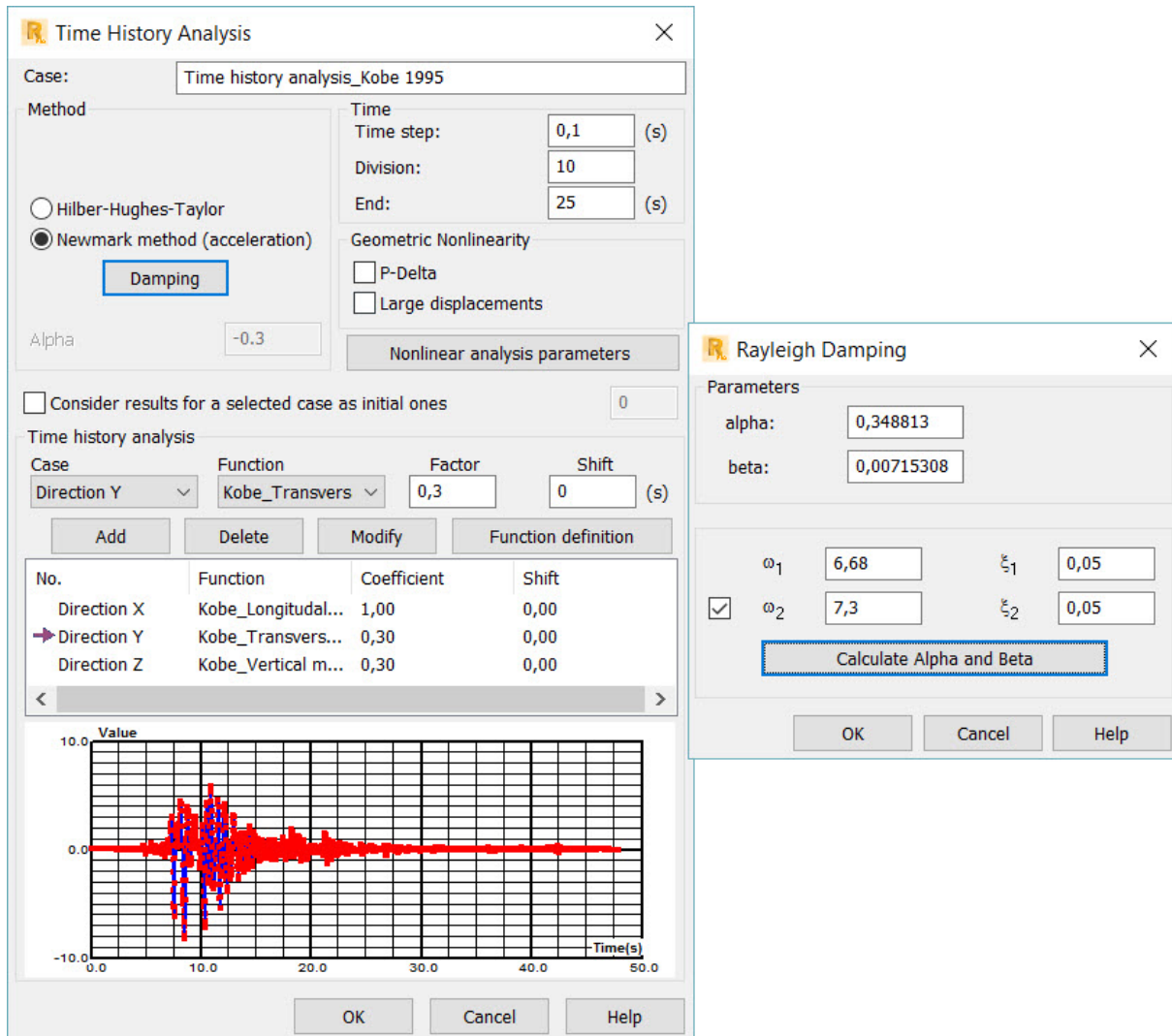


Figure 28 Response History Analysis of Kobe 1995 earthquake and Reileigh damping parameters.

4.1.4 Temperature Load

Finally, the temperature loading was considered in the early stage of the designs, giving very satisfactory results that pose insignificant influence in the operation of the structure in comparison with the other operational loads.

4.2 Analysis assumptions

Three main analysis were used for the design of the structures.

- Linear elastic analysis.
- Elastic analysis with geometric non-linearity. The incremental load application was implemented. (Loads were assigned to the structure gradually)
- Large displacements elastic analysis ("3rd order" effects were taken into consideration)
In any case no initial local or global imperfections were assigned.

4.2.1 Linear elastic analysis

The classic linear elastic analysis was used for all structures without cable elements. (mainly for the traditional Altitude-Azimuth design and Cross-Arch Image Sensor Structure of TheBigLebowSky design). Where cables were present, the second analysis option was used, as the strong geometrical non linearity of the cables had to be taken into consideration for a correct simulation. The structures analysed with this option are the Main Dish Structure of TheBigLebowSky design and the original Image Sensor Structure of the Alt-Azimuth design. (Quadrupod with cables) However, in the final Alt-Azimuth design cables were not present, so the first analysis option was used. Finally, for the Robocrane Image Sensor Structure of TheBigLebowSky design, the 3rd analysis option was used. This was deemed necessary to avoid instabilities, as this structure was very sensitive, due to the pre-stressing of the cable elements. It is also very important to mention, that no material non-linearity was considered at this stage. (only elastic analysis) The difference between the 2nd and the 3rd analysis options are presented below.

4.2.2 Elastic analysis taking into account geometric non linearity with the incremental method

If a structure includes non-linear elements (such as cables, unilateral supports, and material plasticity), calculations applying the incremental method are performed.

With the incremental method, the right-hand load vector is divided into n equal increments. A consecutive load increment is applied to the structure once the state of equilibrium for the previous increment is achieved. The norm of unbalanced forces is specified for each step, allowing for monitoring of the structure force-deformation relations.

The following figure shows an example of a nonlinear process using the incremental process. The values used for non-linear calculations are displayed.

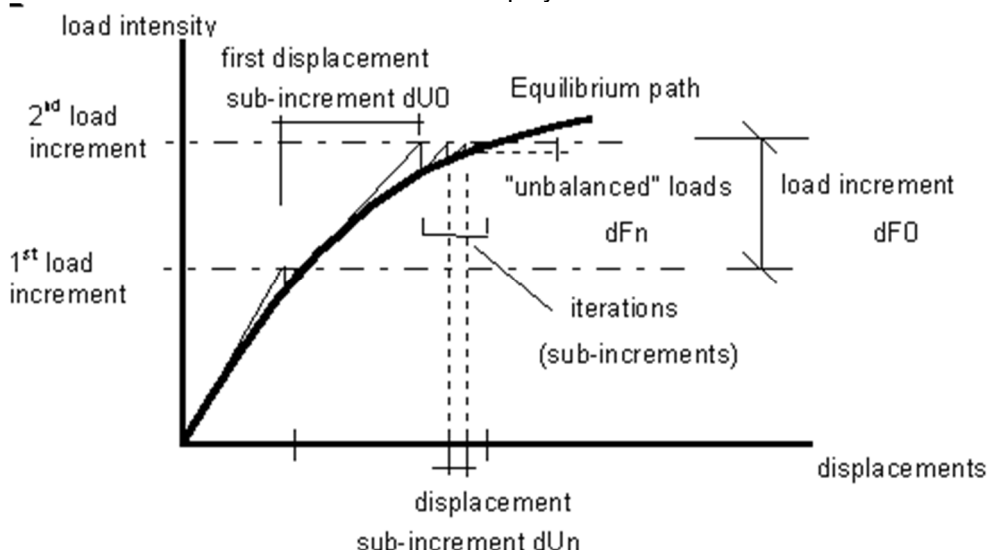


Figure 29 Incremental load application method. (graphical representation)

The load increment is used when dividing a load into smaller segments. For complex structures where the impact of non-linear effects is considerable, it is possible that calculations do not converge if the analysis for the value of a load is applied in one step. The number of load increments influences the number of calculation iterations. The greater the number of increments, the greater the probability for the calculations to reach the point of convergence.[15]

4.2.3 Large displacements elastic analysis

This analysis considers third-order effects, such as the additional lateral rigidity and stresses resulting from deformation or rotation. This effect considers additional forces arising in a deformed structure such as a beam with fixed supports on both ends, loaded by a vertical load, longitudinal forces arise and the deflection decreases.

These analysis parameters can improve the convergence of the calculation process because they consider the actual higher-order effects. This is especially useful, when working with a structure which includes non-linear elements.[15]

4.2.4 Non Linear analysis algorithms

Another important point is the use of the modified Newton Raphson analysis algorithm used for the nonlinear analysis. The Initial Stress algorithm was rejected for convergence reasons, whereas the Full Newton Raphson algorithm was rejected, due to excessive calculation time requirements. The basic algorithm parameters are shown in the following table.

Algorithm	Matrix update after each subdivision	Matrix update after each iteration
Initial Stress	Off	Off
Modified Newton-Raphson	On	Off
Full Newton-Raphson	On	On

Figure 30 Nonlinear analysis algorithms and their basic parameters

Finally, the algorithm of the Broyden-Fletcher-Goldfarb-Shanno (BFGS) procedure modifies the stiffness matrix during calculations.[15]

4.3 Design parameters

As far as the steel design is concerned, the EN 1993-1-1:2005 was used throughout the whole design process. All elements were designed in Ultimate Limit State for strength and stability. For the stability, as no initial imperfections were assigned the respective buckling curves were used. The buckling length was assigned on the safe side as equal to the initial bar length. Moreover, the interaction between axial forces, moments and shear forces was checked, where necessary.

Another simplification of this design was the exclusive implementation of the Circular Hollow Section database, in order to save precious calculation time. The advantages of these Cross-Sections are their symmetry in two axes, which leads to the same in and out of plane buckling resistance and the non-requirement for flexural-torsional buckling.

Moreover, all connections between these elements, even though a thorough design was not made, were considered as welded. This led to the assumption, that there are no bar end releases and the nodes connecting these elements were considered fully stiff. This is the reason for using also the term Space Frame and not Space Truss.[16] Finally, two elements, due to their complexity, could not be designed as the rest and the von Mises stress yield criterion was used. A detailed analysis was conducted in 9.

For simplicity reasons, the elements were grouped and designed for the critical one of the group. This is also the case in reality, as optimizing each element would result in extreme labour costs.

An example of the calculation notes (Software output) is presented in the next page.

STEEL DESIGN

CODE: BS-EN 1993-1:2005/NA:2008/A1:2014, Eurocode 3: Design of steel structures.

ANALYSIS TYPE: Code Group Design with Optimization Options

CODE GROUP: 5 Knickhalterungen

MEMBER: 1278

POINT: 3

COORDINATE: x = 1.00 L =

3.7301 m

LOADS:

Governing Load Case: 3 dl+ll 1*1.35+2*1.50

MATERIAL:

S460 (S460) fy = 460.00 MPa



SECTION PARAMETERS: CHS 76.1x2.5

h=76 mm	gM0=1.00	gM1=1.00	
	Ay=367.813 mm ²	Az=367.813 mm ²	Ax=577.760 mm ²
tw=3 mm	Iy=391664.000 mm ⁴	Iz=391664.000 mm ⁴	Ix=783328.000 mm ⁴
	Wply=13547.608 mm ³	Wplz=13547.608 mm ³	

INTERNAL FORCES AND CAPACITIES:

N,Ed = 38.38 kN	My,Ed = -0.05 kN*m	Mz,Ed = 0.00 kN*m	Vy,Ed = 0.00 kN
Nc,Rd = 265.77 kN	My,Ed,max = -0.05 kN*m	Mz,Ed,max = 0.00 kN*m	Vy,T,Rd = 97.68 kN
Nb,Rd = 53.31 kN	My,c,Rd = 6.23 kN*m	Mz,c,Rd = 6.23 kN*m	Vz,Ed = -0.10 kN
	MN,y,Rd = 6.00 kN*m	MN,z,Rd = 6.00 kN*m	Vz,T,Rd = 97.68 kN
			Tt,Ed = 0.00 kN*m
			Class of section = 2



LATERAL BUCKLING PARAMETERS:

BUCKLING PARAMETERS:



About y axis:

Ly = 3.7301 m	Lam_y = 2.16
Lcr,y = 3.7301 m	Xy = 0.20
Lamy = 143.26	kyy = 1.55



About z axis:

Lz = 3.7301 m	Lam_z = 2.16
Lcr,z = 3.7301 m	Xz = 0.20
Lamz = 143.26	kzz = 1.55

VERIFICATION FORMULAS:

Section strength check:

$$N_{Ed}/N_c, Rd = 0.14 < 1.00 \quad (6.2.4.(1))$$

$$(M_{y,Ed}/M_{N,y,Rd})^2 + (M_{z,Ed}/M_{N,z,Rd})^2 = 0.00 < 1.00 \quad (6.2.9.1.(6))$$

$$V_{y,Ed}/V_{y,T,Rd} = 0.00 < 1.00 \quad (6.2.6-7)$$

$$V_{z,Ed}/V_{z,T,Rd} = 0.00 < 1.00 \quad (6.2.6-7)$$

$$\Tau_{u,ty,Ed}/(f_y/(sqrt(3)*gM0)) = 0.00 < 1.00 \quad (6.2.6)$$

$$\Tau_{u,tz,Ed}/(f_y/(sqrt(3)*gM0)) = 0.00 < 1.00 \quad (6.2.6)$$

Global stability check of member:

$$\Lambda_{b,y} = 143.26 < \Lambda_{b,max} = 210.00 \quad \Lambda_{b,z} = 143.26 < \Lambda_{b,max} = 210.00 \quad \text{STABLE}$$

$$N_{Ed}/(X_y*N_{Rk}/gM1) + kyy*M_{y,Ed,max}/(XLT*M_{y,Rk}/gM1) + kyz*M_{z,Ed,max}/(M_{z,Rk}/gM1) = 0.73 < 1.00 \quad (6.3.3.(4))$$

$$N_{Ed}/(X_z*N_{Rk}/gM1) + kzy*M_{y,Ed,max}/(XLT*M_{y,Rk}/gM1) + kzz*M_{z,Ed,max}/(M_{z,Rk}/gM1) = 0.73 < 1.00 \quad (6.3.3.(4))$$

Section OK !!!

Of course, the aforementioned refer only to steel bar elements. For the design of steel cables, a more intuitive procedure was followed, trying to minimize the inner stresses under operational loads and not exceed the yielding strength for the ultimate loads. However, the cable design, as it can also be seen from the results was not fully optimized, due to the importance of the serviceability limit state and the necessity to keep deformations very low. In other words, cables are, in many cases, oversized in terms of ULS for the sake of SLS. As an example, one can easily apprehend the influence of 1.5Gpa stress on a 100m cable with Elasticity Modulus of 200Gpa. Using Hooke's law ($\sigma = \epsilon E$), the strains are $\epsilon=0.75\%$, so the total elongation results in 0.75m. This deformation, even for structures in our scale could have a huge influence in the overall stability of the structure.

Finally, the concrete columns and foundations were not accurately designed, due to time constraints. Some points were made, though, in the respective chapters.

4.4 Materials

For the whole project the following materials were used.

- For all steel elements, Structural Steel S460

Steel Concrete Aluminum Timber Other

Name:	S 460 N/NL	Description:	S 460 N/NL (EN 10025-3)
Elasticity		Resistance	
Young modulus, E:	210000,00 (MPa)	Characteristic	460,000 (MPa)
Poisson ratio, v:	0,3	Reduction factor for shear:	1,54
Shear modulus, G:	81000,000 (MPa)	Limit strength for tension:	540,000 (MPa)
Specific weight (unit weight):	77,01 (kN/m ³)	<input type="checkbox"/> Annealed steel	
Thermal expansion coefficient:	0,000012 (1/°C)		
Damping ratio:	0,04		

Figure 31 Structural Steel S460 properties.

- For all Cable elements, Steel Y1860

Steel Concrete Aluminum Timber Other

Name:	Y1860S7	Description:	Litzen je 150mm ²
Elasticity		Resistance	
Young modulus, E:	195000,00 (MPa)	Characteristic	1600,000 (MPa)
Poisson ratio, v:	0,3	Reduction factor for shear:	1,54
Shear modulus, G:	81000,000 (MPa)	Limit strength for tension:	1860,000 (MPa)
Specific weight (unit weight):	100,00 (kN/m ³)	<input type="checkbox"/> Annealed steel	
Thermal expansion coefficient:	0,000012 (1/°C)		
Damping ratio:	0,04		

Figure 32 Cable Steel Y1860 properties.

- For the concrete columns C70/85

Steel Concrete Aluminum Timber Other

Name:	C70/85	Description:	EC2 Concrete C70/85
Elasticity Young modulus, E: 41000,000 (MPa) Poisson ratio, v: 0,2 Shear modulus, G: 17083,333 (MPa)		Resistance Characteristic 70,000 (MPa) Sample: Cylindrical	
Specific weight (unit weight): 24,53 (kN/m ³) Thermal expansion coefficient: 0,000010 (1/°C) Damping ratio: 0,04			

Figure 33 Concrete C70/85 properties.

Some other materials that were used for special elements and simulations are:

- For all CFRP elements of the last design (Final Alt-Azimuth design) HexTow_IM10 with 12K Epoxy [17]

Steel Concrete Aluminum Timber Other

Name:	Epoxy_E350Mpa	Description:	HexTow_IM10 12K Epoxy_E350Mpa
Elasticity Young modulus, E: 350000,00 (MPa) Poisson ratio, v: 0,3 Shear modulus, G: 125000,00 (MPa)		Resistance Design resistance: 1793,000 (MPa) Reduction factor for shear: 1,54	
Specific weight (unit weight): 17,00 (kN/m ³) Thermal expansion coefficient: 0,000012 (1/°C) Damping ratio: 0,06			

Figure 34 CFRP HexTow_IM10 with 12K Epoxy properties.

- For all CFRP elements of the first Image Sensor design intuitive values from [18] were used.

Steel Concrete Aluminum Timber Other

Name:	Carbon1	Description:																																							
<table border="1"> <tr> <td colspan="2">Elasticity</td> <td>Resistance</td> </tr> <tr> <td>Young modulus, E:</td> <td>300000,00</td> <td>(MPa)</td> <td>Design resistance:</td> <td>650,000</td> <td>(MPa)</td> </tr> <tr> <td>Poisson ratio, v:</td> <td>0,3</td> <td></td> <td>Reduction factor for shear:</td> <td>1,54</td> <td></td> </tr> <tr> <td>Shear modulus, G:</td> <td>125000,00</td> <td>(MPa)</td> <td></td> <td></td> <td></td> </tr> <tr> <td>Specific weight (unit weight):</td> <td>15,00</td> <td>(kN/m³)</td> <td></td> <td></td> <td></td> </tr> <tr> <td>Thermal expansion coefficient:</td> <td>0,000012</td> <td>(1/°C)</td> <td></td> <td></td> <td></td> </tr> <tr> <td>Damping ratio:</td> <td>0,06</td> <td></td> <td></td> <td></td> <td></td> </tr> </table>			Elasticity		Resistance	Young modulus, E:	300000,00	(MPa)	Design resistance:	650,000	(MPa)	Poisson ratio, v:	0,3		Reduction factor for shear:	1,54		Shear modulus, G:	125000,00	(MPa)				Specific weight (unit weight):	15,00	(kN/m ³)				Thermal expansion coefficient:	0,000012	(1/°C)				Damping ratio:	0,06				
Elasticity		Resistance																																							
Young modulus, E:	300000,00	(MPa)	Design resistance:	650,000	(MPa)																																				
Poisson ratio, v:	0,3		Reduction factor for shear:	1,54																																					
Shear modulus, G:	125000,00	(MPa)																																							
Specific weight (unit weight):	15,00	(kN/m ³)																																							
Thermal expansion coefficient:	0,000012	(1/°C)																																							
Damping ratio:	0,06																																								

Figure 35 CFRP of preliminary design properties.

- Finally, the rigid links properties.

Steel Concrete Aluminum Timber Other

Name:	Rigid_Links	Description:	RL																																						
<table border="1"> <tr> <td colspan="2">Elasticity</td> <td>Resistance</td> </tr> <tr> <td>Young modulus, E:</td> <td>100000000</td> <td>(MPa)</td> <td>Characteristic</td> <td>50000,000</td> <td>(MPa)</td> </tr> <tr> <td>Poisson ratio, v:</td> <td>0,3</td> <td></td> <td>Reduction factor for shear:</td> <td>1,54</td> <td></td> </tr> <tr> <td>Shear modulus, G:</td> <td>81000,000</td> <td>(MPa)</td> <td>Limit strength for tension:</td> <td>55000,000</td> <td>(MPa)</td> </tr> <tr> <td>Specific weight (unit weight):</td> <td>0,01</td> <td>(kN/m³)</td> <td></td> <td></td> <td></td> </tr> <tr> <td>Thermal expansion coefficient:</td> <td>0,000012</td> <td>(1/°C)</td> <td><input type="checkbox"/> Annealed steel</td> <td></td> <td></td> </tr> <tr> <td>Damping ratio:</td> <td>0,04</td> <td></td> <td></td> <td></td> <td></td> </tr> </table>			Elasticity		Resistance	Young modulus, E:	100000000	(MPa)	Characteristic	50000,000	(MPa)	Poisson ratio, v:	0,3		Reduction factor for shear:	1,54		Shear modulus, G:	81000,000	(MPa)	Limit strength for tension:	55000,000	(MPa)	Specific weight (unit weight):	0,01	(kN/m ³)				Thermal expansion coefficient:	0,000012	(1/°C)	<input type="checkbox"/> Annealed steel			Damping ratio:	0,04				
Elasticity		Resistance																																							
Young modulus, E:	100000000	(MPa)	Characteristic	50000,000	(MPa)																																				
Poisson ratio, v:	0,3		Reduction factor for shear:	1,54																																					
Shear modulus, G:	81000,000	(MPa)	Limit strength for tension:	55000,000	(MPa)																																				
Specific weight (unit weight):	0,01	(kN/m ³)																																							
Thermal expansion coefficient:	0,000012	(1/°C)	<input type="checkbox"/> Annealed steel																																						
Damping ratio:	0,04																																								

Figure 36 Rigid links properties.

5 Initial simulations

5.1 “Mock” design of a traditional Altitude Azimuth mount telescope (High Energy Stereoscopic System I)

5.1.1 Introduction

The scope of this simulation is to show that the existing structural systems can not be implemented (or it is relatively cost inefficient) in large scale telescopes with a diameter of more than ~35m.

Due to the fact that there was not a definite structural plan with specific details about the truss bar sections, the connections and the dimensions of the structural elements, a visual approach was used, taking into account scientific papers and photographs of the existing structures. As a definite analysis was not deemed necessary, as the goal of this simulation was neither the design, nor the evaluation of an existing telescope, the simulation can be considered sufficient.

The goal was to show, that even though an Ultimate Limit State (ULS) is not exceeded, the Serviceability Limit State (SLS) is far out of the acceptable results. In this sense, new systems should be implemented such as moveable image sensors or even movable structural parts to counter balance the undesirable deformations. However, it is deemed as cost inefficient to implement such mechanisms in the traditional structures, mainly in terms of cost. Everyone should keep in mind, also, that these systems would increase the self-weight loading, hampering the situation of the structural system even further.

5.1.2 Idea and reasons for this simulation

Telescopes should be able to turn to every position of the celestial concave. Even though there are multiple solutions for this goal, most of the traditional telescope structures use the alt-azimuth design, which is implemented also in this simulation.

The principle behind these traditional structures is rather simple. The structure consists of two main columns that are based on a circular rail (azimuth mount). These two columns are connected on top with the dish main structure through two rotors respectively (altitude mount). The main structure could be described as a cantilever-like beam -although many variations for this design exist- with the most common one the incorporation of space truss structural systems.

5.1.3 Geometry and simulation

For our simulation the telescope structure is grouped in four different structures which will be described further. These are:

- Base structure (Transfers the loads from all structures to the rail of the azimuth mounting and holds the mechanisms for the altitude mechanisms)

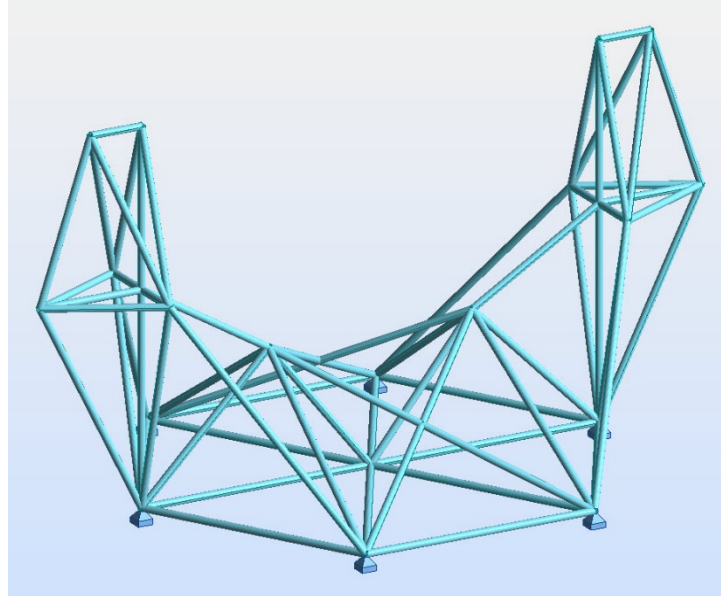


Figure 37 Base structure of “mock” design

- Main dish structure (Holds the weight of the mirror facets and the two following structures)

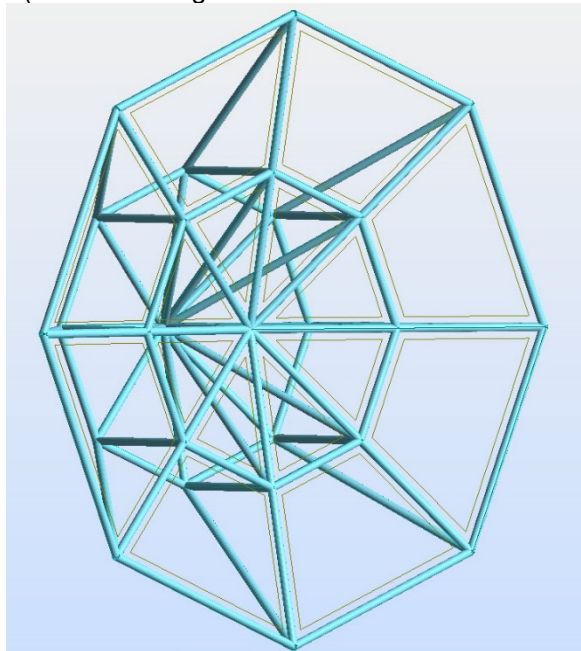


Figure 38 Main dish structure of “mock” design

- Image sensor structure (Holds the weight of the image sensor)

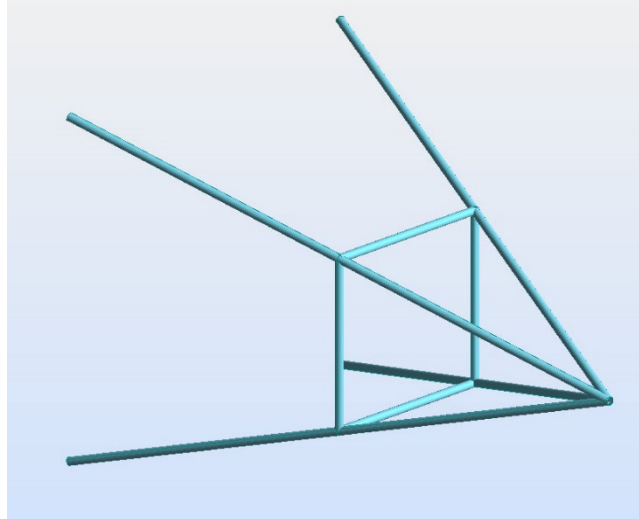


Figure 39 Image sensor structure of “mock” design.

- Counter weight structure (Holds the weight of the counter weight)

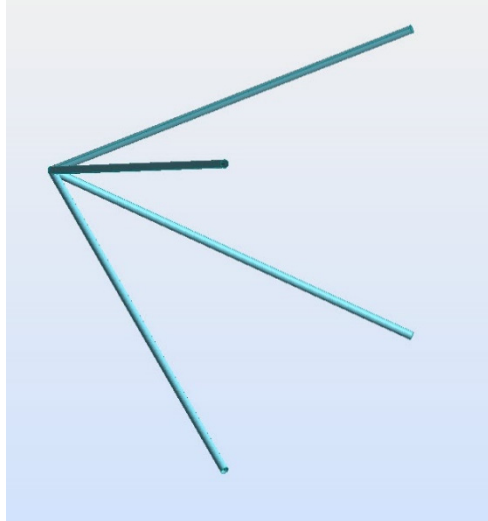


Figure 40 Counter weight structure of “mock” design.

All of these structures have as a base the truss structural systems, due to the size of the telescope. The resulting telescope looks like:

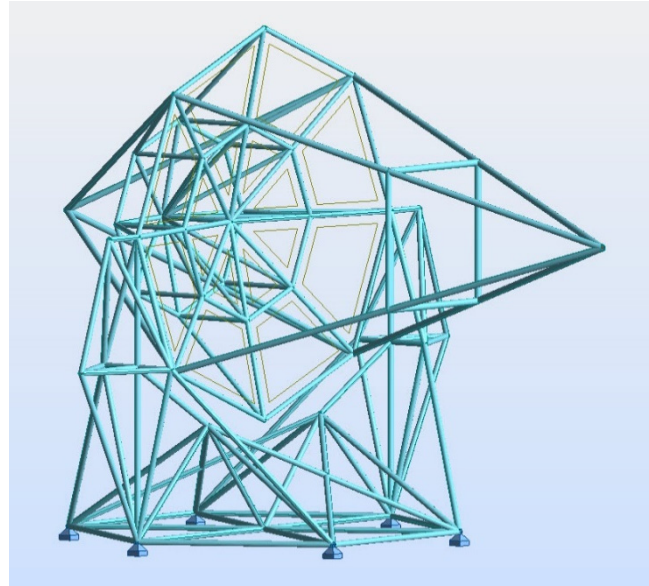


Figure 41 Final "mock" design. Analytical model in 90° from zenith position in structural scale.

For the structural analysis three positions were examined: 0°, 45°, 90°

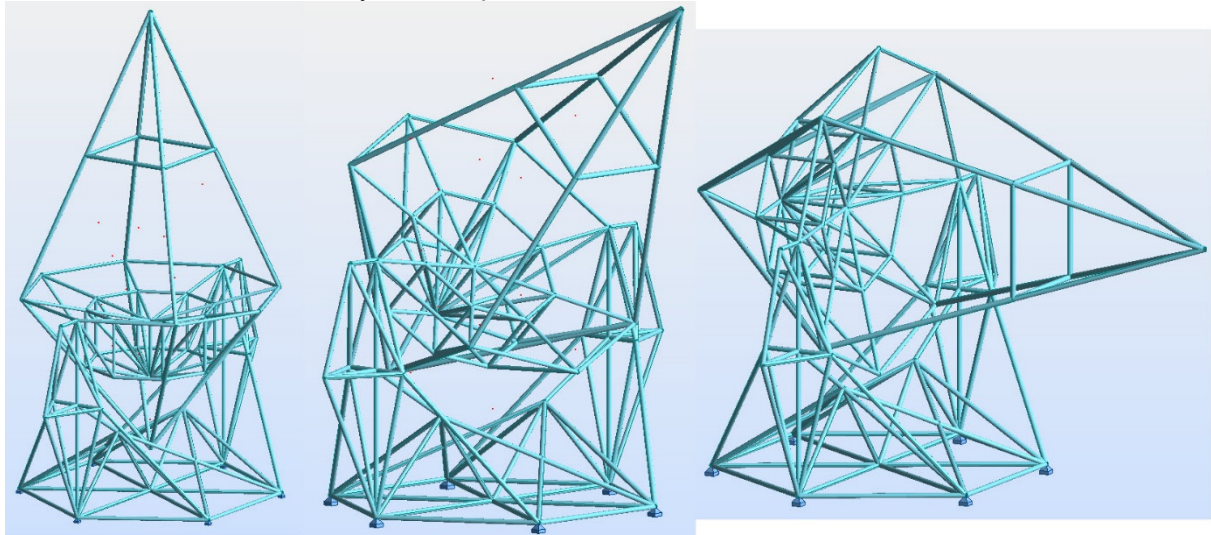


Figure 42 Positions examined for the "mock" design. From left to right: Zenith, 45° from zenith and 90° from zenith position.

The basic dimensions started with a 9m diameter dish, and then scaled three times. In the end, there is a 27m dish with 21m height columns. The length of the image sensor structure is 30m and the length of the counter weight structure was assigned 16,5m, in order to avoid collision with the base structure while the telescope rotates.

5.1.4 Loading of the “mock” design

With respect to mirror facets with actuators, and image sensors of the existing telescopes, the decision to use maximum values for the loading of this structure was made. The loads assigned are:

- Load case 1: Self-weight: Automatically created according to the specific weight of the material and the cross section of the elements.
- Load case 2: Mirror facet+actuators: $0,4\text{kg/m}^2$ surface load on the dish distributed in one way. The load was distributed to a secondary beam structure which is connected to the main beam structure. The secondary beams are circumferentially assigned whereas the main beams are assigned diametrically.
- Load case 3: Image sensor weight: A relatively conservative value of 3tns was assigned at the end of the cantilever image sensor structure.
- Load case 4: Counter weight: A weight of 15tns was assigned on the end of the cantilever counter weight structure.

Essential is to mention at this point, that in a later simulation wind load, earthquake loads and dynamic loads due to the telescope movement were supposed to be assigned. Due to the nature of these loads, as well as the difficulty to define them precisely, it was deemed unnecessary to calculate them at this stage, taking into account the goal of this simulation. In other words, if it is proven that the structure is not able to carry the static loads, it is impossible that the additional loads will act in favor of the structure. Finally, fatigue is also an essential part in this kind of structures, due to the multiple load cycles.

5.1.5 Design procedure

As far as the design parameters are concerned, all the elements are considered as truss elements, meaning that they can carry exclusively axial loads and a small bending moment. (mostly due to their self-weight) The buckling coefficients were assigned according to EN1993 Part 2, Anhang D as $l_{cr}=1^*l$ conservatively, without more detailed calculations. No lateral buckling was considered, as the elements were symmetrical in both axes regarding the Cross Section. This means that only RHS and CHS cross sections were taken into account. The design parameters are shown in the following picture.

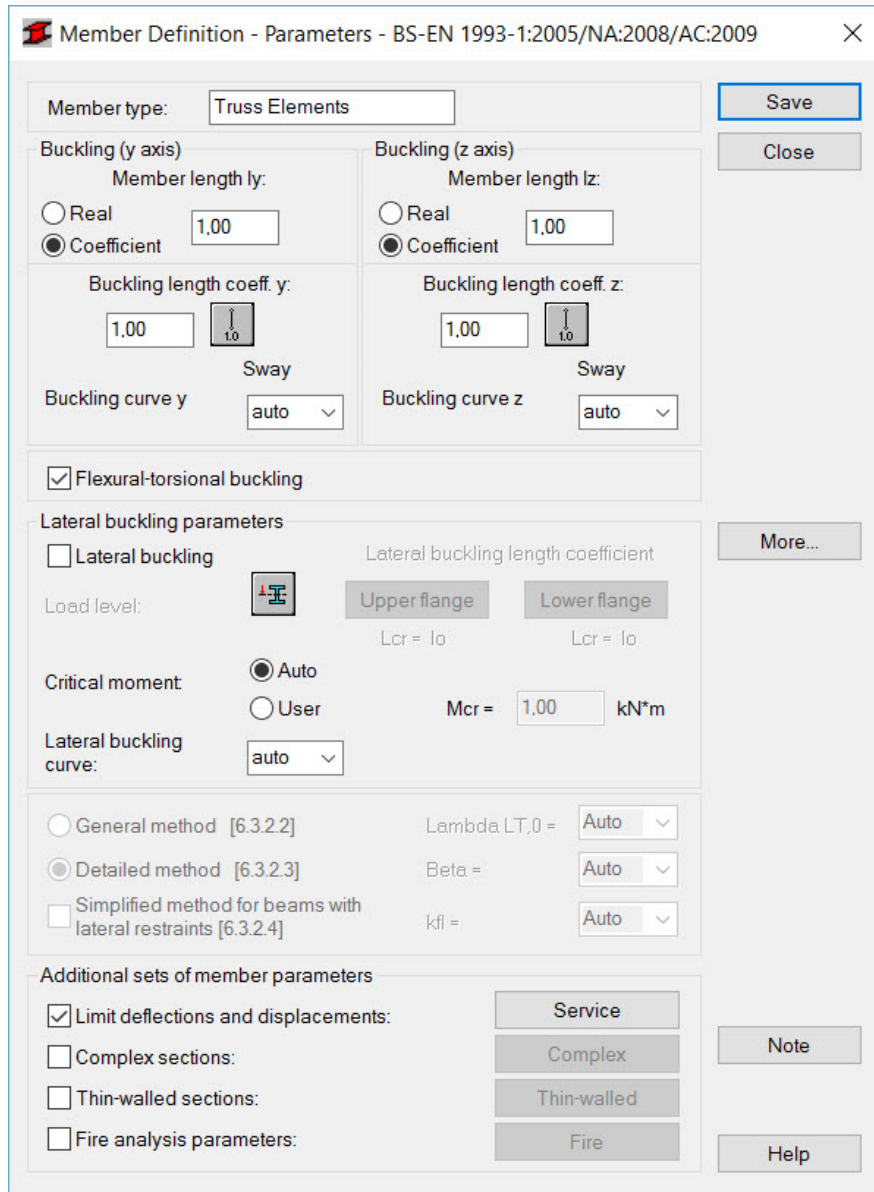


Figure 43 Member definition for the “mock” design.

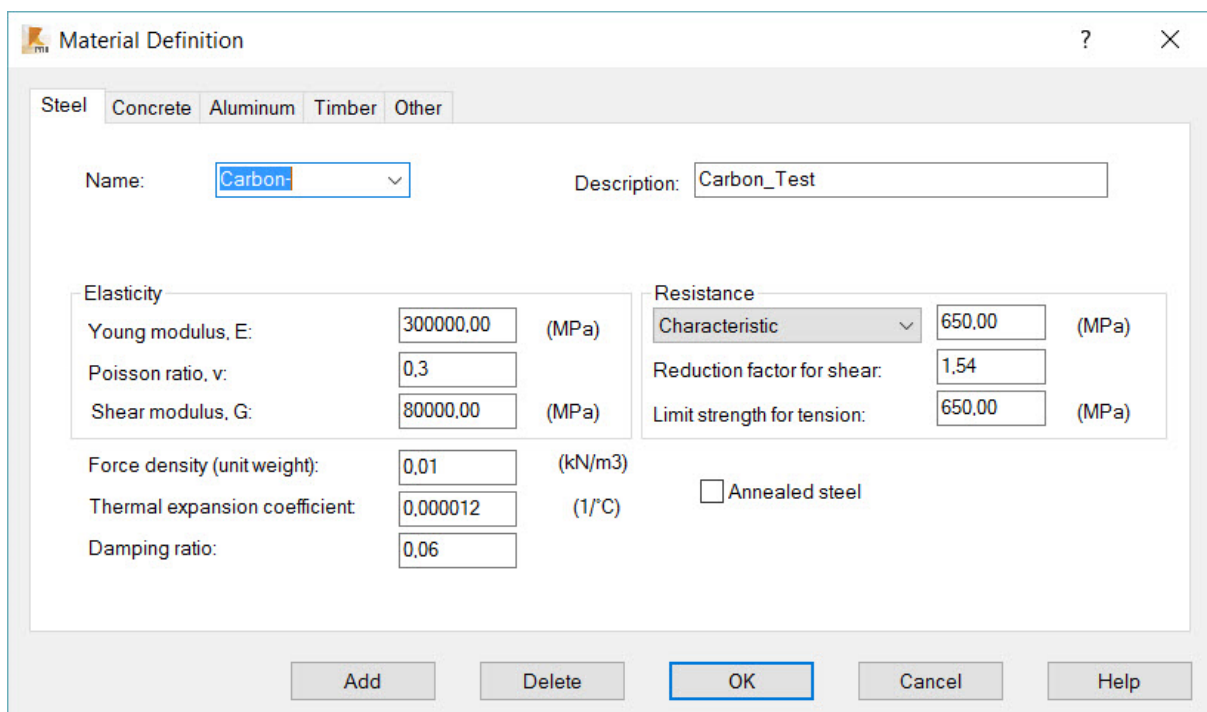
The design procedure started with the calculation of the cross sections in ULS for a Load Combination of the Load case 1-4 multiplied with the coefficient 1,35. The material used was the closest to carbon, steel S460 BS 5950-1 2000. All calculations were done according to EN1993:2005.

The resulting cross sections are:

- Base structure: CHS406.4x6.3
- Dish structure: CHS323.9x5
- Image sensor structure: CHS323.9x5
- Counter weight structure: CHS168.3x4

After the calculations, a maximal displacement of 1024mm was calculated in the edge of the image sensor structure. Although not acceptable in any case, it is a rational value, considering the size of the structural system. However, an improvement of materials could lead us in acceptable results. So, carbon fiber tubes replaced the steel cross sections to improve, on one hand the weight and on the other hand the stiffness. Despite the generally better characteristics of carbon fiber, special care is needed in accurately defining the elements and material characteristics, due to the complex arrangement of the fibers and the big inhomogeneity of the material.

With the same cross sections, a carbon material was assigned and the analysis was run once more to calculate the deflections. It is important to mention, that this new material could not be used to redesign the cross sections, as there is no official code for carbon yet. The properties of Carbon are assigned as shown in the picture below.



The end result is a deformation of the image sensor structure of 634mm a reduction of around 40%, which is considered important but not sufficient to allow the structure to function properly.

5.2 Sebastian's design

The first step was to define a certain geometry and then create a simplified analytical model to evaluate the structure's behavior.

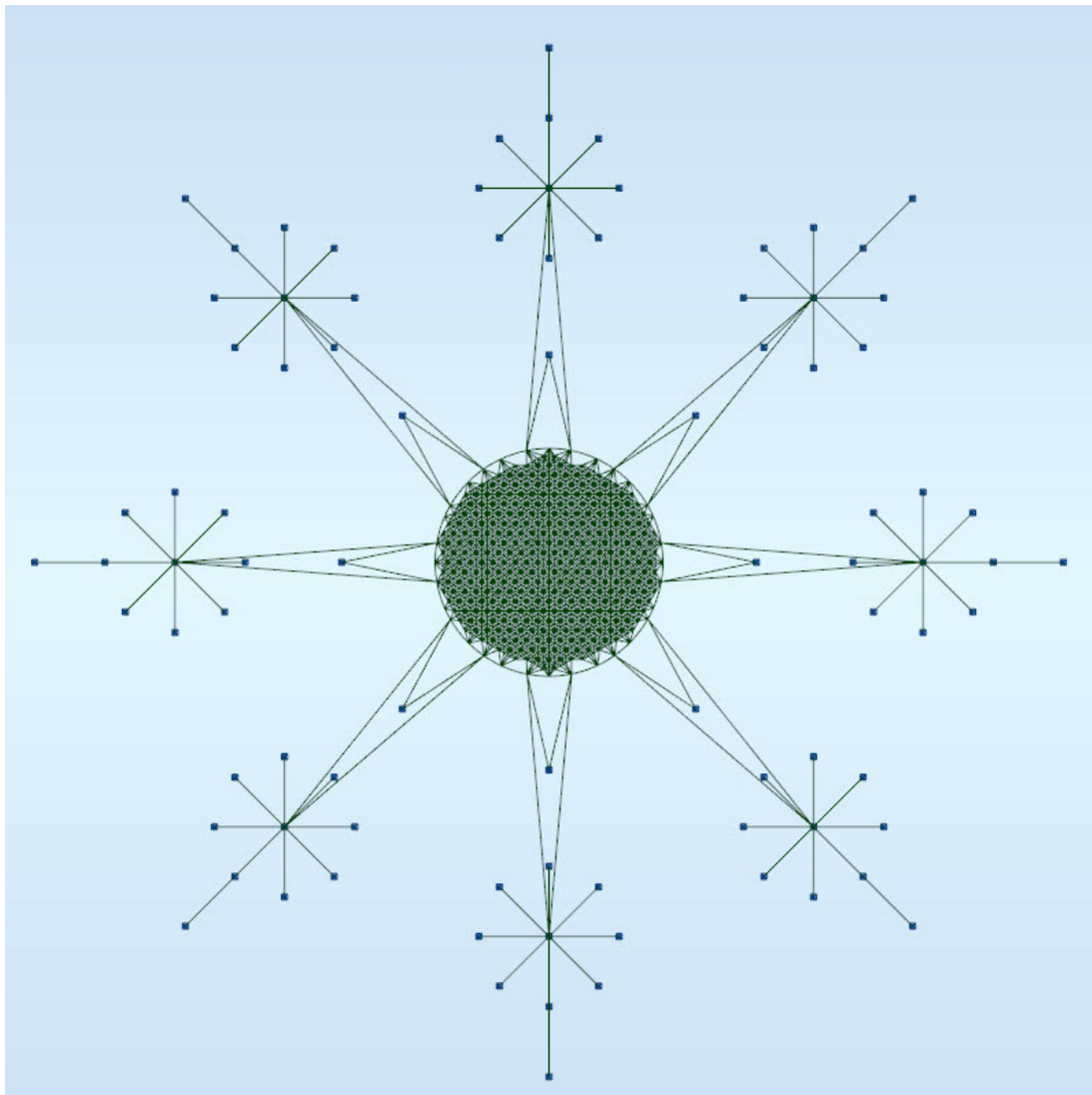


Figure 44 Top view of the analytical model.

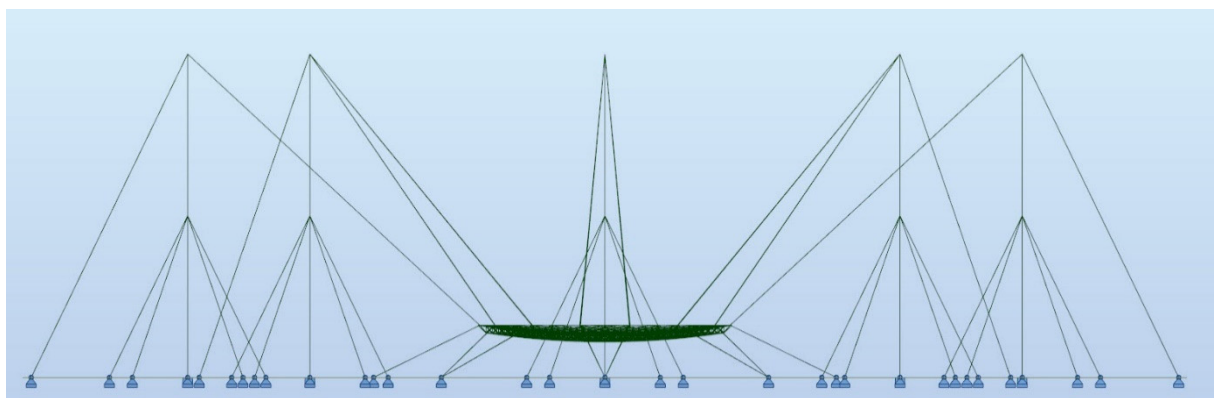


Figure 45 Front view of the analytical model.

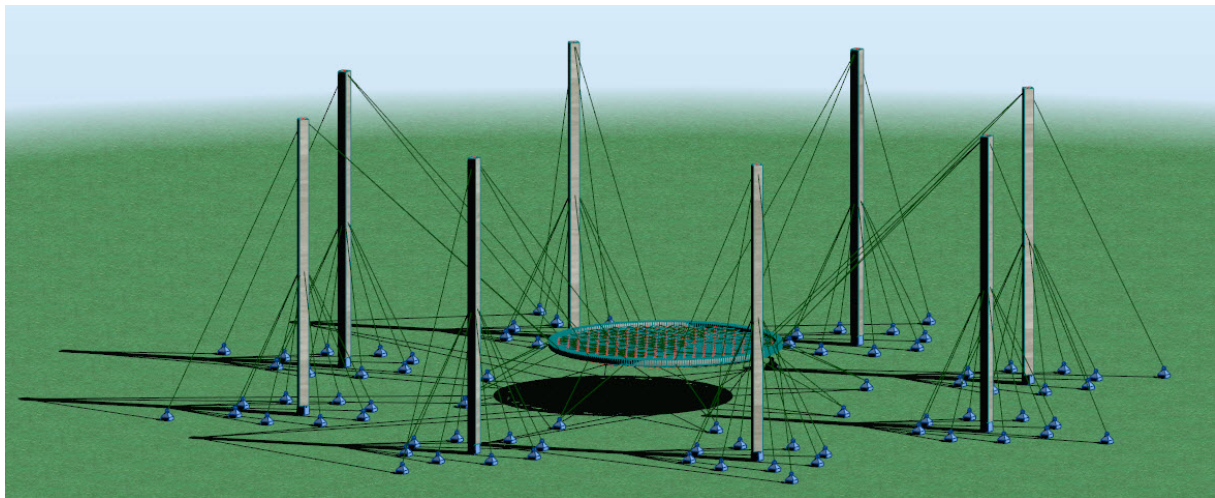


Figure 46 3D View of the first model created.

The final structure in 3D view is presented above and the exact geometry and dimensions are in this part of the research irrelevant, as this model will offer guidelines for the future development of the final solution. (see 10.2) For scalar interest the dish has a 50-meter diameter, the columns 62m height and they lie in the circumference of a circle with radius 80m.

However, it is very important to mention the basic conclusions of this first analytical model.

- The introduction of counter-cables was deemed unavoidable in order to stabilize the dish in its place against dynamic loading. Even intuitively, this is evident, that the conceptual design lacks this stability system.
- In order for the dish to be stabilized two main cables per column were needed as well as two counter-cables, as it can be seen from the image above. This improves the rotational stability of the structure.
- A driving factor for the overall deformations is the deformation of the upper-end node of the columns. As a result, small deflections of the columns induce disproportionately large dish displacements. To avoid this situation, the columns are sustained with the help of back cables in two points. (on the node and in the middle of the column)
- The space frame of the dish is supported on a large circular monolithic steel element, which is supported by the cables. This element is always in tension and from now on it will be referred as a Tension ring. Such constructions are evident most of the time in the roofing of large stadiums or equivalent structures.
- The cables' cross section should be carefully considered beforehand, as in the assembly phase, the dead load of the structure is solely considered. In the second phase, the deformed shape should carry also the mirror facets load.
- Finally, a way to efficiently design the Tension ring, the connections with the space frame on one side, and the connections with the cables on the other one, should be considered.

5.3 Conclusions of initial simulations

- Main problem of the Alt-Azimuth designs is the Image Sensor Structure.
- Especially for the Gamma Ray astronomy, where the f/D parameter is comparatively to e.g. Radio astronomy very large, this problem is highly amplified.
- As a result, need of sophisticated engineering and materials science solutions are necessary in order to increase the size, without disproportionately increase the cost. Cables and pre/post-tension, Carbon Fiber Reinforced Polymers (CFRP) or Glass Fiber Reinforced Polymers (GFRP), shock absorbers and deformations' predictive control are just a few solutions that could lead to acceptable results.
- The position of the altitude axis should be very carefully considered in order for the structure itself to be counter balanced. Thereby, no counter weight is needed, which in general highly increases the internal forces, leading to oversizing of the structural elements.
- Crucial point is the continuous effort to decrease the overall weight, especially along the height of the structure. This is proven as the dynamic loading, and as a result the mass of the structure, are the driving factors for the dimensioning of the structure.
- The base structure should be designed bearing in mind the minimization of the labor in the construction site, which directly affects construction cost and time. Possible solutions could be the modularization of the structure and the prefabrication of the modules.

6 Imaging reflector structure

The imaging reflector structure is designed using the “truss” (also called a “space frame”) approach where all structural loads are carried through beams, columns, and rod elements. A truss can be simple and cost-effective and is an obvious choice when loads enter the structure at several discrete points, as in a mirror cell, where each support point introduces a load. Trusses also tend to be preferable from wind excitation and thermal viewpoints: they offer less wind attack area, do not impede ventilation airflow, and have lower thermal inertia because of their larger surface-area-to-mass ratios.

The imaging reflector area should have the parabolic shape described in 2. The nodes of the space frame in the plane of the reflecting area are derived from the geometry of the mirror facets, as these nodes will serve also as supporting nodes for the actuators. A two-layer design for the space truss is developed that follows the geometrical requirements of the MERO system.

The initial idea of a ribbed dome for the imaging reflector structure will be described in this chapter, although this idea was excluded from further development. The reason of the exclusion was the differential deformations of the structure when rotating in the altitude axis. The solution would require a type of mount of the imaging reflector to the azimuth structure that would allow the support of the reflector from the center and not from its perimeter.

6.1 Mirror facets

The mirror facets and their support will specify the nodes of the space truss in the imaging reflector area. Hexagonal facets with outer radius 1.20m are going to be used, while each mirror facet will be supported with three actuators on the imaging reflector structure. In each node of the space truss three actuators are going to be supported. Figure 47**Error! Reference source not found.** shows the geometry and the dimensions of the mirror facets, their supporting points (black circles) and the supporting points of the actuators (red circles).

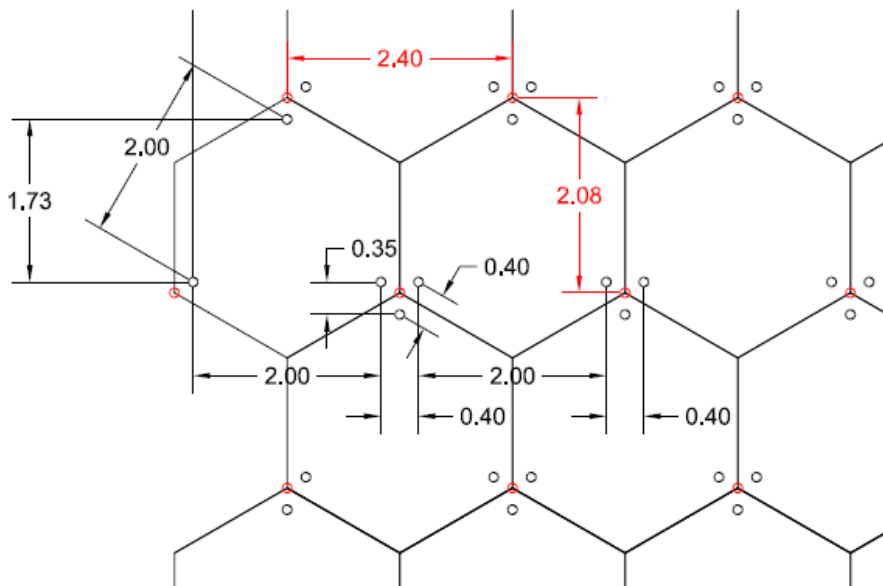


Figure 47 Mirror facets geometry.

The supporting points of the actuators specify the upper nodes of the space frame. By projecting these points into a parabolic surface the nodes of the space truss are being derived. From the projection of the nodes, that are in the same plane to a parabolic surface, the distance between the mirrors becomes larger. This fulfills the need for a small minimum distance between the mirrors for the operation

of the actuators and the alignments of the mirrors, so that they don't interact with each other. Figure 48 shows these distances which result from the projection.

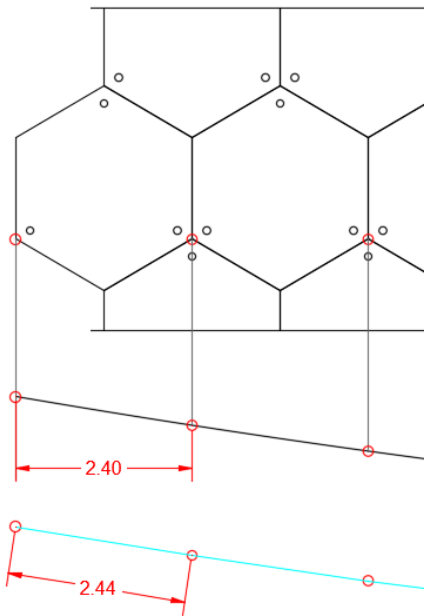


Figure 48 Distance between mirror facets due to projection

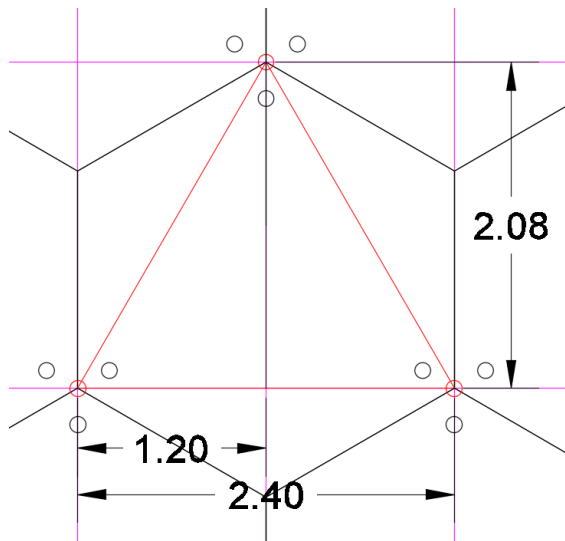


Figure 49 Grid and supporting points

6.2 Space frame

For the development of the space truss a grid should be defined according to the support points of the actuators. Symmetry in both axes should be maintained, so that the reflector deforms similarly (homologous deformations). The triangle produced from the three supporting points of a mirror facet is not symmetrical in two axes and so the grid doesn't have equal distances in both x and y axis. Figure 48 and Figure 49 explain the grid used for the design of the space truss.

In order to guarantee the symmetry, the space truss was designed in the quarter of a circle and this fragment of the imaging reflector was then mirrored in the two axes. The first step, as described before, was to define the grid. Then the grid was projected into a parabolic surface. The nodes were connected with straight lines which represent the bars of the first layer. Figure 50 shows the grid and Figure 51 shows the first layer of the space truss.

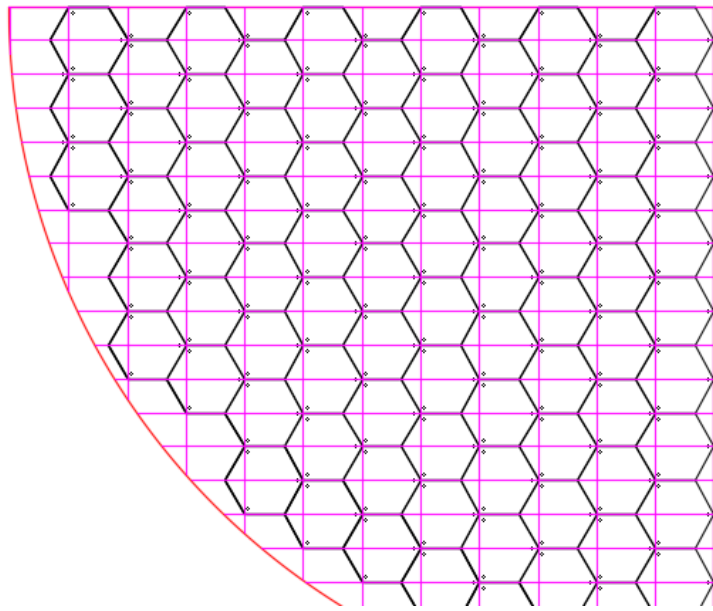


Figure 50 Dish grid. (upper nodes)

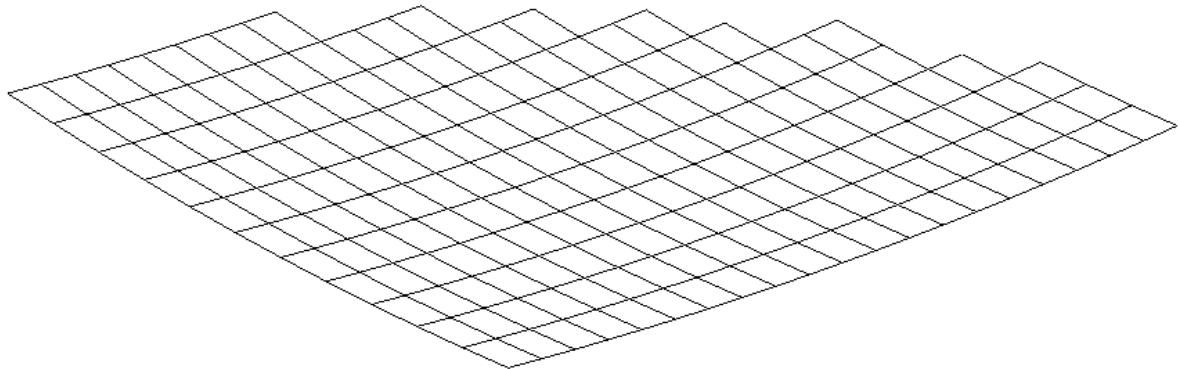
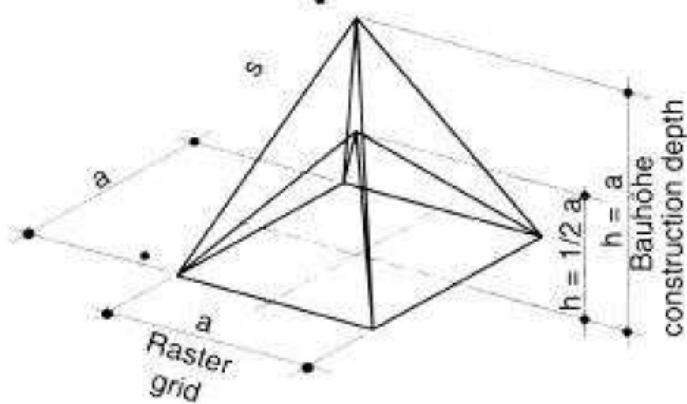


Figure 51 First layer of the Space Frame.

Afterwards, the second layer of the space truss was designed, by projecting the middle points of the rectangles of the grid into a second parabolic surface, that was created 1.20m under the first one. The distance of 1.20m was selected as it is the half of the biggest spacing of the grid according to the MERO specification Figure 52. These nodes were then also connected with straight lines which as before represent the bars of the second layer.



Die Bauhöhe ist in folgenden Grenzen wählbar:

$$a/2 \leq h \leq a$$

Range of ratios of grid module to depth

Standard $a = s \rightarrow a = h \sqrt{2}$

Figure 52 MERO Space frame system properties.

The nodes of the two layers were then connected with straight lines, which represent the diagonal bars of the space truss. The imaging reflector structure of this step of the design procedure is presented in Figure 53 and Figure 54.

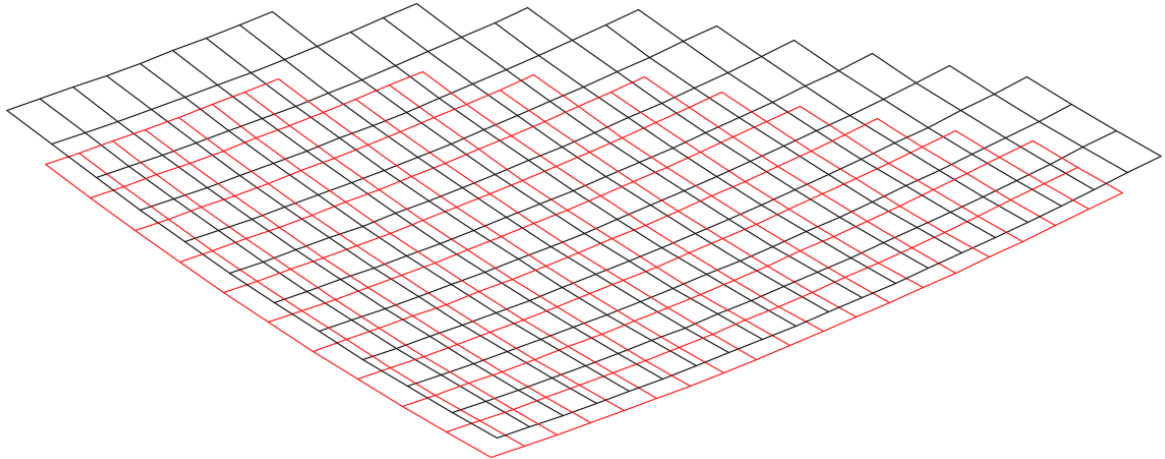


Figure 53 Space Frame. (First and second layer)

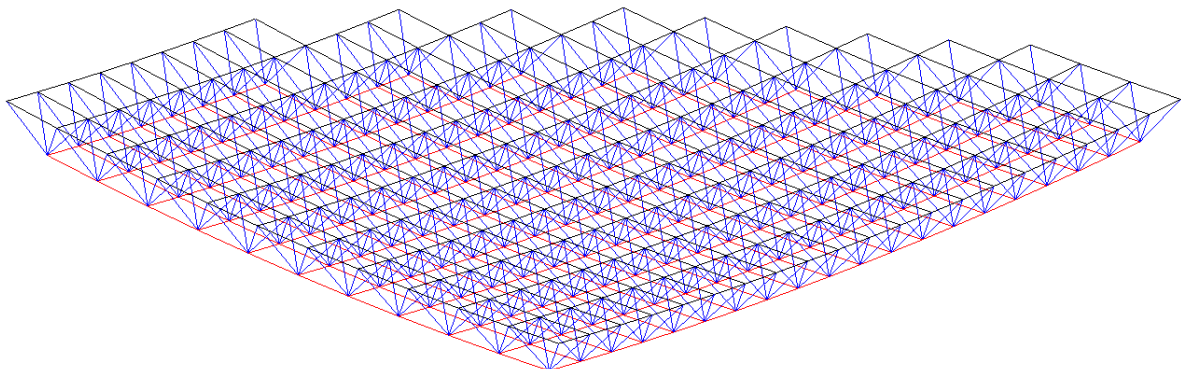


Figure 54 Space frame (First two layers with diagonals)

The same procedure was repeated for the creation of a 3rd layer. The final design of the space frame of the whole imaging reflector structure is presented in Figure 55 and Figure 56

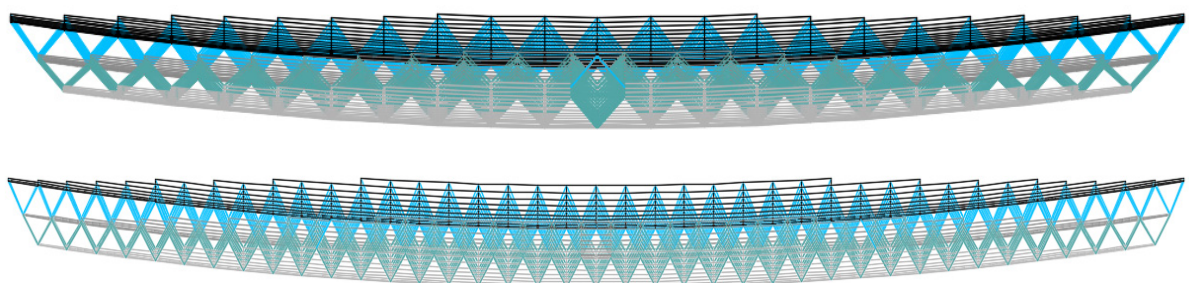


Figure 55 Front and side view of the imaging reflector structure.

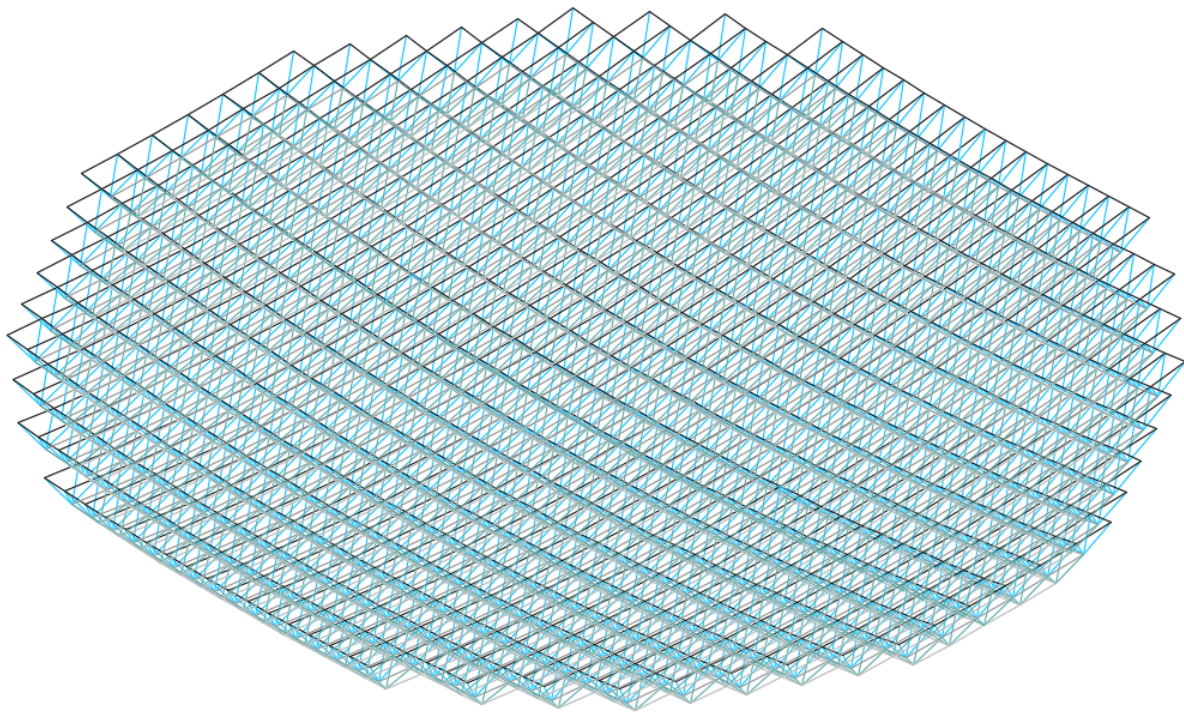


Figure 56 Imaging reflector. 3D representation.

6.3 Alt-azimuth design

For the Alt-azimuth design a 4th layer was constructed. The procedure followed is the same as before, only this time not the whole grid was projected into a fourth parabolic surface. A group of four grid elements (rectangles 1.20m×2.08m) represent now the new grid element (rectangle 2.40m×4.16m). This new bigger grid is projected and the 4th layer is created. Figure 57 shows the 3rd and 4th layer and Figure 58 shows the whole structure of the space truss for the Alt-azimuth approach.

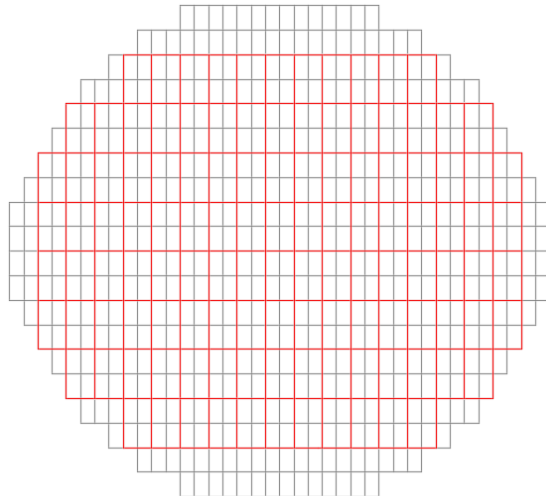


Figure 57 Third (grey) and fourth (red) layer of the space frame for the Altitude-Azimuth design.

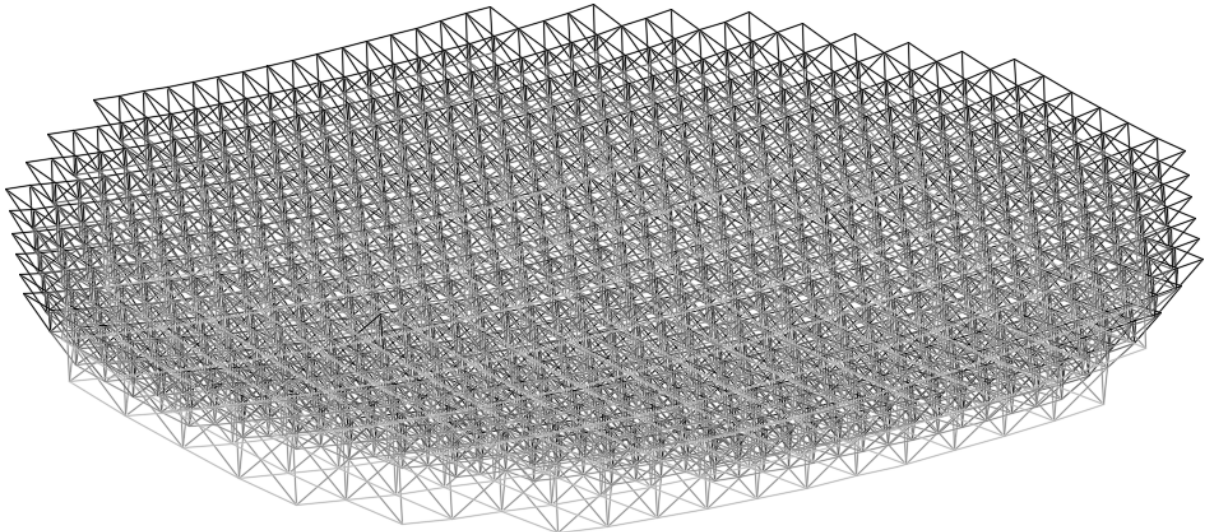


Figure 58 Alt-azimuth imaging reflector space frame.

6.4 TheBigLebowSky design

For the imaging reflector of TheBigLebowSky design the space frame created in 6.2 was used. This space frame should although be mounted on a peripheral tension ring. The design of the tension ring and the procedure followed for the connection of the tension ring with the space truss of the reflector is explained in 9.2 and 8.1 respectively.

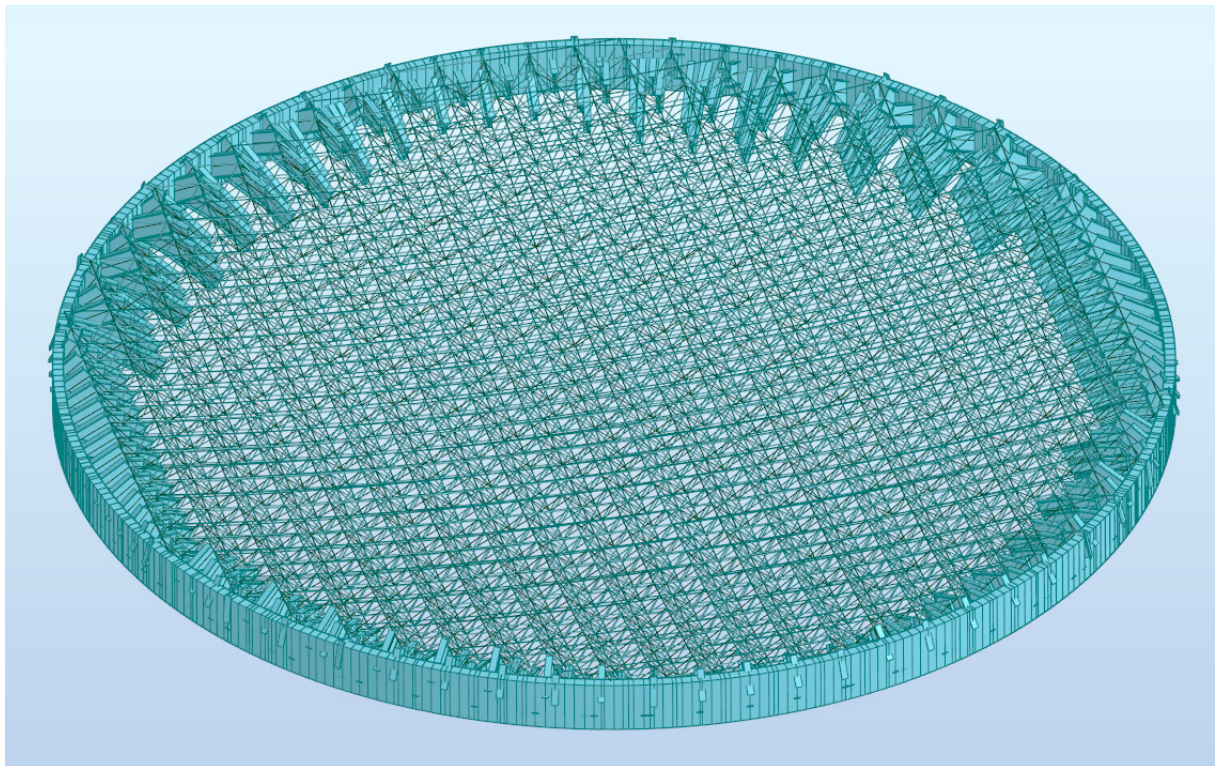


Figure 59 3D visualisation of the Imaging reflector space frame of TheBigLebowSky design in structural scale. (Rigid links are also visible)

6.5 Ribbed dome

An initial idea for the imaging reflector supporting structure was to be designed as a ribbed dome. A ribbed dome is the earliest type of braced dome that has been constructed. It consists of a number of identical meridional solid girders or trusses, interconnected at the crown by a compression ring. The ribs are also connected by concentric rings to form grids in trapezium shape. The ribbed dome is usually stiffened by a steel or reinforced concrete tension ring at its base.

This idea was abandoned because this type of structure would demand a different approach for its support on the azimuth structure. This type of dome is favorable, when the tension ring at its base serves as support for the whole imaging reflector structure. Apart from that, differential, not homologous deformations occur, which have a strong impact in the shape of the reflector surface and thus in the quality of the captured image and in the performance of the telescope in general as shown in Figure 61. This conclusion was made after designing and simulating a ribbed dome dish.

Moreover, at the design stage of this structure the exact geometry to be followed was not specified. As a result, the ribbed dome was constructed with a Davies Cotton geometry. This geometry at a later designing phase was not favorable and the new imaging reflector structures (space frame) from that point on were constructed applying a parabolic geometry. In Figure 60 the difference of the two optical layouts is obvious, as this structure approaches more the sphere, having a bigger depth.

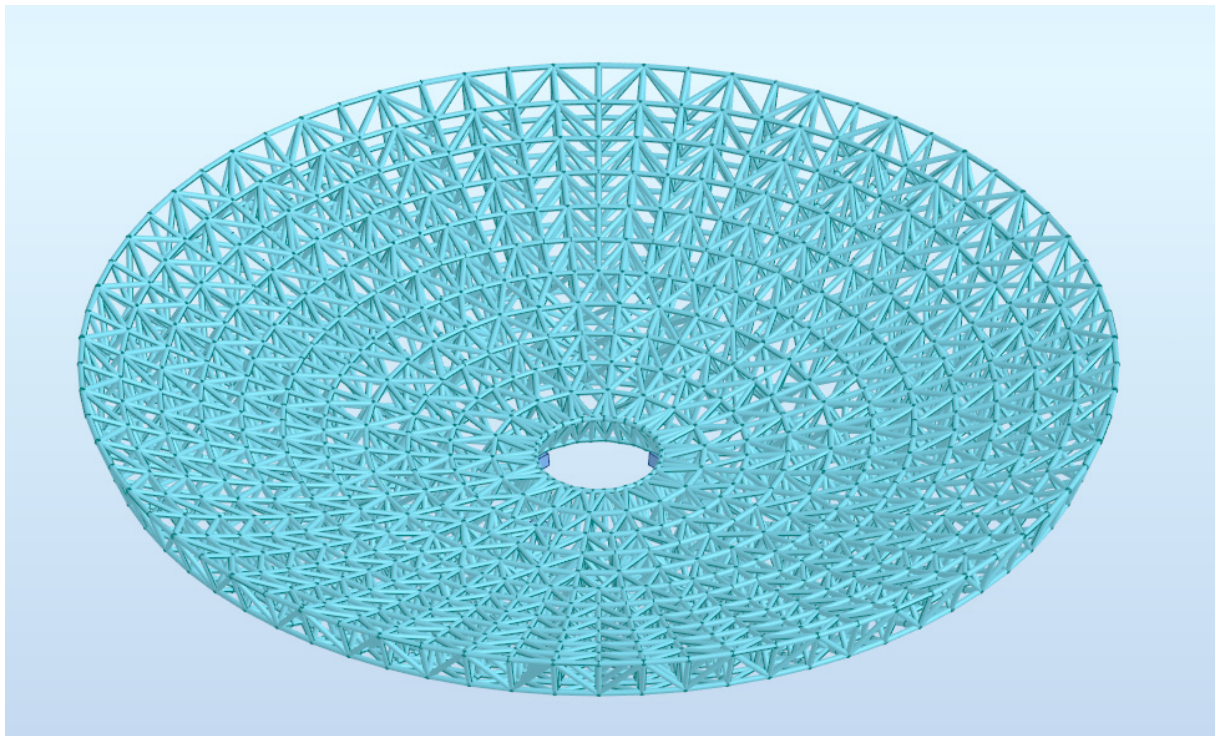


Figure 60 3D visualisation of the Ribbed dome.

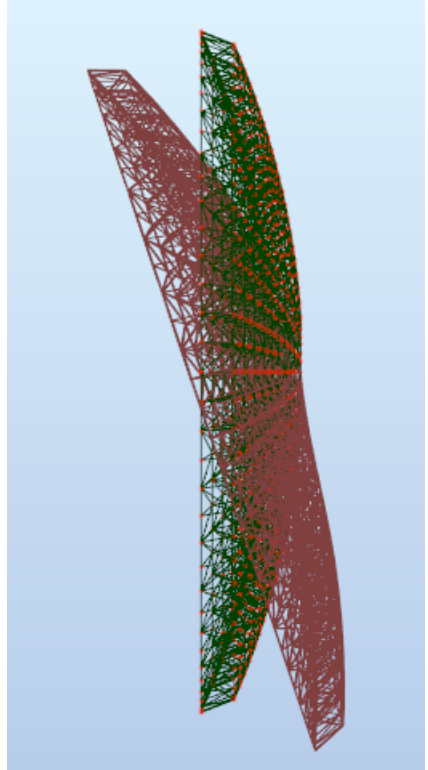


Figure 61 Deformation shape of the ribbed dome structure in 90°. (free rotating supports in the centre)

7 The Altitude-Azimuth concept

7.1 Initial Image Sensor Structure (Quadrupod) for the Altitude-Azimuth concept

7.1.1 Truss topology investigation for the optimal design of the Image Sensor Structure (Quadrupod) for the Altitude Azimuth concept.

Truss 3D topology for the image sensor was chosen by experimenting with different 2D trusses, having the same loading conditions with the original structure (concentrated image sensor load at the edge of the cantilever-like image sensor structure). The overall aim was to find the solution with minimal deformations, bearing in mind also the disadvantage of self-weight. However, in such a big cantilever system, self-weight is as, or more crucial than the concentrated load at the edge, posing the critical impact in deformations. Below, there is the summary of this survey and afterwards, the arguments for the choice of the K-Truss as the ideal topology. In any case, it is important to clarify that all trusses were designed in ultimate limit state according to EN 1993-1-1:2005 and then the deformations and the quantity survey, in order to specify the total weight, have been conducted.

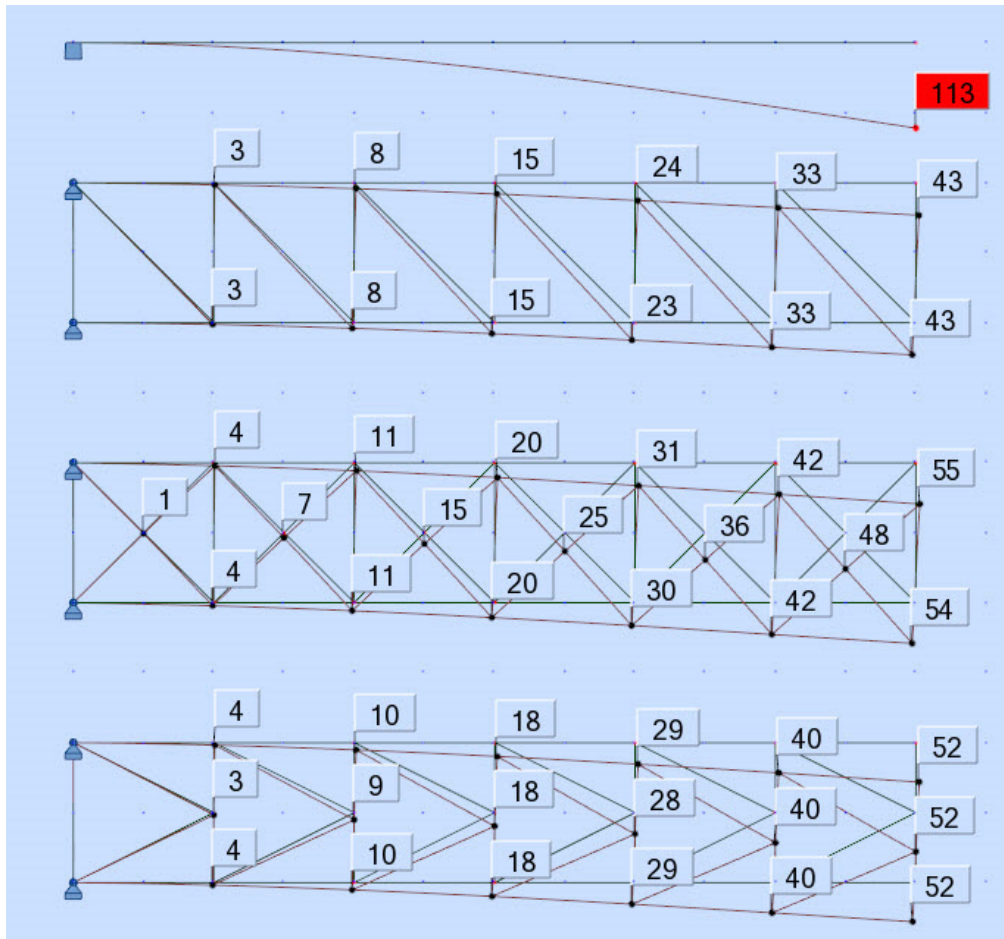


Figure 62 Truss Configurations and their respective nodal displacements. (from top: Simple bar element, Pratt truss, Pratt/Howe combination and K-Truss)

The total weight of these configurations is presented in the following table.

Simple bar element	Pratt truss	Pratt/Howe combination truss	K-Truss
909kG	528kG	328kG	359kG

Table 14 Weight of the truss configurations examined for the truss optimisation of the initial Image Sensor Structure. (Rohbrenne)

Member	Section	Material	Lay	Laz	Ratio	Case
Code group : 1 Simple Cantilever						
26 Cantilever 26	SHS 400x12.5	S355	75.94	75.94	0.94	3 DL+Concentrated Load
Code group : 2 Obere Gurt						
53 Truss element	CHS 139.7x6	S355	21.13	21.13	0.93	3 DL+Concentrated Load
Code group : 3 Untere Gurt						
73 Truss element	CHS 139.7x6	S355	21.13	21.13	0.99	3 DL+Concentrated Load
Code group : 4 Diagonals						
73 Truss element	CHS 139.7x6	S355	21.13	21.13	0.99	3 DL+Concentrated Load
Code group : 5 Pfosten						
113 Truss elem	CHS 88.9x2.5	S355	16.36	16.36	0.95	3 DL+Concentrated Load
Code group : 6 Obere Gurte Xiasti						
53 Truss element	CHS 139.7x6	S355	21.13	21.13	0.93	3 DL+Concentrated Load
Code group : 7 Untere Gurte Xiasti						
54 Truss element	SHS 140x5	S355	18.18	18.18	0.98	3 DL+Concentrated Load
Code group : 8 Pfosten Xiasti						
70 Truss element	CHS 42.4x3	S355	71.58	71.58	0.87	3 DL+Concentrated Load
Code group : 9 Diagonale Xiasti						
85	CHS 48.3x3.2	S355	44.19	44.19	0.94	3 DL+Concentrated Load
Code group : 10 Obere Gurte K						
72 Truss element	CHS 139.7x6	S355	21.13	21.13	0.84	3 DL+Concentrated Load
Code group : 11 Untere Gurte K						
73 Truss element	CHS 139.7x6	S355	21.13	21.13	0.99	3 DL+Concentrated Load
Code group : 12 Pfosten K						
113 Truss elem	CHS 88.9x2.5	S355	16.36	16.36	0.95	3 DL+Concentrated Load
Code group : 13 Diagonale K						
123 Truss elem	SHS 70x2.5	S355	40.84	40.84	0.91	3 DL+Concentrated Load

Figure 63 Design of the aforementioned configuration according to ULS for the combination Dead Load and Concentrated Load on the edge. All trusses were designed maximizing the optimization by grouping the design elements according to their function (e.g. Obere Gurt/Top Chord in tension has different cross section than Untere Gurt/Bottom Chord in compression and the same applies for Diagonals and vertical rods).

7.1.2 Design of the Image Sensor Structure (Quadrupod) for the Altitude Azimuth concept

After finalizing the simulation of the “mock” model (HESS I), the main problem to be solved remained an efficient way to transfer the concentrated Image Sensor load. To do so, a sophisticated and efficient design of the trusses holding the Image Sensor should be implemented, taking into account the minimization of the self-weight of this supporting structure. The choice of the K-Trusses was previously discussed, although the three-dimensional topology was not defined.

First of all, the choice of three cantilever arms was examined, but immediately rejected, due to symmetry reasons. If the Image Sensor Structure was kept in place by three truss-cantilever arms, two solutions for the proper function of the telescope could be implemented. On one hand, the rotation of the dish around the elevation axis could be limited, so that the cantilever arm standing alone on one side, is always under tension. However, this solution would significantly reduce the tracking speed of our telescope, due to the fact that for a full rotation around the elevation axis, the azimuth axis should also rotate 180°. The other solution would be the design of the cantilever arm, that is standing alone on one side, to be able to withstand compression forces, which would lead to oversizing, as a result of buckling in and out of plane.

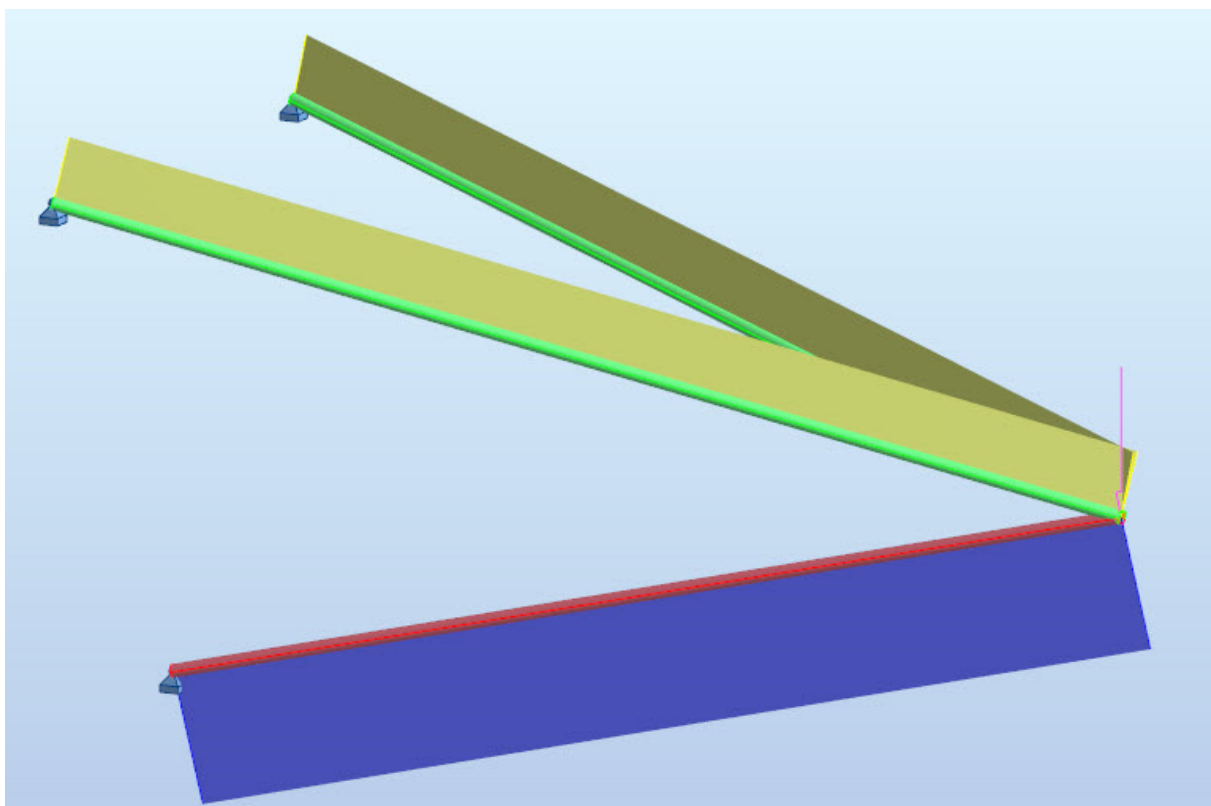


Figure 64 Image Sensor Structure composed of three cantilevers under a concentrated load in the edge and axial force distribution along the members. The Tension is shown in yellow (green bars) and the Compression in blue (red bar).

After deciding in four symmetric, single cantilever arms, the three dimensional geometry of each one was examined. Considering each of these cantilever arms as “columns”, which carry axial loads and a small amount of moment, mainly due to self-weight, the decision of reduction of the cross-section along the length of them was made. The significant advantage of this solution is the reduction of the self-weight while approaching the edge, optimizing the structure in terms of internal forces acting on the members. In a second stage, the choice of simple triangular truss was made mainly due to symmetry reasons.

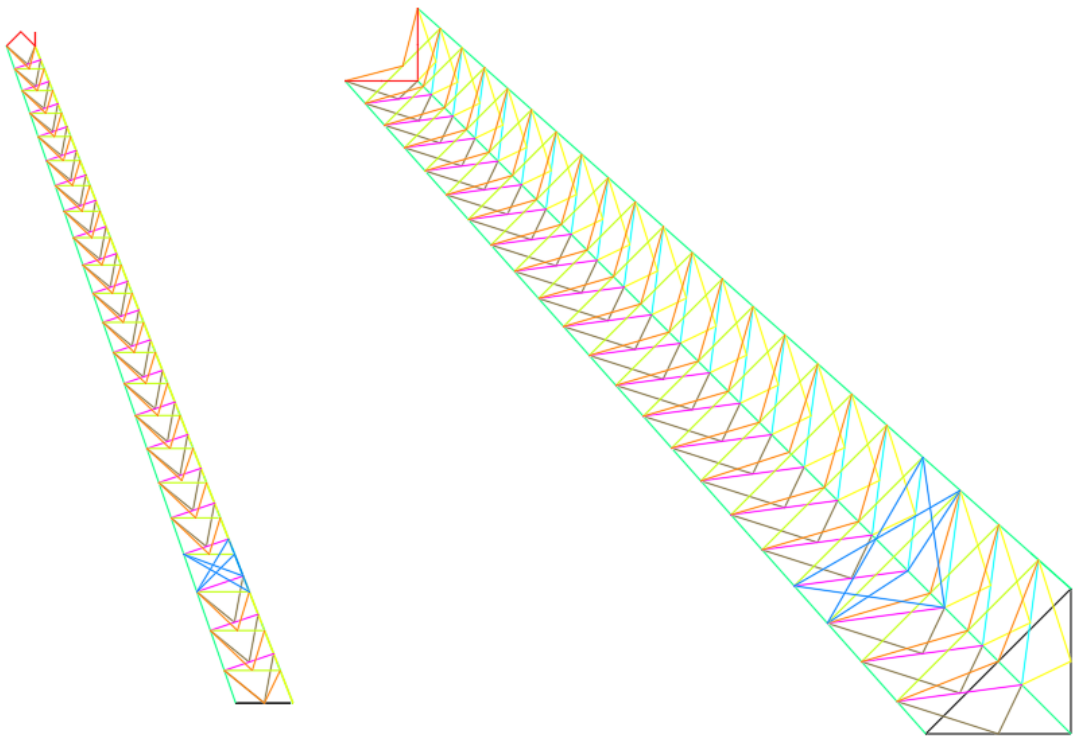


Figure 65 Final configuration of the triangular K-Truss cantilever. Side view (left) and top view (right). Different colors correspond different elements of the truss on each side.

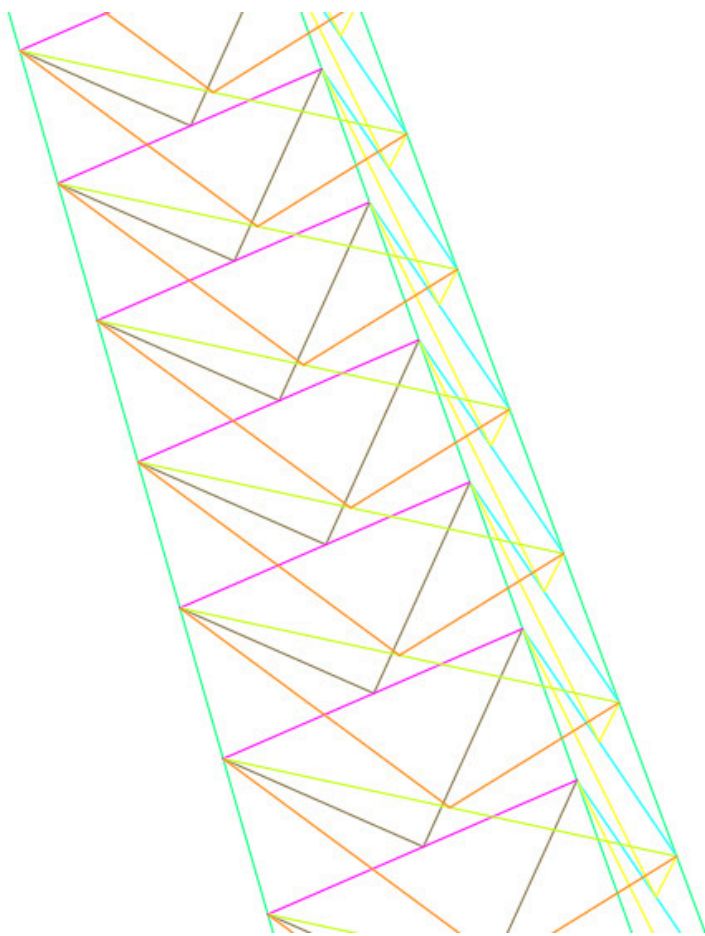


Figure 66 Final configuration of the triangular K-Truss cantilever. Close 3D view. Different colors correspond different elements of the truss on each side.

The final Image Sensor Structure configuration contains also cable elements to examine their contribution and a two dimensional Warren bracing system in the position of the maximum displacement. (around the two thirds of the cantilever length)

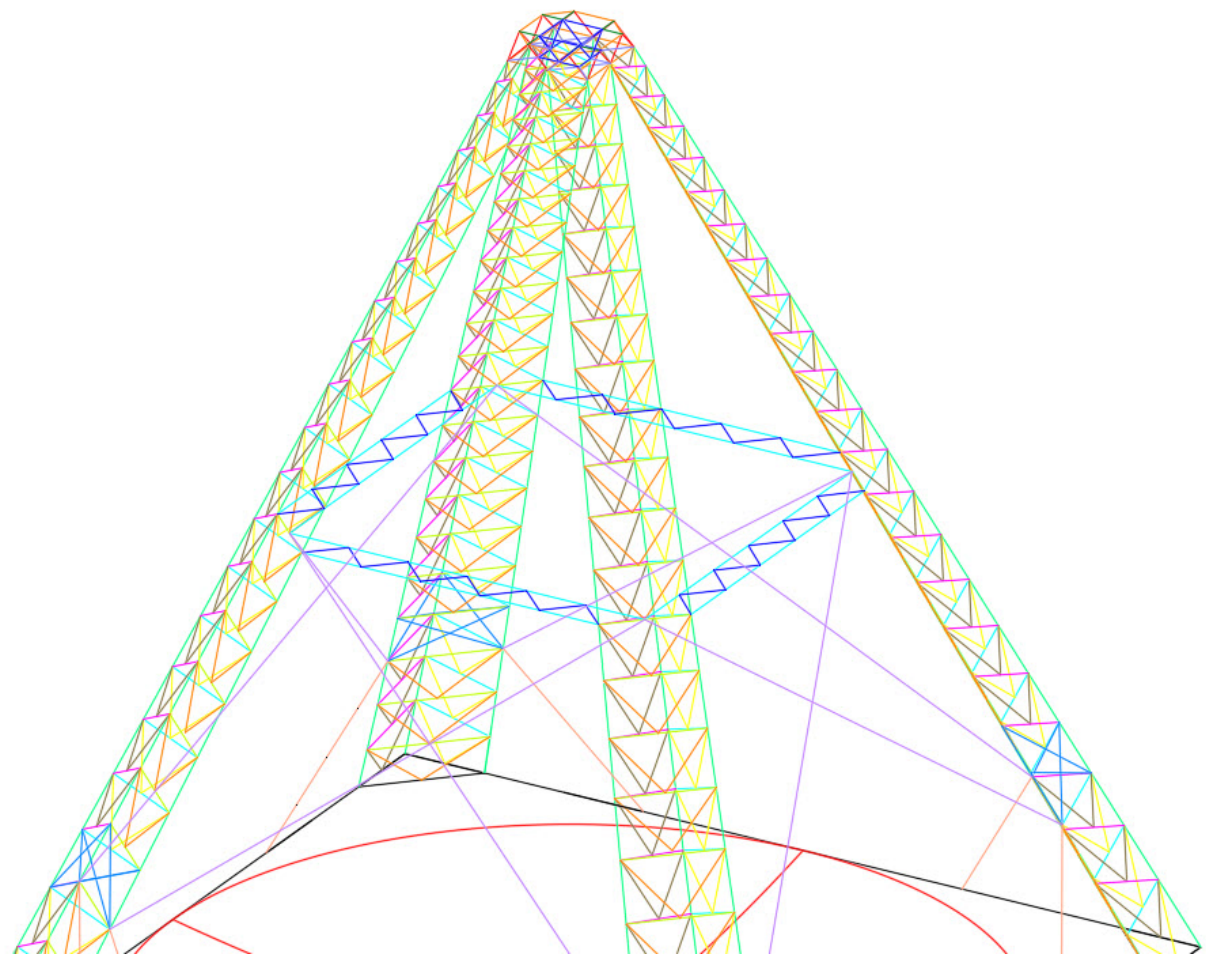


Figure 67 3D view of the Image Sensor Structure System. (Bracing system with light and dark blue, with purple the cables and with orange supporting bars of the triangular truss)

Finally, a three dimensional truss was chosen and created for the edge of the cantilever structure, with the goal to connect the single cantilevers and transfer the concentrated Image Sensor load efficiently.

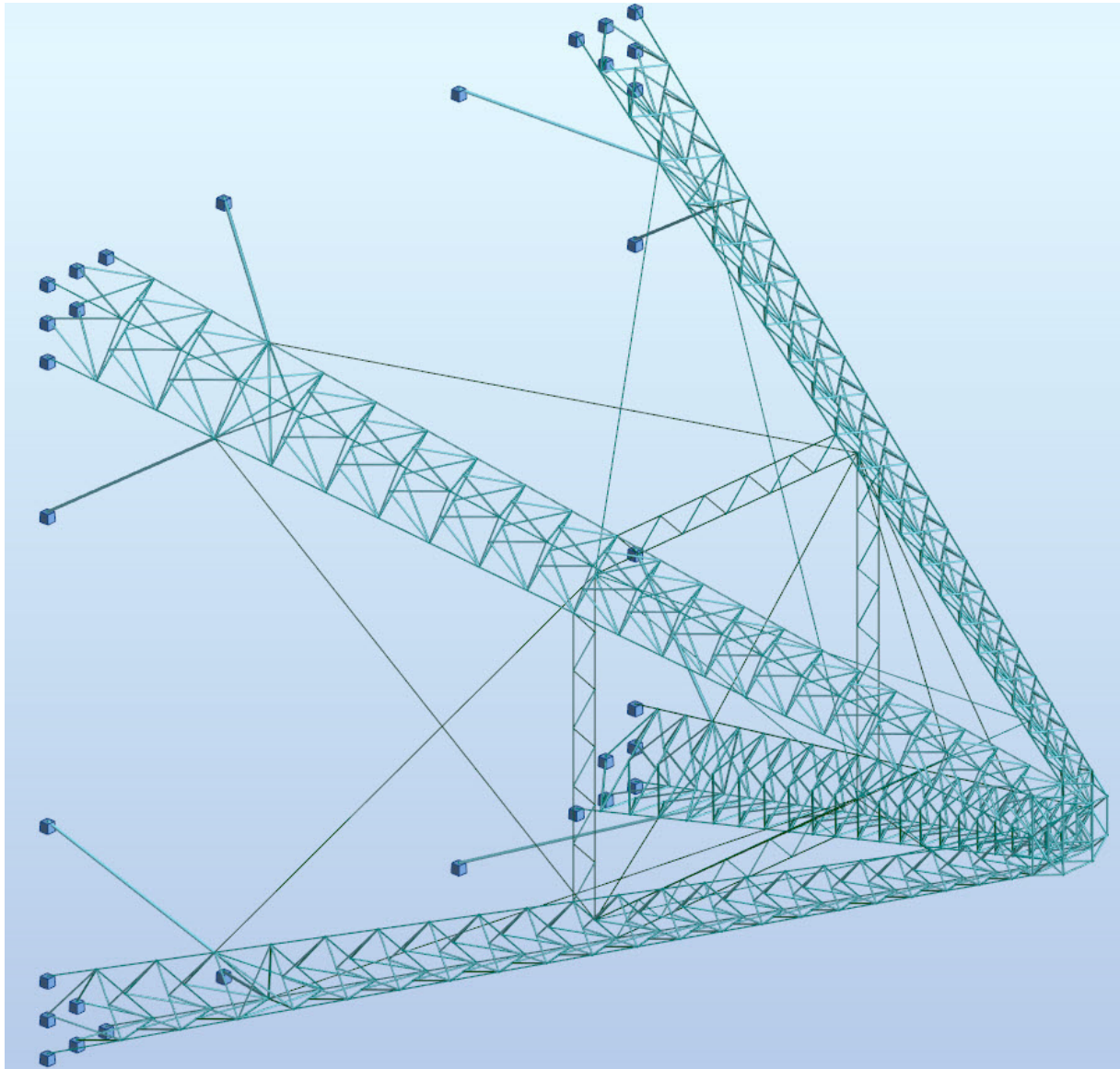


Figure 68 3D view of the final Image Sensor Structure in the analysis software.

The analysis of the structure at this initial design was chosen as linear elastic, taking into account the non-linear behavior, due to the cables geometric non linearity. The incremental load approach was followed. In the first phase (assembly case), the cables were loaded only with the self-weight of the structure. In the second and final phase the Image Sensor concentrated load was assigned in the deformed shape. It is important, here, to mention that a combination of the load cases is not possible, due to non-linearity. (superposition principle not accepted) After assigning the loads and running the analysis, an iterative design procedure was followed. The design groups and their respective final Cross-Sections are shown. An important point is, that this design is still considered abstract and is used only to examine a more realistic behavior of the Image Sensor Structure by optimizing it according to self-weight. For example, no connection constraints were considered. (e.g. the connection of the diagonals/vertical bars with the chords of the K-Truss is not realistic, taking into account the bars' Cross-Sections, which are bigger for the diagonals/vertical bars)

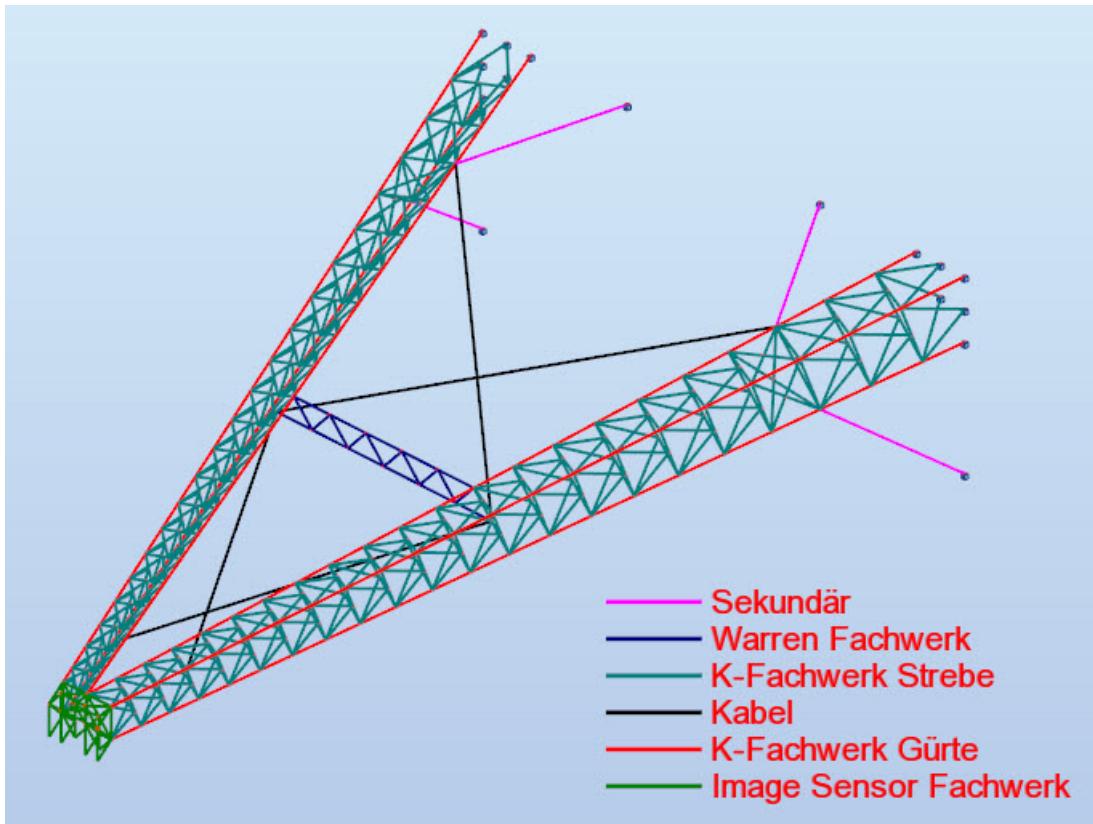


Figure 69 Design of the Image Sensor Structure. Elements' group.

K-Truss chords (red)	CHS 88.9x3 S460
K-Truss diagonals/vertical bars (light blue)	CHS 114.3x3 S460
Warren truss bars (dark blue)	CHS 60.3x3 S460
Image Sensor bars (green)	CHS 114.3x3 S460
Cables (black)	15mm diameter Y1860
Secondary supporting bars (pink)	CHS 193.7x5 S460

Table 15 Final Cross-Sections and their respective material of the design of the Image Sensor Structure. The analysis results are summarized below.

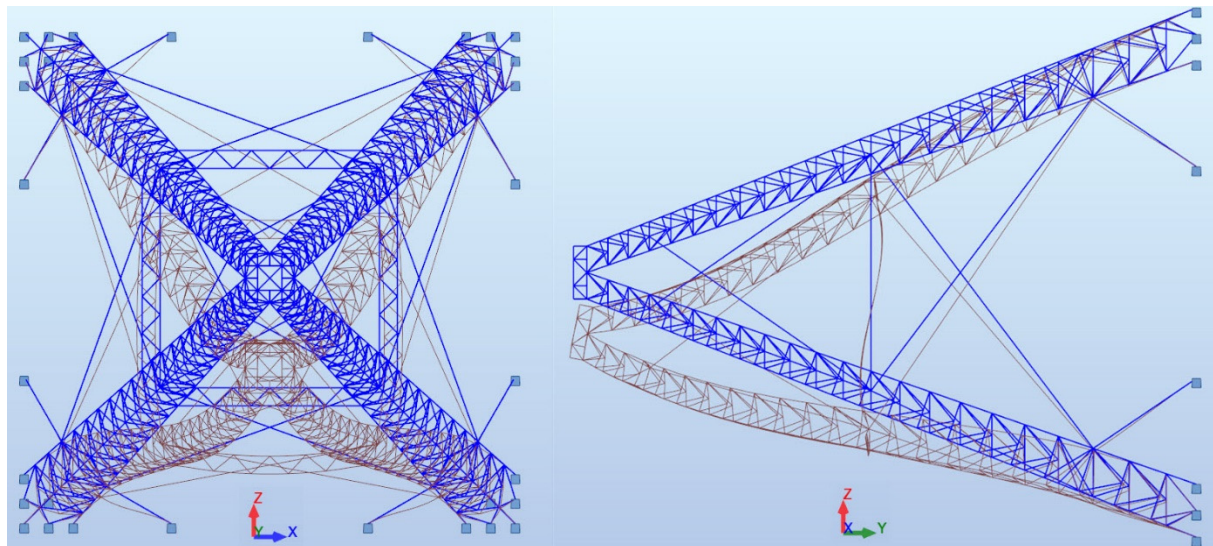


Table 16 Deformation shape of the Image Sensor Structure to Self-Weight and Image Sensor concentrated load.

	Ux(mm)	Uy(mm)	Uz(mm)	Rx(rad)	Ry(rad)	Rz(rad)
Maximum displacements	-17.1	29.1	-164.8	-0.006	-0.007	-0.007
Displacements of Image Sensor	0	2.1	-142.3	-0.005	0	0

Table 17 Maximum Structure displacements and displacements of the Image Sensor (nodal) for the self-weight and concentrated load of the Image Sensor. (Direction of the displacements according to the coordinate system of the images above)

Finally, CFRP elements were used to examine the sensitivity of the structure to its own self-weight and the possibility of bearing them in mind for future simulations. CFRP elements have very diverse characteristics and, due to the inhomogeneity of these in the element local coordinate system, many uncertainties arise. A notable example is the difficulty of designing reliable connections with CFRP elements, as most of the times there is a stress plane where Carbon has no resistance and the stresses should be received only by the epoxy.

The CFRP material that was created in the program had the following characteristics:

Young`s modulus in Gpa	300
Shear modulus in Gpa	125
Design resistance in Mpa	650
Specific weight in kN/m ³	15
Poisson`s ratio	0.3

Table 18 Characteristics of the CFRP material created for the simulation of the Image Sensor Structure.[18]

The Cross-Sections (circular hollow rods) were chosen iteratively according to the following principle and simplification. All elements were considered as truss elements (carrying only compression/tension) and were designed in strength and buckling, (in and out of plane buckling has the same constraints due to symmetry of the Cross-Section), similar to steel elements. The buckling check was performed according to SIA 263 2013 (4.5), taking into account the most critical buckling curve. (curve d) The thickness of the Cross-Section was chosen 4mm. The final step is presented.

Compression Force: $F_x=256.4kN$

Critical length: $L_K=3m$

**Due to the fact that the critical length of the element, that the maximum compression force is acting, is less than 2m and compression forces act also on elements with critical length over 4m a simplified average critical length is used, with the maximum compression force of the structure acting on it.*

$$N_{K,Rd} \geq 256.4kN \Rightarrow \sigma_K * A_{Cross-Section} \geq 256.4kN \Rightarrow \chi_K * f_y * A_{Cross-Section} \geq 256.4kN \quad (1)$$

$$\lambda_E = \pi \sqrt{\frac{E_{Carbon}}{f_y_{Carbon}}} \Rightarrow \lambda_E = 3.14 * \sqrt{\frac{300000}{650}} = 67.458 \approx \lambda_{E_S460} \quad (2)$$

$$\lambda_K = L_K \sqrt{\frac{A_{Cross-Section}}{I_{Cross-Section}}} \quad (3)$$

$$\overline{\lambda_K} = \lambda_K / \lambda_E \quad (4)$$

$$\chi_K = \frac{1}{\Phi_K + \sqrt{\Phi_K^2 - \lambda_K^2}}, \quad (5)$$

$$\chi_K \leq 1$$

$$\Phi_K = 0.5 * \left[1 + \alpha_K (\bar{\lambda}_K - 0.2) + \bar{\lambda}_K^2 \right], \alpha_K = 0.76 \quad (6)$$

$$A_{Cross-Section} = \pi * R^2 - \pi * r^2 = \pi * (r+4)^2 - \pi * r^2 = 8 * \pi * (r+2) \quad (7)$$

$$I_{Cross-Section} = \frac{\pi}{4} * (R^4 - r^4) = \frac{\pi}{4} * ((r+4)^4 - r^4) = \quad (8)$$

$$\frac{\pi}{4} * (r^4 + 16 * r^3 + 96 * r^2 + 256 * r + 256 - r^4) = \frac{\pi}{4} * (16 * r^3 + 96 * r^2 + 256 * r + 256)$$

By solving the equations above, for r, or by using the buckling curves in SIA263 2013 (4.5.1.8), we find the appropriate Cross-Section from the Cross Hollow Section (CHS) database.

CHS114.3x3.2

$$A_{eff} = 1116.333 mm^2$$

$$I_y = I_z = 1723820 mm^4$$

$$(3) \Rightarrow \lambda_K = 76.34$$

$$(4) \Rightarrow \bar{\lambda}_K = 1.1317$$

From SIA263 2013 (4.5.1.8), by choosing curve d, $\chi_K = 0.4 > 1$

$$N_{K,Rd} = N_{Rd} * \chi_K = f_y * A_{eff} * \chi_K = 650 * 1116.333 * 0.4 = 290.2 kN > 256.4 kN \text{ o.k.}$$

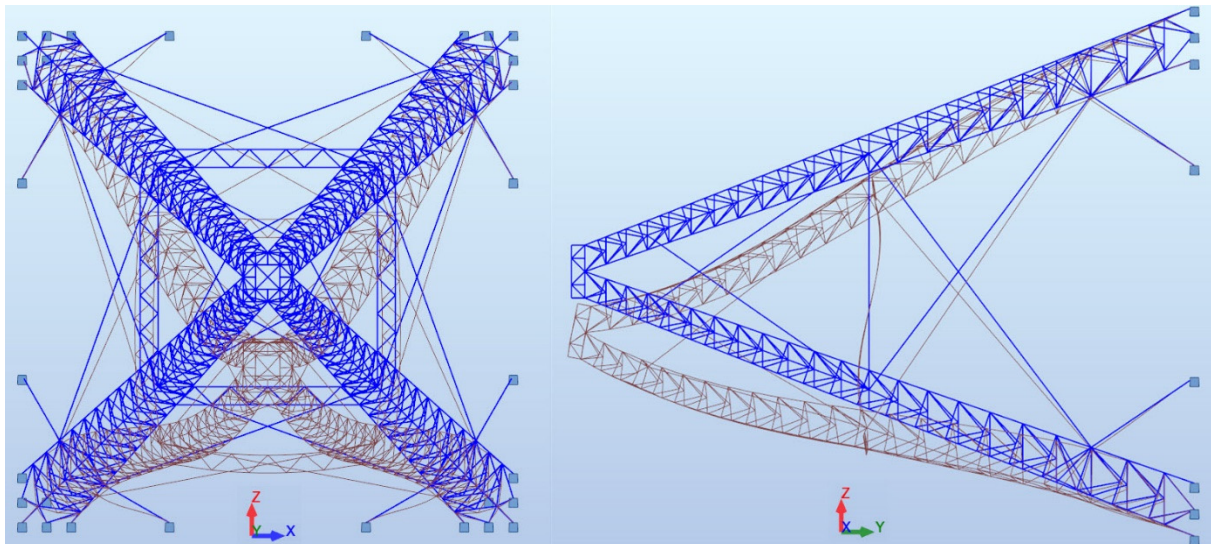


Figure 70 Deformation shape of the CFRP Image Sensor Structure to Self-Weight and Image Sensor concentrated load.

	Ux(mm)	Uy(mm)	Uz(mm)	Rx(rad)	Ry(rad)	Rz(rad)
Maximum displacements	-10.4	8	-51.1	-0.001	-0.004	-0.004
Displacements of Image Sensor	0	1	-49.8	-0.001	0	0

Table 19 Maximum CFRP Structure displacements and displacements of the Image Sensor (nodal) for the self-weight and concentrated load of the Image Sensor. (Direction of the displacements according to the coordinate system of the images above)

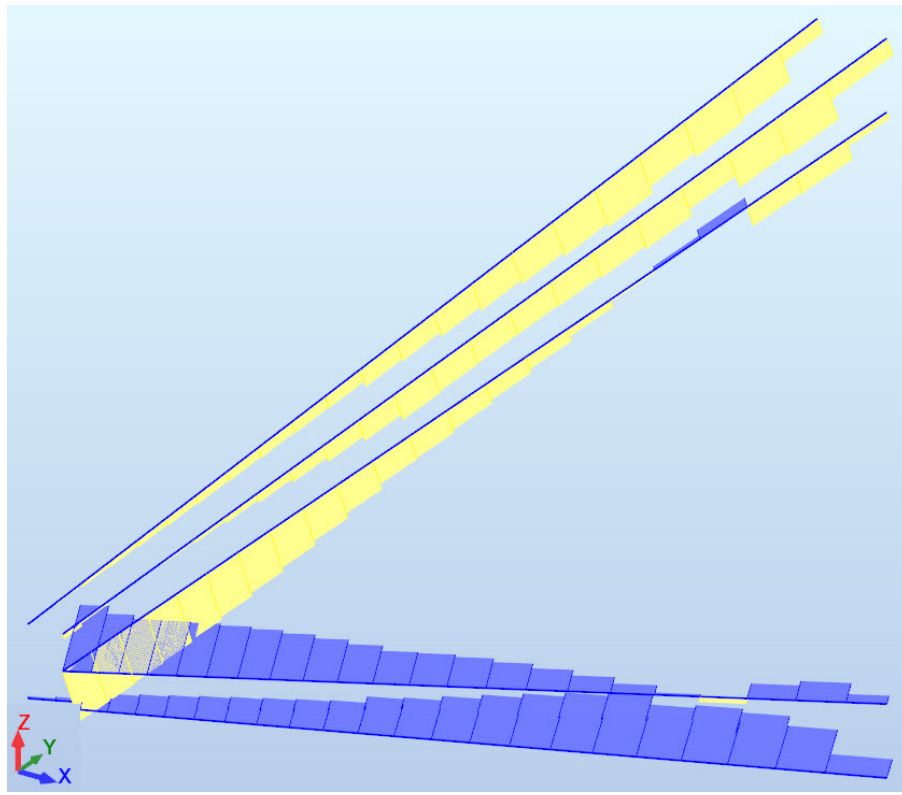


Table 20 Axial force distribution of the K-Truss chords with only one side of the Image Sensor Structure evident. (Tension: Yellow, Compression: Blue)

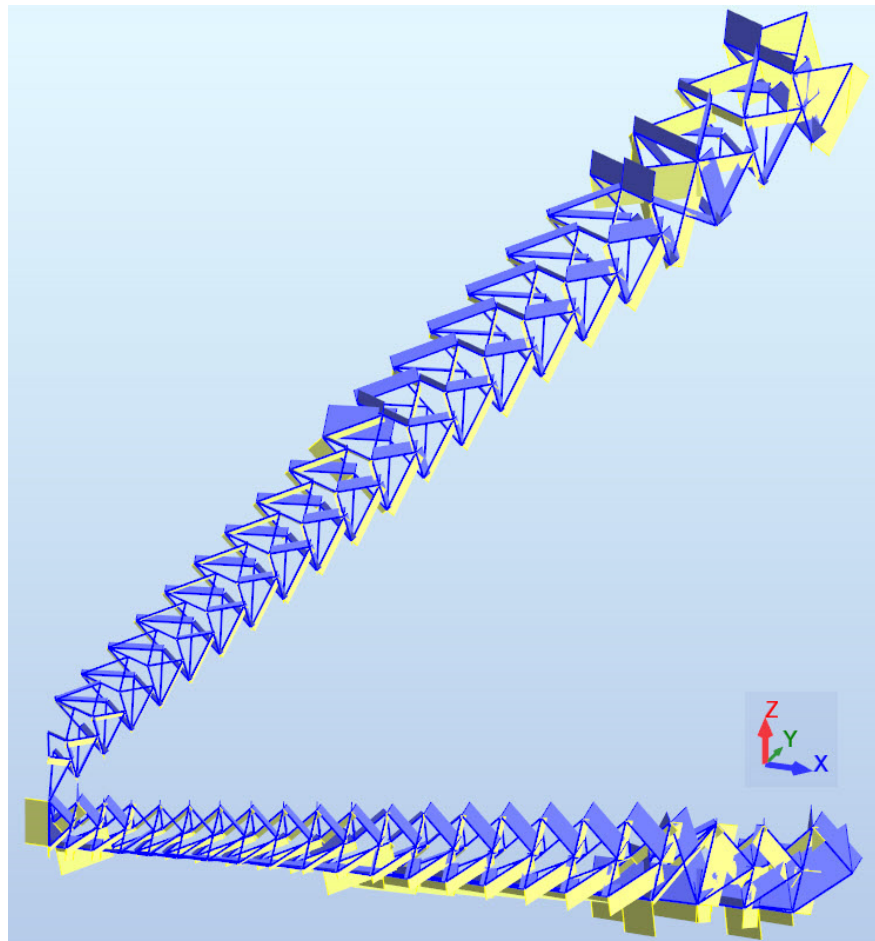


Table 21 Axial force distribution of the K-Truss diagonals/posts with only one side of the Image Sensor Structure evident. (Tension: Yellow, Compression: Blue)

7.2 Base structural designs for the Altitude-Azimuth concept

The structure that supports the dish with the Image Sensor Structure was examined, taking into account the efficient load-transfer to the foundations. Due to the size of the telescope, apart from the weight of the structure, other aspects should be kept in mind in order to minimize the cost. The two basic concepts for the base are:

1. Base structure with custom sized elements, optimizing each of them according to their internal forces.
2. Base structure with modules. The design of a unique modular construction, that could be repeated to construct the base is considered. This module was chosen as a 5m (height) extruded triangle with sides 5mx5mx7.07m.

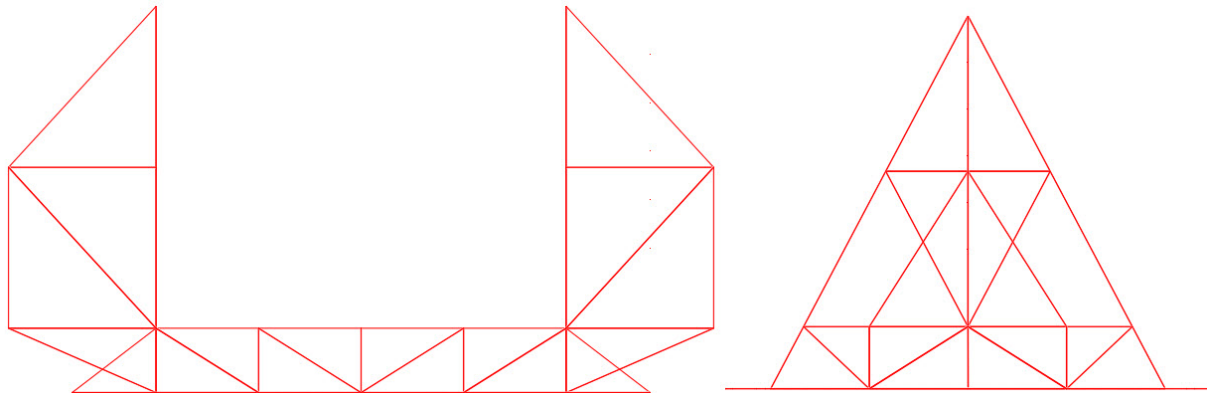


Figure 71 Base design No.1. Custom sized elements. (Front view on the left, Side view on the right)

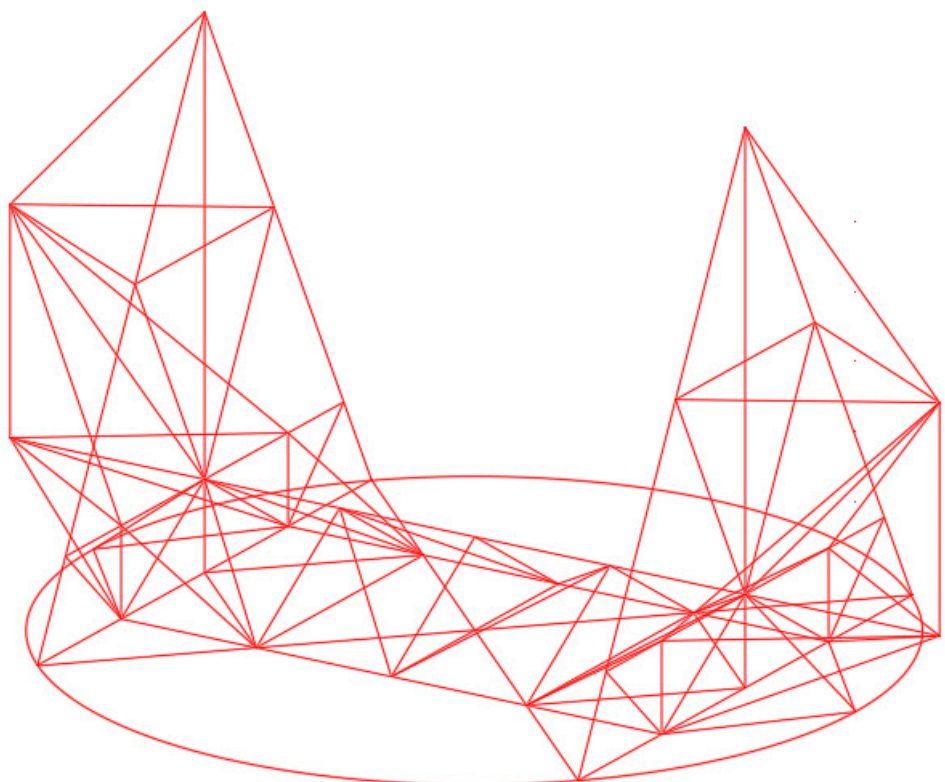


Figure 72 Base design No.1. Custom sized elements. (3D view)

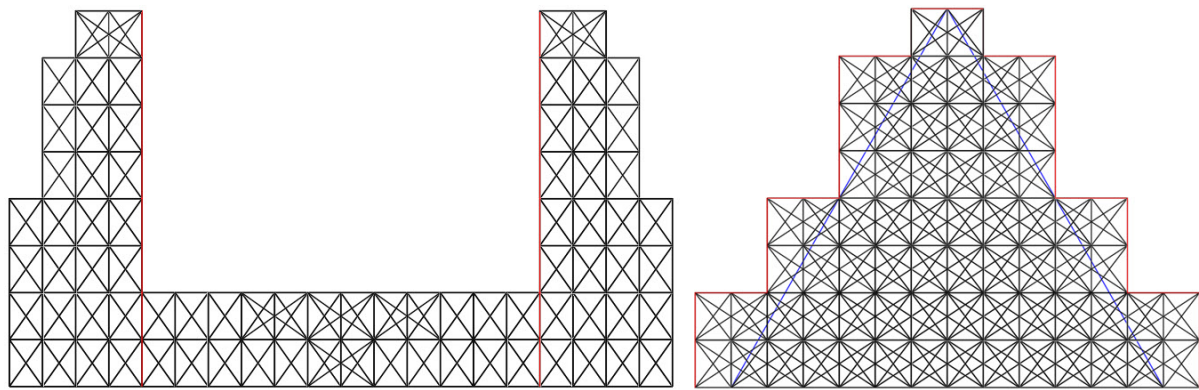


Figure 73 Base design No.2. Modular Design. (Front view on the left and Side view on the right)

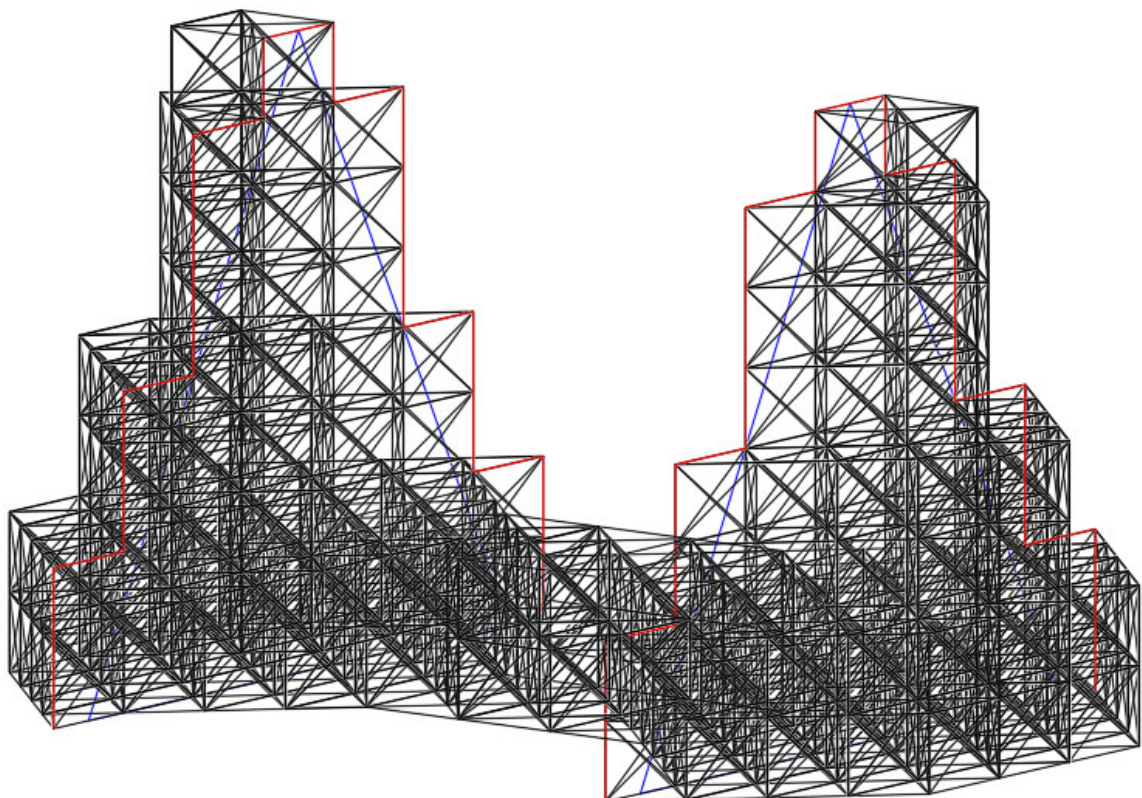


Figure 74 Base design No.2. Modular Design. (3D view)

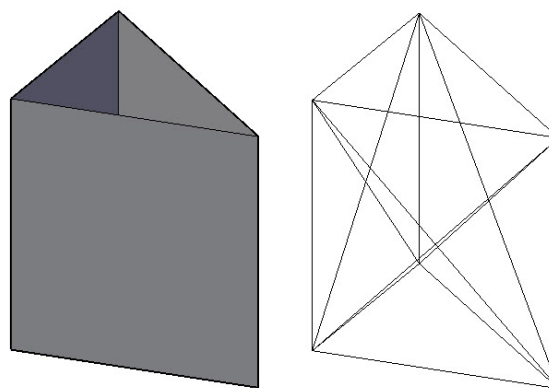


Figure 75 Modules considered for the base design No.2 (Modular design).

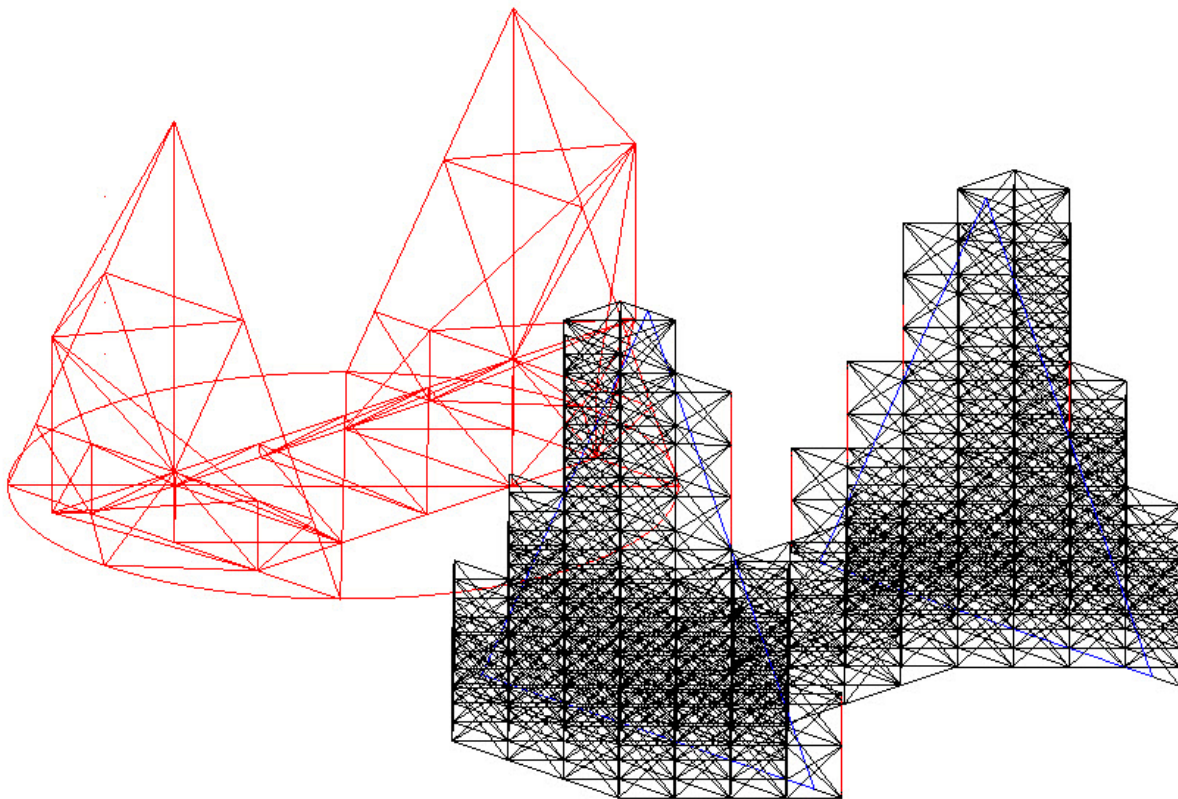


Figure 76 Comparison of the structural scale for the two base designs.

7.3 Construction of the Altitude-Azimuth concept

After the investigation of the “mock” design and the scalar limitations that occurred, a more precise and sophisticated examination of a traditional Alt-Azimuth design was considered necessary, taking into account the requirements in 2. (mainly the f/D ratio required for the Image Sensor)

Two positions of the Image Sensor were extensively examined. The zenith position and the 60° from zenith position. (maximum zenith angle)

This design, even though it follows the traditional way of an altitude-azimuth mount, poses some very big advantages, due to the separation of the Image Sensor construction from the dish support construction. First of all, implementing this concept, the dish deformations remain homogenous, without disturbing completely its shape. Moreover, the load distribution of the image sensor and the dish is far better as the loads follow different paths.

Apart from the static advantages, though, also practical advantages emerge. In stand-by mode the dish could be misaligned from the Image Sensor, so the sun beams are not able to destroy it. Another advantage is the reduced cost for mechanical parts, as they have to transfer reduced loads. Finally, during survival wind or maintenance situations, the Image Sensor Structure can “rest” on the base, improving the static behaviour of the structure.

In the next pages the different parts of this design will be presented, along with their design groups, the geometry and the respective dimensions.

The procedure starts from the base, where the modular approach was followed. The final base and its dimensions are as follows.

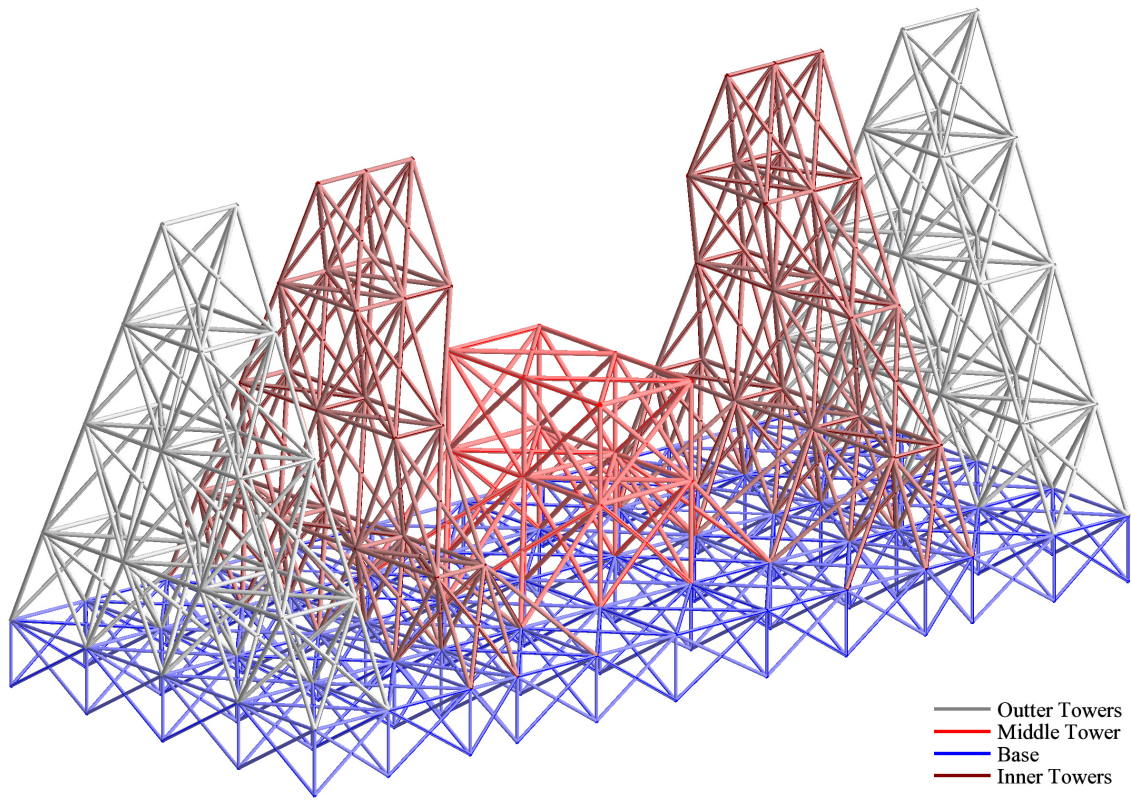


Figure 77 3D visualisation of the base of the Altitude Azimuth design. (Design groups visible)

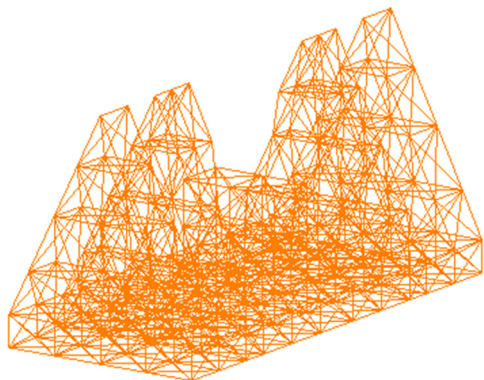


Figure 78 Analytical base model of the Altitude Azimuth design.

Dimensions

Top View: 32.5m x 74m

Total height: 37.5m

Inner tower height: 14.5m (Base: 5m)

Design groups

Outer towers (grey) CHS 406.4x6.3

Middle tower (red) CHS 273x8

Inner towers (brown) CHS 323.9x6

Base (blue) CHS 219.1x5

After the base, the Rack that holds the dish is constructed and placed on the middle tower.

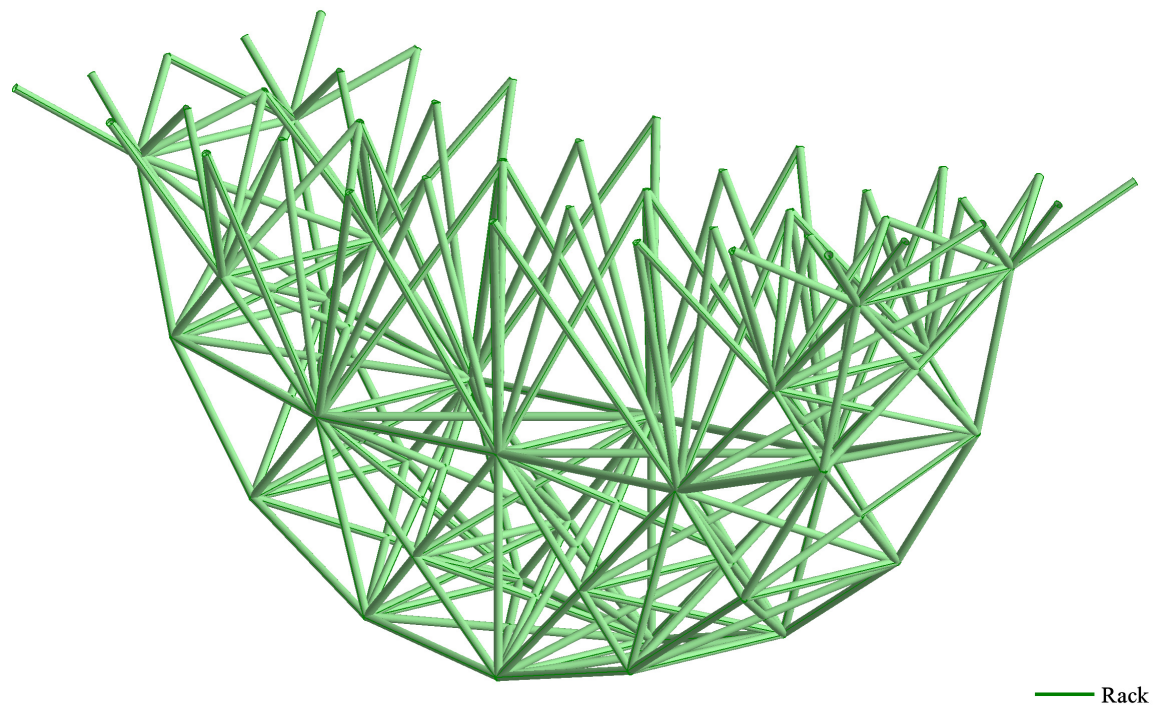


Figure 79 3D visualisation of the dish rack of the Altitude Azimuth design. (Design groups visible)

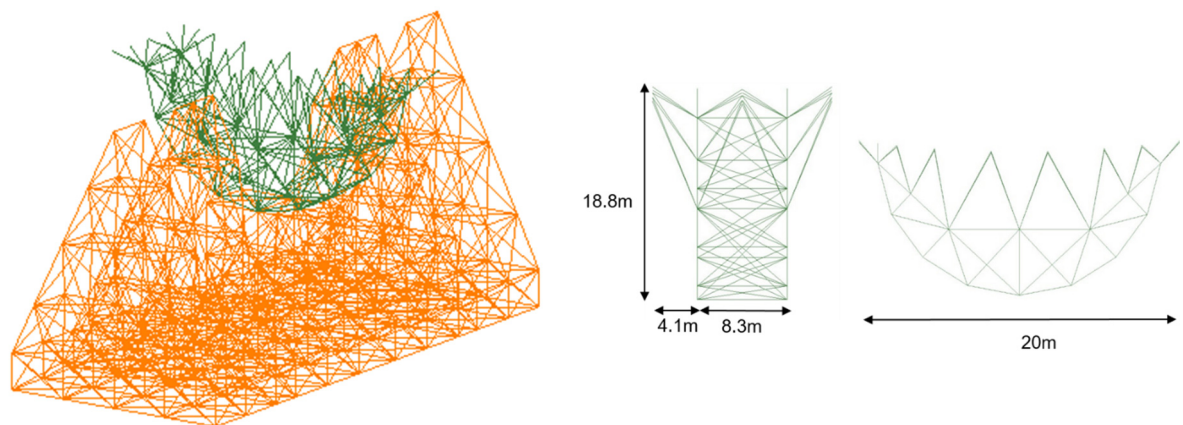


Figure 80 Analytical dish rack model of the Altitude Azimuth design.

The Cross-Sections are CHS 244.5x5.

Then the dish is placed on the rack. The exact geometry of the dish can be found in 6.3. Here, only some basic dimensions and the design groups are evident.

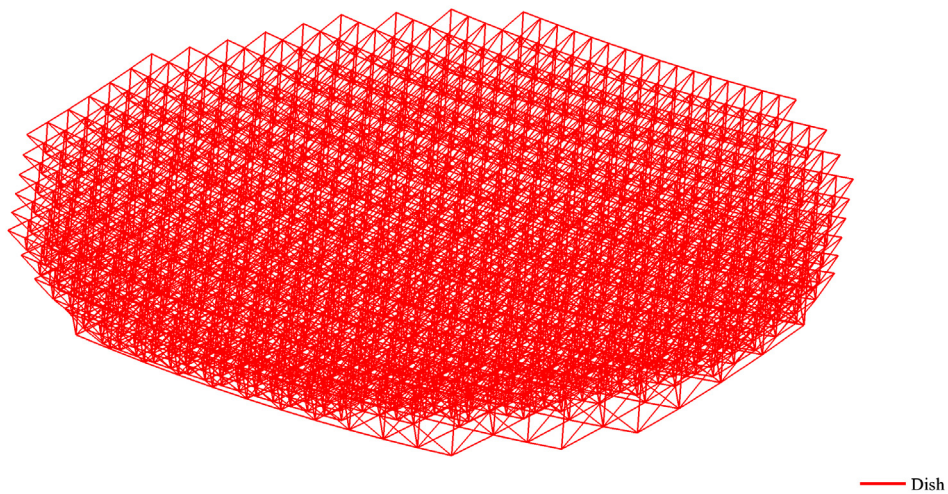


Figure 81 3D visualisation of the dish space frame of the Altitude Azimuth design. (Design group visible)

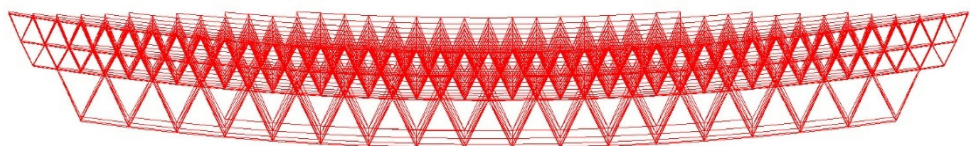


Figure 82 Front view of the dish space frame of the Altitude Azimuth design. (Design group visible)

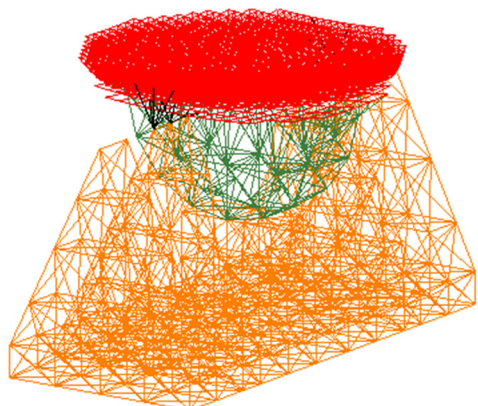


Figure 83 Analytical model of the Altitude Azimuth design. Final dish structure without Image Sensor Structure.

Dimensions

2x1.2m height layers	3 layer MERO structural system
1x2.4m height layer	

Upper layers` diameter 50m

Lower layers` diameter ~35m

Design groups

All dish truss elements CHS 168.3x3.2

Axis mount elements (bars connecting the dish with the top of the inner towers) CHS 323.9x10

At this point, the dish construction is complete and fully functional. In the next stage, the Image Sensor Structure will be added. First of all, the Rack that will support and connect the Image Sensor Structure, is constructed and presented. This Rack is concentric with the dish Rack so the distance of the Image Sensor from the dish remains constant.

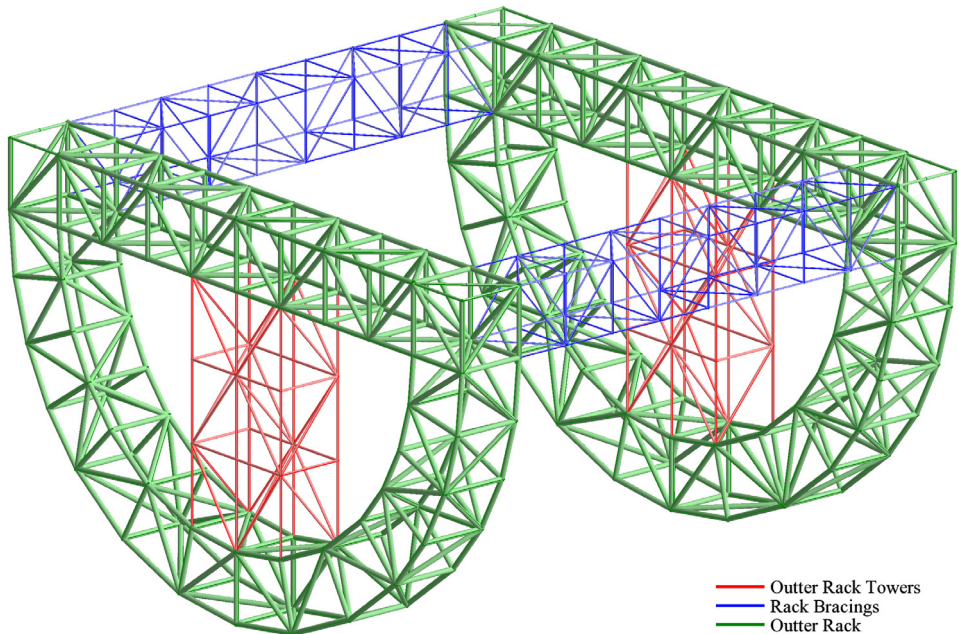
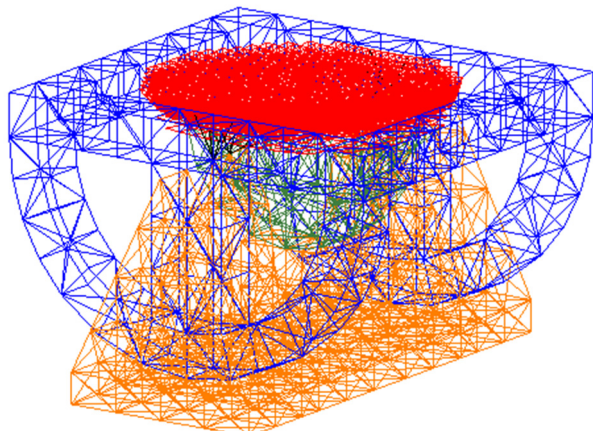


Figure 84 3D visualisation of the Image Sensor rack of the Altitude Azimuth design. (Design groups visible)



Design groups

Outer Rack (green) CHS 406.4x12.5

Outer Rack Towers (red) CHS 244.5x8

Rack Bracings (blue) CHS 193.7x5

Figure 85 Analytical model of the Image Sensor rack of the Altitude Azimuth design. Final dish structure also visible.

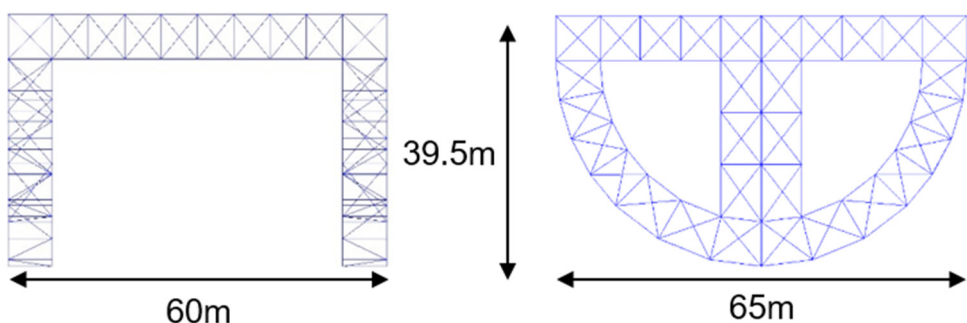


Figure 86 Image Sensor rack dimensions.

Finally, the Image Sensor is mounted on top of the Rack base. Small refinements have been done to the initial Image Sensor simulation to match the exact geometry and improve its behaviour. A notable one is the increase of the lever arm (65m instead of 60m) of the critical direction, without ruining the symmetry. Moreover, as it is evident, no cables were assigned, due to their limited contribution for both zenith and 60° from zenith positions. However, the design with CFRP was promising so a model with CFRP configuration was also constructed. The CFRP bars were not assigned in the whole structure but only on the edge part as it can be seen from the image on the right. This was done in order to accomplish a balance between cost and efficiency.

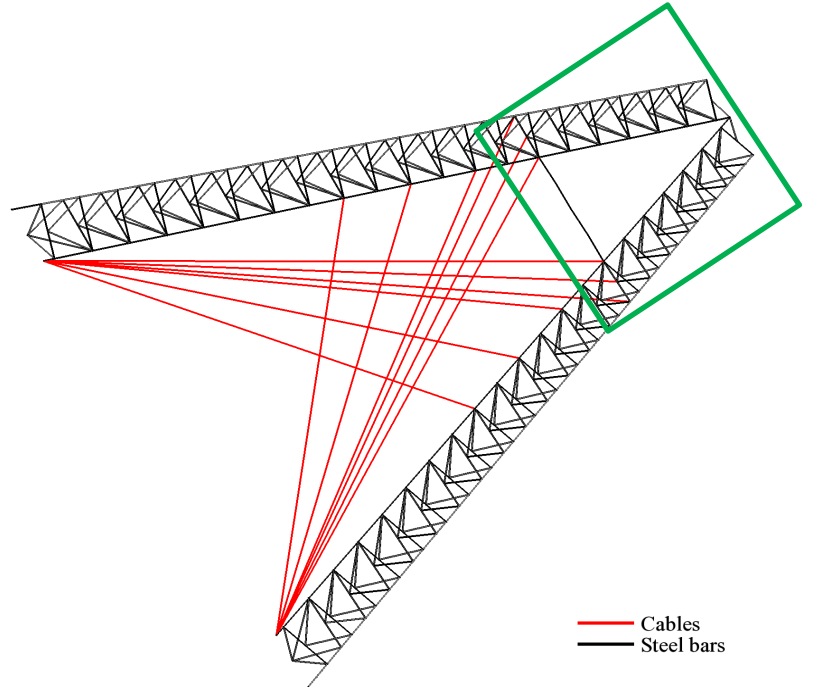


Figure 87 Side view of the Image Sensor Structure with cables and CFRP edge.

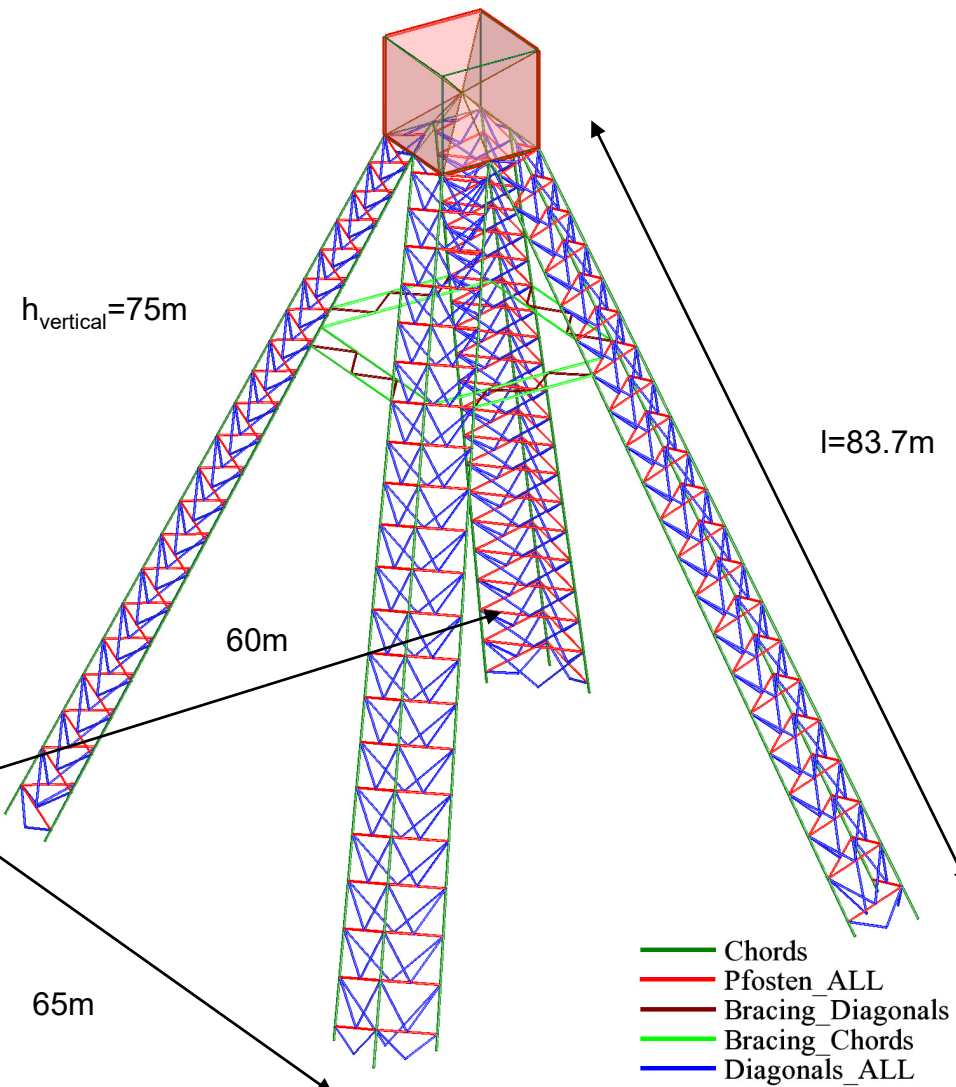


Figure 88 Dimensions of the Image Sensor Structure (Quadrupod)

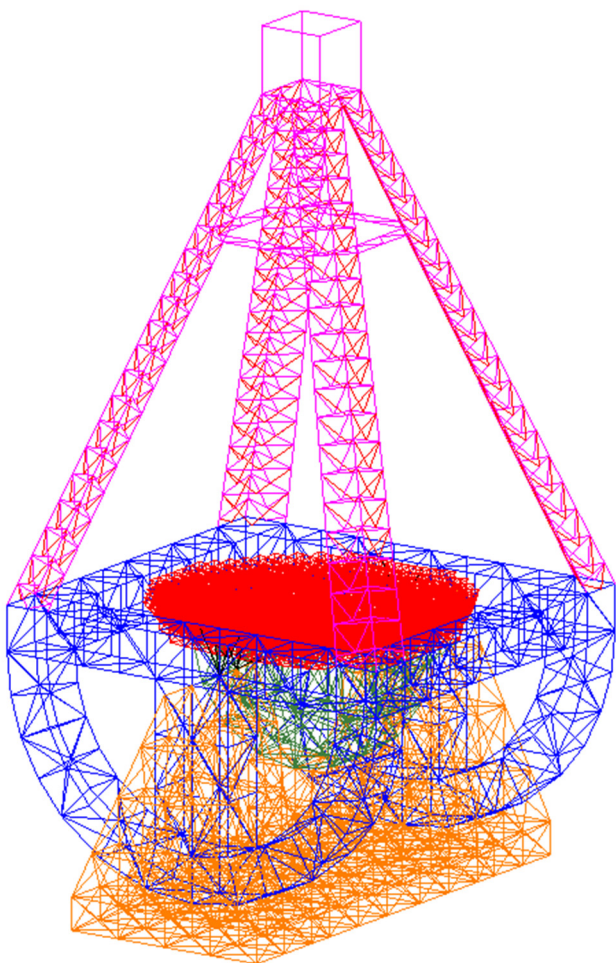


Figure 89 Analytical model of the total Altitude Azimuth design.

Design groups

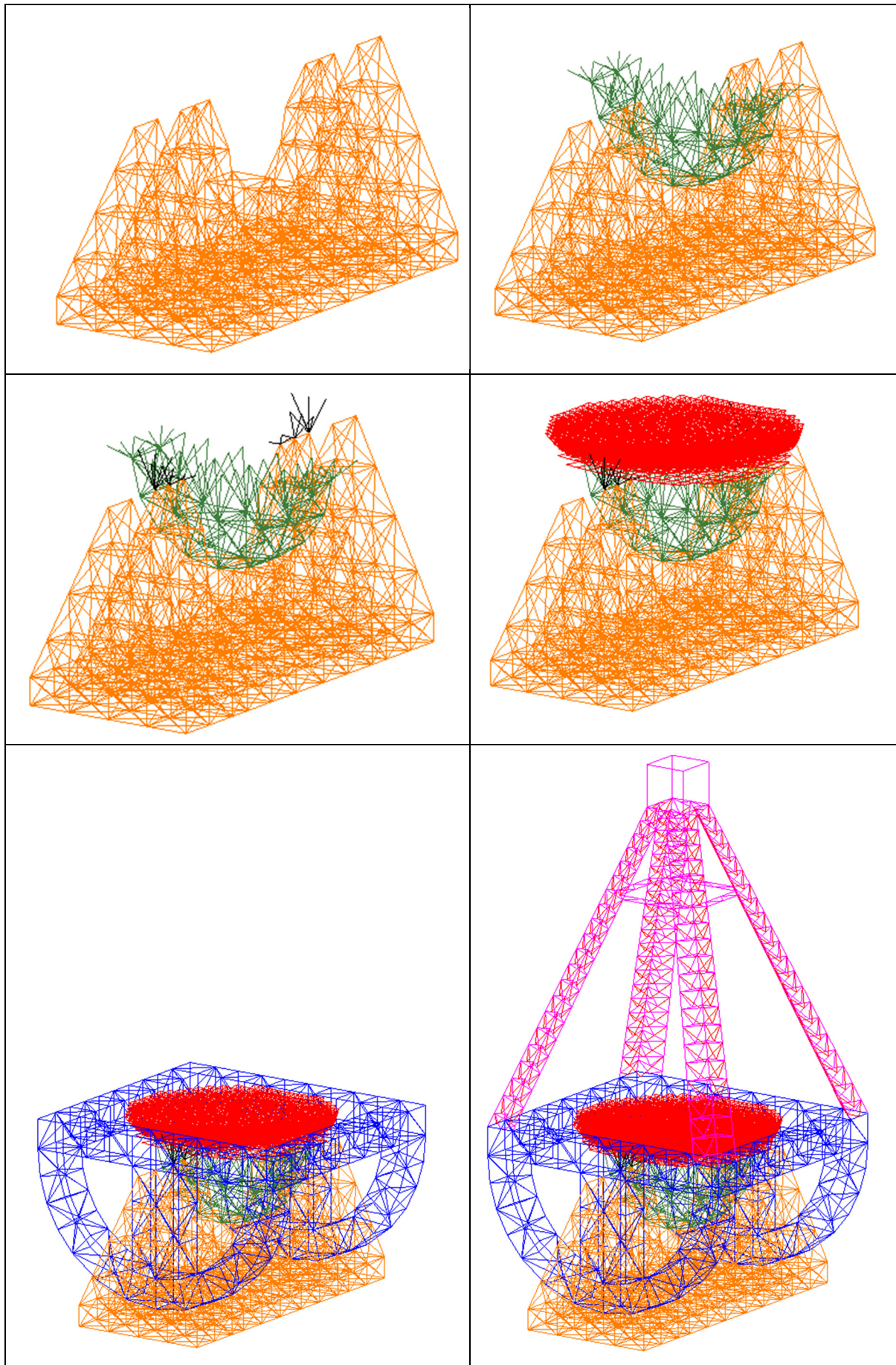
Chords (dark green) CHS 273x8

Vertical truss bars (red) CHS 168.3x3.2

Diagonals (blue) CHS 219.1x5

Chords of the bracing (green) CHS 168.3x6

Diagonals of the bracing (blue) CHS 168.3x3.2



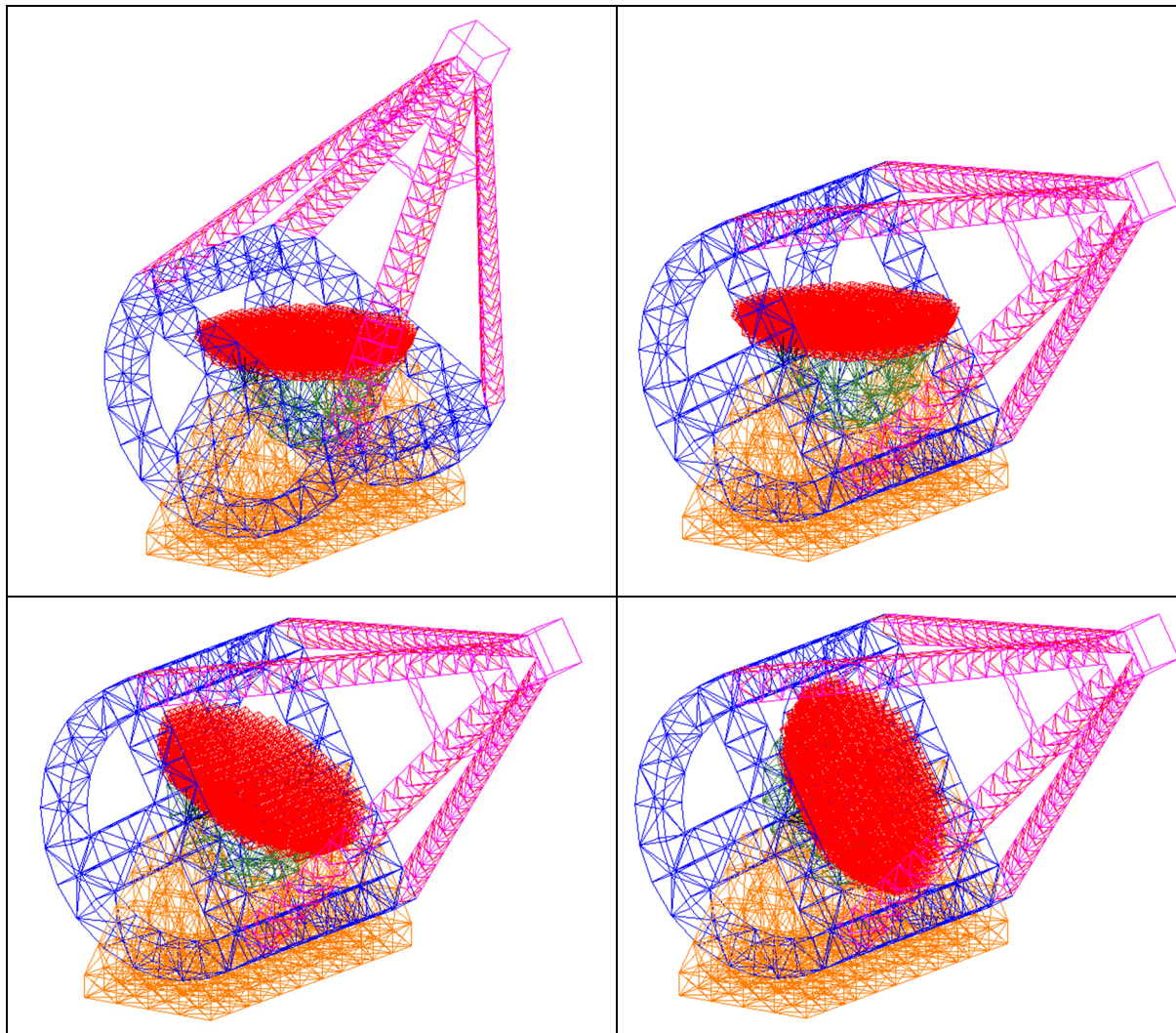


Table 22 Steps of the Altitude Azimuth design construction. From left to right, pictures 1-5 are the construction steps and 5-10 the rotation of the dish and Image Sensor Structure.

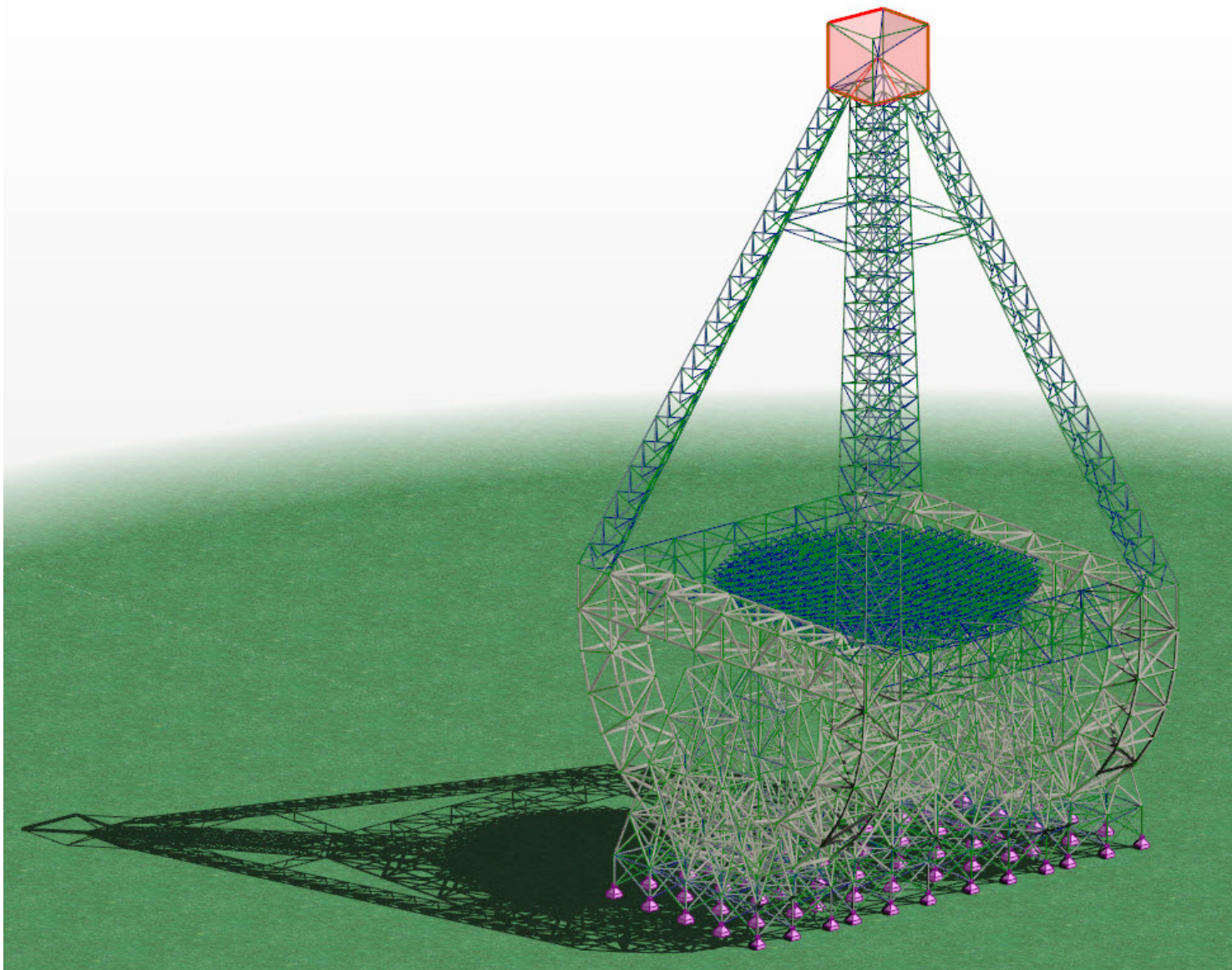


Figure 90 3D illustration of Altitude-Azimuth design in zenith position.

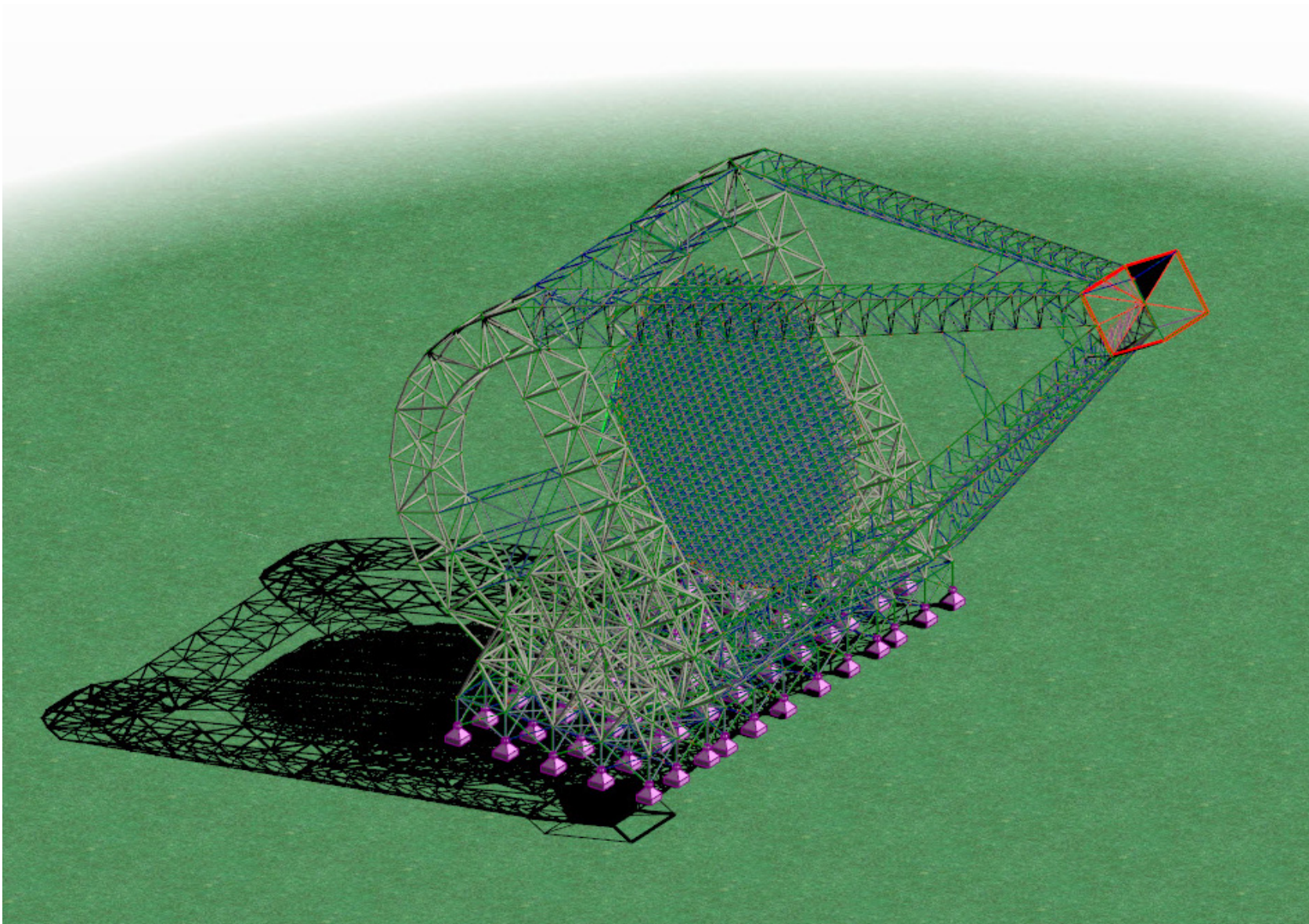


Figure 91 3D illustration of Altitude-Azimuth design 60° from zenith position.

8 TheBigLebowSky concept

TheBigLebowSky concept is based on the design of Sebastian Müller in 3.2.2. It is, actually, the next step of this idea, taking into account the results and conclusions of the first simulations. In this stage the Robocrane Image Sensor Structure is also simulated with an accurate geometry and is combined with the Main Dish Structure. The two structures will be examined in the first place separately, as they pose two different and completely not interrelated structural systems. Finally, an alternative to the Robocrane Image Sensor Structure, the Cross-Arch Structure will be examined afterwards for comparison.

8.1 The Main Dish Structure

The Main Dish Structure follows the exact same design as our first concept, with a 50m diameter dish. However, the Space Frame of the dish is redesigned, composing from two truss layers. The Tension Ring is also accurately redesigned, bearing in mind also the connection of the Space Frame and the cables with it and the total geometry is rearranged so that the minimal shadowing surface on the dish occurs.

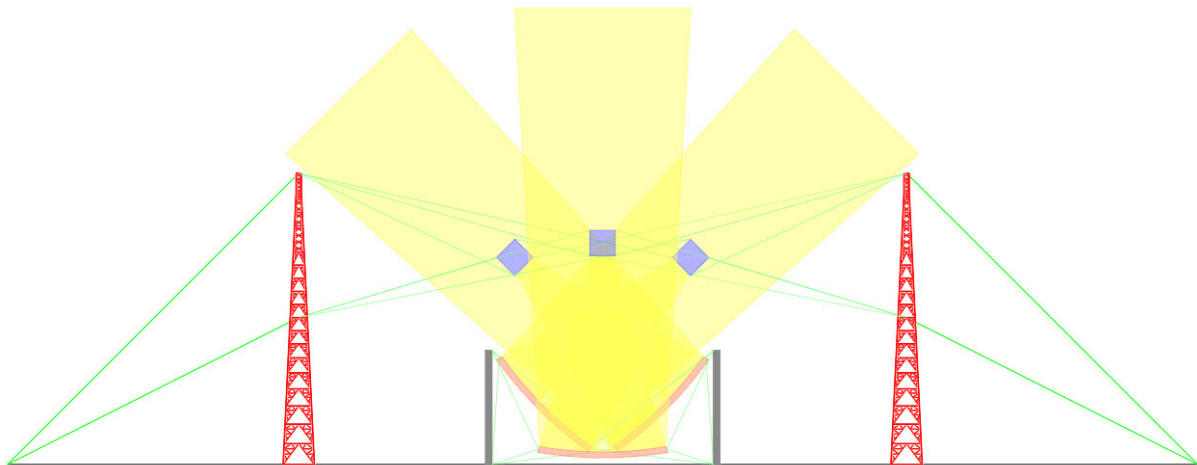


Figure 92 Side view of TheBigLebowSky proposal.

As a starting point to define the geometry, the maximum angle of the dish from the Zenith point should be examined. The reason is, that the need for minimal shadowing surface on the dish (areas with yellow in the above sketch) would result in the minimal column and tower distance. The following cases were examined:

- Case No.1, max. Angle 45°
- Case No.2, max. Angle 50°
- Case No.3, max. Angle 60°

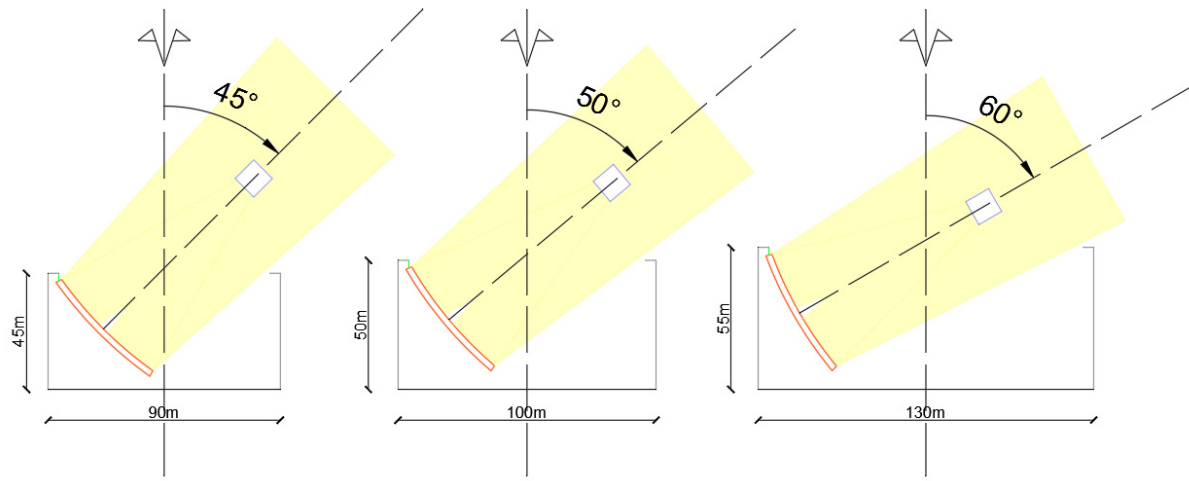


Figure 93 Research for the maximal Zenith angle of the dish, taking into account the shadowing of the columns.

The Case No.1 was chosen for the final design, weighing the pros and cons of a larger-sized structure in comparison with a broader field of view. As the majority of the observations are performed within the 45° field, the only major disadvantage, from the astrophysics point of view, is the lack of the possibility of tracking an event for a long time. So, the disproportional increase in structural size and as a result in cost, led to the decision of the Case No.1. In any case, this proposal is not final and in a later stage, it would be simpler to reconfigure this original geometry.

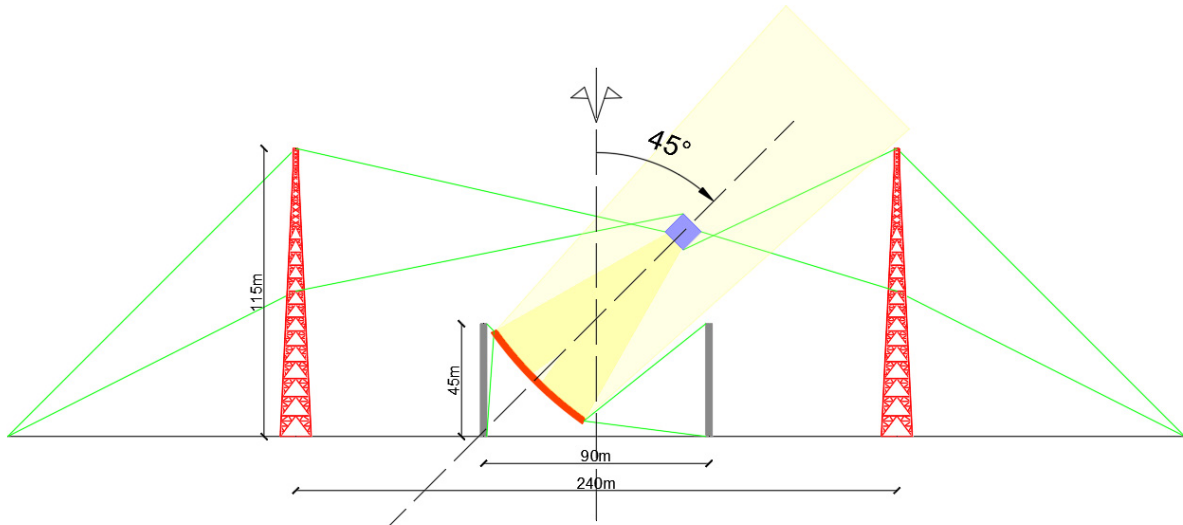


Figure 94 Final choice of the maximum zenith angle and basic dimensions.

As it can be seen from the drawings, the columns supporting the dish are made out of concrete. This choice has been made, due to the weight of the dish and the big amount of stiffness needed. From the preliminary analysis, the sensitivity of the simulation depends highly on the upper nodal displacements of the columns. The implementation of counter-cables can also be seen. As far as the Image Sensor Structure (Robocrane) is concerned, it will be presented in detail later in 8.2.1.

The spatial arrangement of the columns is circumferential. In total, eight columns with a total height of 45m were created. The circle, that these lie upon, has a radius of 45m, as it can be seen from the drawings too.

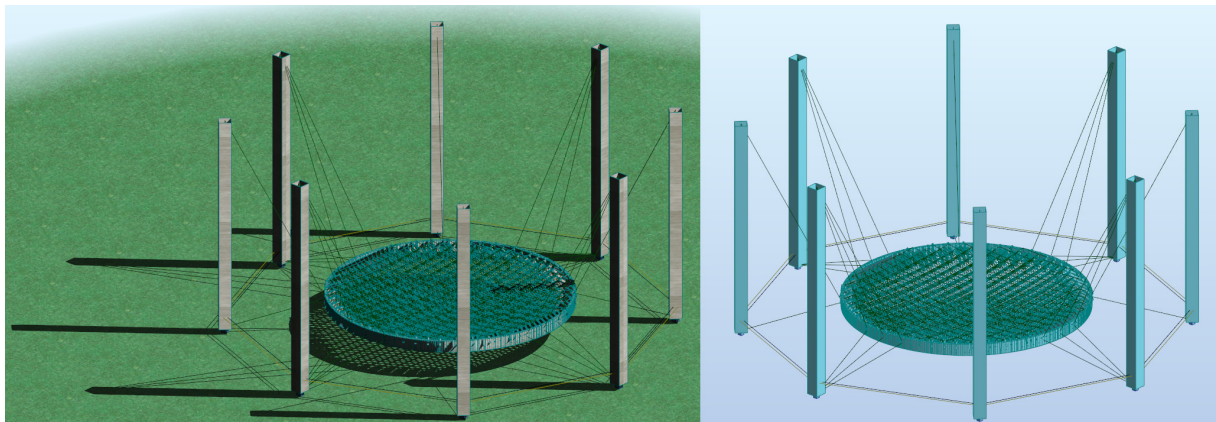


Figure 95 3D view of the final Main Dish Structure (3D visualization on the left and the analytical model in structural scale on the right)

After assigning the exact geometry, the simulation and design procedure follows. The different elements of the structure are grouped as follows.

- Concrete columns
- Tension ring
- Space frame of the dish
- Cables

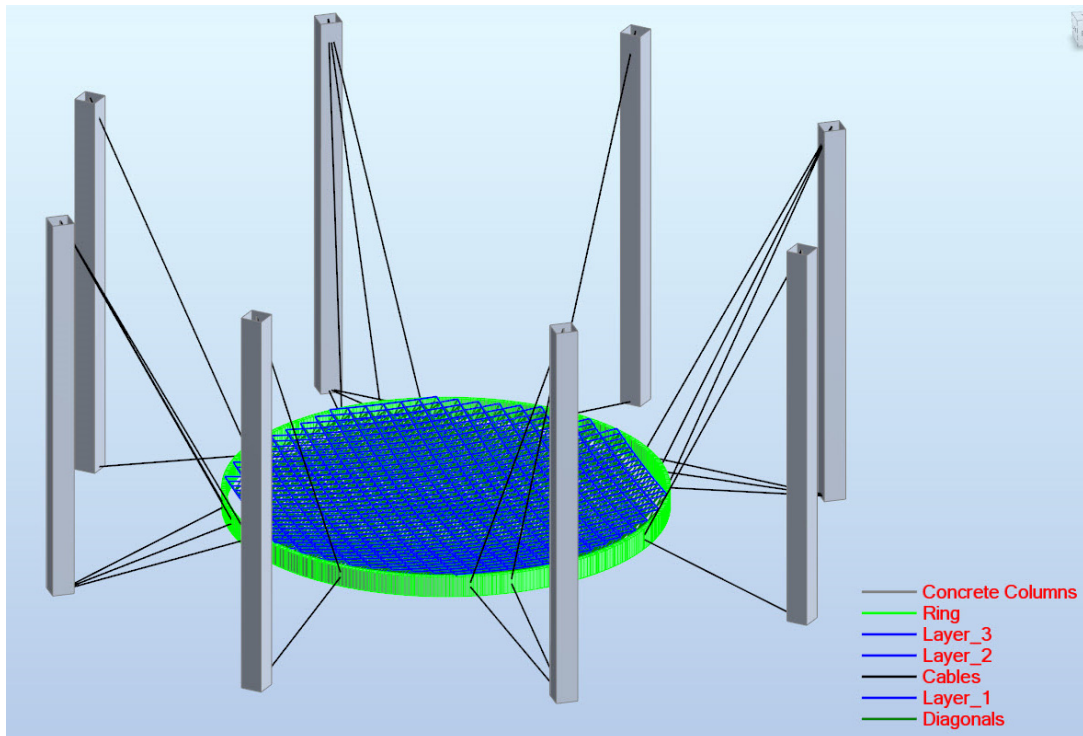


Figure 96 Main dish structure. Analytical model in structural scale and group assignment for design purposes.

A precise design has been done for the whole structure apart from the columns, due to the fact that an accurate design would need significant amount of time and in this stage it was not deemed necessary. However, some points for the design of columns are:

- Consideration of vertical pre-stressing.
- Possible backstay cables to stabilize the upper node.
- Examination of non-uniform Cross-Section along the height of the column. Influence of the stiffness reduction in the overall deformations.
- Fatigue and reduction of stiffness due to excessive cracking examination.
- Influence of second order effects. Exact analysis for the critical combination needed.
- Foundation constraints and soil-structure interaction. Possible connection of the columns' foundations.

The design of the tension ring has been done with the Von Mises yield criterion and is described in more detail in 9 along with the Cross-Arch Image Sensor Structure. (Design of Complex Cross-Sections). However, the main constraint of it is the height of the Cross-Section, in order to be able to facilitate the Space Frame of the dish.



Figure 97 Tension ring Cross-Section dimensions

The Space Frame was designed according to EN 1993-1-1:2005 and the it was separated, for sake of optimization, in two groups. The diagonal elements and the horizontal/layer elements.

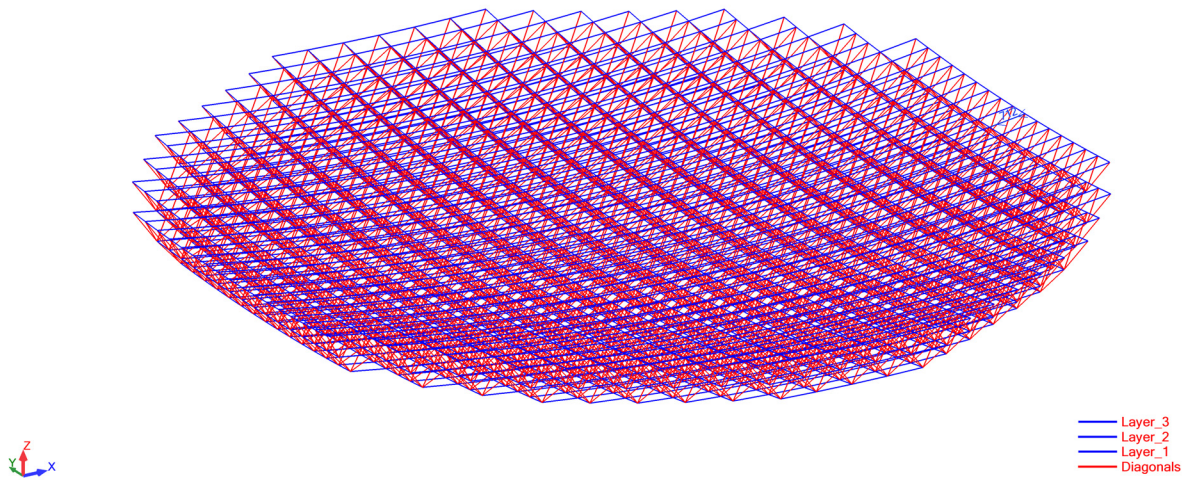


Figure 98 Groups of Space Frame dish structure for design purposes. (horizontal/layer elements with blue and diagonals with red)

The final Cross-Sections are:

- For the horizontal/layer elements CHS 48.3x2.5 S460
- For the diagonals CHS 42.4x2.6 S460

The cables were designed, bearing in mind the minimization of the elastic deformations, which means the minimization of strains according to: $\sigma = \varepsilon E \Rightarrow \frac{T}{A} = \varepsilon E \rightarrow \varepsilon_{\min} \Rightarrow A_{\max}$

The final Cross-Sections are for both the main and the counter-cables:

- 80 strands Y1860 with $150\text{mm}^2/\text{strand}$. $A_{\text{eff}}=12000\text{mm}^2/\text{cable}$

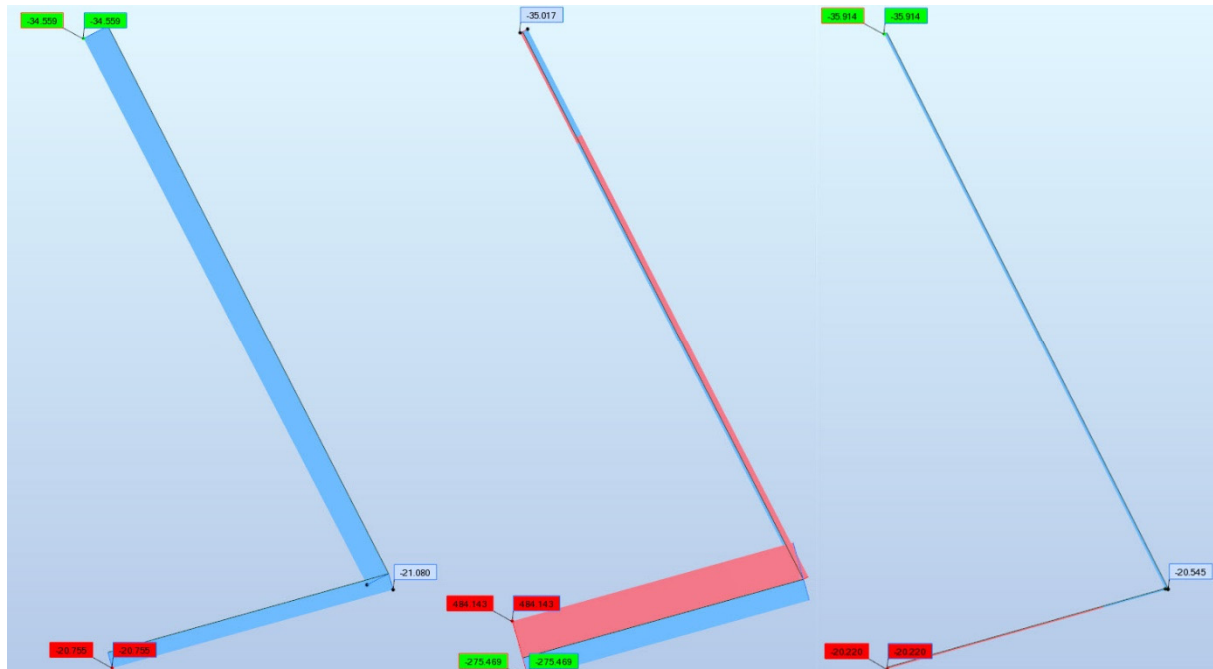


Figure 99 Cables' min/max stress in Dead Load case (left), worst seismic combination (middle) and Dead Load+Operational Wind of 15m/s case (right)

The most critical part of the Main Dish Structure, however, is the connection of the Space Frame and the cables with the Tension ring. Due to the significant size of the Tension ring, connecting the Space Frame elements' nodes and the cable end nodes with the axis/centre line of the Tension ring would produce inaccurate results mainly not on the safe side, which could lead to false Cross-Section design. An early simulation showed, for example, the major influence of the connection points to the torsional loading of the Tension ring.

In order to accurately simulate this demanding detail, without the use of more sophisticated FEM computer software, also dummy bars/rigid links were assigned to connect the Space Frame elements with the Tension ring. These elements had $EI = \infty, EA = \infty, GA = \infty$. Finally, these rigid links were offset to the connection point of the Tension ring. As a result, the deformations of the Space Frame nodes were assigned as equal with the deformations of the Tension ring nodes, without compromising the correct load transfer.

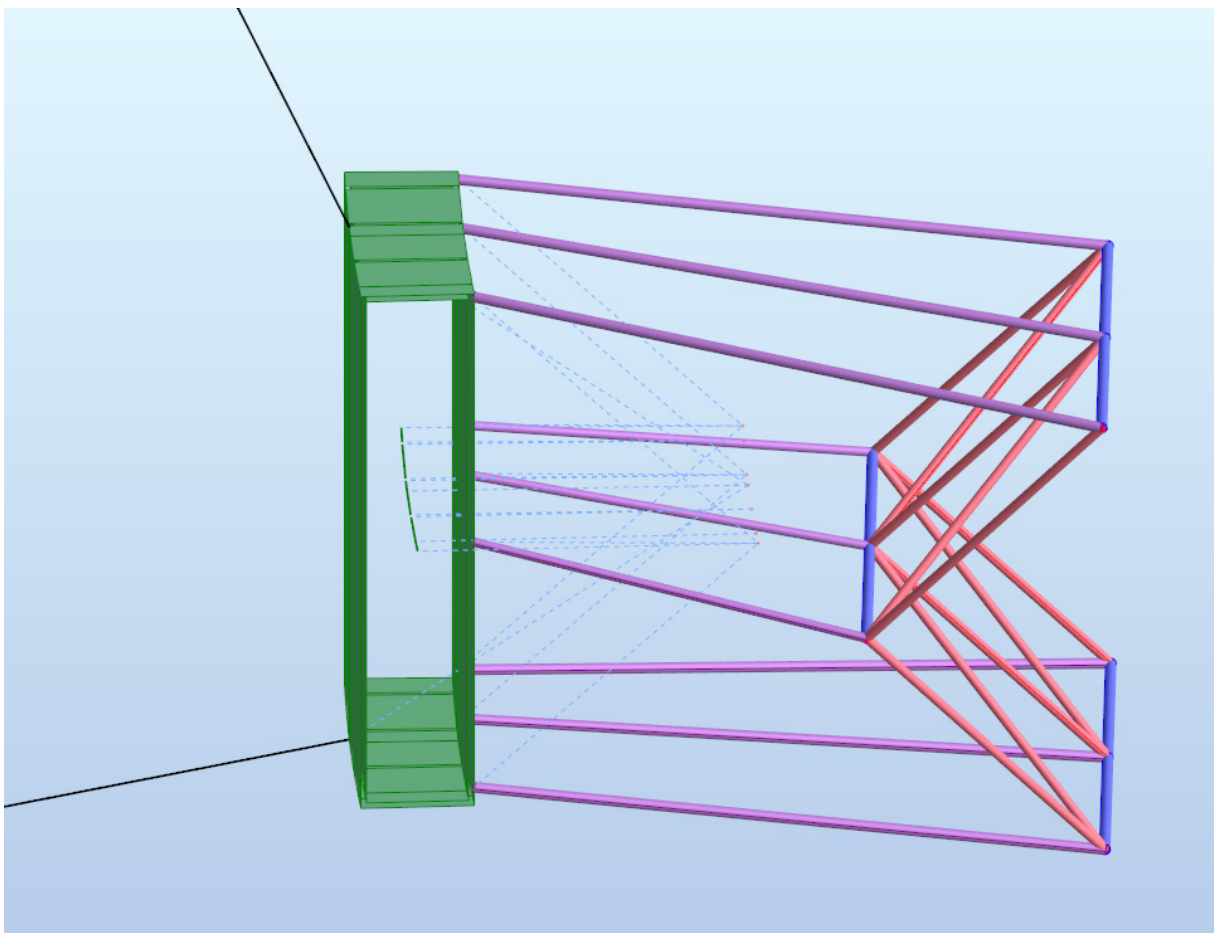


Figure 100 Detail of the Tension ring with the Space Frame and the Cables' connection. (Rigid links with purple, Tension ring with green, Cables with black and Space Frame elements with red and blue) The offsets are with a light blue dashed line evident.

In reality, special elements should be created to correctly connect the Space Frame with the Tension ring.

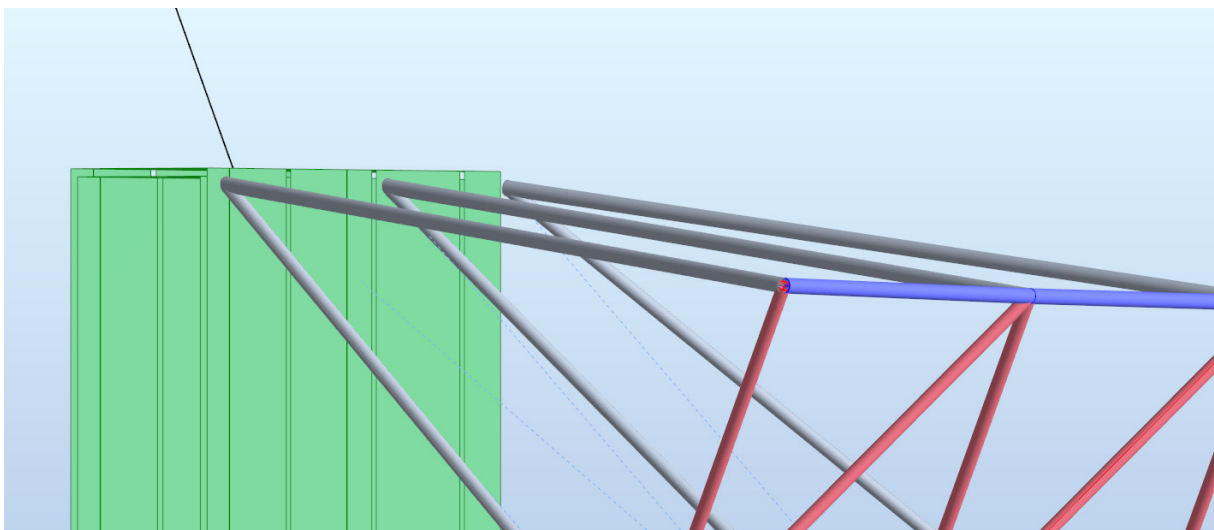


Figure 101 Proposal for the detail of the connection of the Space Frame with the Tension ring. (Special elements with grey)

8.2 The Image Sensor Structure-Robocrane

8.2.1 Robocrane general

The Robocrane Image Sensor Structure was not previously designed or simulated, because many other concepts were preliminarily examined in its place. However, this kind of structure proved to be promising for further development.

The nature of this filigree structure needs experience in many expertise, in order to be sufficiently designed. In this study the statics of this construction, as well as its basic dynamic behaviour in seismic and wind loading will be examined.

The principle is the suspension of the Image Sensor from cables over the dish. These cables should be able, not only to hold and support the Image Sensor, but also position it to the right place with the right angle to the dish. Taking into account the dimensions of the structure, this poses a real challenge, not only in terms of civil and mechanical engineering, but also in terms of robotics and control, as a live feedback loop should be implemented between the Main Dish Structure and the Robocarne Image Sensor Structure. By knowing the governing equations of motion, and their trajectories and the deformations in every position, predictive control could position both structures. The situation gets even more complicated, due to the necessity of cables' pre-stressing.

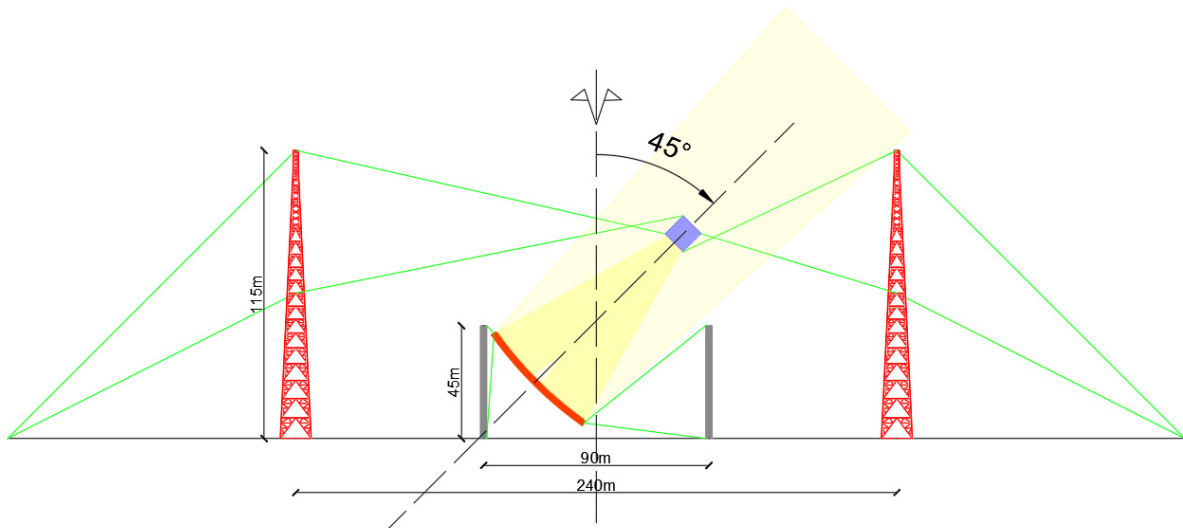


Figure 102 Basic dimensions of the Robocrane Image Sensor Structure.

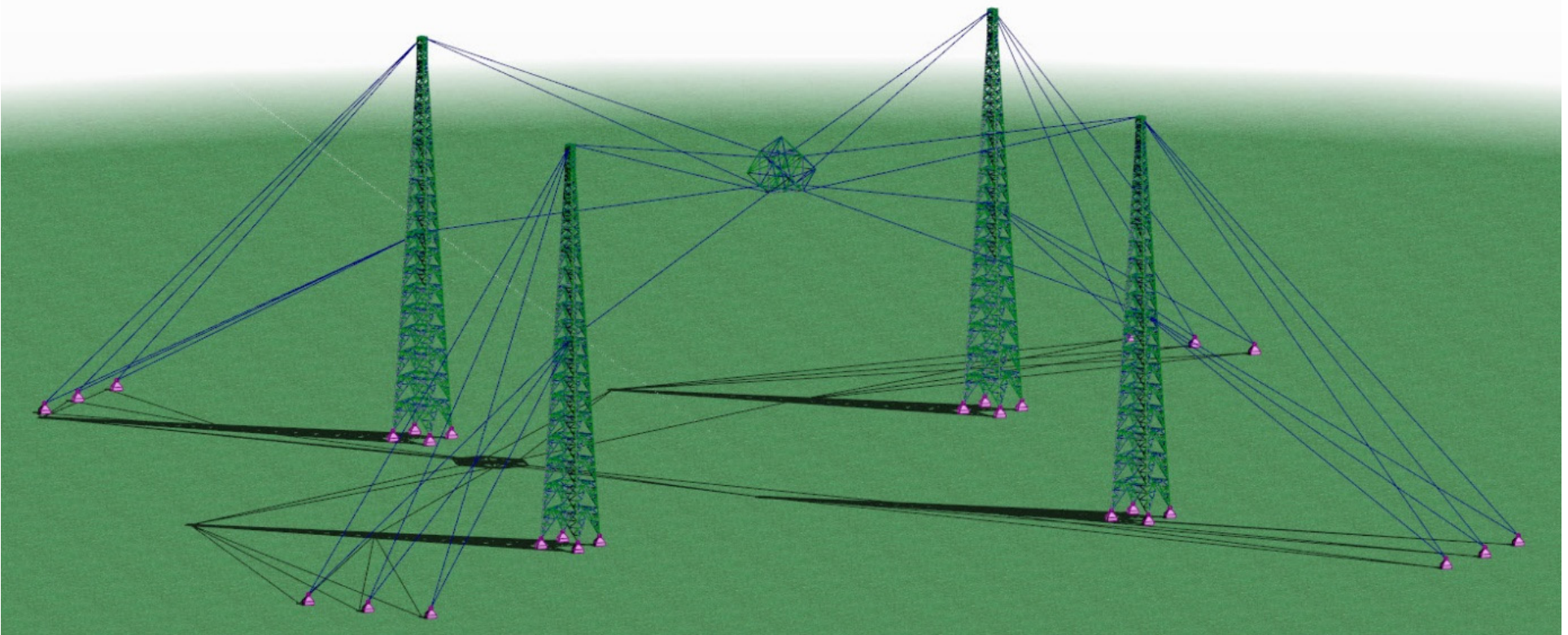


Figure 103 3D illustration of the Robocrane Image Sensor Structure.

As seen in the above drawings, the Robocrane Image Sensor Structure is composed of four vast Steel towers. From these towers, the Image Sensor is fixed in its position over the dish, with the help of eight main upper cables and four main lower cables. These cables are pre-stressed (post-tensioned after the Image Sensor load is applied). The support nodes of the main cables on the towers are also sustained with the help of backstay and auxiliary cables. (three in each node)

The housing of the Image Sensor is a rhomboid Space Truss and the weight of the Image Sensor was assigned with the help of rigid links in the centre of it.

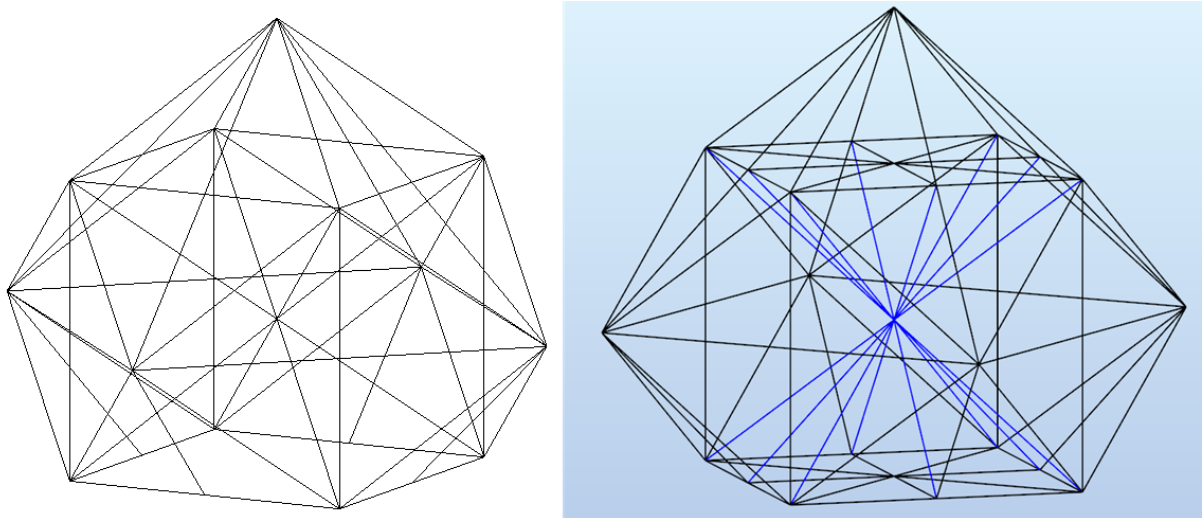


Figure 104 Robocrane housing structure.

In the first stage of the simulation, no pre-stressing was applied to the cables and no main lower cables were used. As a result, the Image Sensor was only suspended from the towers. It was evident, even intuitively, that the structure would be extremely unstable in lateral loads. Running a modal analysis proved this argument and this solution was abandoned. In the second stage the main lower cables were added but still with no pre-stressing. However, the structure remained highly unstable. The use of very large cables was necessary, and their weight started influencing the whole structure behaviour.

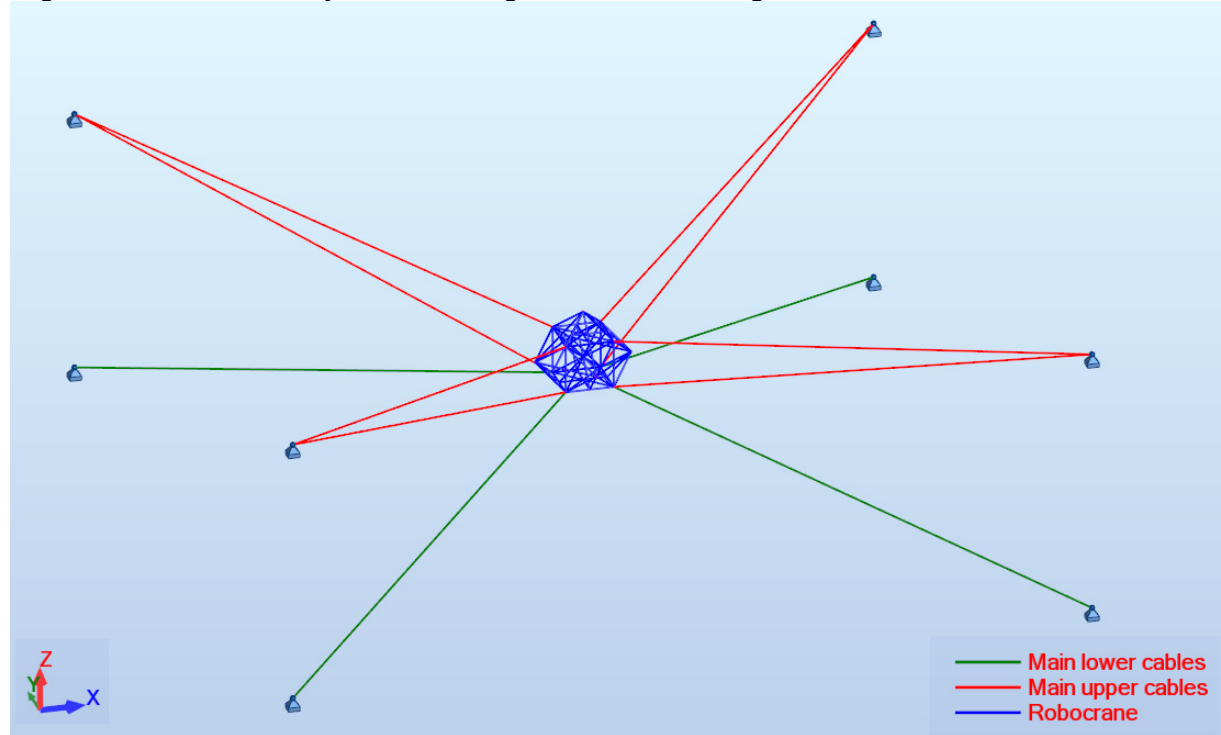


Figure 105 Robocrane Structure. Design groups for the pre-stressing assembly case.

In the third stage pre-stressing was added as follows.

- Phase 1: Dead load of the structure without the Image Sensor and no pre-stressing.
- Phase 2: Post-tension of the cables.
- Phase 3: Addition of the Image Sensor weight and final analysis.

The post-tension forces were added in order to position the Image Sensor in the necessary vertical position. (~0 Uz displacement)

After this stage, the towers were added and an iterative procedure was followed to recalculate the pre-stressing forces, as the nodes, that the cables were fixed, are now not completely stiff, due to the tower deformations. At this step, the design of the towers took also place. The final structure assembly and the design groups are seen in the following image.

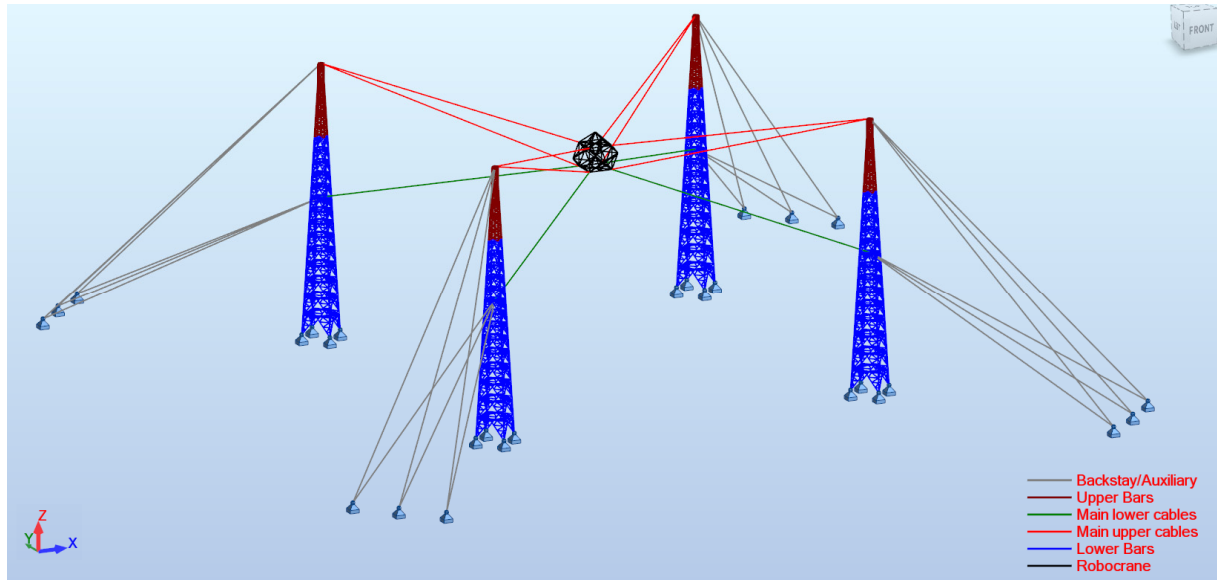


Figure 106 Design groups for the Image Sensor Robocrane Structure.

The final Cross-Sections are:

- Main Upper Cables: $A_p = 600\text{mm}^2$, $\sigma_{Post-Tension} = 0.7f_y = 1302\text{Mpa}$
- Main Lower Cables: $A_p = 1200\text{mm}^2$, $\sigma_{Post-Tension} = 0.5f_y = 930\text{Mpa}$
- Backstay/Auxiliary cables: $A_p = 6000\text{mm}^2$, $\sigma_{Post-Tension} = 0f_y$
- Upper tower bars: CHS219.1x6 S460
- Lower tower bars: CHS273x10 S460
- Robocrane bars: CHS219.1x6.3 S460

The final dimensions and elements of TheBigLebowSky design are shown in the sketch of the following page.

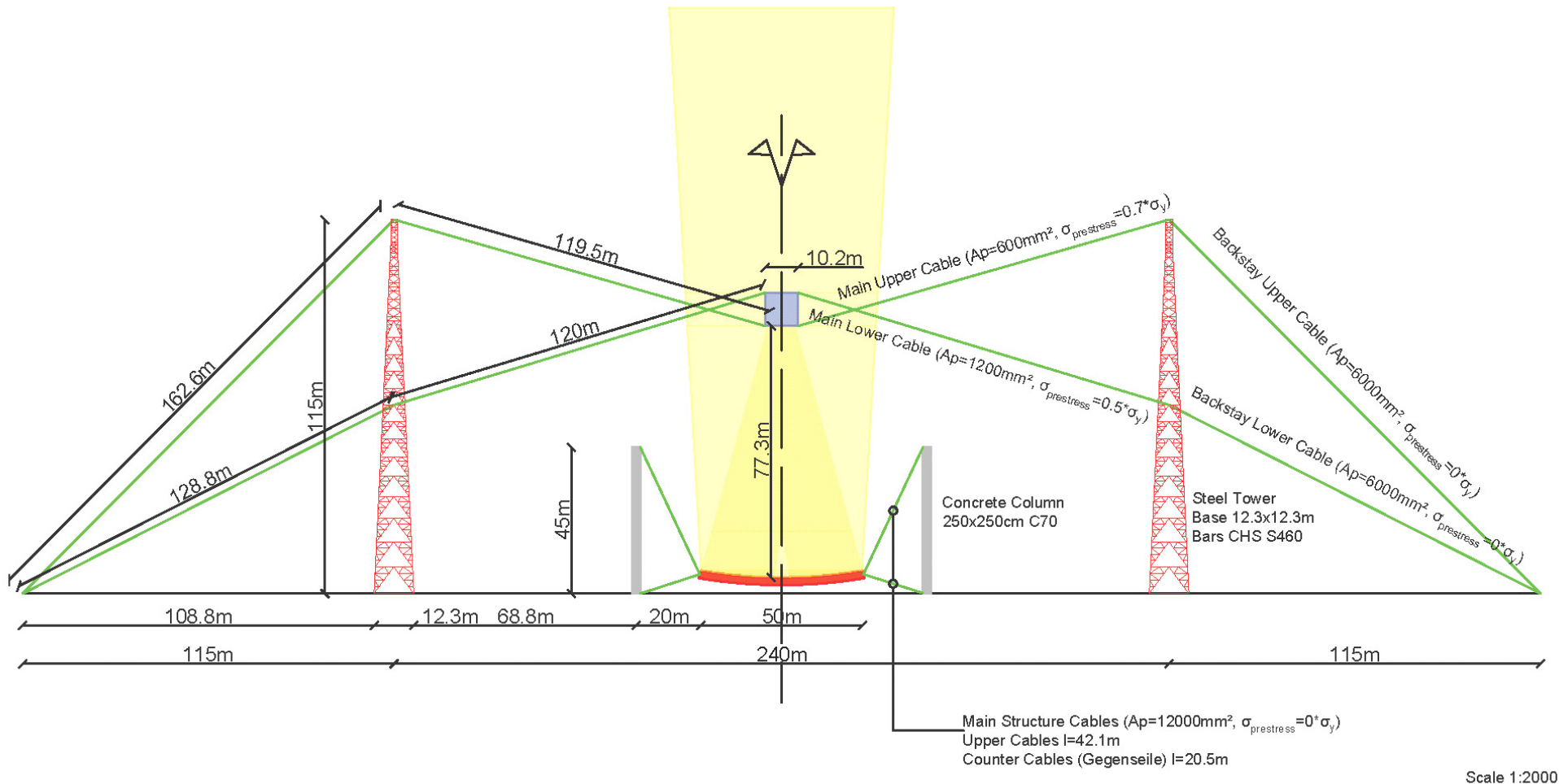


Figure 107 TheBigLebowSky design with the Robocrane Image Sensor Structure. Dimensions and miscellaneous assignments.

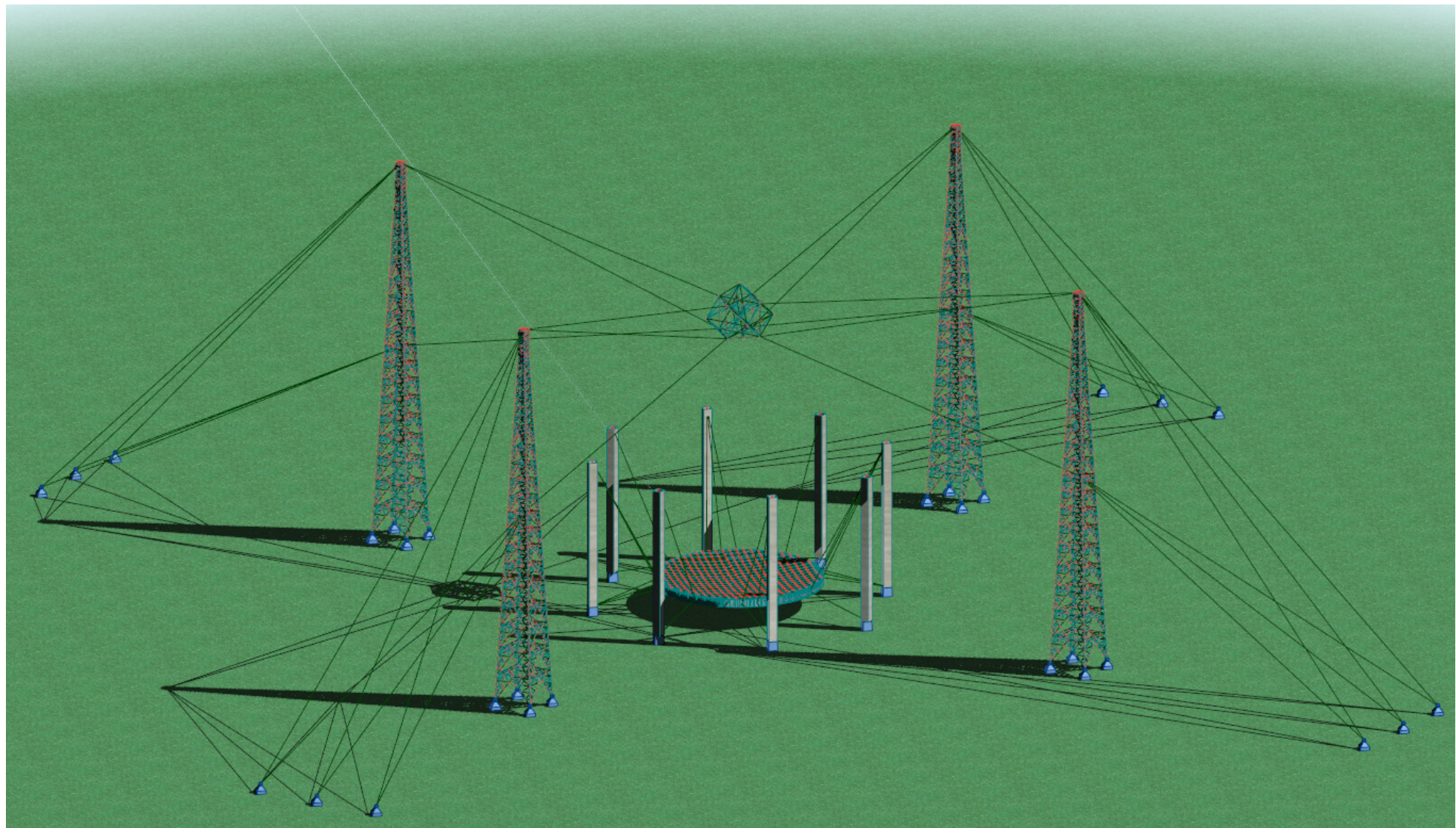


Figure 108 3D Visualisation of TheBigLebowSky design

8.2.2 Towers

The BigLebowSky telescope design includes the design of four steel towers from which the imaging sensor structure will be suspended with cables. The whole structure of the Robocrane, part of which are the street towers, is explained in further detail in 8.2.1. Here, only the design of the steel towers is going to be elaborated.

For the design of the towers once more the AutoCAD software was used for the easier and quicker design of the structure and then taking advantage of the link between AutoCAD and Robot Structural Analysis, the simulation of the towers has taken place. The tower structures were imported to Robot Structural Analysis as well as the imaging sensor structure and the Robocrane structure as a whole was assembled adding cables, assigning materials, cross sections, etc.

As one of the critical goals of this Project was to be cost efficient, the design of the towers was made by taking into consideration once again the fractal design and the design of a typical steel antenna tower. The fractal design with a repeatable module would decrease significantly the construction cost as well as the transport cost. The modules could be prefabricated and assembled in the factory and be transported into tower pieces to the construction site, which also reduces the construction time. Steel antennas already use this idea and the heights of the existing antenna towers prove that the required height of 115m is feasible.

Figure 111 shows the structure of the steel tower. The steel tower is composed of three parts. The first part from the bottom till the level of 83.94m is composed with the module represented in Figure 109. The module is constantly reducing in size with a constant gradient of approximately 3° . This gradient remains constant up to the level of 107.23m, although from 83.94m to 107.23m the structural module changes as seen in Figure 110. The last 7.77m are designed without gradient. The dimensions on the base are $12.33m \times 12.33m$ while on top are $2.07m \times 2.07m$.

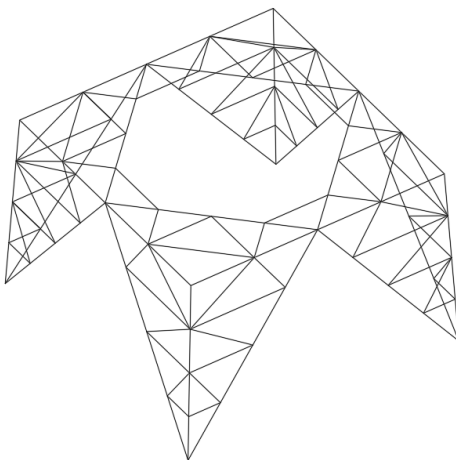


Figure 109 Base module of the steel tower.

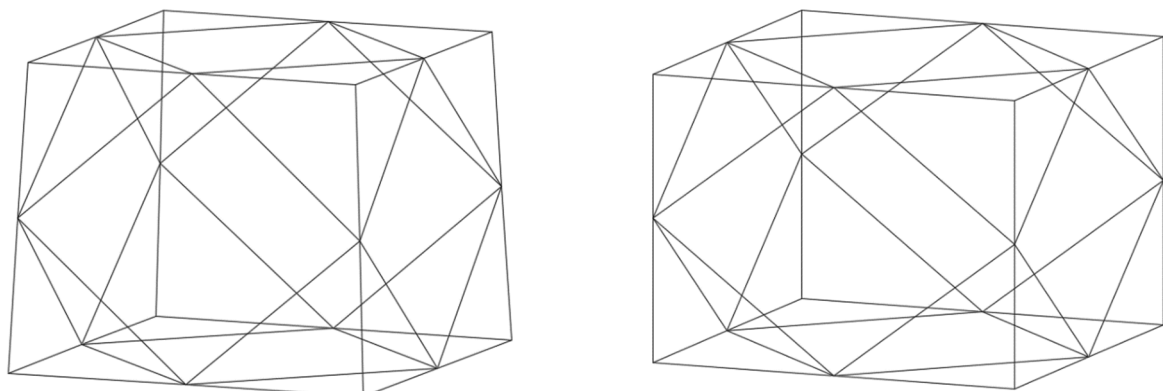


Figure 110 Modules used in the upper parts of the steel tower.

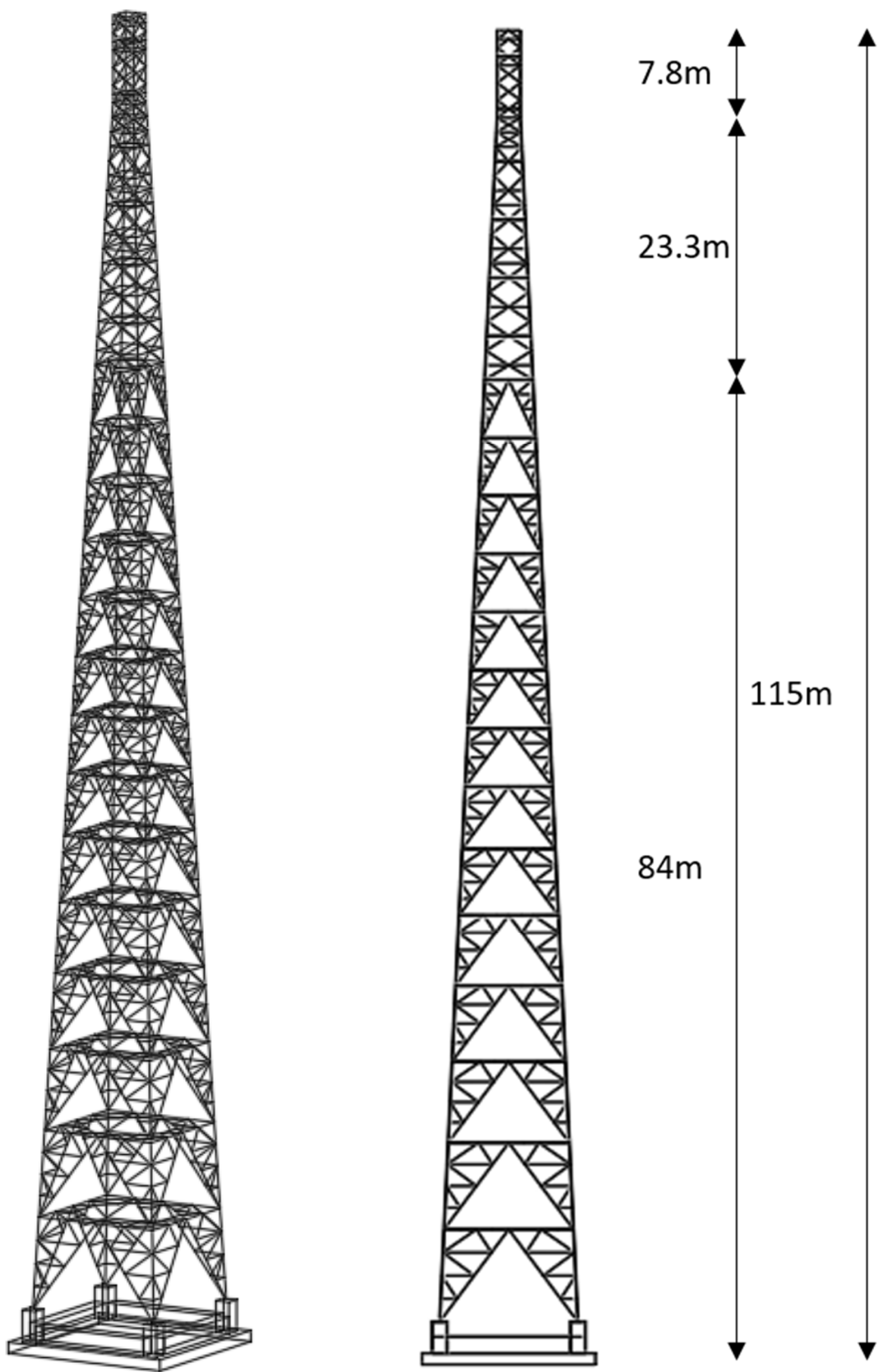


Figure 111 Steel tower 3D view (left) and in front view. (right)

8.3 The alternative Image Sensor Structure-Cross-Arch

While trying to solve the stiffness/softness issue of the Robocrane cable structure of TheBigLebowSky design, the idea of using arches instead of a cable construction emerged. This solution could be easier designed and optimized, in order to support the concentrated Image Sensor load. However, shadowing effect on the dish would appear again, although in small scale if the thickness of the arch is minimized.

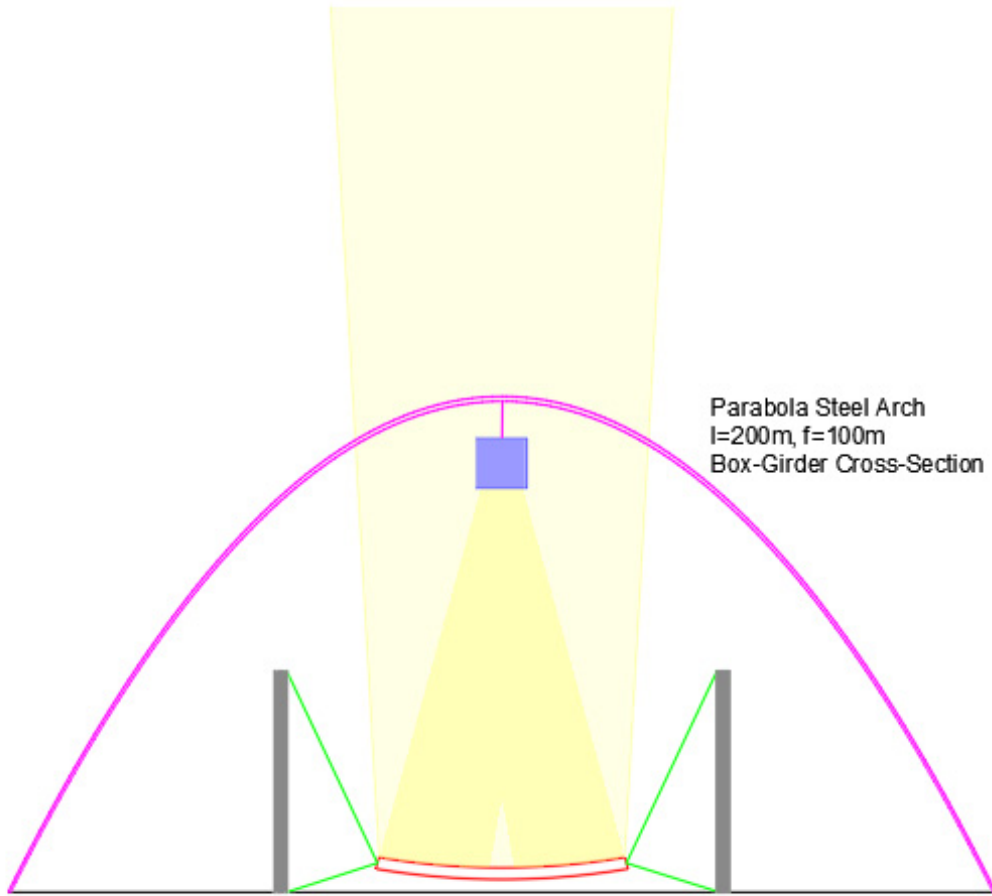


Figure 112 Arched Image Sensor Structure.

Bearing in mind the necessary size of this construction, a preliminary research was made in existing structures to investigate the possibility of being efficient in our case.

Probably, the most notable arch construction standing in free air is the Gateway arch or St. Louis arch in the state of Missouri in the U.S.A. It is the world's tallest arch with a geometry of an inverted weighted catenary and is composed of a steel box-girder Cross-Section. The term weighted-catenary refers to the non-uniform self-weight distribution along the arch length. In other words, this means that the Cross-Section is not continuous along the length of the arch. (more about arches' geometry will be described further later in this chapter) This is done to utmost optimize the constructions' inner forces. Taking into account its 192m height and the cost of 192000000 Dollars in 2015 value, it could easily be considered as a proposal.

At this point it is deemed necessary to present a short summary about the geometry and static behaviour of arch constructions.

The investigation starts from cable statics. The catenary curve describes a uniform chain (meaning continuous Cross-Section) hanging from two points in a gravitational field.[19] The inner forces are exclusively tension forces acting along the cables' axis. The essential thing, here, is the negligible transverse stiffness. By inverting this chain we create an arch, and if the loads remain the same, only compression forces act along the arches' axis. Also here, the transversal stiffness is considered negligible. If the sag of the cable is small the catenary curve approximates a parabola. That means, and can be mathematically proven, that if the load was acting in the global vertical direction the equation that produces no moments on the arch, or the optimal arch geometry, is a parabola. This is in many cases the solution of an arch bridge, as the load of the roadway is acting vertically on the arch. Below, the equations in Cartesian coordinates for both cases are presented.

- Catenary curve: $y = a \cosh\left(\frac{x}{a}\right) = \frac{a\left(e^{\frac{x}{a}} + e^{-\frac{x}{a}}\right)}{2}$
- Parabola curve: $y = \frac{w}{2T_o}x^2 + \beta$ with T_o = Cables' horizontal component of compression.

The parameters α and β are defined taking into account the boundary conditions. (support coordinates)

At this point it is important to be mentioned, that there are also mixed forms of the aforementioned curves to exploit every loading aspect and structural characteristic. For example, an arch is almost never possible to be designed to withstand its own weight or even a certain static load. (e.g. moving loads on bridges) The mixed equation of St. Louis arch, that was described before, is, for example:

$$y = a \cosh\left(\frac{x}{b}\right) + c, \text{ which is called a weighted or a flattened catenary.}[20]$$

Concluding, the two crucial and interrelated aspects of an arch are its loading and geometry. Only by optimizing both of them, we can achieve an efficient result.

Examining the Image Sensor Structure case, the load that is present, apart from the self-weight, is the concentrated Image Sensor load on the top of the arch. Before defining the exact geometry, the solution of a cross arch was implemented to significantly reduce the Cross-Sections (and as a result the shadowing effect) and to offer lateral stability to dynamic loads (wind and earthquake).

Due to the significant amount of time needed to define the exact arch geometry, only the catenary and parabola cases are examined. Their exact equations are:

- Catenary curve: $y = 61.64 \cosh\left(\frac{x}{61.64}\right)$ with a vertical distance $l=200m$ and a total arch length $s=300m$
- Parabola: $y = 0.01x^2 - 2x$ with a total vertical distance $l=200m$ and a maximum sag $f=100m$

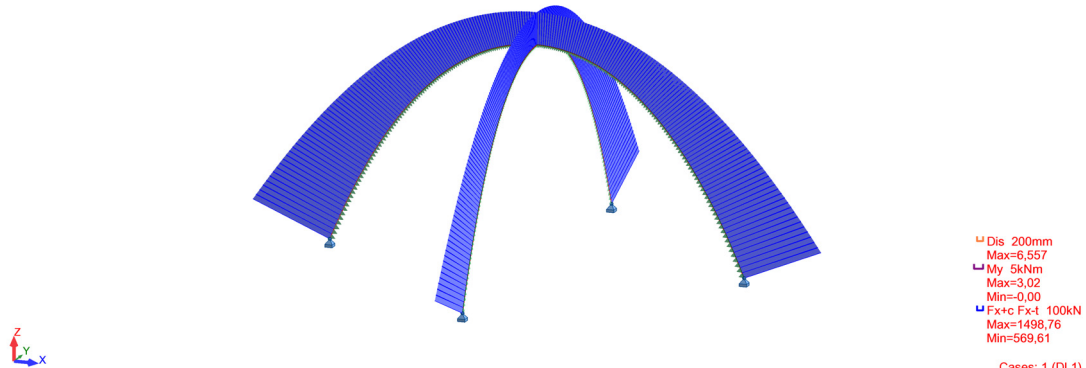


Figure 113 Catenary Bending Moments, Axial forces and displacements to its Dead Load (max $Uz=-5.6mm$, $My_{max}=3.02kNm$, $Cmax=1498.8kN$)-Proof of the correct function of the catenary curve.

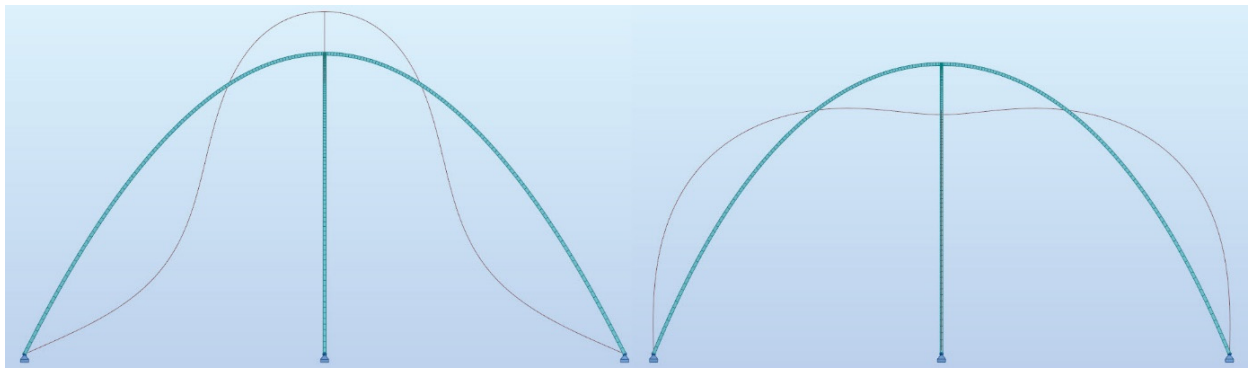


Figure 114 Deformation shape in Side view of the two arch solutions. Catenary on the right ($U_z, \text{max} = -218.5\text{mm}$) and Parabola on the left ($U_z = -337.4\text{mm}$) Notable is that for the Catenary U_z, max occurs on the top node. (Image Sensor) The displacement of the same node (Image Sensor) for the Parabola is $U_z = +181.8\text{mm}$.

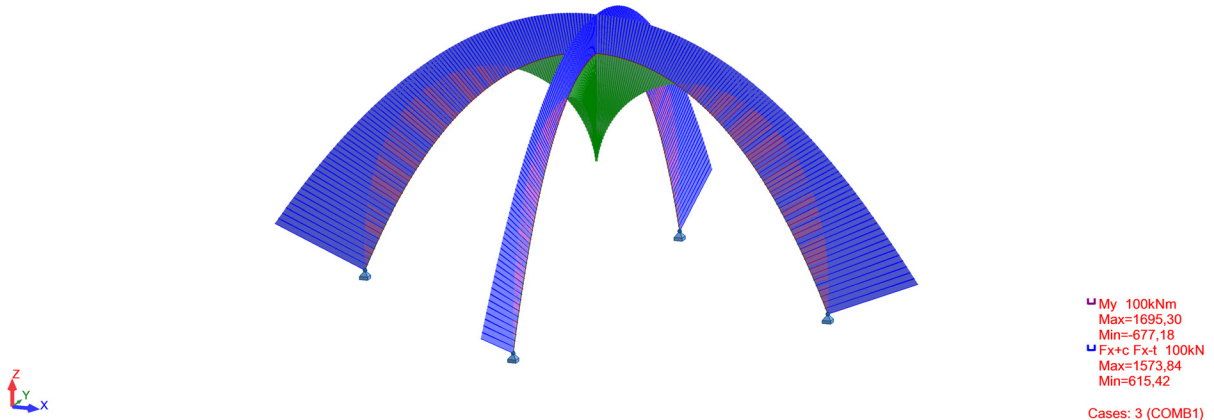


Figure 115 Axial forces and Moment diagrams of the catenary hyperbolic curve with Dead load and Image Sensor concentrated load. (Compression with blue)

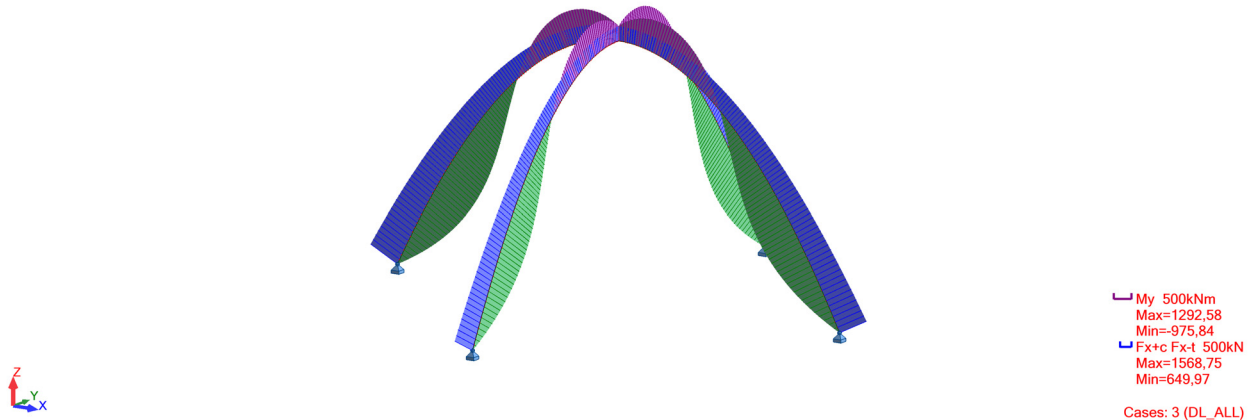


Figure 116 Axial forces and Moment diagrams of the parabolic curve with Dead load and Image Sensor concentrated load. (Compression with blue)

As it can be seen, the Parabola produces less bending moments and identical compression forces. Moreover, the displacements on the important top node are significantly lower and also in the favourable direction. As a result, its shape is more cost efficient and it is chosen as the preferred geometry for these load cases.

For the design of the Cross-Section, refer to the respective Chapter of the Analysis of Complex Cross-Sections, 9.1.

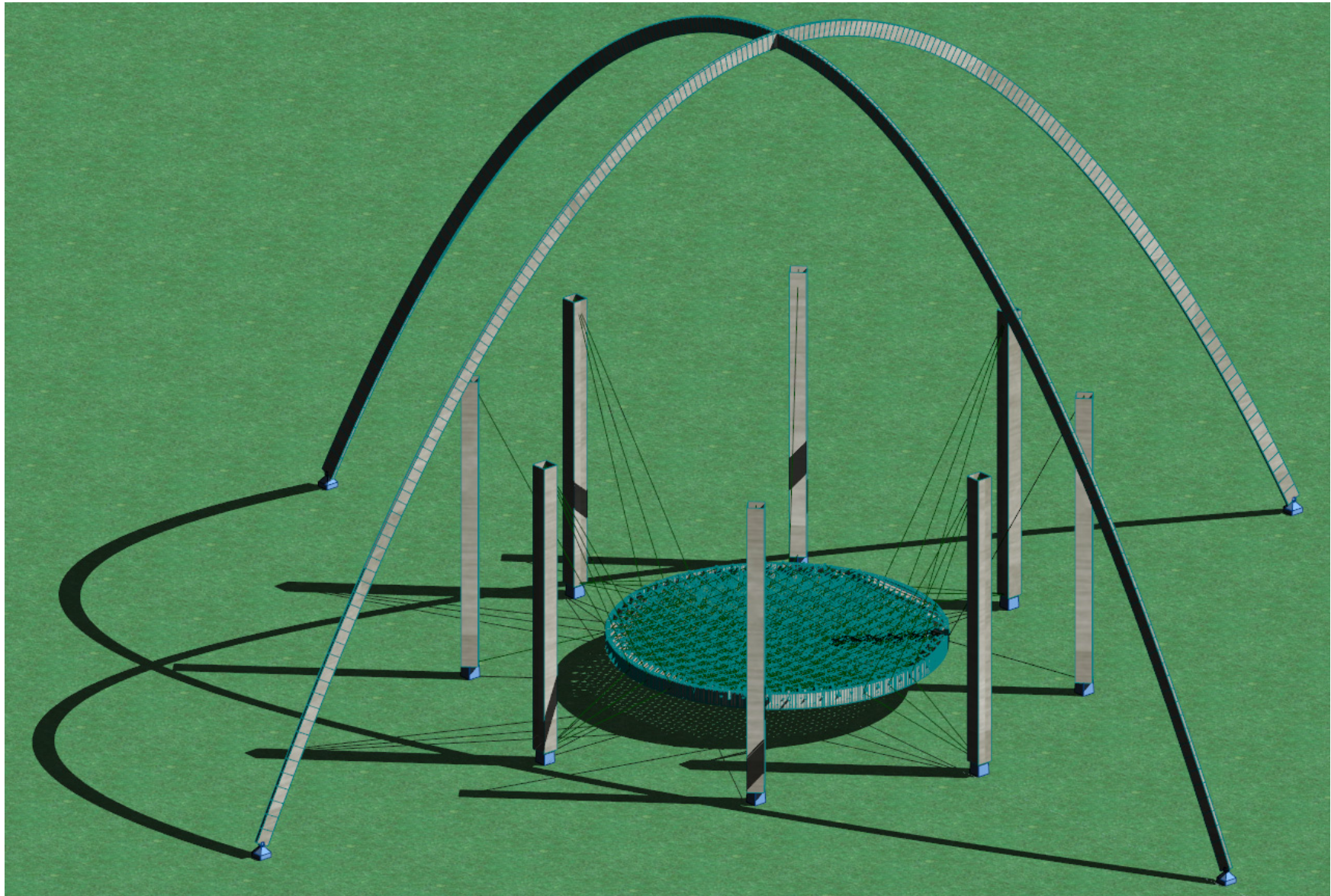


Figure 117 3D visualisation of TheBigLebowSky concept with the Cross-Arch Image Sensor Structure (sun sets/rises)

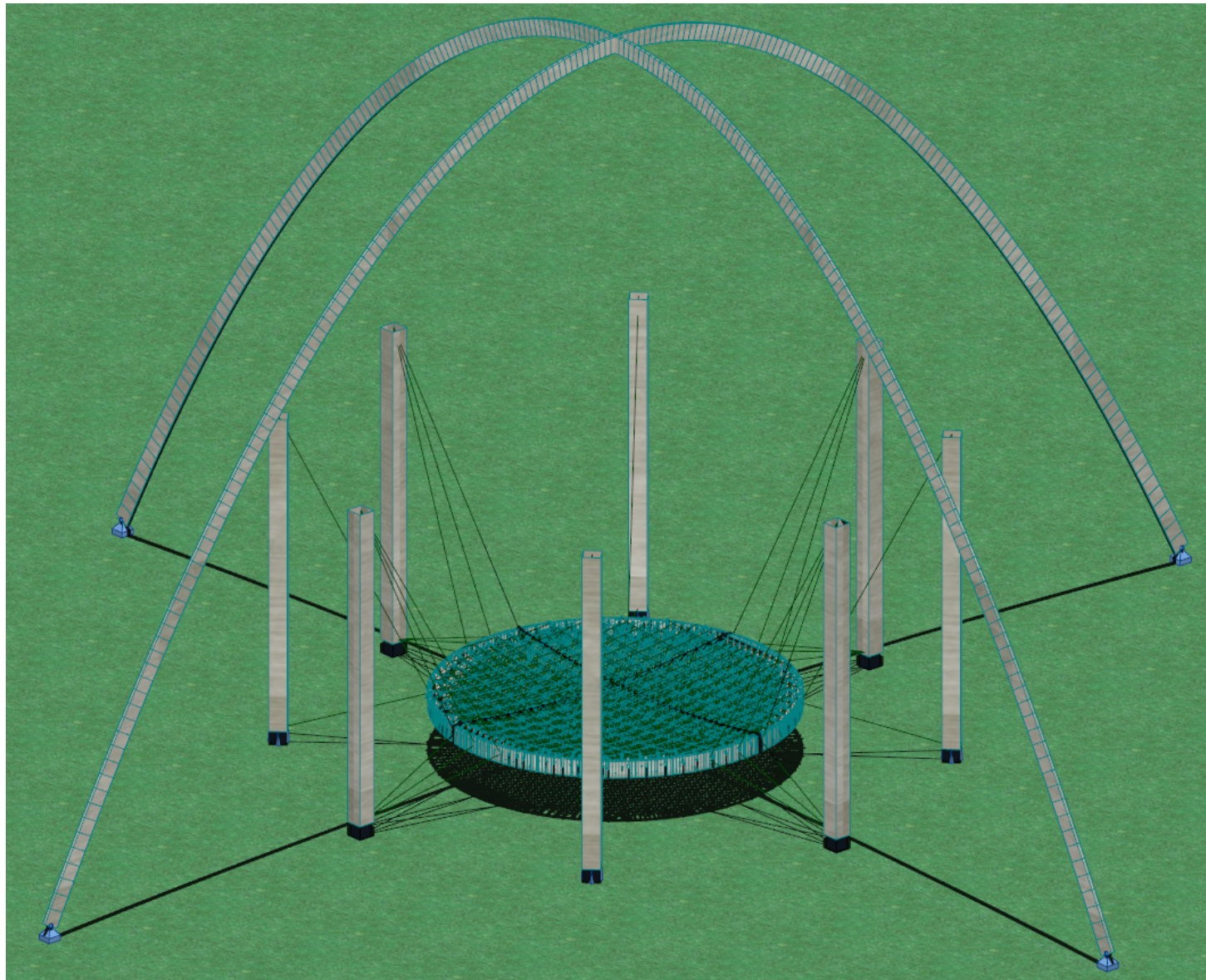


Figure 118 3D visualisation of TheBigLebowSky concept with the Cross-Arch Image Sensor Structure (sun in zenith position)

9 Complex Sections Design

For the Cross-Arch structure and the Tension ring, large sized box girder cross sections were used. Due to the complexity of these Cross-Sections and the possibility of a detailed stress Cross-Section analysis in RSAP 2017, these Cross-Sections were designed according to EN 1993-1-7 (2007) (5.2.3.3). However, it is considered important, that no initial imperfections to these members were considered. Even though this is not conservative, for both structures, other reasons were critical for the Cross-Section decision and as a result the equivalent von Mises stresses never approached the total yield stress.

The procedure followed for both structures was the following.

- Find the critical load combination for the structure.
- Simplified global stress analysis of the structure for this load combination.
- Isolation of the critical element.
- Detailed stress analysis in element level and definition of the critical Cross-Section.
- Detailed stress analysis in Cross-Section level.
- Definition of the point of maximum/minimum stress in Cross-Section.
- Check for yield criterion excess.

9.1 Cross-Arch Structure

The Cross-Arch Structure was designed, so as the deformations of the upper node (Image Sensor node) remain in acceptable limits. The criterion, as a result, was the restriction of the deformations in the operational load combination of Wind and Dead load. However, the procedure of Ultimate Limit State examination is presented here.

1. Critical load combination: Destructive Wind (55m/s) in Direction X

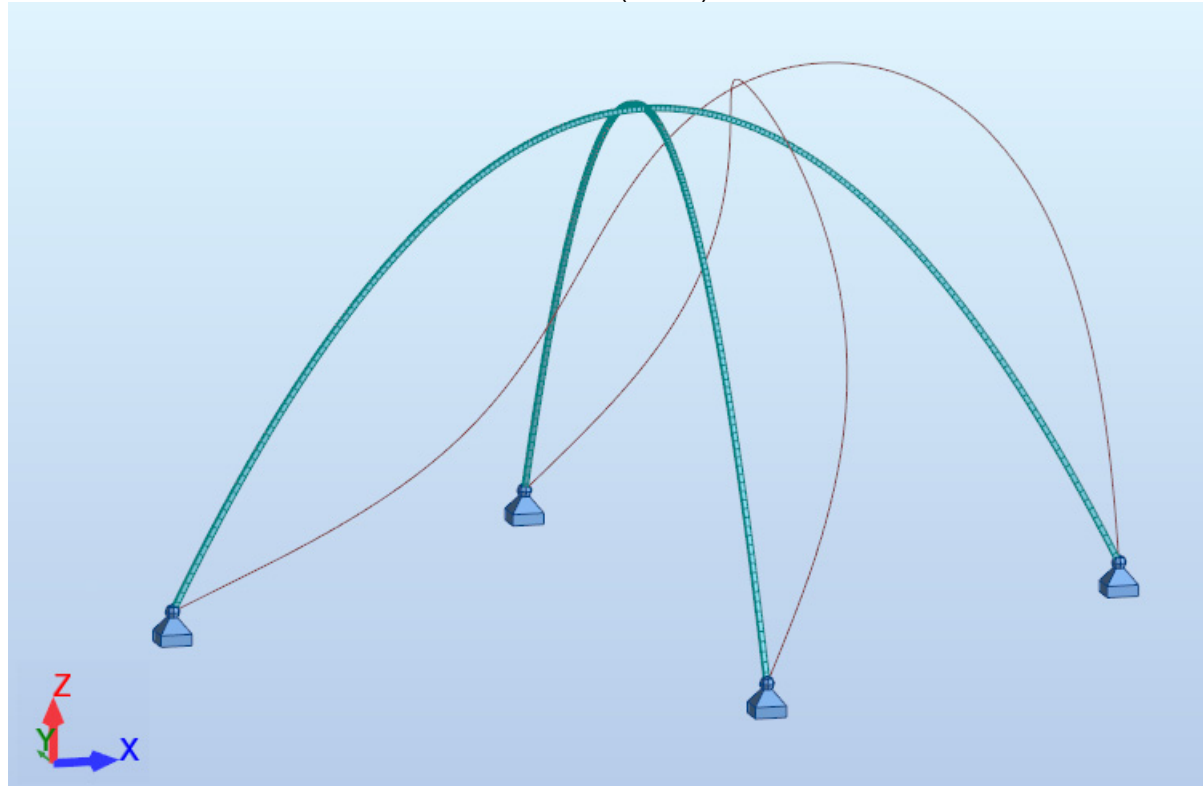


Figure 119 Deformation shape of the Cross-Arch Structure for the critical load combination of destructive wind in X direction.

2. Global stress analysis.

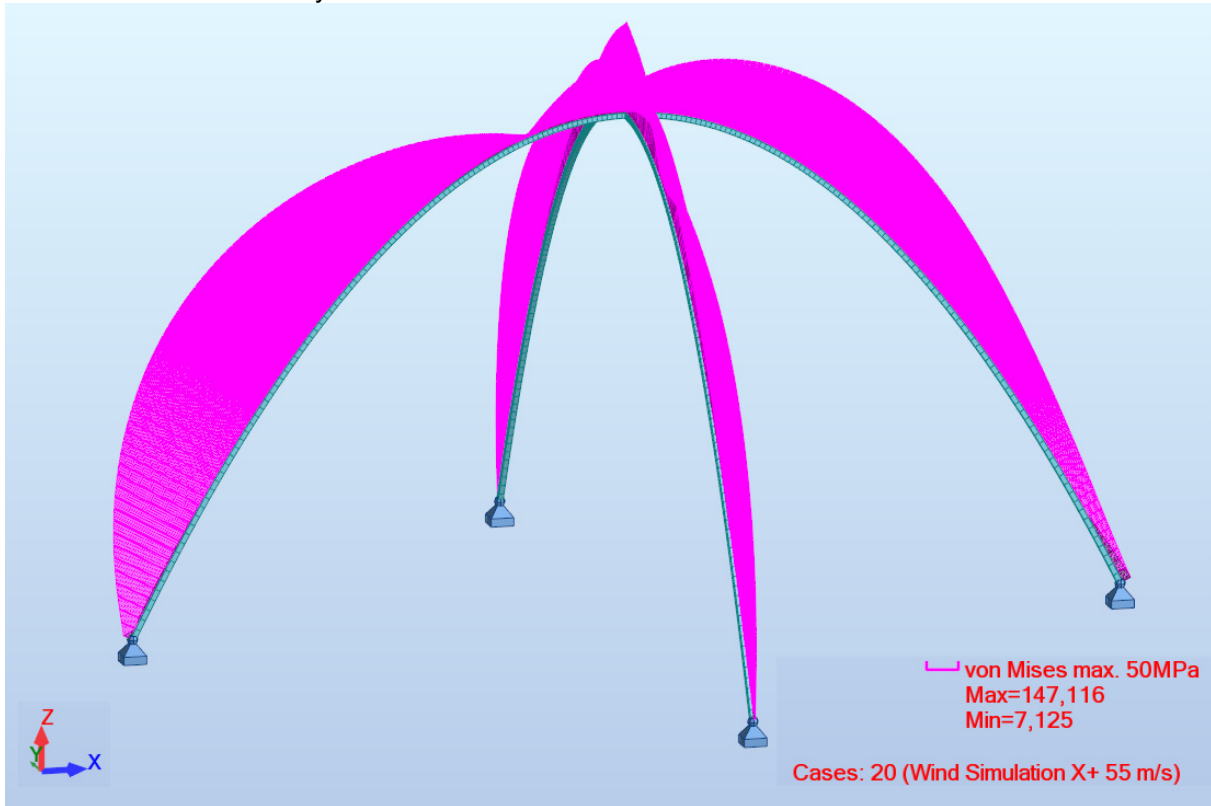


Figure 120 Global stress analysis for the Cross-Arch Structure.

3. Critical element definition.

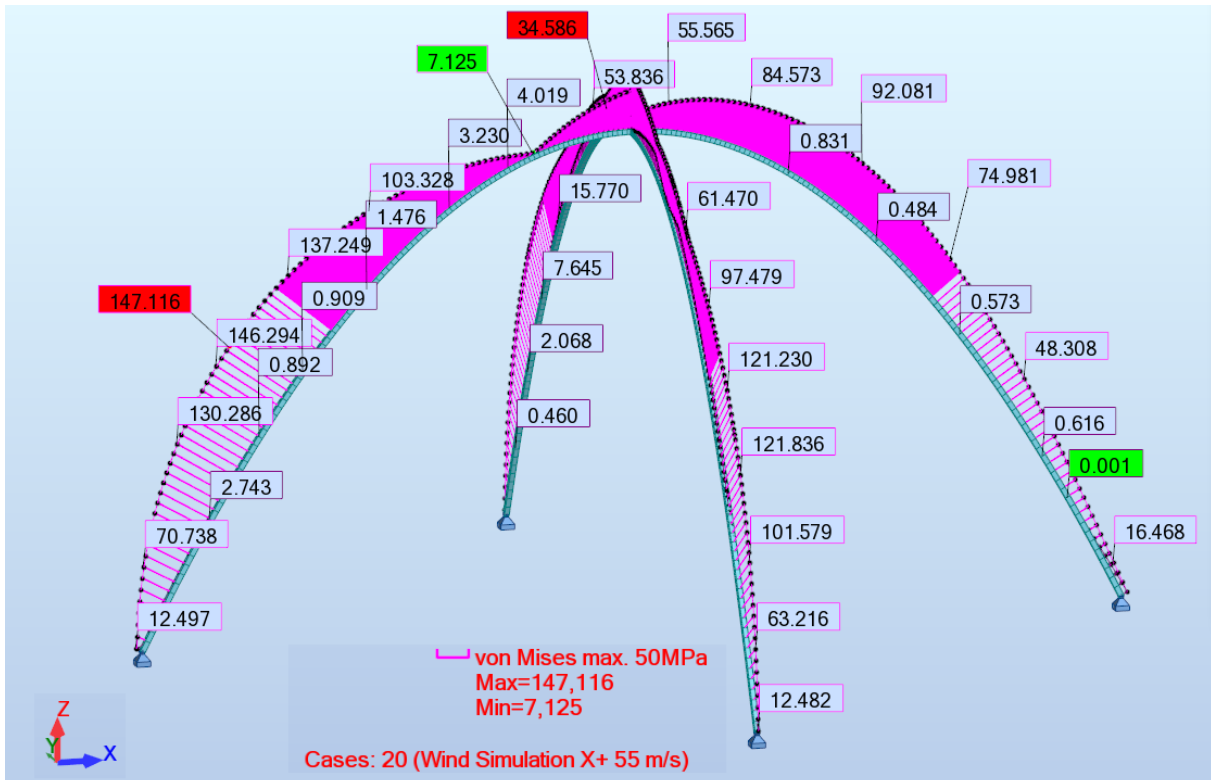


Figure 121 Global stress analysis of the Cross-Arch Structure. (element definition)

4. Stress analysis of element 433 (element with $\sigma_{VonMises,max} = 147.116 \text{ MPa}$) and definition of the critical Cross-Section

5. Detailed stress analysis in the critical Cross-Section

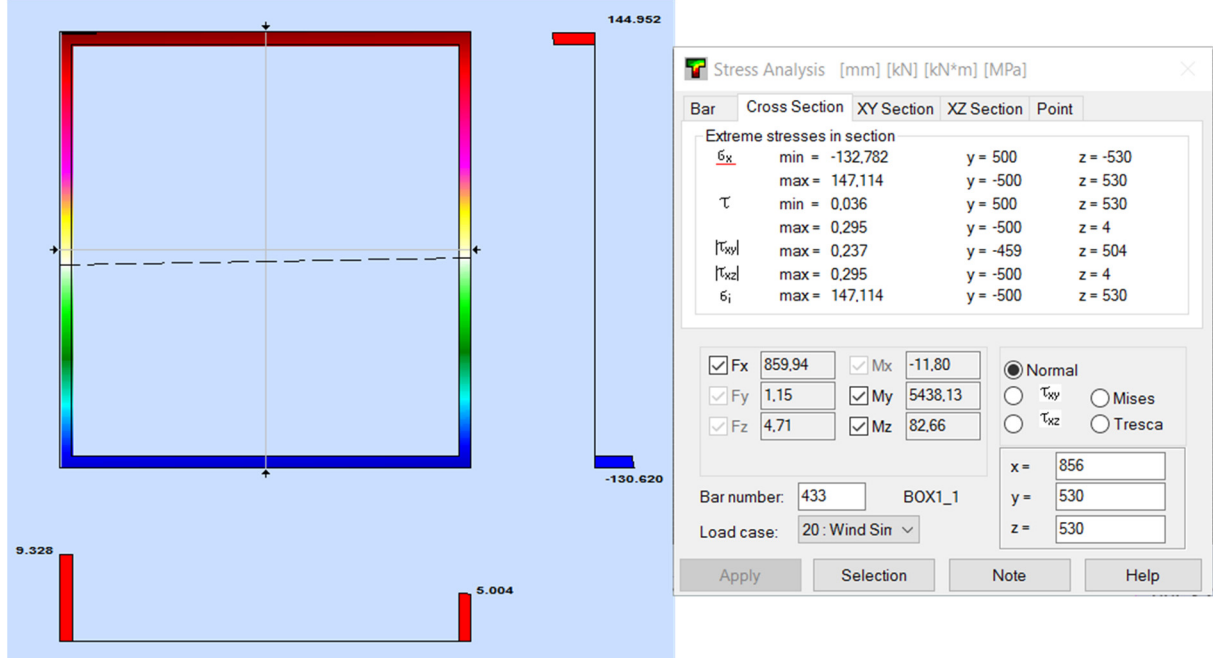


Figure 122 Detailed stress analysis for the critical Cross-Section of the Cross-Arch Structure.

6. Maximum Cross-Section stresses in point x=856mm, y=530mm and z=530mm (upper left corner)
7. $\sigma_{VonMises,max} \prec f_{y,d}$

9.2 Tension ring

As mentioned before, the Ultimate Limit State was not the basic criterion for the analysis of these structures. The Tension ring, has the major restriction that it should shelter the Space Frame, meaning that its height cannot be lower than the maximum distance of the upper and lower nodes of the dish Space Frame. This height is 2.4m and is chosen as the height of the Tension ring. Other solutions can also be examined in future research, such as Truss Tension ring or direct suspension of the Space Frame from the circumferential columns. The procedure of Ultimate Limit State examination is presented here, for completion reasons, as above.

1. Critical load combination: Seismic load combinations ($0.3*X-1*Y-0.3*Z$)

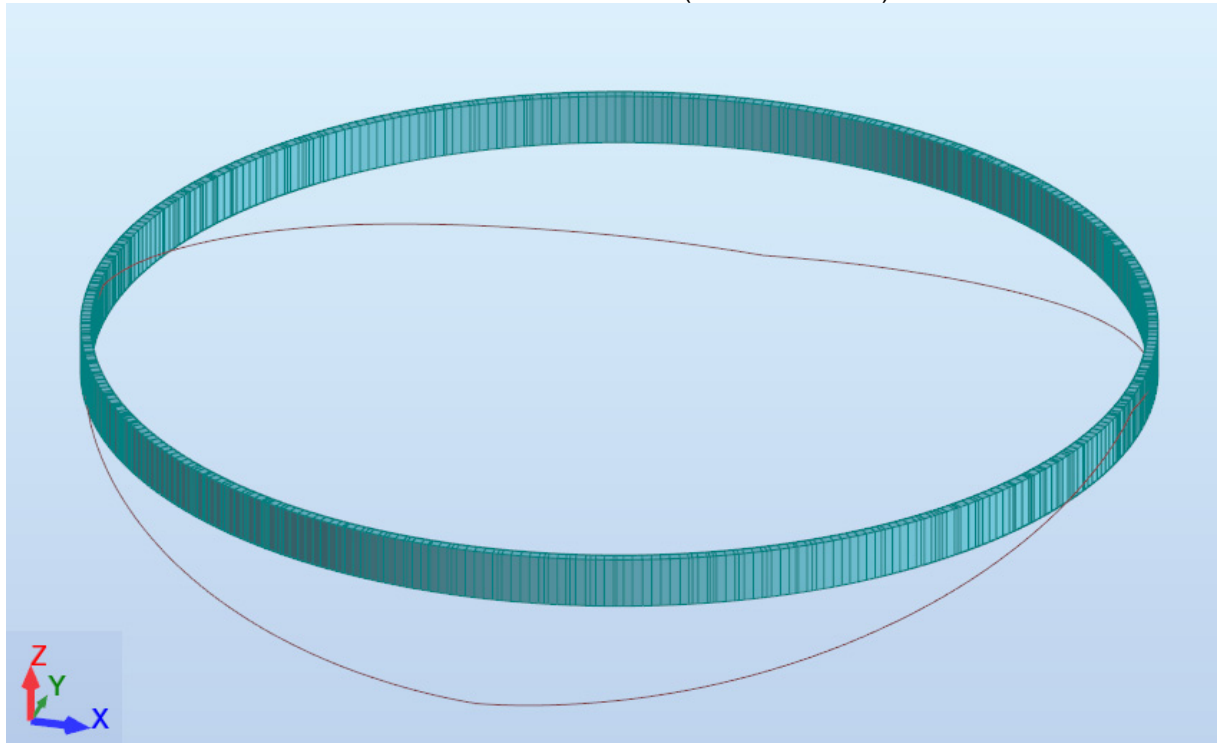


Figure 123 Deformation shape of the Tension ring for the critical seismic load combination.

2. Global stress analysis.

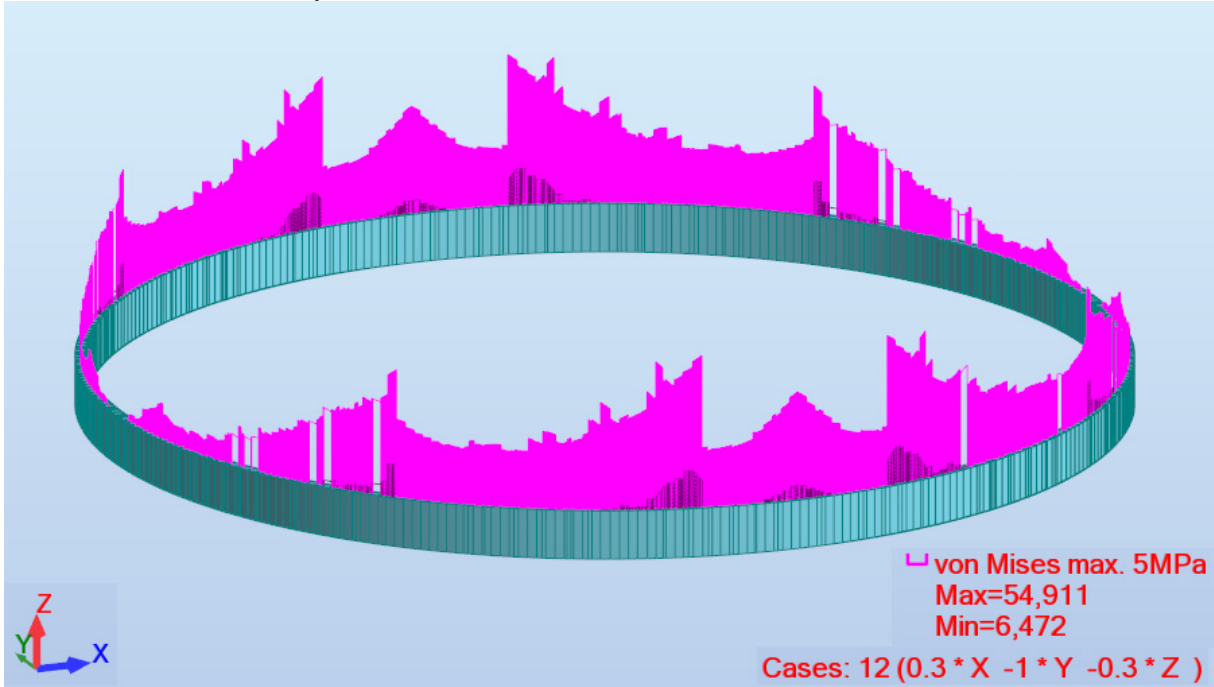


Figure 124 Global stress analysis for the Tension ring Structure.

3. Critical element definition.

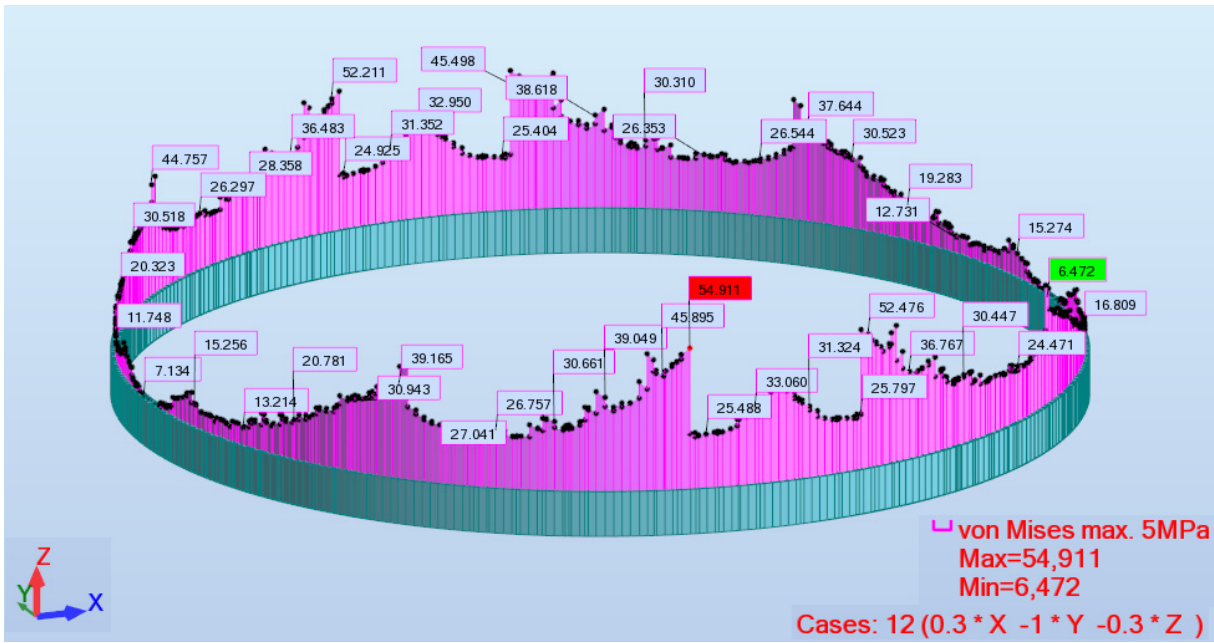


Figure 125 Global stress analysis of the Tension ring Structure. (element definition)

4. Stress analysis of element 9741 (element with $\sigma_{VonMises,max} = 54.911 \text{ MPa}$) and definition of the critical Cross-Section
5. Detailed stress analysis in the critical Cross-Section

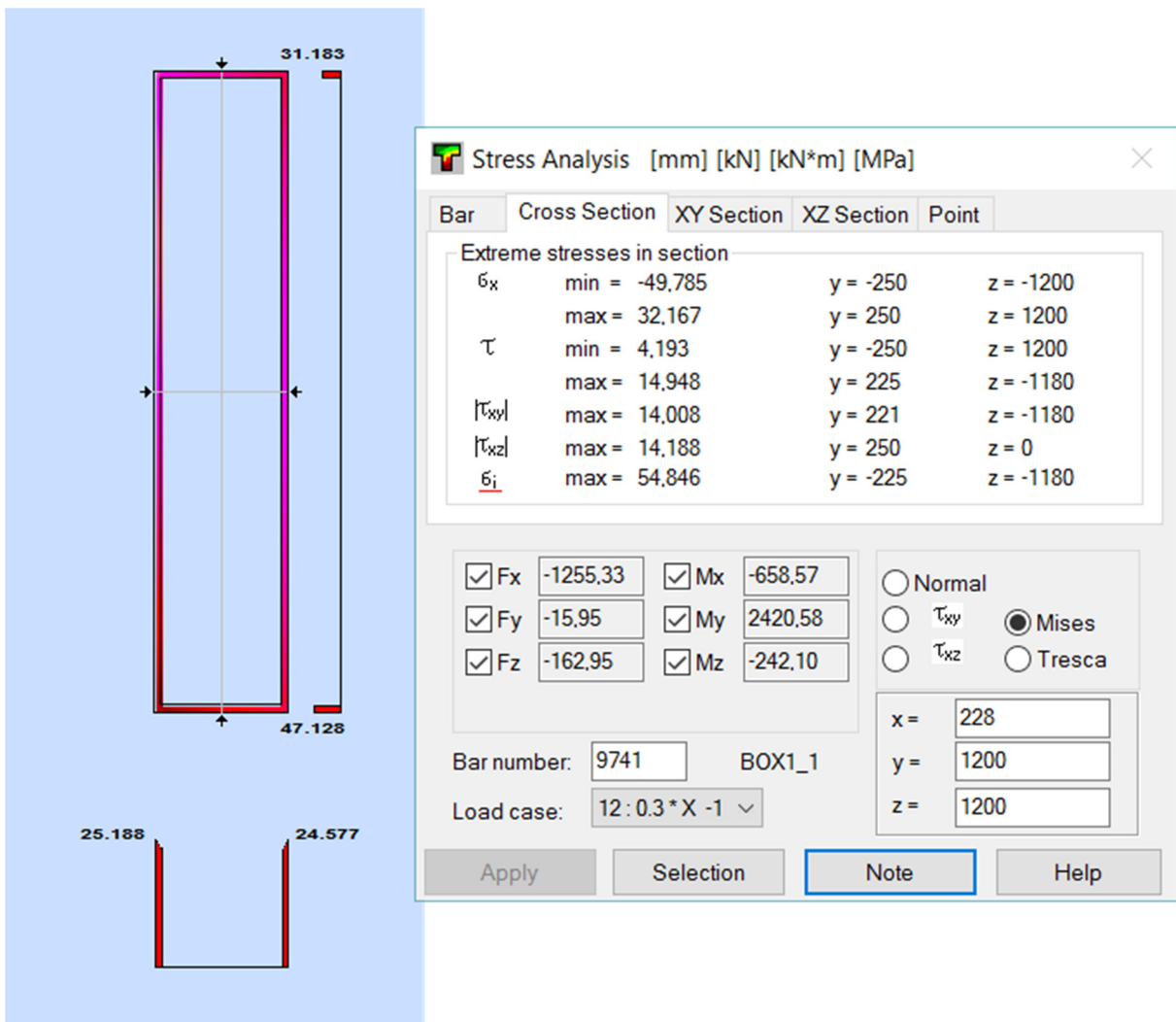


Figure 126 Detailed stress analysis for the critical Cross-Section of the Tension ring Structure.

6. Maximum Cross-Section stresses in point $x=228\text{mm}$, $y=1200\text{mm}$ and $z=1200\text{mm}$ (lower left corner)
7. $\sigma_{VonMises,\max} \prec f_{y,d}$

10 Results of the main concepts

10.1 The Altitude Azimuth concept

10.1.1 Displacements

For the Alt-Azimuth concept, the relative deformations between the dish upper nodes and the Image Sensor are easier to be examined in the operational phase. The structure, due to its stiffness it is mainly designed to withstand the critical earthquake combination. Generally, this chapter, apart from a brief explanation about the survival combination, it will be divided into two parts for the operational displacements. The first part will present the results for the zenith position, whereas the second one will give the necessary information for the 60° from the zenith position. (extreme case)

10.1.1.1 Survival situations

For the zenith position the critical combination is the earthquake combination $1*X+0.3*Y+0.3*Z$, with a maximum nodal displacement of 430.1mm.

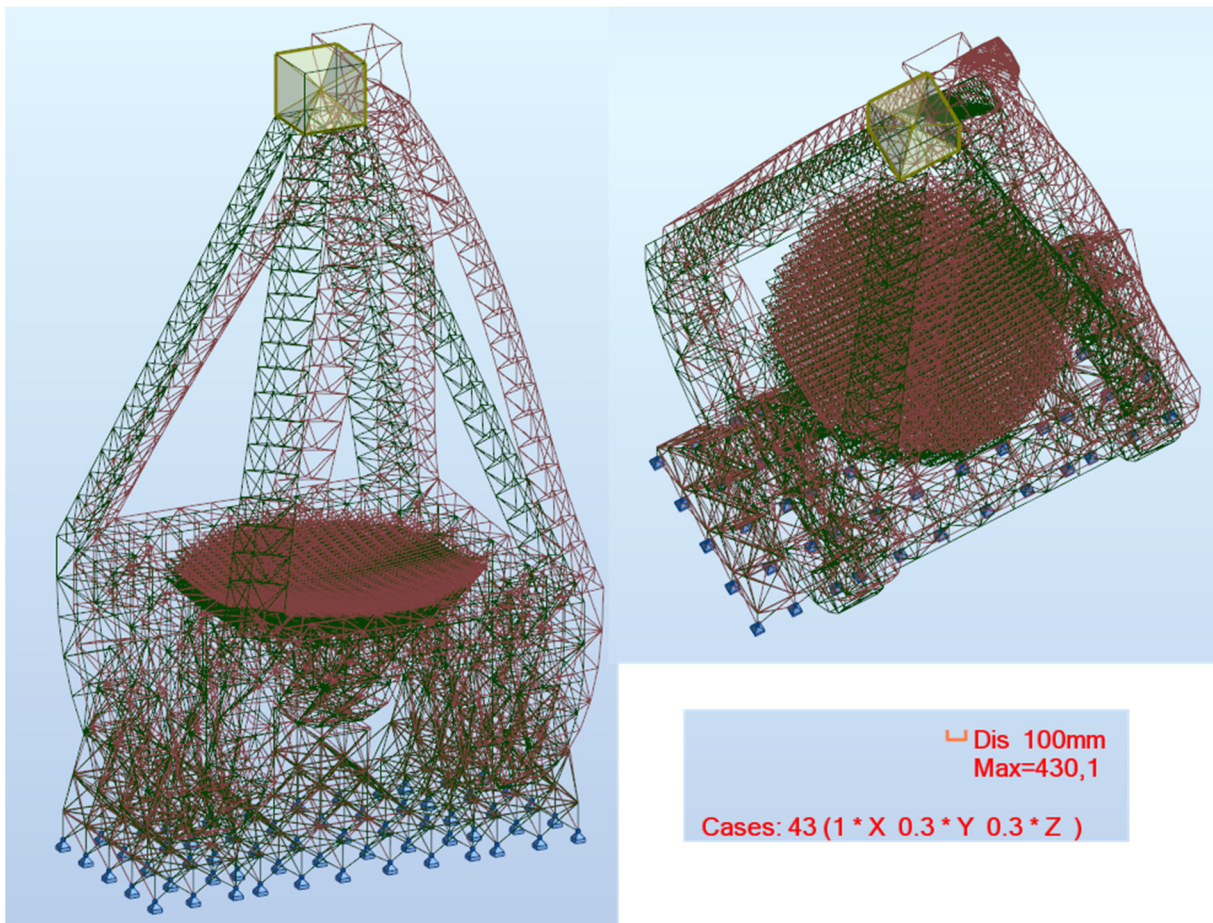


Figure 127 Deformation shape of the Alt-Azimuth design in zenith position for the critical survival combination.
($1*X+0.3*Y+0.3*Z$)

For the 60° from the zenith position, the critical combination is the earthquake combination

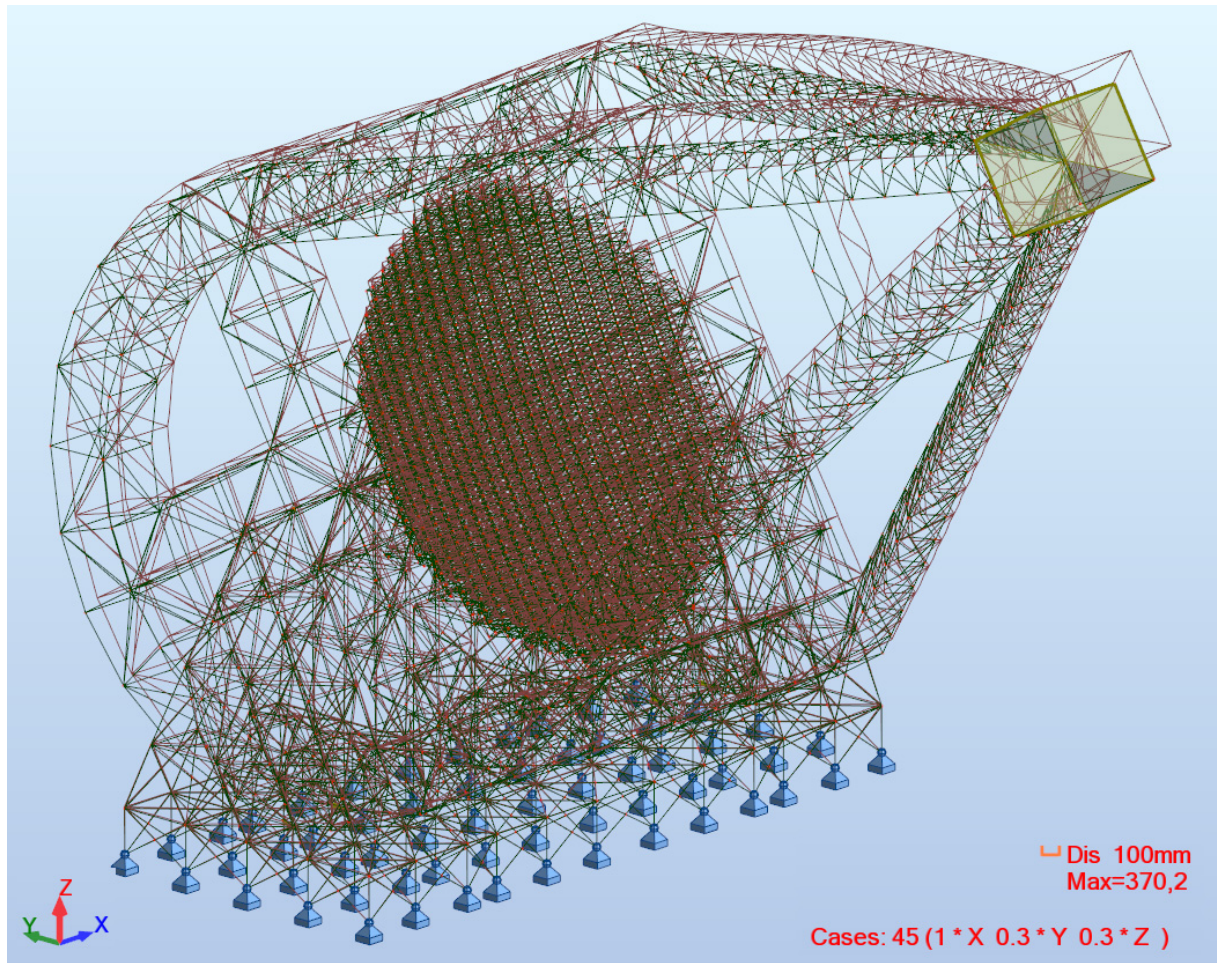


Figure 128 Deformation shape of the Alt-Azimuth design in 60° from the zenith position for the critical survival combination.
($1*X+0.3*Y+0.3*Z$)

10.1.1.2 Operational situations

The operational displacements in 0° position influence mainly the Image Sensor node. As it is evident from the images on the bottom, the maximum relative nodal displacement of the dish upper nodes is ~1.5mm, which is insignificant. Moreover, minimal rotations were observed for this position, too. The nodal displacements of the dish nodes are presented though. In a future research these displacements could be used to run a simulation from the astrophysics point of view and examine the exact influence on the quality of the observations. In this position, it is proved, that there is a considerable possibility, that no actuators regulating the mirror facets are needed.

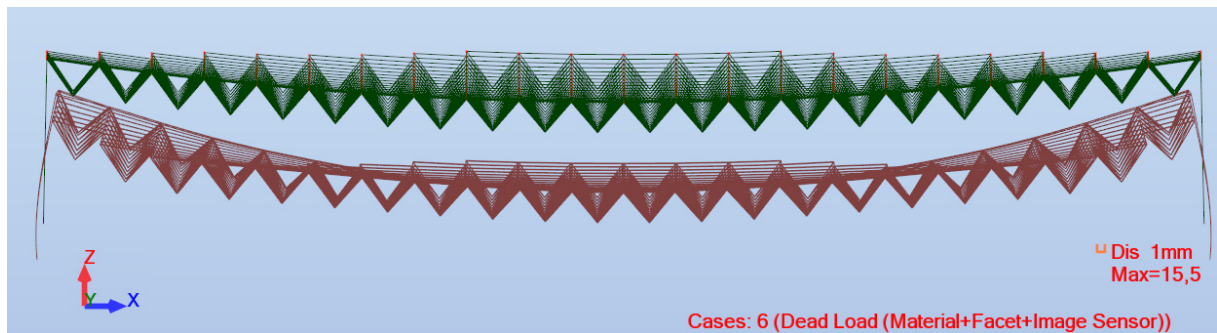


Figure 129 Deformation shape of the dead load case for the dead load case.

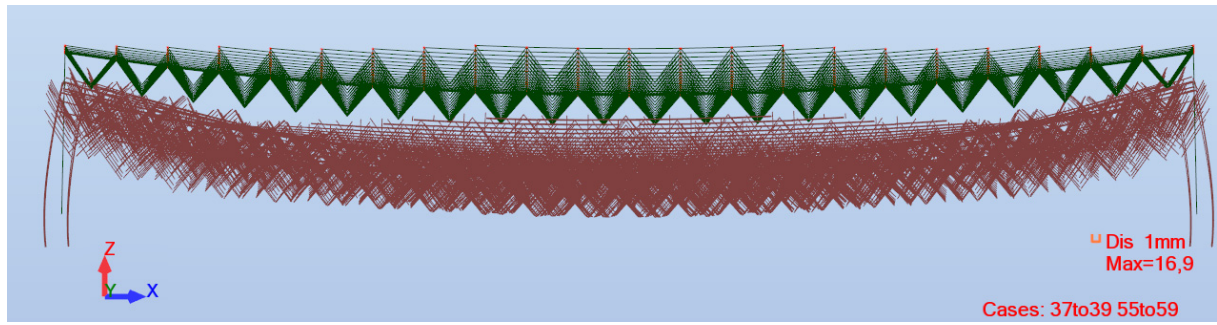


Figure 130 Envelope of the deformation shapes for all operational wind load combinations.

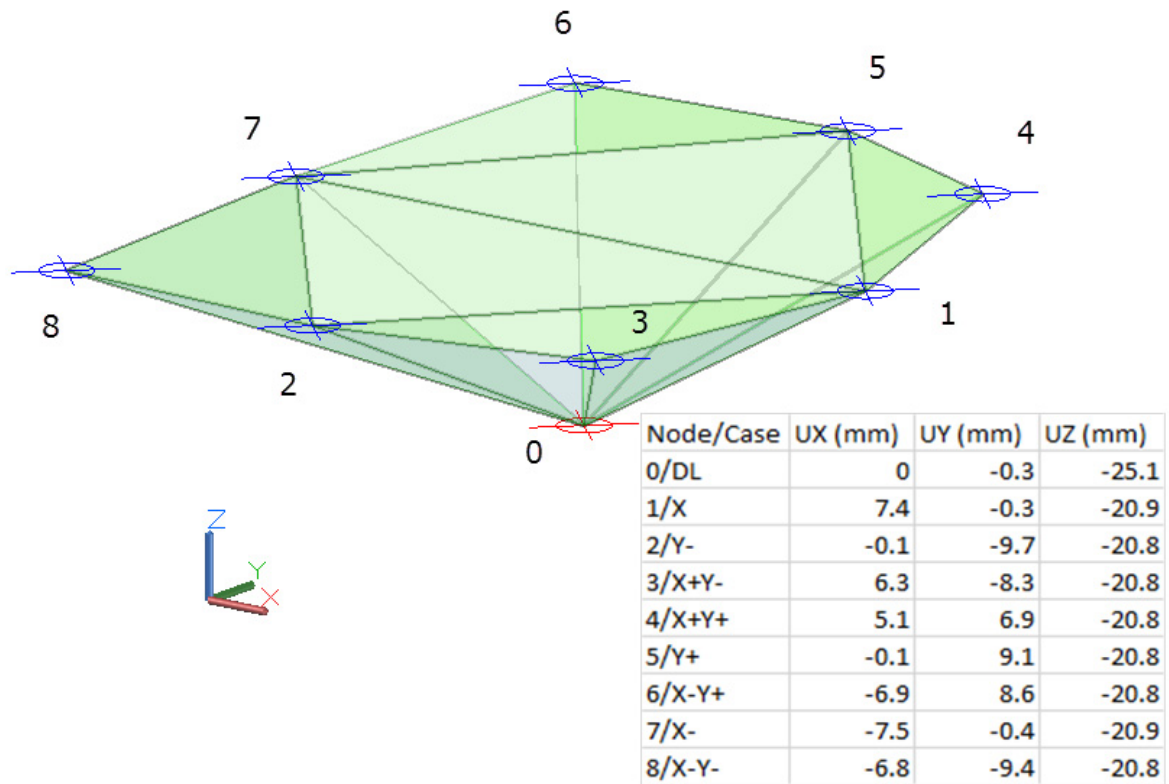


Figure 131 Marginal area of the operational displacements of the Image Sensor in zenith position.

For the zenith position, as aforementioned, the main influence is that of the Image Sensor node. The image above shows the three dimensional space that the Image Sensor node moves. This node is the centre of gravity of the whole Image Sensor Structure. By assuming that this structure is completely rigid, all peripheral nodes have the same displacements. This is a good starting point for a more detailed examination of the total behavior of the structure, as these displacements describe the critical operational situation.

Below the upper nodal displacements of the dish, for the 60° from the zenith position, are shown.

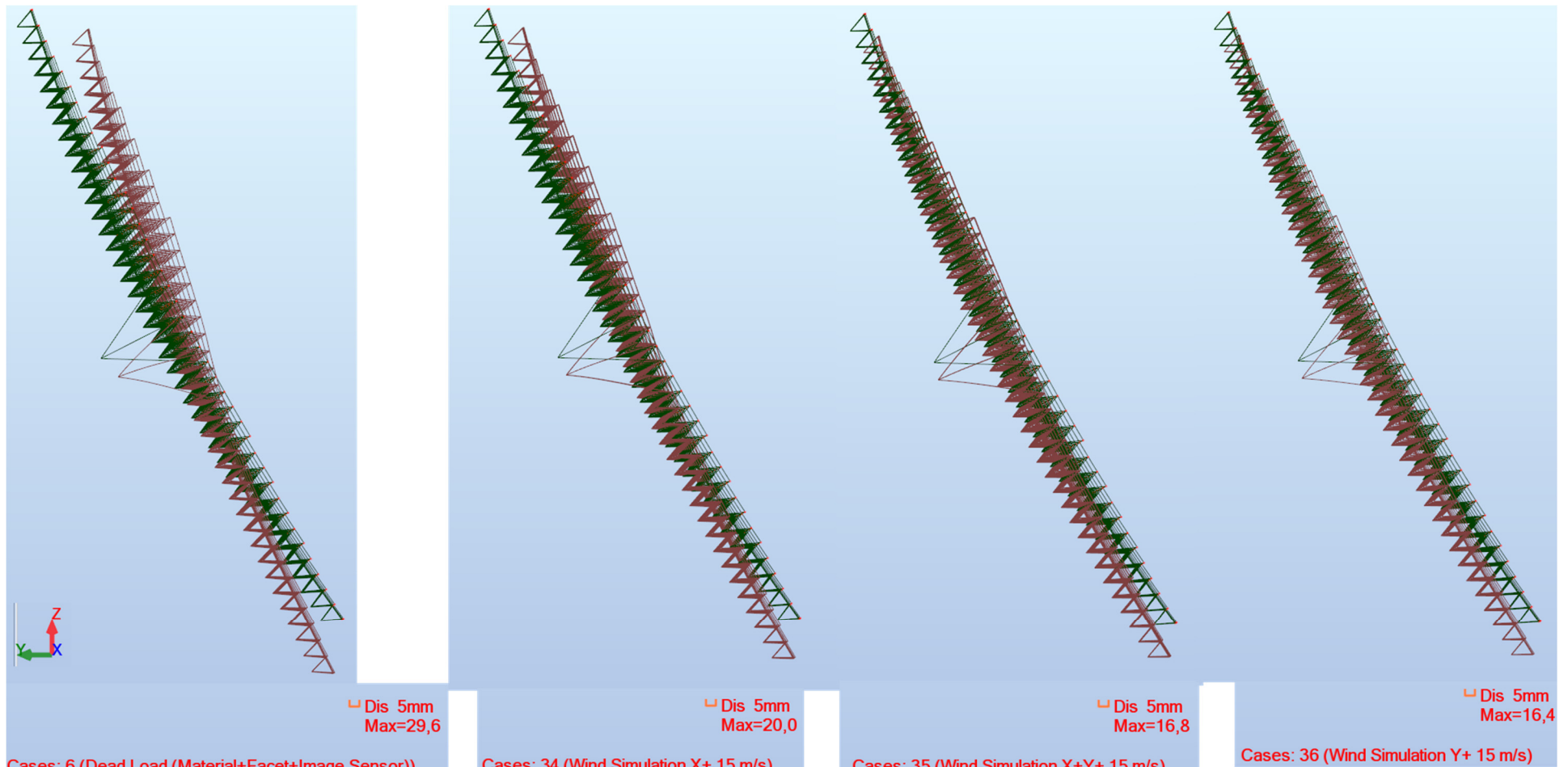


Figure 132 Dish upper nodal displacements for Dead load case and all operational wind load combinations.

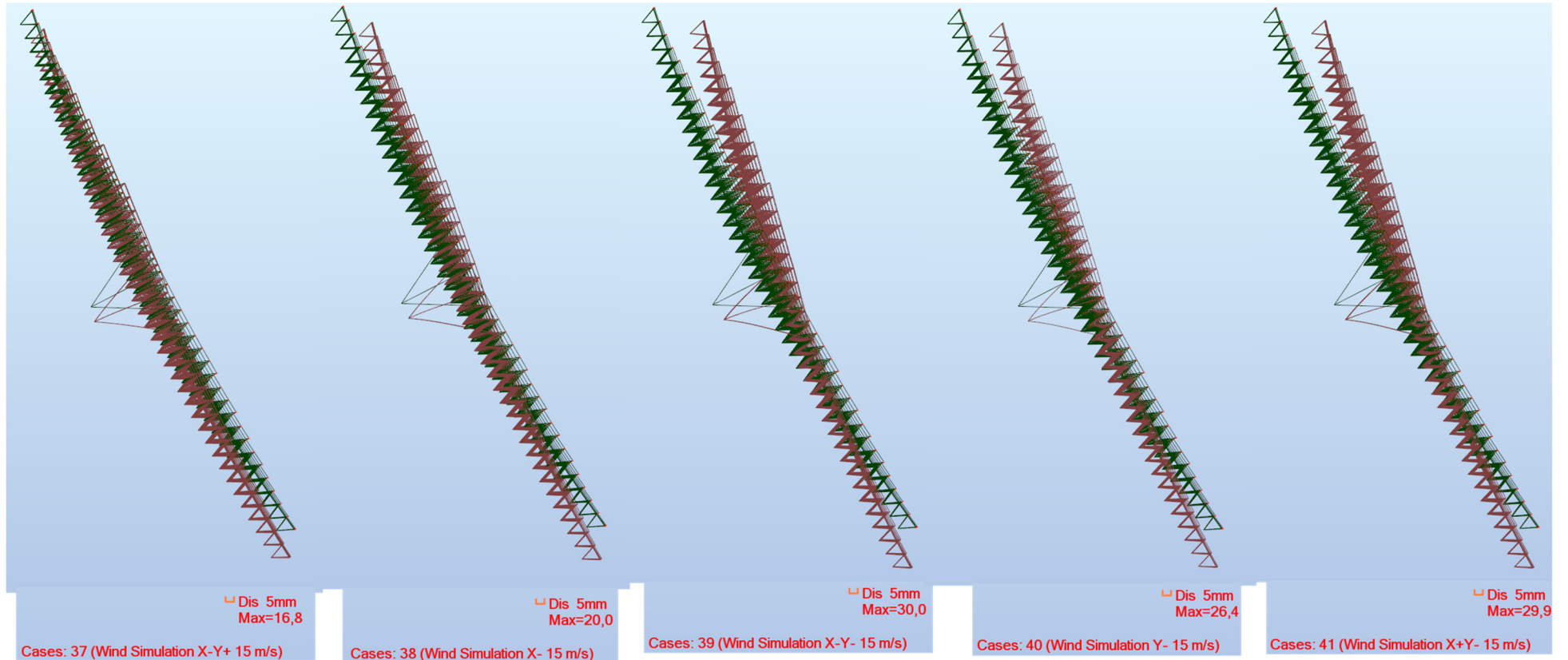


Figure 133 Dish upper nodal displacements for Dead load case and all operational wind load combinations.

From the images above, the influence of the operational wind in the dish upper nodes is observable. The relative displacements from dead load case to wind load combination remain small, but not insignificant. The maximum relative displacement is 13.2mm. Moreover, small rotations appear, so the further investigation in collaboration with the astrophysics simulation is considered for the 60° position necessary. In any case, the possibility of avoiding the use of actuators, is not negligible at all.

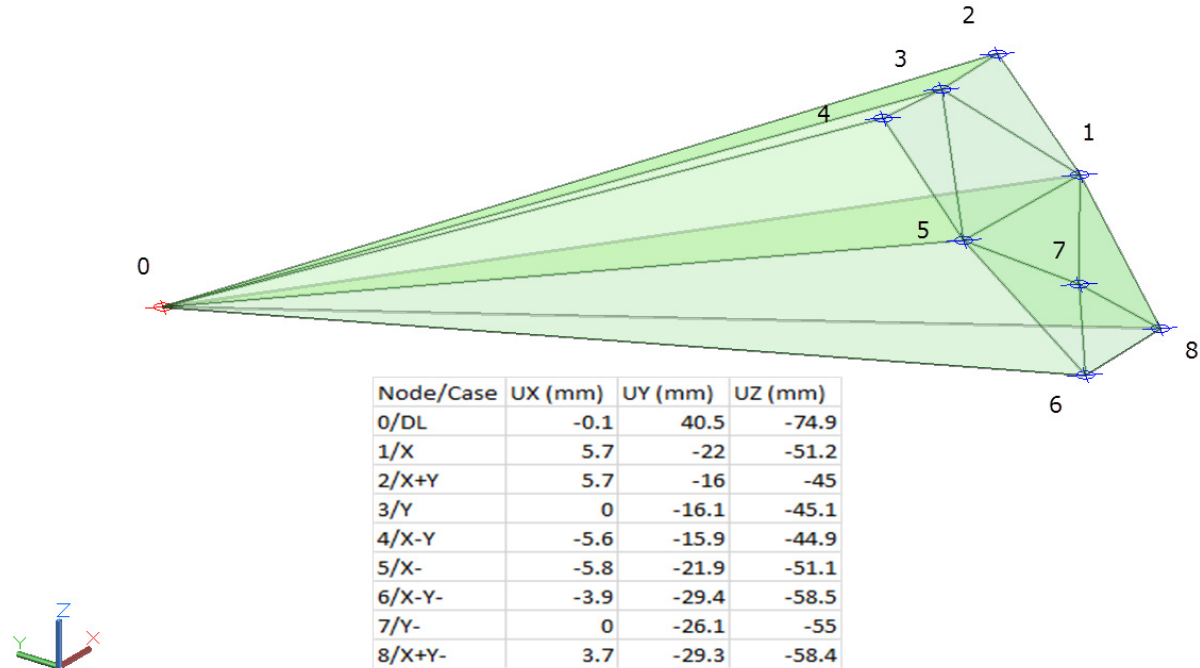


Figure 134 Marginal area of the operational displacements of the Image Sensor in 60° from zenith position.

The next step is the examination of the Image Sensor nodal displacements. As it is observable, the relative displacements of the Image Sensor are considerable. A maximum deviation of ~20mm in Uz direction and ~25mm in Uy directions are evident. However, a more detailed analysis here is deemed as unnecessary. The data exist and in the future a feedback loop will be implemented to examine the influence of these displacements in the quality of the produced images.

10.1.2 Dynamic analysis results

Finally, the modal analysis results are presented. The modal masses consist of the whole Dead Load case. (Material weight and Mirror facets plus actuators weight and Image Sensor weight) This describes accurately the reality, as these loads are permanent throughout the lifespan of the structure. Only the modes needed to reach over 80% Relative Mass Participation in every direction are presented.

Case/Mode	Frequency (Hz)	Period (sec)	Rel.mas.UX (%)	Rel.mas.UY (%)	Rel.mas.UZ (%)
1	1,09	0,92	0,00	33,73	0,00
2	1,19	0,84	37,33	33,73	0,00
3	1,49	0,67	37,33	33,73	0,00
4	1,81	0,55	37,33	41,27	0,00
5	2,04	0,49	76,02	41,27	0,00
6	2,28	0,44	76,02	41,27	0,00
...
195	9,41	0,11	81,02	79,56	71,60
196	9,48	0,11	81,03	79,56	71,60
197	9,51	0,11	81,07	79,80	71,61
198	9,53	0,10	81,07	79,87	71,61
199	9,57	0,10	81,07	84,72	71,61
200	9,59	0,10	81,07	84,75	71,61

Table 23 Modal analysis results for the Alt-azimuth design in the zenith position.

Case/Mode	Frequency (Hz)	Period (sec)	Rel.mas.UX (%)	Rel.mas.UY (%)	Rel.mas.UZ (%)
1	1,06	0,94	0,00	32,49	1,63
2	1,16	0,86	38,25	32,49	1,63
3	1,29	0,77	55,66	32,49	1,63
4	1,66	0,60	55,66	37,97	2,36
5	2,12	0,47	55,66	40,85	5,79
6	2,13	0,47	63,11	40,85	5,79
...
82	0,14	82,74	78,60	79,34	79,95
83	0,14	82,74	78,96	79,34	79,95
84	0,14	82,74	79,61	79,34	79,95
85	0,14	82,75	79,76	79,34	79,95
86	0,13	82,75	79,76	79,34	79,95
87	0,13	82,75	80,20	79,35	80,31

Table 24 Modal analysis results for the Alt-azimuth design in 60° from the zenith position.

10.2 TheBigLebowSky concept

Due to the large amount of produced results, only the most significant will be presented. Mainly, the separation between survival and operational deformations will be presented. In the points needed, more detailed results will be presented. The results are presented separately for the Image Sensor and the Main Dish Structure, as they are completely separate as structural systems. Their interaction for the correct cooperation between the Image Sensor and the Dish is not extensively examined, for the simple reason, that the Robocrane is supposed to be able to achieve any place over the Dish. As a result, the operational deformations of the Dish upper nodes, which are very small and can easily be counterbalanced with the actuators, play a minor, if not insignificant, role in the interaction between the Dish and the Image Sensor.

A very important aspect of the design that should always be kept in mind, is the fact that no material non linearity/plasticity was taken into account. All structures were designed to remain elastic under the influence of the critical load combination. This fact, decreases rapidly the importance of presenting the results for survival/critical load combinations, as for such loads the Telescope is not considered to be operational.

Finally, for each structure the modal analysis results are presented.

10.2.1 Displacements

10.2.1.1 Main Dish Structure

10.2.1.1.1 Survival situations

The critical design combination for the Main Dish Structure was the Seismic combination $0.3*X-1*Y-0.3*Z$. The deformed shape of the structure is shown below.

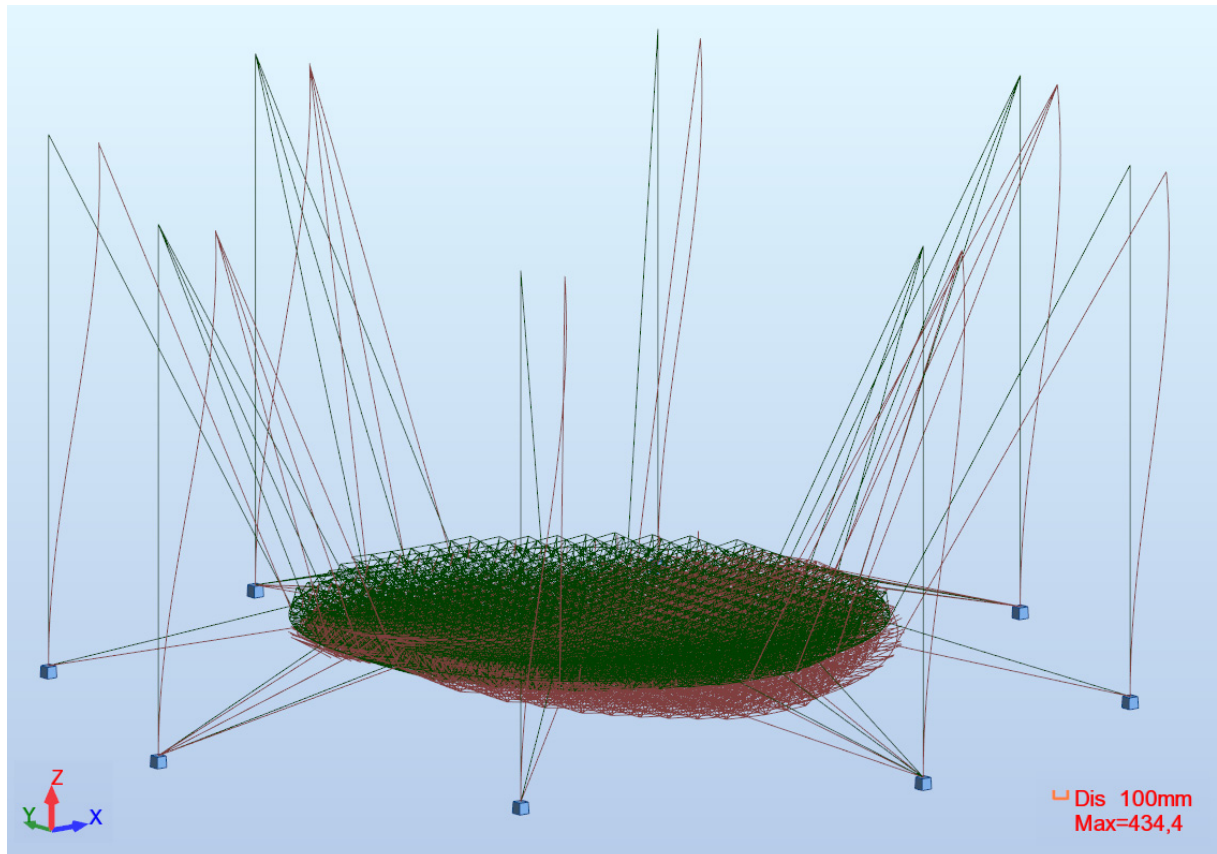


Figure 135 Deformation shape of the Main Dish Structure for the critical survival combination. ($0.3*X-1*Y-0.3*Z$)

The maximum nodal displacement is -406mm in the top of a concrete column (node 2808), although the maximum deformation appears 434.4mm as the sag of a cable. However, it is deemed as unnecessary the presentation of more results for the critical cases.

10.2.1.1.2 Operational situations

The case of dead load and maximum operational wind of 15m/s will be further examined and presented, as it is the critical one for the majority of the lifespan of the structure. Due to the symmetry of the structure in both X and Y axes, the wind in X and X+Y directions is considered. As it is evident from the maximum nodal displacements and the deformation shape, there is minor influence between X and X+Y directions. This is also intuitively the case, due to the symmetry of the structure also in 45° from the axis. Moreover, the major wind influence is on the column surface.

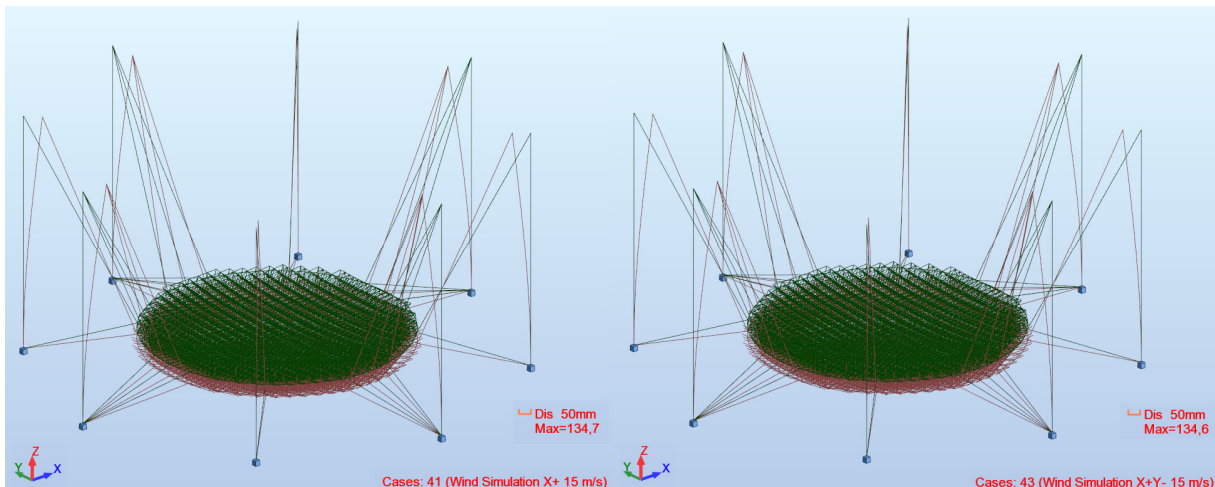


Figure 136 Deformation shape of the Main Dish Structure for the operational load combinations. (Wind X+ left and Wind X+Y- right)

The maximum displacement of 134.7mm is on the upper node of the critically influenced column. However, there is no real interest for this displacement, but only for the upper nodes of the dish. (nodes that support the mirror facets) So, the operational nodal displacements of the dish are presented.

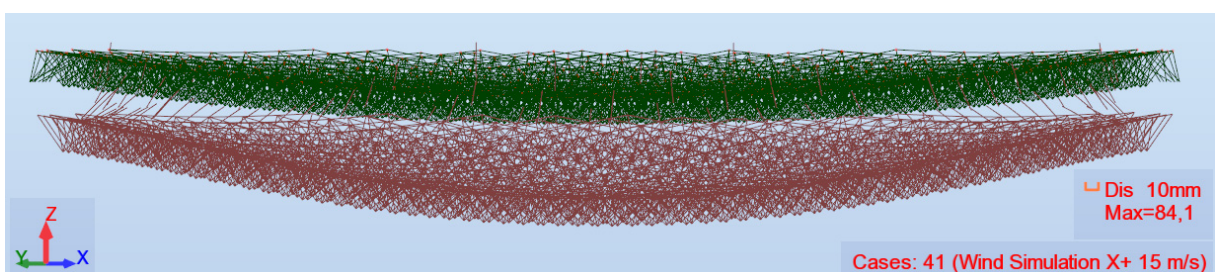


Figure 137 Front view of the dish upper nodal displacements of the Main Dish Structure for the operational load combination (Wind in X+ direction)

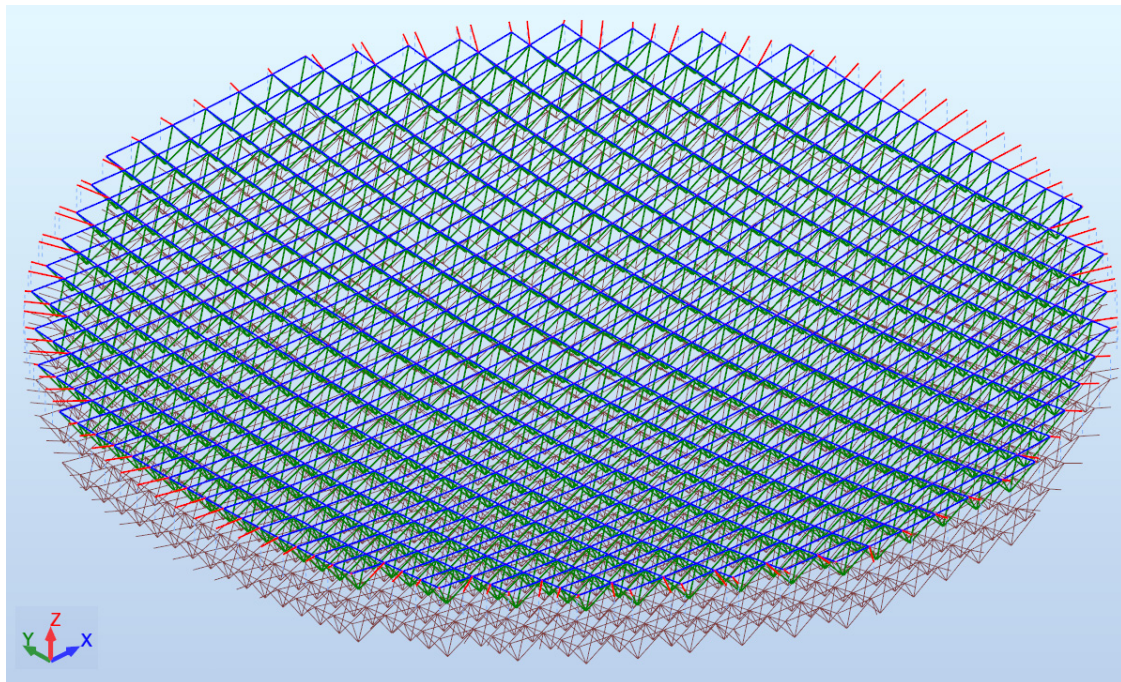


Figure 138 3D view of the dish upper nodal displacements of the Main Dish Structure for the operational load combination (Wind in X+ direction)

Even though the maximum displacement is around 8.5cm, which is an unacceptable value for an actuator to be counter balanced, the dish deformations are completely homogenous and undisturbed. As a result, the relative deformation between two nodes is kept minimal allowing for the actuators to rearrange the mirror facets in order to recreate the original surface. This can be also proven by the maximum rotation of the critical dish node, which is $0.002\text{rad}=0.115^\circ$, easily manageable with an actuator.

10.2.1.2 Image Sensor Structure (Robocrane)

10.2.1.2.1 Survival situations

For the Robocrane Image Sensor Structure, the critical combination is the X+Y survival wind of 55m/s plus the dead loads. It is very important to be mentioned here, that due to the analysis method used (non-linear large displacements analysis), the superposition principle could not be applied. As a result, the load combinations are created as separate load cases applying the loads incremental. In the first phase, the Dead load acts and in the second phase (on the deformed shape), the Wind load acts.

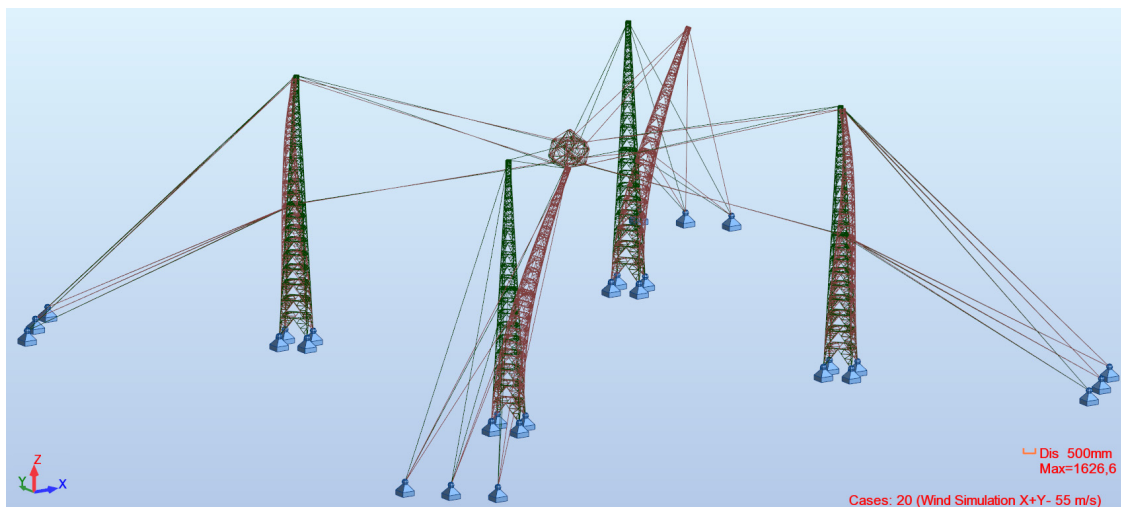


Figure 139 Deformation shape of the Robocrane Image Sensor Structure for the survival wind combination in X+Y- direction.

The maximum nodal displacement occurs on the top node of the critical tower and is 1176.5mm, with a maximum rotation in Rx of 0.02rad=1.15°. The maximum deflection of 1626.6mm is the sag of a backstay/auxiliary cable.

10.2.1.2.2 Operational situations

The deformations in the survival combination though, as aforementioned, pose a minor role in the functionality of the structure. Following, only the operational situations will be examined. Again, due to the symmetry of the structure the X and X+Y wind direction will be considered. The load combinations concern, of course, the Dead Load (structure's and Image Sensor's weight) plus the 15m/s wind. Moreover, only the Image Sensor nodal deformations will be considered.

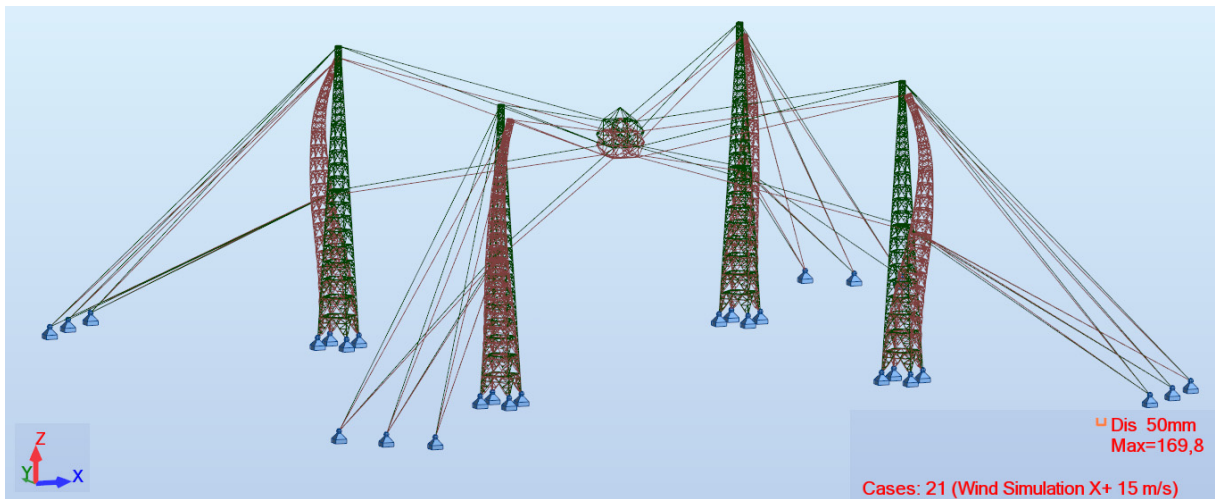


Figure 140 Deformation shape of the Robocrane Image Sensor Structure for the operational load combination. (Wind in X+ direction)

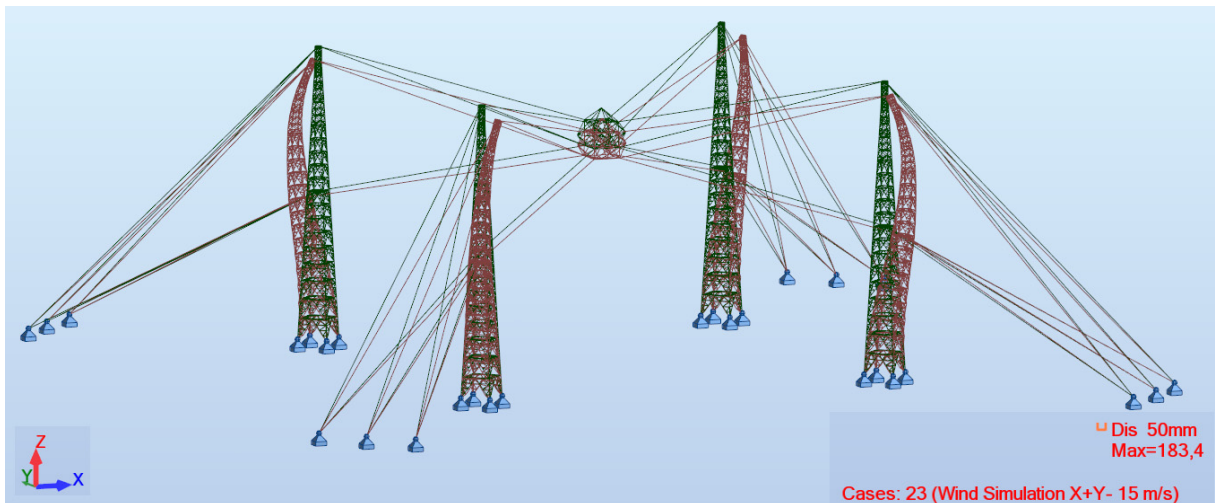


Figure 141 Deformation shape of the Robocrane Image Sensor Structure for the operational load combination. (Wind in X+Y- direction)

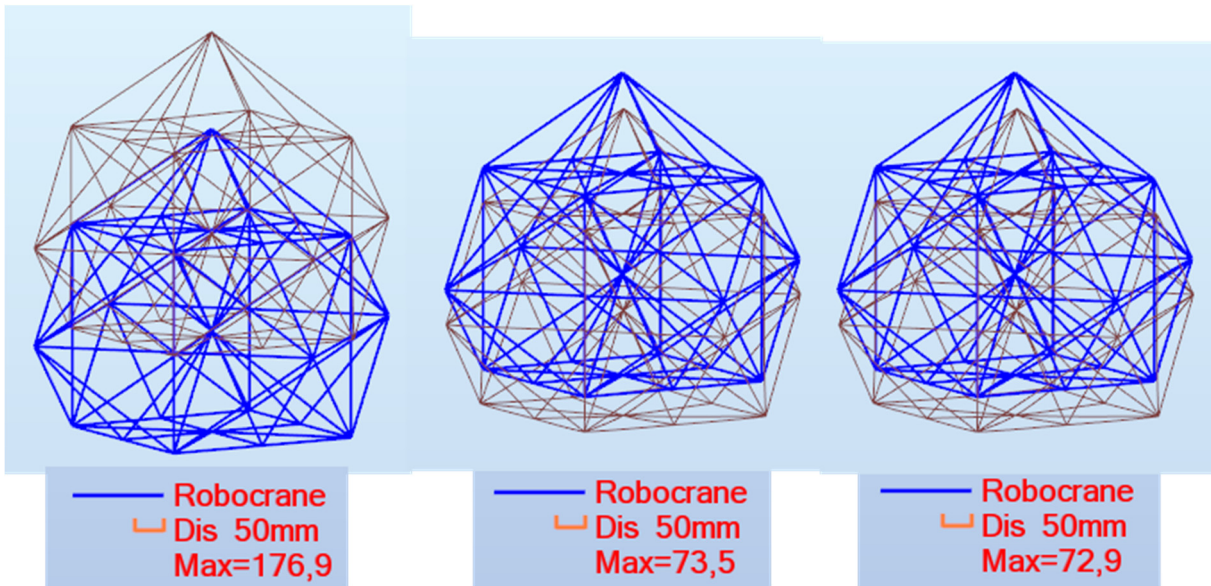


Figure 142 Deformations of the Image Sensor (Housing) for the static/dead load situation (left), operational wind in X+ direction (middle) and operational wind in X+Y- direction.

By checking the deformations in the dead load case and in the wind combinations, it is possible to construct a space in which the Image Sensor lower node will move. These could be considered the marginal errors that have to be counter-balanced from the pre-stress forces. As it is evident in the picture above, the displacement in the Dead Load case is not zero, although by manipulating the pre-stress forces this could be easily achieved. It was not deemed necessary though, as we are not considering the cooperation between the dish and the Image Sensor. This means that the mirror facets receive also deformations and, of course, wind is always present although mostly under 15m/s. As a result, the relative maximum displacements from the Dead Load case are of interest to examine the sensitivity of this structure to minor wind loads. These deformations are in Uz direction around -250mm, whereas the ones in Ux and Uy direction are considered insignificant. Finally, no actual rotation was observed. As a result, the structure is considered sensitive to wind, mostly in the vertical direction. This could prove really challenging for the accurate focus of the Image Sensor, considering also the dynamic behaviour of the structure. Even though further investigation is definitely necessary, the conclusions showed that with the incorporation of a sophisticated control system between the Dish and the Image Sensor the desired results could be accomplished.

10.2.1.3 Alternative Image Sensor Structure-Cross-Arch

10.2.1.3.1 Survival situations

The critical combination for the Cross-Arch Image Sensor Structure is the survival wind combination in X direction, which causes a total deformation of around 3m in the critical point of the structure. This is considered extreme, even for the gigantic size of the structure. However, the exact geometry of the structure was not investigated and the box-girder shaped Cross-Section had a negative influence in the wind pressure maps across the elements. Moreover, the wind load creation is considered very conservative, especially for this kind of structures and a more detailed Computational fluid dynamics analysis could be of interest.

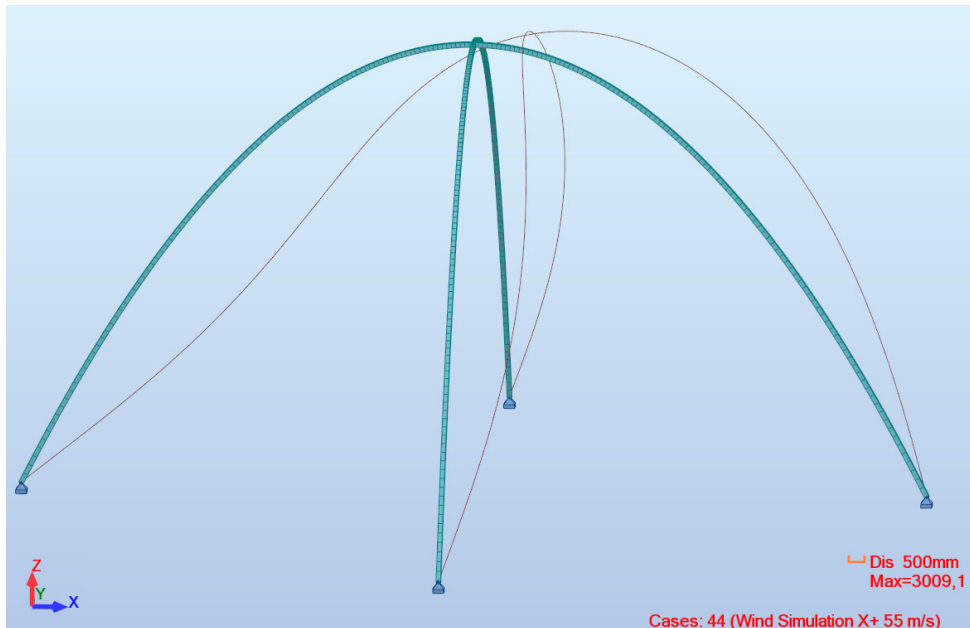


Figure 143 Deformation shape of the Cross-Arch Image Sensor Structure for the survival wind load combination. (55m/s wind in X+ direction)

10.2.1.3.1 Operational situations

The structure, though, proved to be able to compete with the Robocrane Image Sensor Structure in terms of operational displacements. The important Image Sensor nodal displacements, in direction Uz, relatively to the Dead Load case, are insignificant. (around 10mm).

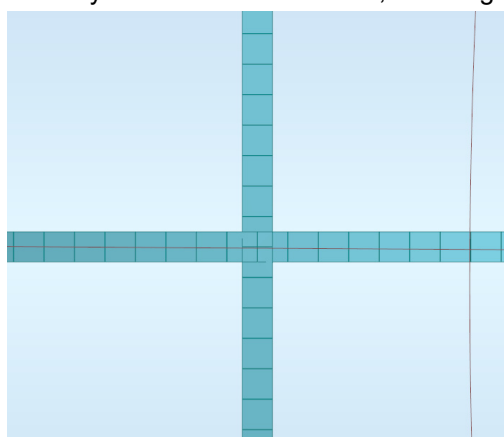


Figure 144 Top view of the operational displacements of the Cross-Arch Structure for wind in X+ direction.

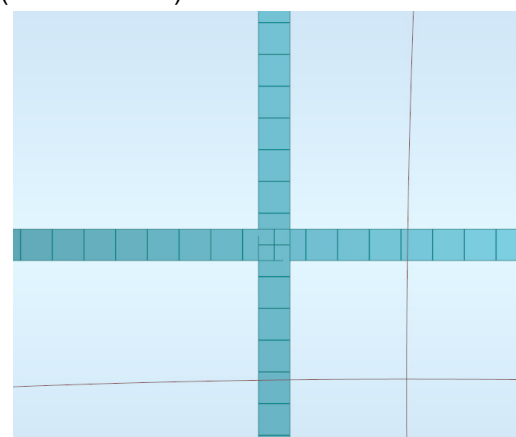


Figure 145 Top view of the operational displacements of the Cross-Arch Structure for wind in X+Y- direction.

However, a disadvantage of this structure compared with the Robocrane Structure is that the Cross-Arch is sensitive to Ux and Uy directions. This is also evident from the images above. As an example, the deformations with the operational wind blowing from the +X direction are $U_x=120.5\text{mm}$.

10.2.2 Dynamic analysis results

Finally, the modal analysis results are presented. The modal masses consist of the whole Dead Load case. (Material weight and Image Sensor weight) This describes accurately the reality, as these loads are permanent throughout the lifespan of the structure. Only the modes needed to reach over 80% Relative Mass Participation in every direction are presented.

10.2.2.1 Main Dish Structure

Mode	Frequency (Hz)	Period (sec)	Rel.mas.UX (%)	Rel.mas.UY (%)	Rel.mas.UZ (%)
1	0.55	1.82	0.78	19.67	0
2	0.55	1.82	20.53	20.44	0
3	0.56	1.8	20.53	20.44	0.34
4	0.56	1.79	26.04	25.95	0.34
5	0.56	1.79	31.59	31.42	0.34
6	0.56	1.79	37.1	36.93	0.34
...
75	20.05	0.05	100	99.99	23.23
76	20.05	0.05	100	99.99	56.27
77	20.07	0.05	100	99.99	56.34
78	20.17	0.05	100	99.99	56.59
79	20.18	0.05	100	99.99	56.7
80	20.2	0.05	100	99.99	99.53

Table 25 Modal analysis results for the Main Dish Structure.

10.2.2.2 Image Sensor Structure (Robocrane)

Mode	Frequency (Hz)	Period (sec)	Rel.mas.UX (%)	Rel.mas.UY (%)	Rel.mas.UZ (%)
1	0,47	2,14	4,37	4,37	0,00
2	0,47	2,13	5,01	5,01	0,00
3	0,47	2,13	15,52	15,52	0,00
4	0,47	2,12	21,17	21,17	0,00
5	0,59	1,71	21,17	21,17	4,49
6	0,82	1,22	21,17	21,17	4,49
...
60	3,90	0,26	81,91	81,91	6,94
61	4,10	0,24	81,91	81,91	6,94
62	4,28	0,23	81,91	81,91	6,94
63	4,28	0,23	81,96	81,96	35,35
64	4,28	0,23	81,96	81,96	72,87
65	4,28	0,23	82,14	82,14	81,37

Table 26 Modal analysis results for the Robocrane Image Sensor Structure.

10.2.2.3 Alternative Image Sensor Structure (Cross-Arch)

Case/Mode	Frequency (Hz)	Period (sec)	Rel.mas.UX (%)	Rel.mas.UY (%)	Rel.mas.UZ (%)
1	0,10	10,08	0,00	0,00	0,00
2	0,10	9,91	77,15	0,02	0,00
3	0,10	9,91	77,17	77,17	0,00
4	0,22	4,65	77,17	77,17	0,00
5	0,24	4,23	78,43	78,85	0,00
6	0,24	4,23	80,11	80,11	0,00
...
74	12,49	0,08	96,82	96,82	79,95
75	12,59	0,08	96,82	96,82	79,95
76	12,68	0,08	96,82	96,82	79,95
77	12,69	0,08	96,83	96,83	79,95
78	13,15	0,08	96,83	96,83	79,95
79	13,57	0,07	96,83	96,83	80,31

Table 27 Modal analysis results for the Cross-Arch Image Sensor Structure.

10.3 Time History analysis results

As far as the Time History Analysis that was discussed in 4.1.3.2 is concerned, the results will be presented in a future report along with the Elasto-plastic analysis of the structures.

11 Quantity survey and cost estimation

The cost estimation of the two telescope projects is based on the quantity survey that was conducted from the finite elements simulation program. Among the results of this survey is the weight of each element according to the assigned material and cross section. The total weight of the structure was then calculated and this value was the starting point of the cost estimation of the whole project.

The first step was to estimate a price per unit ([tn] or [m³]) for the raw material used in the construction. This estimation was based on the current price of the material in the market and on price-lists from manufacturers. In the end the most unfavorable price was assigned in order to result the most unfavorable scenario. For steel S460NL and for circular hollow sections a price of 1800 €/tn was assumed while for concrete C70/80 a price of 300 €/tn. The total cost of the raw material being used was then calculated.

The next step was to estimate the ratio of the raw material cost to the steel construction cost. The other aspects that contribute to the overall cost are the fabrication, construction and support. The relative proportions of the raw material as well as those of the other cost drivers were estimated from the steel industry average. The Figure shows the breakdown of costs of steel frame for a typical multi-story commercial building. The cost breakdown of the telescope structures of this project should not differ from this one as the telescope structure relies on a fractal design, with most parts made of mild steel. Modules will be made of standard pipes and serially produced nodes and will be assembled on-site, while all pipes and pre-assembled nodes can be transported in standard containers. The procedure is the same with a typical industrial building. After specifying these proportions and with the knowledge of the cost of one of these cost-drive elements, that of raw material, an estimation of the total cost of the steel structure was made.

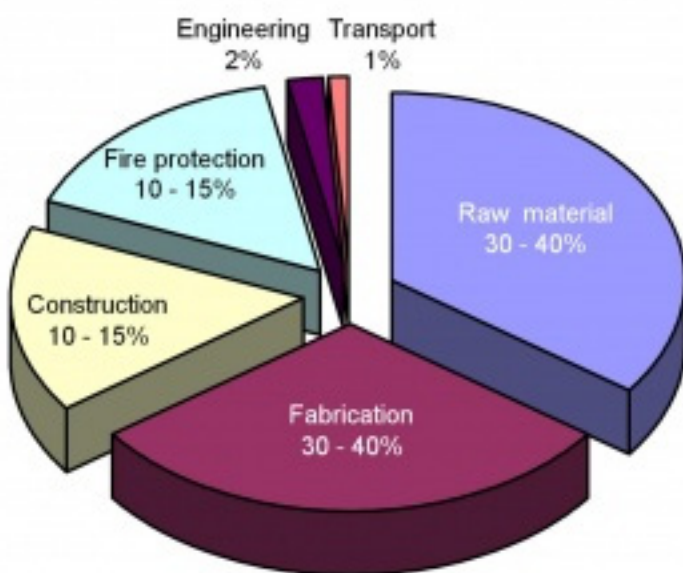


Figure 146 Breakdown of costs of steel frame for a typical multi-storey commercial building.

The costs of other elements of the telescope should be also defined in order to get a total price of the project. The elements which were considered for both telescope approaches (Alt-Azimuth and TheBigLebowSky) were: Project Management, Project Engineering, Site Infrastructure, Telescope Structure, Optomechanical Subsystems, Instrumentation, and Central Control Systems.

By applying the same procedure as before the proportions of these elements to the total cost had to be defined. Reviewing and comparing the cost estimation reports of large telescope projects such as the E-ELT and the OWL the average relative ratios of the above mentioned elements were calculated (Figure). Impressive is the fact that the steel construction counts only for the 15%-20% of the total cost. From this ratio and known the Telescope structure cost, the total cost could then be calculated, as well as the costs of all the other elements.

The lack of a detailed design in this stage of the project hinders the use of a more detailed cost estimation method. The project management methods cannot be implemented as they involve the construction of the Work Breakdown Structure (WBS) which requires a Product Breakdown Structure (PBS) and an Activity Breakdown Structure (ABS). These elements could be used for a detailed cost estimation but they require a great level of detail as input, which is unavailable. For this reason, the resulted value of the total cost is a very rough estimate. In a later stage a greater level of detail in the design will provide a more precise cost estimate.

One more parameter that affects the precision of the cost estimate is the price estimates of the raw material. These vary greatly over time, place, quantity and quality provided and as mentioned before a more unfavorable scenario was selected in order to represent the purposes of this Project. A precise material cost will require a detailed order from the client to the potential supplier and could only be given after the evaluation of the order from the supplier.

11.1 Quantity Survey

Altitude-Azimuth design						
Type	Num-ber	Length (m)	Unit weight (kG/m)	Bar weight (kG)	Total weight (kG)	Painting area (m2)
CHS 76.1x2.9	16	70,96	5,24	371,83	372	16,96
CHS 88.9x3.2	28	225,42	6,77	1525,90	1526	62,89
CHS 114.3x3.2	488	1605,24	8,76	14067,06	14067	576,12
CHS 114.3x6	10315	18733,78	16,02	300115,16	300115	6723,59
CHS 139.7x3.6	503	2595,54	12,08	31346,39	31346	1138,55
CHS 168.3x3.2	22	114,52	13,03	1491,88	1492	60,52
CHS 168.3x5	184	1346,24	20,10	27059,42	27059	712,16
CHS 193.7x5	20	132,12	23,30	3078,40	3078	80,46
CHS 193.7x6.3	260	1000,64	29,10	29118,62	29119	609,39
CHS 244.5x5	841	4634,99	29,52	136811,82	136812	3558,42
CHS 273x16	24	95,60	101,30	9684,43	9684	82,02
CHS 323.9x5	279	1829,26	39,30	71889,92	71890	1860,44
CHS 323.9x6	724	4727,74	46,70	220785,46	220785	4808,33
CHS 323.9x10	30	131,10	77,40	10147,14	10147	133,72
CHS 355.6x6.3	111	720,24	54,24	39067,51	39068	804,21
CHS 508x6.3	570	4394,78	77,91	342390,00	342390	7010,20
Total					1238951	28238,00

Table 28 Quantity survey of the Altitude Azimuth design.

TheBigLebowSky-Main Dish Structure						
Type	Num-ber	Length (m)	Unit weight (kG/m)	Bar weight (kG)	Total weight (kG)	Painting area (m2)
Steel bar elements						
BOX1_1	472	158,000	1119,03	176806,57	176807	916,40
CHS 42.4x2.6	5428	9276,200	2,55	23654,31	23654	1233,73
CHS 48.3x2.5	4066	6672,480	2,82	18816,39	18816	1011,96
Total					219277	3162,10
Steel cable elements						
Gegenseile	16	335,210	122,37	41018,29	41018	0,0
ObereSeile	16	677,710	122,37	82928,62	82929	0,0
Total					123947	0,0
Concrete elements						
C 2500x2500	8	360,000	15633,52	5628068,71	5628069	3600,00
Total					5628069	3600,00

Table 29 Quantity survey of TheBigLebowSky Main Dish Structure design.

TheBigLebowSky-Robocrane Image Sensor Structure						
Type	Num-ber	Length (m)	Unit weight (kG/m)	Bar weight (kG)	Total weight (kG)	Painting area (m2)
Steel bar elements						
CHS 219.1x6	2064	3273,120	31,53	103193,59	103194	2251,82
CHS 219.1x6.3	96	670,640	33,06	22171,65	22172	461,40
CHS 273x10	7616	16020,800	64,86	1039179,79	1039180	13745,85
Total					1164545	16459,07
Steel cable elements						
Back-stay_Oben	12	1956,960	61,18	119732,63	119733	0,0
Backstay_Unter	12	1552,240	61,18	94970,66	94971	0,0
MainOben	8	929,800	6,12	5688,79	5689	0,0
MainUnter	4	461,520	12,24	5647,43	5647	0,0
Total					226040	0,0

Table 30 Quantity survey of TheBigLebowSky Robocrane Image Sensor Structure design.

TheBigLebowSky-Cross-Arch Image Sensor Structure						
BOX1_1	400	593,320	942,34	559109,26	559109	2444,48
Total					559109	2444,48

Table 31 Quantity survey of TheBigLebowSky Cross-Arch Image Sensor Structure design.

	Steel weight(tn)	Concrete weight(tn)
Altitude-Azimuth design	1239	
TheBigLebowSky-Main Dish Structure	343	5628
TheBigLebowSky-Robocrane Image Sensor Structure	1391	
TheBigLebowSky-Cross-Arch Image Sensor Structure	559	

Table 32 Summary of the total weight of the Structures.

11.2 Alt-Azimuth

The Table shows the cost estimation for the Alt-Azimuth design. The amounts of raw material for the various steel structures in [tn] are the ones from the quantity survey. Multiplied with the price per ton they give the total cost of raw material pro steel structure. The sum gives the total cost in raw material and with known the relative proportion of the raw material to the total cost of the Telescope structure the cost of the Telescope structure is calculated. The total cost of the telescope is calculated by applying the same procedure with the relative proportion of the Telescope structure to the Total cost as known. For the price estimates of the optomechanical subsystems the values mentioned on the requirements specification chapter were used.

Item	unit	€ / unit	cost	ratio
Project Management			€ 8,687,281.62	13%
Project Engineering			€ 3,341,262.16	5%
Site infrastructure			€ 6,682,524.32	10%
Telescope structure			€ 10,023,786.49	15%
Steel structure			€ 7,417,602.0	74%
Raw material			€ 2,225,281	30%
Azimuth structure - base [tn]	379.24	1,800	€ 682,636	31%
Altitude structure - imaging sensor [tn]	406.12	1,800	€ 731,011	33%
Altitude structure - imaging reflector [tn]	72.72	1,800	€ 130,891	6%
Imaging sensor support structure [tn]	78.03	1,800	€ 140,445	6%
Imaging reflector [tn]	300.17	1,800	€ 540,299	24%
Fabrication			€ 3,337,921	45%
Construction			€ 1,483,520	20%
Transport			€ 370,880	5%
Foundations			€ 2,606,184	26%
Optomechanical subsystems			€ 33,260,000	47%
Actuators + mirror facets [m ²]	420	3,000	€ 1,260,000	4%
Image sensor	1	32,000,000.00	€ 32,000,000	96%
Instrumentation			€ 3,341,262.16	5%
Central Control Systems			€ 3,341,262.16	5%
TOTAL			€ 66,825,243	

Table 33: Cost estimation of the Alt-Azimuth design

The following charts show the relative proportions of the various cost-drive elements for the steel structure, for the optomechanical subsystems as well as for the whole Project. The ratios of the sub-structures in raw material price represent also the distribution of the steel weight among these structures as the same price for raw steel was implemented in the calculations. The foundations were also included in the calculation again by assuming a reasonable proportion to the whole structure. The image sensor is the biggest expense of the whole project as the estimation of the raw material price for its construction costs approximately 47% of the total cost.

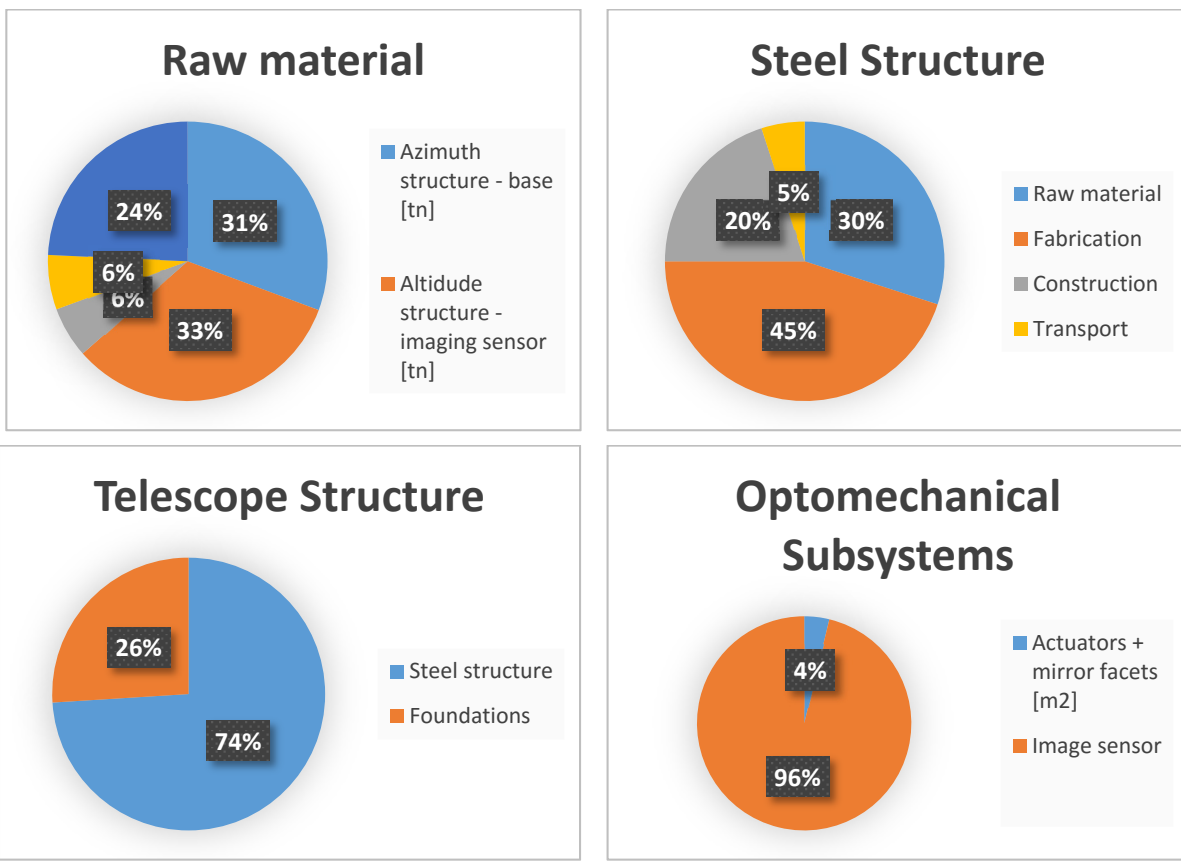


Table 34 Raw Material & Steel Structure cost distribution (top) and Telescope Structure and Optomechanical Systems cost distribution (bottom) of the Altitude-Azimuth design.

11.3 TheBigLebowSky

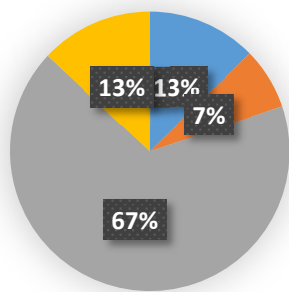
The same procedure applied to this design proposal. The main differences which affect the final cost are the concrete towers used for the suspension of the imaging reflector, the tension ring which had a heavy custom hollow steel section and the steel towers for the suspension of the image sensor. The most crucial of them are the steel towers which have a huge number of elements which require a further optimization in their design. Their weight could be significantly reduced and therefore the cost also. Nevertheless, this proposal has an innovative character not only from the structural part but also from the mechanical and kinetics point of view, which raises the uncertainties in the cost estimation as further research in both of these fields is needed. This model with the mentioned assumptions can although prove an adequate cost estimation.

The table shows the cost estimation of the TBLS project (TheBigLebowSky). The total cost is 18% higher than the one of the Alt-Azimuth design, although this difference as mentioned before is considered insignificant as the total uncertainty of the cost estimation along with the available space for further optimization of the TBLS project covers this percentage.

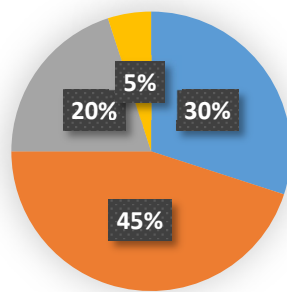
Item	unit	€ / unit	cost	ratio
Project Management			€ 10,313,051.36	13%
Project Engineering			€ 3,966,558.21	5%
Site infrastructure			€ 7,933,116.43	10%
Telescope structure			€ 15,866,232.86	20%
Steel structure			€ 10,402,854.0	70%
Raw material Steel			€ 3,120,856	30%
Imaging reflector [tn]	219.28	1,800	€ 394,699	13%
Cables - Imaging reflector [tn]	123.95	1,800	€ 223,105	7%
Imaging sensor & Towers [tn]	1,164.55	1,800	€ 2,096,181	67%
Cables - Imaging sensor [tn]	226.04	1,800	€ 406,872	13%
Fabrication			€ 4,681,284	45%
Construction			€ 2,080,571	20%
Transport			€ 520,143	5%
Concrete towers - imaging reflector	2,345.03	300	€ 703,509	
Foundations			€ 4,759,870	30%
Optomechanical subsystems			€ 33,260,000	42%
Actuators + mirror facets [m ²]	420	3,000	€ 1,260,000	4%
Image sensor	1	32,000,000.00	€ 32,000,000	96%
Instrumentation			€ 3,966,558.21	5%
Central Control Systems			€ 3,966,558.21	5%
TOTAL			€ 79,331,164	

Figure 147: The cost estimation of TheBigLebowSky design

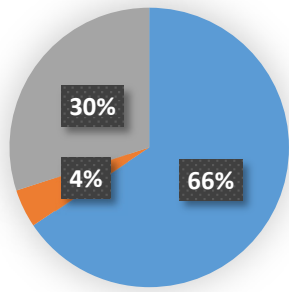
Raw material - Steel



Steel Structure



Telescope Structure



Optomechanical Subsystems

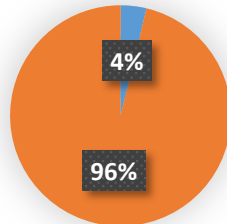


Table 35 Raw Material & Steel Structure cost distribution (top) and Telescope Structure and Optomechanical Systems cost distribution (bottom) of TheBigLebowSky design.

12 Conclusions

From the operational results of both the Altitude Azimuth concept, as well as from TheBigLebowSky, it is evident, that no major conclusions can be made. Both structures behave within acceptable limits and could be candidates for a future final proposal. TheBigLebowSky design is more promising in terms of manipulation of the displacements, but the technology needed to do so, poses a significant disadvantage. On the other hand, the Alt-Azimuth design is considered as a solid and stiff construction. Minor improvements could be implemented, but its overall performance could not be significantly improved.

In terms of cost estimation, it is observable that also no significant deviations occur. Even though the absolute values are not absolutely accurate and reliable at this point of the research, their comparison shows that both concepts cost the same.

In the future a thorough investigation of both concepts will be conducted and final conclusions will be made.

13 Bibliography

13.1 Cables and Arches

[19]–[22]

13.2 Carbon Fibre Reinforced Polymers

[17], [18], [23]–[25]

13.3 Existing telescopes

[1]–[3], [7], [26]–[50], [50]–[80]

13.4 Loading and site specifics

[4]–[6], [8]–[15]

13.5 Truss topology and optimization

[16], [81]–[89]

13.6 Bibliography table

- [1] M. Hayashida, K. Noda, M. Teshima, U. B. de Almeida, M. Chikawa, N. Cho, S. Fukami, A. Gadola, Y. Hanabata, D. Horns, C. Jablonski, H. Katagiri, M. Kagaya, M. Ogino, A. Okumura, T. Saito, R. Stadler, S. Steiner, U. Straumann, A. Vollhardt, H. Wetteskind, T. Yamamoto, T. Yoshida, and for the C. Consortium, “The Optical System for the Large Size Telescope of the Cherenkov Telescope Array,” 2015.
- [2] G. Pareschi, T. Armstrong, H. Baba, J. Bähr, A. Bonardi, G. Bonnoli, P. Brun, R. Canestrari, P. Chadwick, M. Chikawa, P.-H. Carton, V. de Souza, J. Dipold, M. Doro, D. Durand, M. Dyrda, A. Förster, M. Garczarczyk, E. Giro, J.-F. Glicenstein, Y. Hanabata, M. Hayashida, M. Hrabovski, C. Jeanney, M. Kagaya, H. Katagiri, L. Lessio, D. Mandat, M. Mariotti, C. Medina, J. Michalowski, P. Micolon, D. Nakajima, J. Niemiec, A. Nozato, M. Palatka, M. Pech, B. Peyaud, G. Pühlhofer, M. Rataj, G. Rodeghiero, G. Rojas, J. Rousselle, R. Sakonaka, P. Schovanek, K. Seweryn, C. Schultz, S. Shu, F. Stinzing, M. Stodulski, M. Teshima, P. Travniczek, C. van Eldik, V. Vassiliev, Ł. Wiśniewski, A. Wörlein, and T. Yoshida, “Status of the technologies for the production of the Cherenkov Telescope Array (CTA) mirrors,” p. 886103, 2013.
- [3] K. Seweryn, “Technologies of mirrors facets for the telescopes of the CTA observatory,” *Nucl. Phys.*, pp. 1–4, 2009.
- [4] T. Miyata, K. Motohara, S. Sako, M. Tanaka, T. Minezaki, N. Milani, T. Aoki, T. Soyano, T. Tanabe, K. Kawara, K. Kohno, K. Tarusawa, T. Handa, M. Doi, Y. Yoshii, H. Ezawa, L. Bronfman, and M. T. Ruiz, “Site evaluations of the summit of Co. Chajnantor for infrared observations,” *Ground-Based Airborne Telesc. II, Pts 1-3*, vol. 7012, pp. 1–8, 2008.
- [5] M. A. Holdaway, S. M. Foster, D. Emerson, J. Cheng, and F. Schwab, “Wind Velocities at the Chajnantor and Mauna Kea Sites and the Effect on MMA Pointing,” pp. 1–19, 1996.
- [6] S. J. E. Radford, R. Giovanelli, G. E. Gull, and C. P. Henderson, “Submillimeter observing

- conditions on Cerro Chajnantor," *Proc. SPIE*, vol. 7012, p. 70121Z–70121Z–7, 2008.
- [7] J.-L. Dournaux, J.-M. Huet, J.-P. Amans, D. Dumas, S. Blake, and H. Sol, "Seismic analysis of the 4-meter telescope SST-GATE for the Cherenkov Telescope Array," vol. 9145, p. 914558, 2014.
- [8] "Regional Seismological Centre for South America (CERESIS)," 2016. [Online]. Available: www.ceresis.org/.
- [9] "MMA Memo No . 250 National Radio Astronomy Observatory Seismicity and Seismic Hazard at MMA site , Antofagasta , Chile SERGIO E . BARRIENTOS Departamento de Geofisica Universidad de Chile," no. 250, 1996.
- [10] D. Hofstadt, E. S. Observatory, S. J. E. Radford, N. Radio, A. Observatory, and S. Sakamoto, "Alma Memo # 413 Physical Parameters of the Chajnantor Science Preserve," no. figure 1, pp. 1–12, 2002.
- [11] "1999 Athens earthquake," 2016. [Online]. Available: https://en.wikipedia.org/wiki/1999_Athens_earthquake. [Accessed: 01-Jan-2016].
- [12] "Great Hanshin earthquake," 2016. [Online]. Available: https://en.wikipedia.org/wiki/Great_Hanshin_earthquake.
- [13] T. Davis, "1994 Northridge earthquake," *Nature*, 1994. [Online]. Available: ftp://131.215.65.7/pub/avouac/Ge277-2008/Davis-Namson_Nature_1994.pdf.
- [14] "1940 El Centro earthquake," 2013. [Online]. Available: http://en.wikipedia.org/w/index.php?title=1940_El_Centro_earthquake&oldid=559183130.
- [15] Autodesk, "RSAP 2016 Assistant/Manual," 2016. [Online]. Available: <http://help.autodesk.com/view/RSAPRO/2016/ENU/>.
- [16] G. S. Ramaswamy, M. Eekhout, and G. R. Suresh, *Analysis, Design and Construction of Steel Space Frames*. 2002.
- [17] Hexcel, "Carbon fiber," pp. 1–17, 2015.
- [18] L. Artem, "Applying Carbon Fiber in Building," 2010.
- [19] J. B. Calvert, "The Catenary," 10 July 2000, 2011. [Online]. Available: <http://mysite.du.edu/%7Ejcalvert/math/catenary.htm>.
- [20] R. Osserman, "Mathematics of the Gateway Arch," *Not. AMS*, vol. 57, no. 2, pp. 220–229, 2010.
- [21] G. C. Marano, F. Trentadue, and F. Petrone, "Optimal arch shape solution under static vertical loads," *Acta Mech.*, vol. 225, no. 3, pp. 679–686, 2013.
- [22] I. Sasaki and I. Nishizaki, "Tensile Load Relaxation of Frp Cable System During Long-Term Exposure Tests," *6th Int. Conf. FRP Compos. Civ. Eng.*, pp. 1–8, 2012.
- [23] J. N. Coleman, U. Khan, W. J. Blau, and Y. K. Gun'ko, "Small but strong: A review of the mechanical properties of carbon nanotube-polymer composites," *Carbon N. Y.*, vol. 44, no. 9, pp. 1624–1652, 2006.
- [24] R. S. Ruoff and D. C. Lorents, "Mechanical and thermal properties of carbon nanotubes," *Carbon N. Y.*, vol. 33, no. 7, pp. 925–930, 1995.
- [25] T. Young, "Mechanical properties of carbon fiber from different manufacturers (Morgan , Table 1 . Properties of cellulose based Fibers Table 2 . Properties of PAN based Fibers," pp. 50–62, 2005.
- [26] M. Actis, G. Agnetta, F. Aharonian, et al, "Design concepts for the Cherenkov Telescope Array CTA: An advanced facility for ground-based high-energy gamma-ray astronomy," *Exp. Astron.*, vol. 32, no. 3, pp. 193–316, 2011.
- [27] G. Ambrosi, Y. Awane, H. Baba, et al, "The large size telescope of the Cherenkov Telescope Array," p. 91450P, 2014.
- [28] G. Ambrosi, Y. Awane, H. Baba, et al, "The large size telescope of the Cherenkov Telescope Array," vol. 9145, p. 91450P, 2014.
- [29] A. De Angelis, "Status of MAGIC and recent results," *Adv. Sp. Res.*, vol. 51, no. 2, pp. 280–285, 2013.
- [30] I. Appenzeller, G. Bo, M. a Dopita, M. Harwit, R. Kippenhahn, J. Lequeux, a Maeder, P. a Strittmatter, and V. Trimble, *ASTRONOMY AND Series Editors : The Design and Construction of Large Optical Telescopes*. 2002.
- [31] K. Bernlöhr, O. Carroll, R. Cornils, S. Elfahem, P. Espigat, S. Gillessen, G. Heinzelmann, G. Hermann, W. Hofmann, D. Horns, I. Jung, R. Kankanyan, A. Katona, B. Khelifi, H. Krawczynski, M. Panter, M. Punch, S. Rayner, G. Rowell, M. Tluczykont, and R. van Staa, "The optical system of the H.E.S.S. imaging atmospheric Cherenkov telescopes. Part I: Layout and components of

- the system," *Astropart. Phys.*, vol. 20, no. 2, pp. 111–128, 2003.
- [32] E. Brunetto, P. Dierickx, R. Gilmozzi, and M. Le Louarn, "Progress of ESO 's 100 -m OWL optical telescope design," *Spectroscopy*.
- [33] E. Brunetto, F. Koch, F. B. Marchet, and M. Dimmler, "Friction drive and bogies for OWL 's main axes , technological step backwards or cost effective alternative ?"
- [34] T. Butterley, "extremely large telescopes Telescopes," pp. 1–14, 2006.
- [35] R. Canestrari, T. Greenshaw, G. Pareschi, and R. White, "Technological developments toward the small size telescopes of the Cherenkov Telescope Array," *SPIE Proc.*, vol. 8444, no. Lc, pp. 1–14, 2012.
- [36] P. A. Castleberg and K. M. Xilouris, "Arecibo observatory," *IEEE Potentials*, vol. 16, no. 3, pp. 33–35, 38, 1997.
- [37] J. Cortina and others, "Technical Performance of the MAGIC Telescopes," *29th Int. Cosm. Ray Conf. Pune*, pp. 10–13, 2005.
- [38] C. Deil, C. Van Eldik, A. Förster, G. Hermann, W. Hofmann, and M. Panter, "H.E.S.S. II - Telescope structure, reflector and drive system," *AIP Conf. Proc.*, vol. 1085, pp. 693–695, 2009.
- [39] P. Dierickx, J.-L. Beckers, E. Brunetto, R. Conan, E. Fedrigo, R. Gilmozzi, N. N. Hubin, F. Koch, M. Le Louarn, E. Marchetti, G. J. Monnet, L. Noethe, M. Quattri, M. S. Sarazin, J. Spyromilio, and N. Yaitskova, "<title>The eye of the beholder: designing the OWL</title>," *Design*, pp. 151–170, 2003.
- [40] M. Doro, "CTAA project for a new generation of Cherenkov telescopes," *Nucl. Instruments Methods Phys. Res. Sect. A Accel. Spectrometers, Detect. Assoc. Equip.*, vol. 630, no. 1, pp. 285–290, 2011.
- [41] B. Y. Duan, "Review of antenna structural design with mechatronics in China," *Mechatronics*, vol. 12, no. 5, pp. 657–667, 2002.
- [42] B. Y. Duan and J. L. Du, "On analysis and optimization of an active cable-mesh main reflector for a giant Arecibo-type antenna structural system," *IEEE Trans. Antennas Propag.*, vol. 55, no. 5, pp. 1222–1229, 2007.
- [43] P. Emde, W. Hofmann, and H. J. Karcher, "<title>Design studies on large Cherenkov telescopes</title>," vol. 5489, pp. 526–536, 2004.
- [44] S. Engineering, N. M. Street, and M. Wi, "Design concepts for primary mirror support structures of large telescopes for optical and submillimeter astronomy," vol. 7012, pp. 1–11, 2008.
- [45] ESO, "9.Telescope structure and kinematics," *Telesc. Struct. Kinemat.*, 2006.
- [46] European Southern Observatory, "THE E-ELT construction proposal," p. 268, 2009.
- [47] R. Gilmozzi and J. Spyromilio, "The 42m European ELT: Status," *Proc. SPIE*, vol. 7012, no. Ground-based and Airborne Telescopes II, pp. 701219–1 – 701219–10, 2008.
- [48] X. Gong, K. Chen, and X. Cui, "A unique truss for large segmented-mirror telescope," vol. 6273, p. 627337, 2006.
- [49] J. Holder, R. W. Atkins, H. M. Badran, G. Blaylock, S. M. Bradbury, J. H. Buckley, K. L. Byrum, D. A. Carter-Lewis, O. Celik, Y. C. K. Chow, P. Cogan, W. Cui, M. K. Daniel, I. de la Calle Perez, C. Dowdall, P. Dowkontt, C. Duke, A. D. Falcone, S. J. Fegan, J. P. Finley, P. Fortin, L. F. Fortson, K. Gibbs, G. Gillanders, O. J. Glidewell, J. Grube, K. J. Gutierrez, G. Gyuk, J. Hall, D. Hanna, E. Hays, D. Horan, S. B. Hughes, T. B. Humensky, A. Imran, I. Jung, P. Kaaret, G. E. Kenny, D. Kieda, J. Kildea, J. Knapp, H. Krawczynski, F. Krennrich, M. J. Lang, S. LeBohec, E. Linton, E. K. Little, G. Maier, H. Manseri, A. Milovanovic, P. Moriarty, R. Mukherjee, P. A. Ogden, R. A. Ong, D. Petry, J. S. Perkins, F. Pizlo, M. Pohl, J. Quinn, K. Ragan, P. T. Reynolds, E. T. Roache, H. J. Rose, M. Schroedter, G. H. Sembroski, G. Sleige, D. Steele, S. P. Swordy, A. Syson, J. A. Toner, L. Valcarcel, V. V. Vassiliev, S. P. Wakely, T. C. Weekes, R. J. White, D. A. Williams, and R. Wagner, "The first VERITAS telescope," *Astropart. Phys.*, vol. 25, no. 6, pp. 391–401, 2006.
- [50] J. E. Ingvaldsen, ??zlem ??zg??bek, and J. A. Gulla, "Context-aware user-driven news recommendation," *CEUR Workshop Proc.*, vol. 1542, pp. 33–36, 2015.
- [51] P. R. Jewell and R. M. Prestage, "<title>The Green Bank Telescope</title>," vol. 5489, pp. 312–323, 2004.
- [52] H. J. Kaercher, "<title>Experience with the design and construction of huge telescope pedestals</title>," vol. 5382, pp. 233–244, 2004.
- [53] H. J. Kaercher, "<title>Azimuth axis design for huge telescopes: an update</title>," vol. 5495, pp. 67–76, 2004.

- [54] H. J. Kärcher, "Large Telescopes and the Art of Bridge Building," vol. 7012, pp. 1–12, 2008.
- [55] H. J. Kärcher, "Telescope structures worldwide," *Steel Constr.*, vol. 2, no. 3, pp. 149–160, 2009.
- [56] H. J. Kärcher and J. W. M. Baars, "Ideas for future large single dish radio telescopes," vol. 9145, p. 914503, 2014.
- [57] H. J. Kärcher, J. W. M. Baars, M. A. N. Technologie, and G. Gustavburg, "The Design of the Large Millimeter Telescope I Gran Telescopio Milimetrico (LMTIGTM)," vol. 4015, pp. 155–168, 2000.
- [58] F. Krennrich, I. H. Bond, P. J. Boyle, S. M. Bradbury, J. H. Buckley, D. Carter-Lewis, O. Celik, W. Cui, M. Daniel, M. D'Vali, I. de la Calle Perez, C. Duke, A. Falcone, D. J. Fegan, S. J. Fegan, J. P. Finley, L. F. Fortson, J. Gaidos, S. Gammell, K. Gibbs, G. H. Gillanders, J. Grube, J. Hall, T. A. Hall, D. Hanna, A. M. Hillas, J. Holder, D. Horan, A. Jarvis, M. Jordan, G. E. Kenny, M. Kertzman, D. Kieda, J. Kildea, J. Knapp, K. Kosack, H. Krawczynski, M. J. Lang, S. LeBohec, E. Linton, J. Lloyd-Evans, A. Milovanovic, P. Moriarty, D. M??ller, T. Nagai, S. Nolan, R. A. Ong, R. Pallassini, D. Petry, B. Power-Mooney, J. Quinn, M. Quinn, K. Ragan, P. Rebillot, P. T. Reynolds, H. J. Rose, M. Schroedter, G. Sembroski, S. P. Swordy, A. Syson, V. V. Vassiliev, G. Walker, S. P. Wakely, T. C. Weekes, and J. Zweerink, "VERITAS: The Very Energetic Radiation Imaging Telescope Array System," *New Astron. Rev.*, vol. 48, no. 5–6, pp. 345–349, 2004.
- [59] E. Lorenz, "Status of the 17 m ??? MAGIC telescope," *New Astron. Rev.*, vol. 48, no. 5–6, pp. 339–344, 2004.
- [60] E. Lorenz and M. Martinez, "The MAGIC telescope," *Astron. Geophys.*, vol. 46, no. 6, pp. 247–252, 2005.
- [61] A. McPherson, R. Gilmozzi, J. Spyromillo, M. Kissler-Patig, and S. Ramsay, "Recent Progress Towards the European Extremely Large Telescope (E-ELT)," *ESO Messenger*, vol. 148, no. June, pp. 2–8, 2012.
- [62] J. Melorose, R. Perroy, and S. Careas, "No Title No Title," *Statew. Agric. L. Use Baseline 2015*, vol. 1, 2015.
- [63] M. H. Merck, E. Lorenz, and R. Mirzoyan, "<title>MAGIC 2: an ultimate imaging Cherenkov telescope</title>," *Proc. SPIE - Int. Soc. Opt. Eng.*, vol. 4858, pp. 327–337, 2003.
- [64] R. Mirzoyan, "Brief history of ground-based very high energy gamma-ray astrophysics with atmospheric air Cherenkov telescopes," *Astropart. Phys.*, vol. 53, no. C, pp. 91–99, 2014.
- [65] K. Miura and Y. Miyazakit, "Concept of the Tension Truss Antenna," vol. 28, no. 6, pp. 1098–1104, 1989.
- [66] R. NAN, D. LI, C. JIN, Q. WANG, L. ZHU, W. ZHU, H. ZHANG, Y. YUE, and L. QIAN, "the Five-Hundred-Meter Aperture Spherical Radio Telescope (Fast) Project," *Int. J. Mod. Phys. D*, vol. 20, no. 06, pp. 989–1024, 2011.
- [67] Y. Qiu, "A novel design for giant radio telescopes with an active spherical main reflector," *Chinese Astron. Astrophys.*, vol. 22, no. 3, pp. 361–368, 1998.
- [68] N. Radio, A. Observatory, P. O. Box, and G. Bank, "The Green Bank Telescope," vol. 6267, no. March, pp. 1–15, 2006.
- [69] R. Rashad, "Dynamics of the arecibo radio telescope," no. February, 2005.
- [70] J. Rousselle, K. Byrum, R. Cameron, V. Connaughton, M. Errando, S. Griffiths, V. Guarino, T. B. Humensky, P. Jenke, P. Kaaret, D. Kieda, M. Limon, I. Mognet, R. Mukherjee, D. Nieto, A. Okumura, A. Peck, A. Petrashyk, D. Ribeiro, B. Stevenson, V. Vassiliev, and P. Yu, "Toward the construction of a medium size prototype Schwarzschild-Couder telescope for CTA," *Proc. SPIE - Int. Soc. Opt. Eng.*, vol. 9603, p. 960305, 2015.
- [71] T. A. Sebring, S. T. Project, N. Optical, A. Observatories, F. N. Bash, F. B. Ray, M. Observatory, L. W. Ramsey, and D. Lali, "The Extremely Large Telescope: Further Adventures in Feasibility," vol. 3352, no. March, pp. 792–800, 1998.
- [72] G. support Staff, "The Proposer 's Guide for the Green Bank Telescope," 2013.
- [73] Y. X. Su and B. Y. Duan, "Mechanical design and kinematics accuracy analysis of a fine tuning stable platform for the large spherical radio telescope," *Mechatronics*, vol. 10, no. 7, pp. 819–834, 2000.
- [74] A. T. Tokunaga and R. Jedicke, "New Generation Ground-Based Optical/ Infrared Telescopes," 2007.
- [75] G. T. van Belle, A. B. Meinel, and M. P. Meinel, "The Scaling Relationship Between Telescope Cost and Aperture Size for Very Large Telescopes," *Astron. Telesc. Instrum.*, vol. 5489, pp. 563–570, 2004.

- [76] S. von Hoerner, "Design of large steerable antennas," *Astron. J.*, vol. 72, p. 35, 1967.
- [77] Q. Wang, L. Zhu, and R. Nan, "Development of active reflector of the 30-meter FAST model," *Proc. SPIE*, vol. 7018, no. 2008, p. 70184A–70184A–8, 2008.
- [78] D. Yang, S. Xue, D. Wang, W. Lu, and J. Cheng, "<title>Design of a 50-m pulsar radio telescope</title>," *Millim. Submillim. Detect. Astron. Ed. by Phillips, Thomas G.; Zmuidzinas, Jonas. Proc. SPIE*, Vol. 4855, pp. 528-539 (2003)., vol. 4855, pp. 528–539, 2003.
- [79] "The future of filled aperture telescopes_ OWL.pdf."
- [80] "OWL-TRE-ESO-0000-0001 Issue 2," vol. OWL - Blue, no. 2.
- [81] F. Dinu, "Mast, towers, chimneys," 2014.
- [82] J. D. Dolan, *Handbook of Structural Engineering, Second Edition*. 2005.
- [83] A. Kaveh and S. Talatahari, "Particle swarm optimizer, ant colony strategy and harmony search scheme hybridized for optimization of truss structures," *Comput. Struct.*, vol. 87, no. 5–6, pp. 267–283, 2009.
- [84] K. Knebel, M. Wahl, and M. Maloblocki, "Raumfachwerke für große Spannweiten," 2008.
- [85] S. Krenk and J. Høgsberg, *Statics and mechanics of structures*. 2013.
- [86] S. Page, M. Midi, and M. Midi, "M12 Plus System M12 Midi M6 System Bauteilkatalog , Preisliste 2010 Component Catalogue , Price List 2010," 2010.
- [87] L. A. SCHMIT and B. FARSHI, "Some Approximation Concepts for Structural Synthesis," *AIAA J.*, vol. 12, no. 5, pp. 692–699, 1974.
- [88] J. Smith, J. Hodgins, I. Oppenheim, and A. Witkin, "Creating models of truss structures with optimization," *ACM Trans. Graph.*, vol. 21, no. 3, pp. 295–301, 2002.
- [89] S. Truss, "Structural Analysis : Space Truss Space Truss Analysis : Method of Joints • Method of Joints."